UNIVERSITY OF SOUTHAMPTON

FACULTY OF ENGINEERING AND THE ENVIRONMENT

Aerodynamics and Flight Mechanics

Aerodynamic Noise from Undulated Leading Edge Aerofoils

by

Jacob Mansel Turner

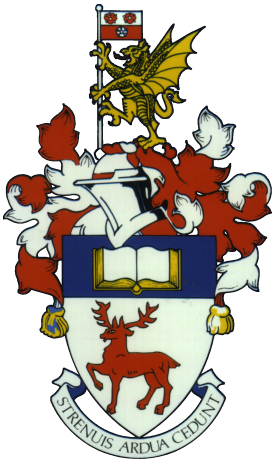

Thesis for the degree of Doctor of Philosophy

May 2, 2019

UNIVERSITY OF SOUTHAMPTON

ABSTRACT

FACULTY OF ENGINEERING AND THE ENVIRONMENT
Aerodynamics and Flight Mechanics

AERODYNAMIC NOISE FROM UNDULATED LEADING EDGE AEROFOILS

by Jacob Mansel Turner

A series of high fidelity numerical simulations are conducted to investigate the noise generated by aerofoils undergoing interaction with vortical disturbances. In particular the focus is on aerofoil leading edge undulations, which have been previously shown to effectively reduce broadband interaction noise. The main objective of this work is to ascertain a comprehensive understanding of the physical mechanisms behind the noise reductions, which to a large extent are still unexplained. The simulations are based on the interaction of zero thickness aerofoils with a prescribed spanwise vortex model. The approach is particularly convenient in that it captures non-linear motions, while also maintaining a clean broadband spectra which aids in identifying fundamental trends. The work is split into two main sections, primary leading edge and secondary trailing edge mechanisms. In the first half a number of unique findings are presented concerning the aeroacoustic source mechanisms of the wavy leading edge (WLE). One of the most significant findings is the generation of horseshoe vortex systems which are directly linked to source differences observed at the WLE peak and root. Both source strength reduction and destructive interference mechanisms are investigated in order to determine their contribution towards an increasing noise reduction vs. frequency trend. It is found how the source characteristics over the full surface need to be considered in order to avoid erroneous interpretations of the physics. The findings therefore have important consequences for future approaches concerning which characteristics are crucial for modelling the WLE. In the latter half of the work, the secondary interaction noise sources are investigated in detail. This includes both acoustic backscattering (ABS) and trailing edge vortical scattering (TEVS) effects. Surprising discoveries are made concerning the importance of TEVS at high frequencies, particularly when a WLE is concerned. The TEVS is investigated for both inviscid and viscous flows, and found to be highly dependent on Reynolds number and vortex strength. This highlights an important limitation to WLE performance for implementation purposes, as well as a possible avenue for future research.

Declaration of Authorship

I, Jacob Mansel Turner , declare that the thesis entitled *Aerodynamic Noise from Undulated Leading Edge Aerofoils* and the work presented in the thesis are both my own, and have been generated by me as the result of my own original research. I confirm that:

- this work was done wholly or mainly while in candidature for a research degree at this University;
- where any part of this thesis has previously been submitted for a degree or any other qualification at this University or any other institution, this has been clearly stated;
- where I have consulted the published work of others, this is always clearly attributed;
- where I have quoted from the work of others, the source is always given. With the exception of such quotations, this thesis is entirely my own work;
- I have acknowledged all main sources of help;
- where the thesis is based on work done by myself jointly with others, I have made clear exactly what was done by others and what I have contributed myself;
- parts of this work have been published, as listed in: §1.6.2

Signed:.....

Date:.....

Contents

Declaration of Authorship v

Acknowledgements xxiii

Nomenclature xxv

1 Introduction 1
- 1.1 Research motivation . . . 1
- 1.2 Analytical modelling of aerofoil interaction noise . . . 3
  - 1.2.1 Amiet's model and extensions . . . 3
  - 1.2.2 Rapid distortion theory . . . 5
  - 1.2.3 Theory of vortex sound . . . 6
- 1.3 Effects of realistic geometry and flow conditions . . . 7
  - 1.3.1 Synthetic turbulence approaches . . . 10
- 1.4 Leading edge undulation . . . 11
  - 1.4.1 Previous studies on leading edge undulation . . . 13
    - 1.4.1.1 Aerodynamic performance of undulated aerofoils . . . 13
    - 1.4.1.2 Previous experimental and numerical work on WLE noise reduction 14
    - 1.4.1.3 Analytical predictions for WLE noise reduction . . . 17
    - 1.4.1.4 Improved WLE geometries . . . 19
- 1.5 Research aims and objectives . . . 20
- 1.6 Original contributions . . . 20
  - 1.6.1 Thesis outline . . . 21
  - 1.6.2 List of publications and conference proceedings . . . 23

2 Computational Methodology 25
- 2.1 Current computational approach . . . 25
  - 2.1.1 Computational domain and aerofoil geometry . . . 26
  - 2.1.2 Sponge treatment . . . 27
  - 2.1.3 Governing equations . . . 29
  - 2.1.4 Numerical methods . . . 30
    - 2.1.4.1 Spatial discretisation . . . 30
    - 2.1.4.2 Temporal discretisation . . . 34
  - 2.1.5 Algorithm for compact schemes . . . 35
  - 2.1.6 Boundary conditions . . . 37
    - 2.1.6.1 Inflow condition . . . 39
    - 2.1.6.2 Non-reflecting outflow . . . 39
    - 2.1.6.3 Wall boundary conditions . . . 40

2.1.6.4 Characteristic interface at block boundaries . . . 40
2.1.7 Parallel routines . . . 41
2.1.8 Definition of variables for post-processing . . . 42
2.1.9 Signal processing routines . . . 42

3 Primary Leading Edge Source Mechanisms 45
3.1 Problem description and computational set-up . . . 45
3.1.1 Prescribed spanwise vortex model . . . 45
3.1.2 Computational grid . . . 46
3.2 Initial findings and the questions emerged . . . 48
3.2.1 Wall and acoustic pressure fluctuations . . . 48
3.2.2 Horseshoe vortex systems induced by WLE . . . 51
3.3 Consistent source strength at the root . . . 54
3.4 Variations in source strength at the peak . . . 57
3.5 Additional findings and discussions . . . 62
3.5.1 WLE aspect ratio and source strength . . . 62
3.5.2 The effect of a three-dimensional profile in the impinging vortex . . . 64
3.6 Concluding remarks . . . 65

4 Noise Reduction Modelling and Underlying Mechanisms 67
4.1 Motivation . . . 67
4.2 Problem description and computational set-up . . . 69
4.2.1 Prescribed spanwise vortex model . . . 69
4.2.2 Computational grid and domain . . . 70
4.3 Observed noise reduction trends . . . 72
4.4 One-dimensional modelling of the leading edge . . . 75
4.4.1 Effective source length . . . 75
4.4.2 LE phase interference modelling . . . 76
4.4.3 Influence of realistic source on leading-edge model . . . 78
4.5 Consideration of distributed source . . . 80
4.5.1 Surface source distribution . . . 80
4.5.2 Quantification of destructive interference and source reduction mechanisms 86
4.6 Concluding remarks . . . 90

5 Secondary Noise Sources 93
5.1 Problem background . . . 93
5.1.1 Description of problem and the computational set-up . . . 95
5.2 The secondary sources associated with aerofoil vortex interaction . . . 95
5.2.1 Initial findings . . . 97
5.2.2 Dominance of TE vortical scattering at high frequencies . . . 99
5.3 The effect of vertical miss distance . . . 103
5.4 Provision for analytical predictions . . . 104
5.5 The effect of flow viscosity on TE vortex scattering . . . 107
5.5.1 Grid independence study for viscous simulations . . . 108
5.5.2 Weak vortex interactions . . . 108
5.5.3 Impact of high vortex strength . . . 110
5.5.4 Three-dimensional effects . . . 113

5.6 Concluding remarks . . . 117

6 The Effect of WLEs on Secondary Sources 119
6.1 The secondary sources associated with a wavy leading edge . . . 119
6.1.1 Initial findings . . . 120
6.1.2 Dominance of TE vortical scattering at high frequencies . . . 122
6.2 Phase relationships between noise sources . . . 123
6.3 The effect of secondary sources on acoustic directivity . . . 126
6.4 Undulated trailing edge . . . 131
6.5 WLEs with a laminar boundary layer profile . . . 134
6.6 Concluding remarks . . . 137

7 Conclusions and Future Work 141
7.1 Summary of findings . . . 141
7.2 Future work arising from this study . . . 143

A Sensitivity test for the measure of interaction obliqueness 144

B Discussion of vortex models 145

C Additional noise reduction trends 148
C.1 Sensitivity of results to vortex parameters . . . 148
C.2 Effect of leading edge wavelength for a spanwise infinite disturbance . . . 150

D Additional analysis of WLE TEVS response 152
D.1 Wall pressure observations . . . 152
D.2 Application of Howe's theory . . . 154
D.3 Dynamic mode decomposition . . . 155

E Dual-wavelength wavy leading edges 159

F Signal processing code 162

References 163

List of Figures

1.1 Aircraft noise contributions during take-off and approach conditions. Taken from: Astley *et al.* (2007). 1

1.2 (a) Leading Edge Vortex Scattering (LEVS). (b) Acoustic Back-Scattering (ABS) at the TE. (c) Trailing Edge Vortex Scattering (TEVS). 3

1.3 (a) Leading edge tubercles of the humpback whale's pectoral flipper (photo credit: Robbie Shade flickr.com) (b): Leading edge serrations of a Barn Owl's flight feather, (photo credit: Kay Schultz). 12

1.4 (a) Acoustic pressure contours generated during aerofoil-turbulence-interaction (ATI) by a flat plate aerofoil with a straight leading edge (SLE). (b) Equivalent plot for a wavy leading edge (WLE) geometry. Taken from: (Kim & Haeri, 2015; Kim *et al.*, 2016). 12

2.1 (a) Previous synthetic turbulence approach based on randomly distributed Gaussian eddies (Kim *et al.*, 2016). (b) Current aerofoil-vortex interaction approach. 26

2.2 Surface meshes (coarsened for illustration purposes) on the flat-plate aerofoils used in the present study, with (a) straight and (b) wavy leading edges (SLE and WLE, respectively). The case of $h_{LE}/L_c = 1/15$ and $\lambda_{LE}/L_c = 2/15$ is shown in this figure. Specific details of the grid resolution are contained within the relevant results sections. 26

2.3 Sponge coefficient profiles 28

2.4 Modified wavenumber curves produced by a standard 2nd order central scheme, and 4th order compact used in the current methodology Kim (2007) 34

2.5 Real and imaginary modified wavenumber curves produced by boundary closure schemes used in the current methodology Kim (2007) 35

2.6 Effect of varying window length on the calculation of the Fourier transform. (a) Semi-infinite chord length WLE simulation. (a) Finite-infinite chord. 44

2.7 Effect of varying window shape on the calculation of the PSD (2.60). (a) Semi-infinite chord WLE simulation. (a) Finite-infinite chord. 44

3.1 The initial velocity field induced by the spanwise vortex model given by (3.2): (a) induced velocity magnitude contours and (b) the vertical velocity profile along the centreline ($y = 0$). 45

3.2 Description of the current problem: a prescribed spanwise vortex impinging on a thin aerofoil with a wavy leading edge: (a) schematic diagram, (b) initial condition, (c) during the interaction and (d) after the interaction. 47

3.3 A grid convergence test of the current numerical simulation by using three different levels of grid resolution, based on the far-field acoustic pressure signal (p_a/p_∞) and its PSD (S_{ppa}/p_∞^2) obtained at the observer point $\boldsymbol{x}_0 = (0, 5L_c, 0)$ for $h_{LE}/L_c = 1/15$ and $\lambda_{LE}/L_c = 2/15$ (corresponding to figure 3.5). 48

3.4 Fluctuating wall pressure time signals, $\Delta p_w(t^*)/p_\infty$, and the corresponding power spectral density (PSD), $S_{ppw}(f^*)/p_\infty^2$, obtained at three different locations on the WLE (peak, hill centre and the root) for three different values of the WLE amplitude ($h_{LE}/L_c = 1/30$, $1/15$ and $1/10$) with its wavelength fixed ($\lambda_{LE}/L_c = 2/15$), compared with the SLE baseline case. 49
3.5 Far-field acoustic pressure time signals, $p'_a(t^*)/p_\infty$, the corresponding PSD, $S_{ppa}(f^*)/p_\infty^2$, and the relative noise reduction spectra, $\Delta SPL(f^*)$, obtained at an observer location, $\boldsymbol{x}_o = (0, 5L_c, 0)$, from three different WLE geometries ($h_{LE}/L_c = 1/30$, $1/15$ and $1/10$ with $\lambda_{LE}/L_c = 2/15$), compared with the SLE baseline case. 50
3.6 Snapshots of WLE-vortex interaction in temporal order: contour plots for perturbed acoustic pressure (p'_a/p_∞), spanwise vorticity ($\omega_z L_c/a_\infty$) and the Q-criterion ($||\Omega_{ij}L_c/a_\infty||^2 - ||S_{ij}L_c/a_\infty||^2$ where Ω_{ij} and S_{ij} are the vorticity and rate-of-strain tensors, respectively). The figures show secondary vortices (Q-criterion) and sound waves (p'_a/p_∞) generated at the leading edge during the interaction. The bottom left corner of images (b)–(f) provides a zoomed out perspective visualising the radiating sound waves. $h_{LE}/L_c = 1/30$. 52
3.7 Q-criterion iso-surfaces coloured by streamwise vorticity ($\omega_x L_c/a_\infty$) taken at two different points in time during (a) the downwash and (b) upwash strokes of the impinging vortex. The red and blue surfaces indicate positive (clockwise) and negative (anti-clockwise) rotations around the x-axis, respectively. The dashed yellow curves indicate the WLE-induced horseshoe vortex systems. 53
3.8 Simplified illustration of the WLE-induced vorticity distribution exhibited in Figures 3.6 and 3.7: (a) the sideview on the WLE showing the contribution of spanwise vorticity components induced during the downwash stroke of the impinging vortex; and, (b) the frontview on the WLE describing the streamwise vorticity contribution creating an upwash at the peak and a downwash at the root as a result. 53
3.9 The distribution of maximum values (taken from time signals) of the perturbed vertical velocity ($|v|_{max}/a_\infty$) and the vorticity magnitude ($|\boldsymbol{\omega}|_{max}L_c/a_\infty$) on the horizontal plane ($y = 0$): (a/b) for a SLE baseline case and (c/d) for a WLE case with $h_{LE}/L_c = 1/15$. The vertical velocity plots are shown in the flow field only, and the vorticity magnitude plots on the aerofoil's upper surface only. 54
3.10 A comparison between the induced vertical velocity and wall pressure fluctuation (v/a_∞ and $\Delta p_w/p_\infty$) at the WLE root for various WLE amplitudes (h_{LE}/L_c): (a) time signals of v/a_∞ obtained one grid point upstream of the root; (b) time signals of $\Delta p_w/p_\infty$ obtained one grid point downstream of the root; (c) an instantaneous contour plot of v/a_∞ taken at $t^* = 8.08$ (when the induced vertical velocity reaches its maximum, for $h_{LE}/L_c = 1/15$) indicating an oblique interaction with the root, where the value 0.0098 is the maximum of the SLE baseline case; and, (d) time signals of $v\cos[(\phi_1 + \phi_2)/2]/a_\infty$ which includes the obliqueness effect. The values of ϕ_1 and ϕ_2 are listed in table 3.2. 55
3.11 Spectral similarity at the root between the wall pressure fluctuation and the induced vertical velocity including the obliqueness effect: (a) PSD of $\Delta p_w/p_\infty$ and (b) PSD of $v\cos\phi/a_\infty$ from figure 3.10b and 3.10d, respectively. 55
3.12 Mean vertical velocity signals calculated from (3.5) around the root area for various values of h_{LE}/L_c (WLE amplitude), in relation to the consistent source strength at the root irrespective of h_{LE}. 57

3.13 Instantaneous contour plots of streamwise vorticity ($\omega_x L_c/a_\infty$: left) and spanwise vorticity ($\omega_z L_c/a_\infty$: right) on the upper surface of the aerofoil for three different WLE amplitudes, obtained when the induced vertical velocity in front of the peak reaches its maximum amplitude: (a/b) $ta_\infty/L_c = 7.540$, (c/d) 7.461 and (e/f) 7.305 – see figure 3.15*a*. 58

3.14 Vorticity distributions in span along the leading edge for various values of h_{LE}/L_c obtained when the induced vertical velocity in front ot the peak reaches its maximum amplitude: (a) streamwise vorticity ($\omega_x L_c/a_\infty$) and (b) spanwise vorticity ($\omega_z L_c/a_\infty$) on the upper surface of the aerofoil – see figure 3.13. The spanwise coordinate of the peak is denoted by z_0 in the x-axis labels. 59

3.15 A comparison between the induced vertical velocity and wall pressure fluctuation (v/a_∞ and $\Delta p_w/p_\infty$) at the WLE peak for various WLE amplitudes (h_{LE}/L_c): (a) time signals of v/a_∞ obtained one grid point upstream of the peak; and, (b) time signals of $\Delta p_w/p_\infty$ obtained one grid point downstream of the peak. The case with "Free field" indicates a free-field solution (without the aerofoil) recorded at $(x, y) = (-0.7L_c, 0)$. 59

3.16 Schematic of the horseshoe vortex (HV) system used to estimate the WLE-induced vertical velocity in front of the peak, in relation to (3.8). 60

3.17 Semi-analytic predictions of the HV-induced vertical velocity components in front of the peak, obtained by using (3.8) for various values of h_{LE}/L_c. The predictions are made at $ta_\infty/L_c = 7.770$, 7.540, 7.461 and 7.305 for $h_{LE}/L_c = 0$, 1/30, 1/15 and 1/10, respectively, when the vertical velocity reaches its maximum amplitude (see figure 3.15). 61

3.18 Profiles of $\mathrm{d}v_A/\mathrm{d}z$ (normalised by a_∞ and L_c) from (3.8): (a) entire and (b) zoomed-up views, showing local piecewise contributions of the bound vortex to the overall induced vertical velocity in front of the peak resulted in figure 3.17. 61

3.19 Far-field acoustic pressure PSD profiles, $S_{ppa}(f^*)/p_\infty^2$, obtained at an observer location, $\boldsymbol{x}_o = (0, 5L_c, 0)$, for three different WLE aspect ratios ($AR = 2h_{LE}/\lambda_{LE} = 0.5$, 1 and 1.5). The aspect ratios with "$*$" indicate that the size of the WLE is doubled ($AR^* = 2h^*_{LE}/\lambda^*_{LE}$ where $h^*_{LE} = 2h_{LE}$ and $\lambda^*_{LE} = 2\lambda_{LE}$). The dotted curves are from the SLE baseline case. 62

3.20 Wall pressure PSD profiles, $S_{ppw}(f^*)/p_\infty^2$, obtained at three different locations on the WLE (peak, hill centre and the root) for three different WLE aspect ratios ($AR = 2h_{LE}/\lambda_{LE} = 0.5$, 1 and 1.5). The aspect ratios with "$*$" indicate that the size of the WLE is doubled ($AR^* = 2h^*_{LE}/\lambda^*_{LE}$ where $h^*_{LE} = 2h_{LE}$ and $\lambda^*_{LE} = 2\lambda_{LE}$). 63

3.21 Schematics of a wavy vortex (WV) interacting with three different leading-edge geometries: (a) SLE, (b) WLE and (c) the WLE inverted. The centreline of the wavy vortex is undulated along the span in the same fashion applied to the WLE profile – based on (2.2). The inverted WLE (IWLE) has an out-of-phase formation against the prescribed WV. 64

3.22 Far-field acoustic pressure time signals and the corresponding PSD: (a) $p_a(t^*)/p_\infty$ and (b) $S_{ppa}(f^*)/p_\infty^2$ obtained at an observer location, $\boldsymbol{x}_o = (0, 5L_c, 0)$, from the additional simulations described in figure 3.21. The new results are compared with the earlier cases (SV-SLE and SV-WLE) that used a straight vortex. The WLE and WV profiles are based on $h_{LE}/L_c = 1/30$ and $\lambda_{LE}/L_c = 2/15$. 64

4.1 Grid-dependency test for the acoustic power spectra obtained at $\boldsymbol{x}_o/L_c = (0, 5, 0)$ based a finite chord aerofoil using three different levels of grid resolution described in table 4.1: (a) SLE; (b) a comparison to the background noise level produced on the SLE grid; (c) WLE $h_{LE}/L_c = 1/15$ and $\lambda_{LE}/L_c = 2/15$; (d) comparison to the background noise level produced on the WLE grid. 71
4.2 Grid dependence test for the acoustic directivity based a finite chord aerofoil. (a) and (b) SLE $f^* = 2$ and 6. (c) and (d) WLE ($h_{LE}/L_c = 1/15$ and $\lambda_{LE}/L_c = 2/15$) $f^* = 2$ and 6. 72
4.3 (a) Vertical velocity profile produced by stationary vortex in the centre of the skewed grid (aerofoil LE) at various times. (b) Corresponding wavenumber spectrum. . . . 73
4.4 Acoustic pressure data obtained at observer $\boldsymbol{x}_o/L_c = (0, 5, 0)$ for SLE and three WLE geometries with differing amplitude ($h_{LE}/L_c = 1/20$, $1/15$ & $1/10$, $\lambda/L_c = 2/15$). (a) time signals of $p_a(\boldsymbol{x}_o, t)/p_\infty$; (b) the corresponding power spectra; (c) an instantaneous contour plot of $p_a(\boldsymbol{x}_o, t^* = 7.34)/p_\infty$ taken at mid-span ($z = 0$) for the SLE case; and, (d) LE source strength (wall power spectra) for the SLE, WLE Peak, Hill centre and Root, taken one grid point downstream of the LE with $h_{LE}/L_c = 1/15$. 74
4.5 (a) Noise reduction spectra ($\Delta SPL(\boldsymbol{x}_o, f^*_{h_{LE}})$) obtained for the three WLE amplitudes at observer $\boldsymbol{x}_o/L_c = (0, 5, 0)$. (b) Noise reduction re-plot vs Strouhal number (based on WLE amplitude) $f^* = fh_{LE}/U_\infty$ demonstrating the linear trend in question. Comparison is also made to the experimental data obtained by Chaitanya *et al.* (2017) for $h_{LE}/L_c = 1/10$ at the optimum wavelength $\lambda/\Lambda = 4$. 75
4.6 Effective source edge lengths $\mathcal{L}$ (peak and root regions) as predicted by (4.6). For comparison the change in length required to constitute the far field noise reduction is also included as $(S^{WLE}_{ppa}/S^{SLE}_{ppa})\mathcal{L}(f^* = 0)$. 76
4.7 (a) Comparison between numerical noise reduction spectra ($\Delta SPL(\boldsymbol{x}_o, f^*)$) and that predicted by the erroneous 1D semi-analytical model of (4.12). Models **A**-**C** provide different representations of the LE source characteristics. **A**: constant source along the edge (equivalent to SLE). **B**: cosine of local sweep angle ($\cos(\Phi)$). **C**: realistic phase and source obtained from numerical data. For all cases the WLE geometry is constant at $h_{LE}/L_c = 1/15$ and $\lambda/L_c = 2/15$. 78
4.8 (a) WLE-SLE source strength ratio at three selected frequencies $f^* = 1$, 3 and 5, compared to the cosine of the local LE sweep angle Φ. (b) Source strength ratio scaled by dl/dz 80
4.9 Comparison of numerical and modelled two-point phase spectra taken between LE hill and peak. 80
4.10 Surface source strength distribution $S_{ppw}(x, z, f^*)$ for SLE and WLE geometries plot as SPL (dB scale). (a) SLE $f^* = 0.2$; (b) WLE $f^* = 0.2$; (c) SLE $f^* = 1$; (d) WLE $f^* = 1$. 81
4.11 Surface source strength distribution $S_{ppw}(x, z, f^*)$ for SLE and WLE geometries plot as SPL (dB scale). (a) SLE $f^* = 4$; (b) WLE $f^* = 4$; (c) SLE $f^* = 6$; (d) WLE $f^* = 6$. 82
4.12 Comparison of wall pressure spectra distribution ($S_{ppw}(x, z, f^*)$) plot as SPL (dB scale) obtained by baseline and refined grids. $(a$-$b)$ $f^* = 4$; $(c$-$d)$ $f = 6$. The refined grid contains $1920 \times 960 \times 128 = 236M$ grid cells (factor 1.5 refinement in the streamwise directions, and factor 2 in span). 84
4.13 Surface source strength distribution $S_{ppw}(x, z, f^*)2$ for WLE geometry plot as SPL (dB scale) at the maximum interference frequencies of the LE line model. (a) $f^* = 1.32$; (b) $f^* = 3.04$; (c) $f^* = 4.76$. 85

4.14 Validation of FW-H solver for predicted (a) far field acoustic pressure for SLE and WLE cases; (b) corresponding power spectra. 86
4.15 FW-H predicted noise reduction spectra obtained by integrating incrementally increasing proportions of the aerofoil surface. (a) Schematic diagram indicating the incrementally increasing surface integration region. (b) three integration regions starting from the LE and extending to $x = x_{LE} + 0.025L_c$, $x = x_{LE} + h_{LE}$ and $x = x_{hill} + 2h_{LE}$ respectively. (c) further extensions to the integration region increasing in increments of h_{LE} until $x_{hill} + 5h_{LE}$; (d) extensions increasing by $2h_{LE}$ until $x_{hill} + 12h_{LE}$; (e) extensions increasing by $7.5h_{LE}$ until $x_{hill} + 30h_{LE}$. Comparison is consistently made to the full surface integration. 87
4.16 One-to-one source strength difference spectra (4.15). (a) $f^* = 0.2$; (b) $f^* = 1$; (c) $f^* = 2$; (d) $f^* = 6$. 88
4.17 Effective source area $\mathcal{A}$ as predicted by (4.16). As in figure 4.6, the required reduction with frequency is also plot for comparison, showing a good match until $f^* = 4$. . . 89
4.18 (a) Source strength integrated along the LE line as in (4.18) compared with surface integrated source strength (4.19). (b) Corresponding ISS difference spectra $10\log_{10}[ISS_{SLE}(\boldsymbol{x}_o, f^*)/ISS_{WLE}(\boldsymbol{x}_o, f^*)]$. 90
4.19 Modified FW-H noise reduction predictions highlighting contributions from destructive interference and source strength variation respectively. The phase effect prediction is obtained by mapping the SLE surface pressure data onto the WLE geometry. Meanwhile the source alone prediction is obtained by eliminating the spanwise variation in retarded time from the WLE case. Comparison is also made to the 1D model **B** outlined in §4.4. 91

5.1 The current numerical simulation of aerofoil noise due to an impinging vortex: (a) the initial and boundary conditions where the prescribed vortex is visualised by isocontour surfaces of vertical velocity; (b) the initial condition viewed from the mid span ($z = 0$) in the xy-plane where the origin of the coordinates is located at the mid chord; (c & d) instantaneous contour plots of acoustic pressure (p_a/p_∞) in the case of a semi-infinite-chord aerofoil at the dimensionless time of $t^* = ta_\infty/L_c = 4.68$ and 7.34; and, (e & f) equivalent plots in the case of a finite-chord aerofoil. The aerofoil has a SLE in (c to f). The acronyms are defined as follows: S1 = primary source; S2 = secondary source; LEVS = leading-edge vortical scattering; TEVS = trailing-edge vortical scattering; and, ABS = acoustic backscattering. 96
5.2 Acoustic pressure data obtained at an observer location from the current simulations with two different chord lengths (finite and semi-infinite, where the former includes all noise sources and the latter contains S1 only): (a) time signals of $p_a(\boldsymbol{x}_o, t)/p_\infty$ where $\boldsymbol{x}_o/L_c = (0, 5, 0)$; ($b$) the corresponding power spectra. It is worth noting here that S1 = LEVS and S2 = TEVS+ABS. 97
5.3 Contours of spanwise vorticity ($\omega_z L_c/a_\infty$) in the xy-plane at initial condition (a), after LE interaction $ta_\infty/L_c = 2.81$ (b), and at $ta_\infty/L_c = 6.33$ for semi-infinite chord (c), and finite chord cases (d). 99
5.4 Acoustic pressure generated by the secondary sources (with the primary source excluded) obtained by using (5.1): (a) instantaneous contours of the acoustic pressure $p_{a\text{-S2}}/p_\infty$ at $t^* = 9.0$; (b) the time signals of $p_{a\text{-S2}}/p_\infty$ obtained at the observer location $\boldsymbol{x}_o/L_c = (0, 5, 0)$; and, ($c$) the corresponding power spectra. The acronyms are defined in figure 5.1 (as well as in the text). 100

5.5 An additional simulation procedure in order to isolate the TEVS event: (a) continue the original simulation with the finite-chord aerofoil until $ta_\infty/L_c = 25/6$ by which time the upstream vortex is bisected and convected down to the mid-chord location ($x = 0$); (b) restore the unperturbed freestream condition outside a radius of $r/L_c = 1/4$ from the mid-chord location to remove all the acoustic waves that have propagated but keep the bisected vortices contained inside the radius (on both the upper and lower sides of the aerofoil); and, (c) extend the wall boundary condition upstream to create an inverse semi-infinite-chord aerofoil (with no LE) and restart the simulation with the filtered solution in (b) as the initial condition. 101
5.6 Far-field acoustic pressure signal obtained through the procedure outlined in figure 5.5 compared to the original signal produced by the finite-chord length WLE. . . . 101
5.7 Acoustic power spectra for each individual TEVS and ABS components of the secondary source. The observer location is $\boldsymbol{x}_o/L_c = (0, 5, 0)$. The curve denoted by TEVS+ABS is that presented in figure 5.4c. 102
5.8 Directivity profiles (on a logarithmic scale) of $S_{ppa}(f^*)/p_\infty^2$ at two different frequencies: (a) $f^* = 2$ and (b) $f^* = 6$, around a circle of $\boldsymbol{x}_o/L_c = (5\cos\theta, 5\sin\theta, 0)$, obtained from each individual noise source and also from all sources combined (S1+S2). Lower half planes are not repeated due to symmetry. 102
5.9 Comparison of the far-field acoustic pressure and wall pressure loading fluctuations at the TE due to the TEVS, averaged over the span: (a) the time signals of $\Delta \mathrm{p}_{\text{w-TEVS}}/\mathrm{p}_\infty$ and p_a/p_∞ scaled to the wall pressure fluctuation magnitude. (b) the corresponding power spectra. 103
5.10 Magnitude scaled acoustic pressure data obtained at an observer location from the current simulations with three different vertical miss distances ($y_0 = 0$ (exactly parallel), $y_0 = 0.03$ and $y_0 = 0.06$): (a) time signals of $p_a(\boldsymbol{x}_o, t)/(\max p_a)$ where $\boldsymbol{x}_o/L_c = (0, 5, 0)$; ($b$) the corresponding power spectra. 104
5.11 Amiet's model predictions of the acoustic power spectra at $\boldsymbol{x}_o/L_c = (0, 5, 0)$ given by (5.4) and (5.5) compared with the current SLE simulation results, with respect to two different source scenarios: (a) LEVS only; and, (b) LEVS and ABS-A combined. The velocity power spectrum (Φ_{vv}) required in the Amiet's models is given by (4.1). 105
5.12 Amiet's model predictions of the acoustic power spectra at $\boldsymbol{x}_o/L_c = (0, 5, 0)$: ($a$) by using (5.6) for TEVS and ABS-C; and, (b) by adding (5.4) and (5.6) to represent a combination of LEVS, TEVS, ABS-A and ABS-C (without complete phase interactions between them). The current simulation result (Total: S1+S2) includes all noise sources (LEVS, TEVS and ABS-A to D) and their phase interactions. The S_{QQ} term required in (5.6) is calculated by using the simulation data ($\Delta \mathrm{p}_\mathrm{w}$) consisting of TEVS and ABS-C. 106
5.13 Results of the current grid-dependency test by using three different levels of grid resolution described in table 5.1: (a) acoustic power spectra obtained at $\boldsymbol{x}_o/L_c = (0, 5, 0)$ for $Re_\infty = 4{\times}10^4$ weak vortex interaction 2D; (b) $Re_\infty = 4{\times}10^5$ weak vortex interaction 2D; (c) $Re_\infty = 4{\times}10^5$ strong vortex interaction 3D; (d) $Re_\infty = 8{\times}10^5$ strong vortex interaction 2D. 109
5.14 Boundary layer profiles obtained two Reynolds numbers $Re_\infty = 4.0 \times 10^5$ and 8.0×10^5: (a) streamwise velocity profile at $x/L_c = 0.4$; (b) skin friction coefficient $C_f = 2\tau_w/(\rho U_\infty^2)$. 109
5.15 Comparison of the acoustic pressure data obtained at the observer location $\boldsymbol{x}_o/L_c = (0, 5, 0)$ for a weak vortex interaction (2.5% strength) at Reynolds numbers 40,000, 400,000 and ∞. (a) time signals, (b) corresponding PSD. 110

5.16 (a) Spanwise vorticity $\omega_z L_c/u_\infty$ contours obtained at four instances for $Re_\infty = 4\times10^5$ and $\sigma = 0.377$: (i) after the vortex is bisected by the LE; (ii) vortex near the mid-chord; (iii) vortex interacting with the wake; (iv) secondary vorticity interacting with the wake. (b-c) Corresponding acoustic pressure contours obtained during the last two vorticity snapshots. 111

5.17 Comparison of the acoustic pressure data obtained at the observer location $\boldsymbol{x}_o/L_c = (0,5,0)$ for a strong vortex interaction (25% strength) at Reynolds numbers 4×10^5 and 8×10^5. (a) time signals of $p_a(\boldsymbol{x}_o,t)/p_\infty$; ($b$) the corresponding power spectra; (c) Power spectra obtained for $t^* < 11$ (approximate LEVS contribution + ABS A+B); (c) Power spectra obtained for $t^* \geq 11$ (approximate TEVS contribution + ABS C+D). 112

5.18 Comparison of approximate LEVS, TEVS and wake noise contributions to the overall acoustic spectra. Each component is obtained by windowing the time signal $t^* < 11$ for LEVS, $t^* \geq 11$ for TEVS, $10 \geq t^* \leq 14$ for wake. LEVS and TEVS solutions also contain ABS A+B, and C+D components respectively. (a) $Re_\infty = 4.0\times10^5$; ($b$) $Re_\infty = 8.0\times10^5$. 113

5.19 Iso-surfaces of spanwise vorticity $\omega_z L_c/u_\infty$ (50 levels shown) and contours of acoustic pressure p_a/p_∞ obtained for the 3D $Re_\infty = 4.0\times10^5$ ($\epsilon = 0.377$) case shortly after the vortex has convected past the LE at $ta_\infty/L_c = 4.33$ (a). $ta_\infty/L_c = 8.66$, as the secondary vorticity passes the TE (b). Solution repeated in span for visualisation. 114

5.20 Boundary layer profiles taken at $t^* = 0$ and $t^* = 20$ (before and after the aerofoil-vortex interaction) for the 3D $Re_\infty = 4.0\times10^5$ simulation ($\epsilon = 0.377$): (a) streamwise velocity profile for $x/L_c = 0.4$; (b) skin friction coefficient $C_f = 2\tau_w/(\rho U_\infty^2)$. . 115

5.21 Comparison of acoustic pressure data obtained for 2D and 3D simulations for $Re_\infty = 4.0\times10^5$ and $\epsilon = 0.377$. The TEVS signals are obtained through the windowing procedure outlined in section 5.5.3: (a) power spectra of acoustic pressure at $\boldsymbol{x}_o/L_c = (0,5,0)$;; ($b$) directivity profiles for $fL_c/a_\infty = 7.0$. 116

5.22 Power spectra comparison for LEVS and TEVS obtained for the 3D $Re_\infty = 4.0\times10^5$ simulation at $\boldsymbol{x}_o/L_c = (0,5,0)$ (a). Directivity profiles (linear scale) at frequencies $fL_c/a_\infty = 6.0, 6.5$ and 7.5 where TEVS is the dominant source of noise (b-d). The TEVS and LEVS components are obtained through the windowing procedure outlined in section 5.5.3 which also includes ABS components. 116

6.1 Acoustic pressure data obtained at an observer location from the current simulations with two different LE geometries (SLE and WLE) and two different chord lengths (finite and semi-infinite, where the former includes all noise sources and the latter contains S1 only): (a) time signals of $p_a(\boldsymbol{x}_o,t)/p_\infty$ where $\boldsymbol{x}_o/L_c = (0,5,0)$; ($b$) the corresponding power spectra; (c) an instantaneous contour plot of $p_a(\boldsymbol{x},t^* = 7.34)/p_\infty$ taken at the mid-span ($z = 0$) for the SLE finite-chord case; and, (d) the spectra of the noise reduction due to the WLE defined by (2.61) in comparison with a semi-empirical prediction by Chaitanya *et al.* (2017) ($\Delta\text{SPL} = 10\log_{10}(fh_{LE}/u_\infty) + 10$). It should be noted that the plot in (d) for the S1-only case is terminated at $f^* = 6.5$ due to the value of $S_{ppa}(f^*)/p_\infty^2$ for WLE falling below the lower bound of the machine accuracy (double precision used). 120

6.2 Acoustic pressure generated by the secondary sources (with the primary source excluded) obtained by using (5.1): (a) instantaneous contours of the acoustic pressure $p_{a\text{-S2}}/p_\infty$ at $t^* = 9.0$ from the SLE case; (b) the time signals of $p_{a\text{-S2}}/p_\infty$ obtained at the observer location $\boldsymbol{x}_o/L_c = (0,5,0)$ for the SLE and WLE cases; and, (c) the corresponding power spectra. The acronyms are defined in figure 5.1 (as well as in the text). 121

6.3 Acoustic power spectra for each individual component of the secondary sources: (a & b) comparing S2-TEVS and S2-ABS in each of the SLE and WLE cases; and, (c & d) comparing the SLE and WLE cases for each of the individual components. The observer location is $\boldsymbol{x}_o = (0, 5L_c, 0)$. The curves denoted by S2 (all) in (a) and (b) are those presented in figure 6.2c. 122
6.4 Wall pressure loading fluctuations at the TE due to the TEVS, averaged over the span: (a) the time signals of $\Delta p_{\text{w-TEVS}}/p_\infty$ and (b) the corresponding power spectra, comparing the SLE and WLE cases. 123
6.5 Spectral oscillations appeared in the overall acoustic power spectra (S1+S2 in figure 6.1b) due to the phase relationships between S1 and S2: (a) the SLE case at low frequencies, (b) the SLE case at high frequencies and (c) the WLE case. The values of $\Delta f^*_{\text{LEVS}\mid\text{ABS-A}}$ and $\Delta f^*_{\text{LEVS}\mid\text{TEVS}}$ are calculated from (6.1) and listed in table 6.1. 125
6.6 Spectral oscillations appeared in the acoustic power spectra from the secondary sources only (figure 6.2c) due to the phase relationships between ABS-A and TEVS: the (a) SLE and (b) WLE cases. The values of $\Delta f^*_{\text{ABS-A}\mid\text{TEVS}}$ are calculated from (6.3) and listed in table 6.1. 126
6.7 Directivity profiles (on a logarithmic scale) of the variance of the acoustic pressure $\langle p_a^2\rangle/p_\infty^2$ around a circle with a radius of $5L_c$ with its origin at centre of the finite-chord aerofoil (on the centre plane, $z = 0$), obtained from (a) all noise sources combined and, individually from (b) LEVS, (c) TEVS and (d) ABS. Comparisons are made between the SLE and WLE cases. Lower half planes are not repeated due to symmetry. 127
6.8 Acoustic power spectra obtained from individual noise sources: (a & b) LEVS, (c & d) TEVS and (e & f) ABS, at three different observer locations: $\boldsymbol{x}_o/L_c = (5\cos\theta, 5\sin\theta, 0)$ for $\theta = 30°$, 90° and 150°. The left and right columns are for the SLE and WLE cases, respectively. 128
6.9 Acoustic power spectra obtained at three different observer locations: $\boldsymbol{x}_o/L_c = (5\cos\theta, 5\sin\theta, 0)$ for (a & b) $\theta = 30°$, (c & d) $\theta = 90°$ and (e & f) $\theta = 150°$, from individual noise sources (LEVS, TEVS and ABS). The left and right columns are for the SLE and WLE cases, respectively. 129
6.10 Directivity profiles (on a logarithmic scale) of $S_{ppa}(f^*)/p_\infty^2$ at two different frequencies: (a & c) $f^* = 2$ and (b & d) $f^* = 6$, around a circle with a radius of $5L_c$ with its origin at centre of the finite-chord aerofoil (on the centre plane, $z = 0$), obtained from each individual noise source. The top and bottom rows are for the SLE and WLE cases, respectively. Lower half planes are not repeated due to symmetry. . . 130
6.11 Directivity profiles (on a decibel scale) of the noise reduction made by WLE compared to SLE, i.e. ΔSPL defined by (2.61), at two different frequencies: (a) $f^* = 2$ and (b) $f^* = 6$, based on the result shown in figure 6.10. The inner semicircle area outlined indicates noise increase (negative ΔSPL). 131
6.12 (a) Power spectral density of the far field fluctuating pressure ($S_{ppa}(f^*)/p_\infty^2$) obtained by SLE baseline, WLE, WLE+WTE, WLE+IWTE (Inverted WTE) and SLE+WTE cases. The amplitude and wavelength for both LE and TE serrations is $h_{LE}/L_c = 1/15$ and $\lambda/L_c = 2/15$. (b) Noise reduction spectra obtained for each case. 132
6.13 (a & c) Acoustic power spectra for S2-TEVS and S2-ABS for SLE, WLE and WLE+WTE cases. (b & d) Secondary source noise reduction spectra obtained by WLE and WLE+WTE cases for TEVS (b) and ABS (d) respectively. 132

6.14 Iso-surfaces of Q-criterion ($||\Omega_{ij}L_c/a_\infty||^2 - ||S_{ij}L_c/a_\infty||^2$ where Ω_{ij} and S_{ij} are the vorticity and rate-of-strain tensors, respectively) coloured by spanwise vorticity ($\omega_z L_c/a_\infty$) obtained during interaction of the prescribed vortex and the LE ($t^* = 2.2$) (a), and after the now bisected vortex has travelled further downstream ($t^* = 5.2$) (b). (c) & (d) Equivalent plots recoloured by streamwise vorticity ($\omega_x L_c/a_\infty$). 133
6.15 Boundary layer profiles obtained for WLE geometry at Reynolds numbers $Re_\infty = 4.0 \times 10^5$: ($a$) streamwise velocity profile for $x/L_c = 0.4$; (b) skin friction coefficient $C_f = 2\tau_w/(\rho U_\infty^2)$ at WLE hill; (c); WLE peak and (d) WLE root. 134
6.16 Acoustic pressure data obtained for SLE and WLE geometries from the current 3D viscous ($Re_\infty = 4.0 \times 10^5$) simulations based on the linear 2.5% and non-linear 25% strength vortex interactions: (a & c) time signals of $p_a(\boldsymbol{x}_o, t)/p_\infty$ for weak and strong interactions respectively; (b & d) the corresponding power spectra. 135
6.17 Iso-surfaces of spanwise vorticity $\omega_z L_c/a_\infty$ and contours of acoustic pressure p_a/p_∞ obtained during interaction of the weak vortex disturbance and a WLE. (a) Non-dimensional time $ta_\infty/L_c = 8.33$ showing 3D tertiary structures generated on the aerofoil lower side. (b) $ta_\infty/L_c = 10$, when the tertiary structures are scattered by the TE. 136
6.18 Noise reduction spectra obtained by the WLE case at $Re_\infty = 4.0 \times 10^5$ for the total noise and LEVS+ABS AB components. The LEVS+ABS AB contribution is obtained through the windowing procedure described in §5.5. (a) Default weak vortex case; (b) enhanced strength vortex. Also shown is the noise reduction trend of Chaitanya *et al.* (2017) based on $h_{LE}/L_c = 0.025$. 137

B.1 Comparison of the vertical velocity profiles obtained by the vortex models utilised in the current with classical models from literature. 146
B.2 PSD of vertical velocity fluctuations obtained by the two vortex models utilised in the current study. (a) Linear scale; (a) Log scale. 147
B.3 Effect of changing the vortex size on the frequency bandwidth of the r^2 vortex model. $L_v = 1.2\lambda_{LE}$ is the default vortex size ($\sigma = 44.25$) used in §5-6. 147

C.1 (a) Time signals of acoustic pressure $p_a(\boldsymbol{x}_o, t)/p_\infty$ obtained at observer location $\boldsymbol{x}_o/L_c = (0, 5, 0)$ for SLE and WLE geometries with two different impinging vortex strengths. (b) The corresponding power spectra of the former. The pressure and spectra are scaled by $\max(p_a^{SLE})$ and $\max(p_a^{SLE})^2$ so that direct comparison can be made. 149
C.2 Comparison of the SIC noise reduction obtained using the two vortex shape functions utilsing the same vortex diameter $L_v|_{1\%} = 0.17L_c$. 149
C.3 Effect of changing vortex diameter L_v on the undulated LE noise reduction spectra with WLE amplitude and wavelength fixed at $h_{LE}/L_c = 1/15$ and $\lambda/L_c = 2/15$ respectively. 150
C.4 Comparison of noise reduction spectra obtained by the default WLE ($h_{LE}/L_c = 1/15$ and $\lambda_{LE}/L_c = 2/15$) and one with twice the WLE wavelength compared to the LE line model **B** of §4.4.2. 151

D.1 Comparison of the wall pressure loading fluctuations at the TE due to the TEVS obtained directly downstream of the WLE peak, hill and root compared to the SLE. Signals extracted one grid point upstream of the TE: (a) the time signals of $\Delta p_{\text{w-TEVS}}/p_\infty$ and p_a/p_∞. (b) The corresponding power spectra. 153

D.2 Cosine of the two-point phase spectra ($\cos[\phi_{ppw}(x_1, x_2, f^*)]$) of wall pressure fluctuations between the TE point directly downstream of the LE peak and four points equally spaced in span. Hill 25% and 75% refer to the mid points of peak–hill, and hill–root respectively. 153
D.3 Acoustic power spectra for ABS (a) and TEVS (b) components of the secondary source obtained with two WLE amplitudes ($h_{LE}/L_c = 1/15$ and $1/10$). The observer location is $\boldsymbol{x}_o/L_c = (0, 5, 0)$. 154
D.4 Contours of spanwise vorticity $\omega_z L_c/a_\infty$ obtained on the aerofoil upper side taken at $ta_\infty/L_c = 5.5$, just before the disturbances are scattered at the TE: (a) WLE; (b) SLE. 156
D.5 Dynamic mode for $f^* = 6$ obtained at $y = 0^+$ for SLE (a) and WLE (b) cases . . . 157

E.1 Comparison of the noise reduction spectra obtained by four DWLE geometries compared to the corresponding averaged WLE components of the same amplitude. (a) $h_{LE}/L_c = 1/15$ and $\phi = 3\pi/2$; (b) $h_{LE}/L_c = 1/15$ and $\phi = 0$; (c) $h_{LE}/L_c = 1/10$ and $\phi = 3\pi/2$; and (d) $h_{LE}/L_c = 2/15$ and $\phi = 3\pi/2$; 160

List of Tables

2.1 Number of processor cores and approximate run time for the simulations in the following sections. NP_ξ, NP_η and NP_ζ are the streamwise, vertical and spanwise number of processor cores respectively. 41

3.1 Supplementary information for the grid convergence test shown in figure 3.3, where n_ξ, n_η and n_ζ denote the number of grid cells in the ξ-, η- and ζ-directions, respectively – see (2.6) and (2.7). 47
3.2 The cosine angles representing the oblique interaction between the induced vertical velocity and the WLE shown in figure 3.10*c*. 56

4.1 Three different levels of grid resolution used for the current grid-dependency tests shown in figures 4.1 and 4.2. N_ξ, N_η and N_ζ denote the number of grid cells used in the streamwise, vertical and spanwise directions, respectively. $\Delta \mathrm{x}_{\mathrm{min}}$ is the smallest cell size used at LE and TE of the aerofoil. CPW (cells per wavelength) indicates the minimum number of grid cells used across the acoustic wavelength. CPW is measured at the far-field observer location $\boldsymbol{x}_o/L_c = (0, 5, 0)$. 71
4.2 Percentage of source surface area satisfying various magnitude constraints at frequencies $f^* = 0.2$, 1, 4 and 6. Only the first $1L_c$ of the surface is considered. . . . 83
4.3 Percentage of source surface area satisfying various magnitude constraints at frequencies $f^* = 1.26$, 3.04, 4.76. Only the first $1L_c$ of the surface is considered. . . . 84

5.1 Grid resolution levels used for the four grid-dependency tests shown in figure 5.13. N_ξ, N_η and N_ζ denote the number of grid cells used in the streamwise, vertical and spanwise directions, respectively. $\Delta \mathrm{x}_{\mathrm{min}}$ is the smallest cell size used at LE and TE of the aerofoil. CPW (cells per wavelength) indicates the number of grid cells used across the acoustic wavelength at the frequency of $f^* = 8$. CPW is measured at the far-field observer location $\boldsymbol{x}_o/L_c = (0, 5, 0)$. 107

6.1 The calculated values of (6.1) and (6.3) for the periods of spectral oscillations (due to phase interactions between the noise sources) that appear in figures 6.1*b* and 6.2*c* with the observer location given at $\boldsymbol{x}_o/L_c = (0, 5, 0)$. 124

A.1 The estimation of ϕ for various thresholds in the case of $h_{LE}/L_c = 1/30$. 144
A.2 The estimation of ϕ for various thresholds in the case of $h_{LE}/L_c = 1/15$. 144
A.3 The estimation of ϕ for various thresholds in the case of $h_{LE}/L_c = 1/10$. 144

E.1 Predicted maximum noise reduction frequencies obtained via. E.3 for the DWLE geometries presented in figure E.1. 161

Acknowledgements

Firstly and foremost I would like to thank my supervisor Dr Jae-Wook Kim for his continual support and guidance throughout the project. I have thoroughly enjoyed my time in Southampton, and I am grateful that you encouraged me to pursue a PhD. I would also like to thank Dr Chaitanya Paruchuri of the ISVR for his useful discussions of the noise reduction mechanisms, and continued collaboration during the PhD. I also gratefully acknowledge the support of the ICSS (Institute for Complex Systems Simulation) DTC (Doctoral Training Centre) through ESPRC (Engineering and Physical Sciences Research Council) grant (EP/G03690X/1). In addition I acknowledge the support of the high-performance computing facilities and services of the University of Southampton's local supercomputing facility IRDIS4, as well as the UK national supercomputer ARCHER via the UK Turbulence Consortium (EP/L000261/1). I would also like to thank my colleagues in the AFM group: Robert Bleischwitz, Alex Barbu, Markus Zauner and Antonio Reyes Barraza, for their valuable discussions of results and methodology. Lastly, but not least, I would like to thank my family for their continued support and encouragement throughout the past years.

Nomenclature

Roman characters	
a	Speed of sound
B	Stagnation enthalpy
d	LE streamwise distance
e	Internal energy
f	Frequency
G	Green's function
h	Amplitude
H	Horseshoe vortex span
j	Imaginary unit
J	Jacobian
k	Wavenumber
L	Length
M	Mach number
NP	Number of processor cores
p	Pressure
Pr	Prandtl number
q	Heat flux
Q	Q-criterion
ret	Evaluated at retarded time
r	Euclidean distance
Re	Reynolds number
S	Sponge zone forcing term
St	Strouhal number
t	Time
T	Period
u, v, w	Streamwise, vertical and spanwise velocities
x, y, z	Cartesian coordinates
Greek characters	
γ	Ratio of specific heats
Γ	Circulation
Δ	Change in quantity

λ	Wavelength
μ	Dynamic viscosity (sponge zone coefficient)
ρ	Density
ϵ	Vortex strength
σ	Vortex size parameter
ξ, η, ζ	Body fitted coordinates
τ	Retarded time
ϕ	Phase shift (oblique interaction angle)
φ	Half-plane velocity potential
Φ	Sweep angle (turbulence velocity spectra)
Ψ	Vortex vector potential
ω	Vorticity (scaled wavenumber)
θ	Observer angle
ν	Kinematic viscosity
Ω	Domain size
Superscript and subscript	
$()'$	Perturbation value
$()^*$	Normalised quantity (conjugate)
$()_\infty$	Free-stream quantity
$()_a$	Acoustic quantity
$()_c$	Chordwise
$()_w$	Wall quantity
$()_{x,y,z}$	Streamwise, vertical, spanwise
$()_{LE}$	evaluated at leading edge
$()_{TE}$	evaluated at trailing edge
$()_{S1}$	Primary source
$()_{S2}$	Secondary source
Abbreviations	
ABS	Acoustic Back Scattering
ACARE	Advisory Council for Aviation Research in Europe
AGI	Aerofoil-Gust Interaction
AR	Aspect ratio
ATI	Aerofoil-Turbulence Interaction
AVI	Aerofoil-Vortex Interaction
BEM	Boundary Element Method
BVI	Blade-Vortex Interaction
CAA	Computational Aeroacoustics
CFD	Computational Fluid Dynamics
CPW	Cells Per Wavelength
DWLE	Dual-wavelength Wavy Leading Edge
DNS	Direct Numerical Simulation

DMD	Dynamic Mode Decomposition
FC	Finite Chord
FW-H	Ffowcs-Williams and Hawkings
HIT	Homogeneous Isotropic Turbulence
HV	Horseshoe Vortex
LE	Leading Edge
LEE	Linearised Euler Equations
LES	Large Eddy Simulation
LEVS	Leading Edge Vortex Scattering
NSE	Navier-Stokes Equations
OASPL	Overall Sound Pressure Level
OGV	Outlet Guide Vane
PWL	sound Power Level
RANS	Reynolds Averaged Navier-Stokes
RDT	Rapid Distortion Theory
S1	Primary Generated Sound
S2	Secondary Generated Sound
SIC	Semi-Infinite Chord
SEM	Synthetic Eddy Method
SLE	Straight Leading Edge
SPL	Sound Pressure Level
TE	Trailing Edge
TEVS	Trailing Edge Vortex Scattering
WLE	Wavy Leading Edge
WTE	Wavy Trailing Edge

Chapter 1

Introduction

1.1 Research motivation

In recent years the volume of air traffic in the UK and Europe has continued to grow rapidly, and is anticipated to do so for the foreseeable future. The UK Department for Transport (DfT) predicts that the annual number of airline passengers will increase to 445 million by 2050, more than double compared to 2013 levels (Department of Transport, 2013). A significant environmental consequence of this trend is an increase in noise pollution primarily in the vicinity of major airports. The World Health Organisation (WHO) predicts that noise pollution contributes to approximately 1.6 million DALYs (disability adjusted life years) across western Europe. This figure considers the impact of more minor annoyances such as sleep disturbance and tinnitus, as well as connection between noise pollution and more serious health issues such as ischaemic heart disease and cognitive impairment of young children (World Health Organization, 2011).

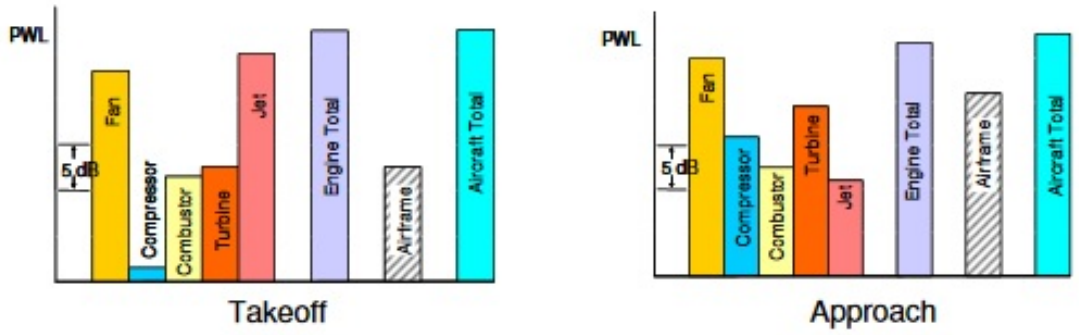

Figure 1.1: Aircraft noise contributions during take-off and approach conditions. Taken from: Astley *et al.* (2007).

Recently the Advisory Council for Aviation Research in Europe (ACARE) introduced FlightPath 2050 outlining environmental targets for the civil aviation industry, including a reduction of 65% to perceived aircraft noise relative to year 2000 technology levels. An overview of the current noise

contributions from a modern hi-bypass turbofan engine is shown in figure 1.1 (obtained from Astley *et al.* (2007)). It is apparent for both take-off and landing conditions that aerodynamic sound from turbo-machinery represents one of the most significant noise sources, primarily from the fan on approach. This is largely attributed to significant reductions to jet noise by nozzle suppressors (chevrons) and ever increasing engine fan bypass ratios, both of which reduce the velocity of the exhaust flow. In addition to turbofan applications, aerofoil noise represents a significant concern for aircraft propellers, helicopter rotors, and wind turbines.

Aerofoil noise may be separated into two main categories, self-noise, and interaction noise. Self-noise constitutes all sources of sound which the aerofoil generates in the absence of impinging disturbances. At low angles of attack and at relatively high Reynolds numbers the primary component is at the aerofoil trailing edge (TE), generated by the scattering of unsteady surface pressure fluctuations contained within a turbulent boundary layer. Aerofoil self-noise also includes sound generated by viscous hydrodynamic effects such as flow separation, vortex shedding and tip vortex generation (Migliore & Oerlemans, 2004). On the other hand, interaction noise concerns the impingement of upstream disturbances on the solid body, most typically gusts, vortices or turbulence. In the case of an aircraft turbofan engine this primarily concerns interaction between the fan wake and outlet-guide-vanes (OGV), as well as rotor-stator interaction in the compressor/turbine. Additionally, interaction noise is prominent for wing high lift devices such as aerofoil flaps and slats, counter rotating propellers (rotor-rotor interaction) including open rotor concept engines, helicopter rotor noise during forward flight (aerofoil tip-vortex interaction), and during gust interaction with wind turbines. Generally, for flows where there exists significant upstream disturbances, interaction noise is dominant (Migliore & Oerlemans, 2004), typically occupying the higher energy, lower frequency range. As a consequence interaction noise has attained substantial interest from the research community in recent years through a wide range of approaches, analytical, experimental, and numerical.

Unlike self noise contributions, interaction noise is primarily an inviscid mechanism. For aerofoils with a compact chord it manifests mainly as dipole sound which may be decomposed into primary and secondary sources. The primary mechanism (which contributes the largest acoustic pressure signature) is the scattering of the impinging disturbance at the aerofoil leading edge (LE). This event is herein referred to as leading-edge-vortex-scattering (LEVS). It is associated with the rapid deformation of the impinging vortical field due to the no penetration condition on the aerofoil surface (zero normal velocity), leading to the generation of unsteady pressure fluctuations which will radiate to the far-field. It is characterised by a downstream orientated cardioid directivity (Ffowcs Williams & Hall, 1970).

As for the secondary effects, the most well studied is sound from acoustic back-scattering (ABS). This concerns the diffraction and scattering of impinging acoustic waves at sharp edges. It typically manifests as a negative feedback mechanism of progressively damped acoustic waves travelling back and forth between the LE and TE, although most commonly in literature only the principle scattered wave is considered (Amiet, 1975). For aerofoil interaction noise, the most notable

contribution is the scattering of the main LEVS sound at the TE. This prompts higher order upstream travelling waves which are subsequently scattered at the LE, repeating the process. The other secondary effect, more often overlooked in the study of interaction noise, is the scattering of incident disturbances at the trailing edge. This occurs in a similar fashion to boundary layer self-noise, although is generated by the now bisected upstream vortical disturbances (in addition to secondary structures generated via the LE interaction). Throughout this work, this mechanism will be referred to as trailing-edge-vortex-scattering (TEVS). Counter to LEVS, TEVS is characterised by an upstream orientated cardioid directivity (Ffowcs Williams & Hall, 1970). Representations of all three interaction noise components are shown in figure 1.2 for the case of a flat plate aerofoil with an impinging spanwise vortex. The following sections contain a detailed overview of the current state of the art concerning aerofoil LE interaction noise and wavy leading edges. Meanwhile further discussions of the secondary sources (most notably TEVS) are provided in §5.

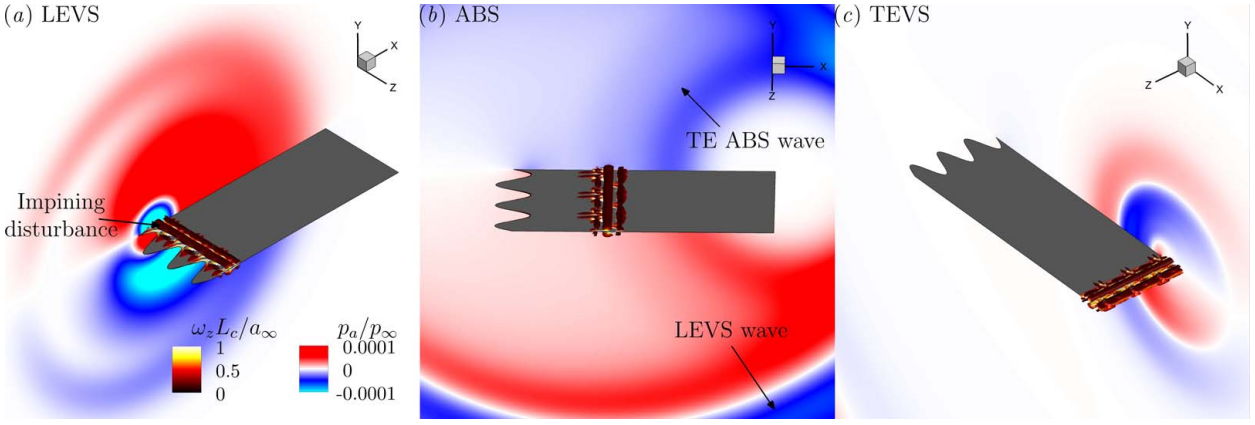

Figure 1.2: (a) Leading Edge Vortex Scattering (LEVS). (b) Acoustic Back-Scattering (ABS) at the TE. (c) Trailing Edge Vortex Scattering (TEVS).

1.2 Analytical modelling of aerofoil interaction noise

1.2.1 Amiet's model and extensions

One of the earliest contributions to interaction noise theory was introduced by Sears (1941), who derived an expression for the unsteady lift (which directly relates to the radiated sound) produced by a 2D aerofoil in an incompressible mean flow undergoing a harmonic gust. This work has since been extended by Atassi (1984) for more realistic geometries including small camber, thickness and angle of attack, achieved through a linear superposition of three Sear's lift solutions for each respective effect. An approximate solution for the compressible problem incorporating an oblique gust and an infinite span swept aerofoil was later proposed by Adamczyk (1974). Adamcyzk derived the unsteady lift response function through an iterative procedure which firstly treats the aerofoil as a downstream semi-infinite flat plate with no Kutta condition (no TE). This solution is then updated by a second solution for an upstream semi-infinite plate (no LE), therefore correcting the TE and wake surface pressure jump to zero. Further iterations may then be performed to correct

the pressure jump upstream of the aerofoil LE, however typically the two leading order terms are considered sufficient.

Perhaps the most well established analytical approach to the interaction noise problem is the classical work of Amiet (1975) which considers a three-dimensional flat plate interacting with a frozen turbulent field. The result incorporates an important result earlier identified by Graham (1970), who realised "similarity rules" between the 2D and 3D problem based on whether the impinging disturbance was sub- or supercritical. Graham showed that when the gust wave-front translates the aerofoil LE at a rate less than the speed of sound the 3D problem is similar to a skewed gust in incompressible fluid, meanwhile if the gust is supersonic a 2D compressible solution is similar. Thus allowing Amiet to implement the lift response function of Adamczyk (1974), and obtain a solution to the Helmholtz equation based on a previously developed iterative Schwarzchild technique (Amiet, 1974). The approach is particularity useful for validation purposes as it only requires knowledge of the impinging turbulence velocity spectrum, relatively easy to measure in both simulations and experiments. An overview of the various limitations (small angle, thickness, camber), and subsequent extensions of Amiet's original theory is provided by Roger & Moreau (2010). This also includes similar procedures based on Amiet's Schwarzchild technique such as TE self noise due to turbulent boundary layers (Amiet, 1976), and vortex shedding noise of a blunt trailing edge (Roger *et al.*, 2006). Another notable contribution is the work of Christophe *et al.* (2009, 2008), who considered an Amiet model for spanwise varying impinging turbulence. The model was based on a segmentation method, where the aerofoil is sliced into chord-wise strips each with its own specified upstream conditions. The contribution from each strip is then summed to get the net radiated noise. A similar approach was first used by Rozenberg *et al.* (2007) to calculate aerofoil self-noise. However, introduction of small span strips can lead to major inaccuracies if the noise generated by adjacent strips is correlated, e.g. if $L_z < \Lambda$. This was overcome by Christophe *et al.* (2009, 2008) by implementing a new inverse strip theory. In their approach the contribution from each small span segment is determined by subtracting the solution for two overlapping large span aerofoils differing by the strip width.

Other extensions include Blandeau *et al.* (2011), who considered a strictly two-dimensional formulation of the Amiet model to investigate the sound radiated from 2D isolated aerofoils and cascades. Additionally, Santana *et al.* (2016) identified significant over estimations of the standard Amiet model for low frequencies, and consequently proposed an extension for aerofoils of compact chord ($kL_c \ll 1$) including further iterations of the Schwarzchild technique. Most recently Karve *et al.* (2017) accounted for wall effects by application of the Method of Images, thus extending the existing theory to installed noise applications such as that from open rotors and un-ducted fans.

There are also semi-analytical methods based on the Amiet approach such as in Christophe *et al.* (2007). In this paper the noise generated during low speed jet-aerofoil interaction was computed with a combination of Curle's acoustic analogy (Curle, 1955) at low frequencies where the source can be considered compact, and Amiet's model at high frequencies where non-compactness effects are significant. The statistical input for the Amiet model was obtained through LES simulations utilising ANSYS Fluent. Later, Kucukcoskun *et al.* (2013) extended this model by incorporating a

near-field correction to the Amiet model in addition to the inverse strip theory of Christophe *et al.* (2009, 2008). The new model was used in conjunction with the Boundary Element Method (BEM) to account for scattering off rigid bodies. Comparison was made to an experiment of an aerofoil in a turbulent jet placed directly above a rigid scattering screen. Reasonably good agreement was obtained across all frequencies.

1.2.2 Rapid distortion theory

Rapid distortion theory considers a potential steady flow superimposed with unsteady linearised velocity perturbations. The main principle of the theory is that the unsteady flow may be separated into two components. The first which describes vortical effects, namely the distortion of the vortex in mean flow gradients; The second a wave equation which describes the scattered acoustic pressure generated by interaction with the solid body. It therefore accounts for two sources of sound: disturbance scattering, and vortex source noise, but neglects viscosity and non-linear interactions between disturbances.

The first to apply rapid distortion theory for compressible flow applications was Goldstein (1978). However the derived formulation consisted of variable coefficients and hence had no general closed form for a compressible mean flow. An asymptotic closed form representation was later introduced by Myers & Kerschen (1995) for 2D flat plate aerofoils at low angles of incidence by considering only high frequency gusts. A solution to the equations is then found through application of the Weiner-Hopf technique. Their theory predicted a strong dependence between radiated sound power and angle of attack particularly at high Mach numbers, increasing by an order of magnitude between $0°$ and $10°$ for $M_\infty = 0.75$ and an aerodynamic reduced frequency of $\omega L_c/(2U_\infty) = 7$. In a later publication Myers & Kerschen (1997) extended their analysis to flat plate cambered aerofoils by introducing an acoustic boundary layer which deals with diffraction effects such as creeping waves. Camber was found to have a fairly large influence on sound directivity even in modest amounts, introducing asymmetry between the upper and lower aerofoil surfaces.

Evers & Peake (2000) introduced a counterpart to the Myers & Kerschen (1997) theory for transonic flows, taking into account the effects of angle of attack, camber and small but non-zero thickness. They discovered that the sound directivity was limited to two main lobes above and below the aerofoil, with no significant radiation in the upstream direction. In a later paper Ayton & Peake (2013) extended the theory this time to model noise scattering from incoming sound waves rather than vortical disturbances. Additionally the effect of LE radius has been investigated by Ayton & Paruchuri (2016) by including sharp/blunt edges of the form $y \sim x^m$, whereas the theory was previously limited to parabolic leading edges ($y \sim \sqrt{x}$). The most general application of the theory is provided by Ayton (2016), which incorporates camber, thickness and angle of attack effects in the gust-aerofoil interaction problem.

1.2.3 Theory of vortex sound

The main principle behind the theory of vortex sound is to reformulate Lighthill's acoustic analogy (Lighthill, 1952) in term of the stagnation enthalpy of the flow (B). Howe (1997) shows that the resulting inhomogeneous wave equation for H then contains a source term based on the Lamb vector ($\boldsymbol{\omega} \times \boldsymbol{u}$). In a homentropic irrotational flow it may be shown that H may be expressed as the time derivative of a velocity potential $B = -\partial\psi/\partial t$, thus in a steady flow B must be constant, and the unsteady acoustic waves may be represented by perturbations of the stagnation enthalpy. Assuming the Mach number is low $M \ll 1$ the stagnation enthalpy may then be related to the acoustic pressure by $B = p_a/\rho$. However, this does neglect the effects of sound scattering and changes in propagation speed due to mean flow. The solution for H involves application of a Green's function, typically resulting in an integral of the vorticity source term multiplied by the gradient of an incompressible velocity potential term over the volume. The theory has been applied to various applications including the aerofoil-vortex interaction problem (Howe, 1988), and unsteady lift from aerofoils in a turbulent boundary layer (Howe, 2001). Recently it has been used in conjunction with a drift function to model the effects of aerofoil thickness on aerofoil-gust interaction by Lysak *et al.* (2013). Further details of Howe's approach are provided in Appendix D.2.

Both the LEVS and TEVS for flat aerofoils events have been studied analytically by Howe (1988, 2014) through the vortex sound approach. This includes the parallel interaction of point vortices with a non-zero vertical miss distance, and perpendicular collisions for vortices with finite velocity defect. Typically the method requires modelling contributions from two vortex sources: the original impinging vorticity; and secondary vorticity generated by application of the Kutta condition at the trailing edge. Howe showed that the majority the radiated sound pressure emitted as a vortex passes the TE is effectively eliminated through destructive interference with sound generated by the shed "Kutta" or "wake vorticity". However due to compact source approximations, this analysis was mainly restricted to low frequency, focusing solely on the radiated pressure signal rather than high frequency spectra. In the present work it is found that at high frequencies the TE vortical scattering contribution makes a substantial impact on the radiated sound, despite greatly reduced sound pressure amplitude relative to the LE scattering due to the aforementioned TE cancellation effect. Interestingly in later work conducted by Howe (2001) and Glegg & Devenport (2009), both including non-compactness effects, the shed wake vorticity response is shown to be mainly limited to low frequency. The key distinction here is likely the existence of LE generated vorticity captured in the current simulation approach which convects over the aerofoil surface. The secondary vorticity is based on a smaller length scale and therefore probably corresponds to higher frequency noise. Details of the secondary vorticity generation are contained in §3, while §5 provides further discussion of the TEVS mechanism.

1.3 Effects of realistic geometry and flow conditions

A substantial proportion of the existing literature concerns the influence of realistic geometric parameters such as aerofoil camber, angle of attack and thickness. The effect of aerofoil thickness is generally unanimous, although differing explanations for its mechanism exist. On the other hand there is some disagreement in the literature concerning the importance of angle of attack and camber effects, which appear to be dependent on the type of inflow disturbance.

Paterson & Amiet (1976) performed experimental investigations into the acoustic radiation of a two-dimensional NACA0012 aerofoil at Mach numbers ranging from 0.1 to 0.5. The inflow conditions were approximately homogeneous isotropic turbulence (HIT), with an intensity of around 4%. They found that the interaction of the incident turbulence with the aerofoil produced a broadband sound spectrum, more significant than other noise sources such as flow separation and turbulent boundary layer effects. Cross-correlations between the aerofoil surface and the far field demonstrated that the entire surface of the aerofoil was responsible for acoustic radiation, but by far the most prominent radiating region was the aerofoil LE. Comparing the far field results to theoretical predictions produced by Amiet's model (Amiet, 1975) yielded good agreement up until a reduced frequency $fL_{th}/U_\infty = 1$, where L_{th} is the aerofoil thickness, and U_∞ is the freestream velocity. Beyond this point there was a discrepancy of around 5 dB, which Paterson & Amiet (1976) attribute to thickness effects present in the experimental case (reduced noise with increased thickness). Angle of attack on the other hand was found to be of secondary importance, producing at most $1-2$ dB increase in far field noise for all tested Mach numbers.

Atassi *et al.* (1990) on the other hand explored the effects of aerofoil thickness and angle of attack from a computational aeroacoustics (CAA) approach. Their method consisted of solving the unsteady linearised Euler equations (LEE) to obtain the near field solution, and application of Kirchoff's formula to obtain to the far field acoustic pressure. Simulations were based on a two-dimensional Joukowski aerofoil interacting with both transverse and oblique gusts. At low Mach numbers, and reduced frequencies $fc/(2U_\infty) < 1$ the influence of aerofoil thickness was found to be insignificant. However a higher reduced frequencies increased thickness was found to have an effect on sound directivity, tilting it towards an upstream bias. This resulted in increased noise level upstream of the aerofoil, and reduced downstream. Variation of angle of attack revealed a positive correlation with far-field acoustic pressure, although the extent of the noise increase was found to be heavily dependant on the gust conditions and aerofoil geometry.

Thickness and angle of attack effects were also considered by Glegg & Devenport (2009), who developed a generalised Blasius theorem to predict the unsteady lift response of 2D aerofoils in incompressible flow. Both aerofoil-vortex interaction (AVI) and step upwash gust cases were considered. For AVI it was found that the influence of angle of attack depends on whether the vortex passes on the pressure or suction side of the aerofoil, with the pressure side resulting in a reduction of the unsteady loading pulse. Comparatively for the step upwash angle of attack was shown to

have negligible impact on amplitude, but rotated the direction of the unsteady loading force forward by the angle of attack. As with previous approaches, aerofoil thickness was found to reduce unsteady loading at high frequency. It was suggested this is due to smoothing of the unsteady blade response.

Glegg & Devenport (2010) later developed an unsteady panel method, effectively extending their work to aerofoils of arbitrary shape, and accounting for mean flow distortion of disturbances. Similar conclusions were drawn for both angle of attack and aerofoil thickness. Two methods were considered: A standard panel method where the velocity is calculated based on the classical Biot-Savart law; and a second approach based on a velocity potential derived from the stagnation enthalpy, with the incident vorticity described by its Lamb vector $\omega \times \boldsymbol{u}$. The advantage of the second approach is that it can account for streamwise and vertical vorticity contributions whereas the first approach is only suitable for spanwise vorticity. Despite this, Glegg & Devenport (2010) demonstrates that for a 2D aerofoil in 3D HIT only the spanwise component of vorticity is required to predict the noise. This result is similar to that of Howe (1988), who predicts the response of a flat plate aerofoil undergoing a vortex interaction based only on the spanwise component of vorticity.

A comprehensive study investigating the effect of realistic aerofoil geometry on aerofoil-turbulence interaction was later conducted by Devenport *et al.* (2010). Noise measurements taken in the Virginia Tech Stability Wind Tunnel, with two symmetric aerofoils of varying thickness (NACA0012 and NACA0015), as well as a heavily cambered S831 aerofoil were compared to predictions made by an incompressible vortex panel method. Investigations based on the symmetric foils in Homogeneous Isentropic Turbulence (HIT) yielded a similar result to Paterson & Amiet (1976), that the influence of angle of attack on the LE noise is minimal. However upon conducting further calculations based on non-homogeneous turbulence they discovered that the LE noise was a strong function of angle of attack, increasing by $5-10$ dB between $0°$ and $12°$. Additionally, experimental measurements obtained with the S831 aerofoil in grid generated HIT showed that LE noise increased by 4 dB between $0°$ and $4°$. This implies that the influence of angle of attack on LE noise is in fact dependant on the inflow condition and geometric parameters, which may explain the discrepancies between previous studies. In particular the disagreement between Myers & Kerschen (1995, 1997) theory and the experimental results of Paterson & Amiet (1976). Further to this the noise generated by the S831 aerofoil was found to be higher than the NACA0015 aerofoil despite the S831 having a higher overall thickness (18%). It was also much lower than the NACA0012 aerofoil despite its smaller LE radius. This result implies that the thickness effect is not governed solely by either one of these parameters, but a combination of both. Devenport *et al.* (2010) also found that the far field noise spectra produced by the NACA0012 aerofoil began to deviate from that obtained by a flat plate at frequencies greater than $fL_{th}/U_\infty = 0.12$, significantly lower than the frequency suggested by Paterson & Amiet (1976).

These observations were investigated in detail by Gill *et al.* (2013), who utilised an LEE solver to investigate the acoustic response of twenty four aerofoil geometries undergoing harmonic gust disturbances. A total of six LE radii and four thickness values (ranging from 6-24%) were analysed.

Gill showed that both LE radius and thickness are responsible for noise reductions relative to a flat plate, although the aerofoils were more sensitive to thickness changes. Additionally, the reductions are enhanced for high frequencies and Mach numbers. The main mechanism was found to be related to the LE stagnation region. Effectively a blunter edge was found to distort the incoming disturbances more severely due to large velocity gradients. The consequence is that the gust wave-front is more spread out and the amplitude is reduced. However there are still some inconsistencies regarding this explanation in the literature. Santana *et al.* (2012), utilising the same panel method approach as Glegg & Devenport (2010) pointed out that high frequency noise reduction due to aerofoil thickness was captured, despite neglecting LE vortex distortion.

There have also been efforts to quantify the effect of aerofoil thickness through empirical correction factors. Gershfeld (2004) utilised the vortex sound acoustic analogy to investigate aerofoil LE thickness effects. The procedure utilised a Green's function for an arbitrary thick (t) half-plane first used by Howe (1998) to investigate TE noise. It was shown that the effect of thickness is to exponentially decay the sound power at high frequencies. An empirical correction factor for flat plate aerofoils was therefore introduced: $\exp\left(-\omega t/(2U_\infty)\right)$, and compared to the experimental data of Paterson & Amiet (1976) with reasonably good agreement.

A simplified "Geometric" inflow turbulence model was suggested by Moriarty *et al.* (2005). A prior developed BEM approach was implemented to calculate the noise reduction of six thick aerofoils relative to a flat plate. After noticing that the aerofoil thickness noise reduction was approximately linear, Moriarty *et al.* (2005) introduced a "inflow turbulence noise indicator" to predict the slopes obtained by the BEM calculations. The noise indicator coefficients were optimised by a simulated annealing approach, yielding a simplified model requiring only the aerofoil thickness at 1% and 10% of the chord to predict the noise reduction slope. The geometric model was tested on seven additional aerofoils showing good agreement.

Another example is Lysak *et al.* (2013), who analytically modelled the high frequency response of aerofoils with thickness to a step function gust. The method incorporated the distortion of the gust vorticity through application of a drift function (Goldstein, 1978; Lighthill, 1956) which describes the time for a gust to travel to an arbitrary point in space. The resulting vorticity is then used to predict the unsteady lift based on vortex theory of Howe (2001). The model was compared to the linear result of Sears (1941), allowing Lysak to developed a correction factor so that the classical theory could be applied to NACA-65 aerofoil profiles.

Investigations have also been made regarding the influence of viscous effects on interaction noise. Lockard & Morris (1998) applied a 2D Navier-Stokes code to investigate the radiated noise produced by NACA aerofoils experiencing single frequency vortical gusts. Despite the inclusion of the viscous terms, the same general trends were found for both thickness and angle of attack as Atassi *et al.* (1990). By comparing the results to Euler simulations, it was found that viscosity had little effect on the radiated noise. Although it did effect the sound directivity in the downstream direction, due to instability introduced into the aerofoil wake. Somewhat similar findings have been made

by Sandberg & Sandham (2006), who reported additional downstream directivity lobes in viscous simulations of the trailing edge scattering of convected Tollmien-Schlichting waves.

1.3.1 Synthetic turbulence approaches

More recently efforts have turned towards obtaining more realistic CAA simulations based on synthetic turbulence approaches. These have the distinct advantage of producing a broadband noise spectrum which may be directly compared to experiments. However, numerically generating realistic turbulence is far from trivial due to its non-linear chaotic nature. Perhaps the most widely used procedure for its generation is the discrete Fourier mode summation approach, first developed by Kraichnan (1970). The popularity of this method can be attributed to its capability of generating a divergence free velocity field in a relatively straightforward manner. This is critical for computational aeroacoustic simulations in order to ensure zero noise from the upstream disturbances. However, since the method is based on a discrete summation it cannot represent a continuous spectrum.

An example of the Fourier summation mode approach applied to interaction noise is provided by Gill *et al.* (2015), utilising the aforementioned LEE solver and a von Kármán energy spectrum. The main purpose of this study was to investigate the modelling requirements for turbulence interaction concerning the use of one, two, or three-dimensional disturbances. Gill *et al.* (2015) showed that for symmetric aerofoils with low angle of attack ($\alpha < 2°$) a model only consisting of transverse velocity perturbations was sufficient to capture the interaction noise. This can be explained by considering the blockage to the flow caused by the aerofoil no-penetration condition. Unless the aerofoil represents a large blockage in the streamwise direction through large thickness or high angle of attack, or the spanwise direction through large sweep angle, it is likely the vertical perturbations will be most distorted by the wall. These findings have significant implications for the current study by providing justification for the use of a spanwise uniform impinging disturbance.

Another approach firstly proposed by Jarrin *et al.* (2006) for 3D Large Eddy Simulations (LES) is the synthetic eddy method (SEM). This approach was made applicable to aeroacoustic simulations by Sescu & Hixon (2013), by extending the method to satisfy a divergence free velocity field. Sescu & Hixon (2013) also reported that additional spurious noise is generated during the simulation if the convection velocity of the turbulent eddies is not in sync with that of the mean flow. This has yet to be considered in the alternative methods, giving the SEM a distinct advantage over other synthetic turbulence generation method in terms of reduced numerical noise.

Quite recently improvements were made to the method by Kim & Haeri (2015) with application to the ATI noise problem. A series of constraints were introduced for the eddy sizes, strengths and shape functions, which were subsequently optimised through use of a genetic algorithm (GA) to reproduce a realistic HIT spectra. The method also takes advantage of a sponge zone technique (Kim *et al.*, 2010*a*) allowing the disturbances to be injected into the domain relatively noise free. The far field sound pressure level (SPL) produced by a flat plate aerofoil was compared to that

predicted by both Amiet (1975) and experimental data, with good agreement at all frequencies. Additionally, the level of spurious noise produced during the simulations was shown to always be least two orders of magnitude below the physical level.

Another approach for synthetic turbulence is the random vortex particle method (RPM). This method has been used successfully by Ewert (2008) for slat noise predictions, and by Dieste & Gabard (2012) to study wake-fan interaction noise. However as of yet only a two-dimensional formulation exists for this method. A combination of both RPM and SEM approaches was recently introduced by Gea-Aguilera (2017) who used the mathematical description of turbulent eddies from RPM with the numerical implementation of SEM. The approach utilised a superposition of Gaussian eddies to approximate a target von Kármán spectrum.

1.4 Leading edge undulation

As more traditional methods for aircraft noise reduction reach their practical limitations it becomes inevitable that new novel technologies will be required to reach the ambitious noise targets. Passive geometry treatments for the reduction of broadband interaction noise have received a great deal of attention from the research community in the past few years. One of the most widely researched is aerofoil LE undulation (wavy leading edges), which have been demonstrated to obtain noise reductions as high as 10 dB at certain frequencies (Chaitanya *et al.*, 2017; Chong *et al.*, 2015; Narayanan *et al.*, 2015). Such geometry was originally considered for its aerodynamic properties (Hansen *et al.*, 2011; Johari *et al.*, 2007; Miklosovic *et al.*, 2004), inspired by the leading-edge tubercles of the humpback whale's pectoral flippers, shown in figure 1.3(a). It is believed that these protrusions are responsible for the animals impressive manoeuvrability in the water while catching its prey (Fish *et al.*, 2008). More recently wavy leading edges (WLE) have also been considered for there noise reduction capabilities. Another well known example occurring in nature is the comb-like LE serrations of barn owl's primary flight feathers, which are widely regarded as one of the main features which contribute towards its silent flight (Graham, 1934) (see figure 1.3(b)). However this geometry has generally received less attention, in part due to its less certain aerodynamic performance at higher Reynolds numbers (Ito, 2009), as well as materials/structural considerations.

The noise reduction capabilities of wavy leading edges (WLE) have been exhibited for harmonic gusts, turbulence and vortex disturbance types utilising analytical (Ayton, 2017; Lyu & Azarpeyvand, 2017; Mathews & Peake, 2018), experimental (Biedermann *et al.*, 2017; Chaitanya *et al.*, 2017; Chong *et al.*, 2015; Hansen *et al.*, 2010; Narayanan *et al.*, 2015; Roger & Moreau, 2016), and numerical methodologies (Clair *et al.*, 2013; Kim *et al.*, 2016; Lau *et al.*, 2013; Reboul *et al.*, 2017; Tong *et al.*, 2018*b*; Turner & Kim, 2017*b*). Generally speaking the LE noise reduction increases with frequency in an approximately linear fashion (until masked by additional sources of sound). The underlying trend has been demonstrated to be related to the Strouhal number based on the WLE amplitude ($2h_{LE}$) as $\Delta PWL = 10\log_{10}(10fh_{LE}/U_\infty)$ (Chaitanya *et al.*, 2017). Consistently it is

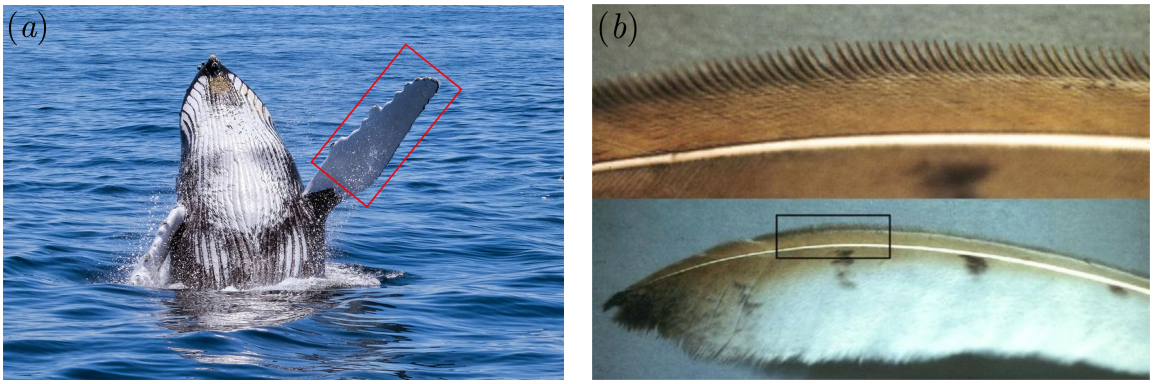

Figure 1.3: (a) Leading edge tubercles of the humpback whale's pectoral flipper (photo credit: Robbie Shade flickr.com) (b): Leading edge serrations of a Barn Owl's flight feather, (photo credit: Kay Schultz).

found that the noise reductions are determined mainly by the WLE amplitude ($2h_{LE}$). Increasing $2h_{LE}$ shifts the noise reduction spectrum to the left, resulting in an increase over the majority of the frequency range. Recently, the influence of the various parameters on overall noise reductions $\Delta OASPL$ have been systematically ranked through a design of experiments (DOE) based approach (Biedermann *et al.*, 2017). Thus revealing amplitude, followed by Reynolds number, then leading edge wavelength (λ_{LE}) as the major factors for noise reduction. The noise reduction capabilities of WLEs demonstrated in figure 1.4, which shows the acoustic pressure contours (p'/p_∞) generated by baseline SLE (straight leading edge) and WLE zero-thickness aerofoils respectively. The data is obtained through numerical simulations of synthetically generated turbulence (Kim & Haeri, 2015; Kim *et al.*, 2016). It is apparent how the WLE geometry produces a smoother acoustic pressure profile, suggesting significant damping of higher frequency noise components.

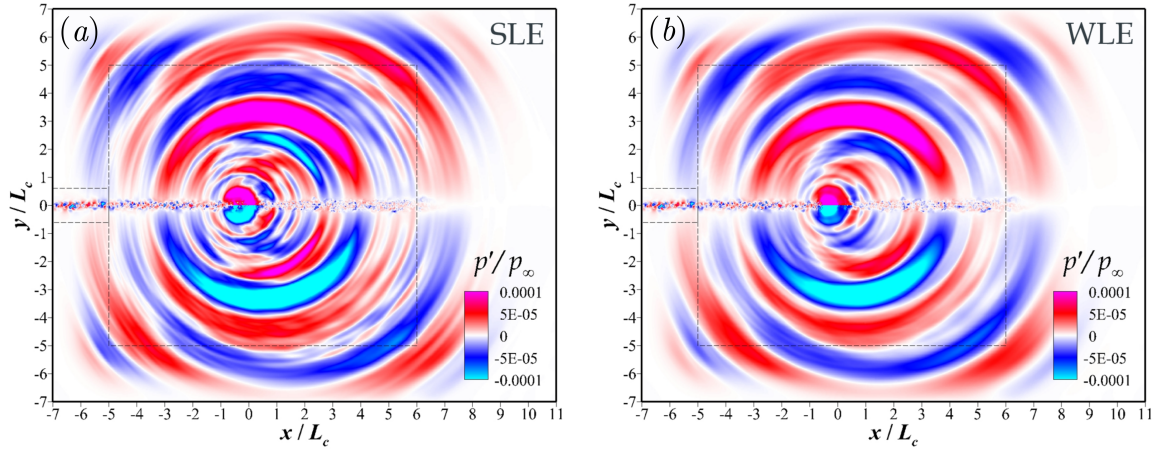

Figure 1.4: (a) Acoustic pressure contours generated during aerofoil-turbulence-interaction (ATI) by a flat plate aerofoil with a straight leading edge (SLE). (b) Equivalent plot for a wavy leading edge (WLE) geometry. Taken from: (Kim & Haeri, 2015; Kim *et al.*, 2016).

1.4.1 Previous studies on leading edge undulation

Since they were first identified by Graham (1934), many studies have focused on the noise reduction capabilities of owl inspired LE serrations and their engineering applications. An early example is the experimental study conducted by Soderman (1973). Soderman carried out noise measurements for low speed rotors with saw-tooth brass strips applied to their leading edge. It was found that the serrations could obtain high frequency noise reductions in the range of around 4 dB overall sound pressure level (OASPL) for a rotor 2.59 m in diameter with serration heights of 0.13-0.64 cm. Regarding their aerodynamic properties, Ito (2009) carried out wind tunnel experiments of NACA63 − 414 aerofoils with saw-tooth serrations. He found that the serrated cases provided an improvement to maximum lift coefficient and post-stall lift and drag. However this was only observed at a low Reynolds number of 2.1×10^4, increasing the Reynolds number to 2.1×10^5 yielded no notable improvement.

1.4.1.1 Aerodynamic performance of undulated aerofoils

Unlike sawtooth serrations, sinusoidal serrations first gained attention for their impressive aerodynamic capabilities at high angles of attack. This is most likely due to the function of tubercles on the pectoral flippers of the humpback whale. It has been demonstrated extensively that they have the potential to vastly improve performance at high angle of attack, specifically delaying onset of stall, producing a softer stall profile, and increasing maximum lift coefficient (Hansen *et al.*, 2011; Johari *et al.*, 2007; Miklosovic *et al.*, 2004). The aerodynamic enhancements WLEs offer do come at the cost of some small reduction in pre-stall aerodynamic efficiency, but importantly they are observed at a wide range of Reynolds numbers, making them appropriate for a variety of applications. This includes turbofan OGVs and wind turbines where the angle of attack relative to the mean flow can be reasonable high.

The improved stall characteristics have been attributed to three primary mechanisms (Bolzon *et al.*, 2016). Firstly that streamwise vortices generated by the WLE act as vortex generators, mixing high momentum fluid into the tired boundary layer. The second theory is that the streamwise vortices produce vortex lift (a change in effective angle of attack due to downwash). Thirdly it is possible that there exists a compartmentalisation effect where the propagation of stall in the spanwise direction is delayed (much like a wing fence).

The development of the streamwise vortex structures have been described in detail by Rostamzadeh *et al.* (2014) and Hansen *et al.* (2016) for transitional and laminar flow regimes respectively. They proposed that a surface flux of vorticity is generated due to strong LE pressure gradients. The vorticity is stretched and tilted by pressure gradients, as well as diffused by viscous forces eventually leading to the creation of streamwise coherent structures located in between the LE peaks. Another interpretation from Rostamzadeh *et al.* (2014) is that the spanwise vorticity contained in the boundary layer is turned into the streamwise direction by a “flow skewness” effect, which is created

by the curvature of streamlines at the LE. This mechanisms is referred to as Prandtl's secondary flow of the first kind.

Similar observations were also made by Skillen *et al.* (2015), who conducted an LES simulation of a NACA0021 aerofoil for Reynolds number $Re_\infty = 1.2 \times 10^5$. Strong spanwise pressure gradients were observed resulting in secondary flow developing in the WLE troughs. The re-energisation of the boundary layer caused by the secondary flow resulted in a significantly reduced separated region. Additionally, Skillen *et al.* (2015) noted that the unsteady force fluctuations (lift and drag) were reduced for the WLE. This is also important for the aeroacoustic performance of WLEs as the unsteady lift is proportional to the radiated sound at low Mach numbers (Curle, 1955). The power spectral density of the unsteady lift revealed a reduced magnitude for the WLE throughout the frequency range, as well as reduced tonal peaks. This result suggests that the WLE geometry may be effective at reducing noise from both separation and coherent vortex shedding.

Further insight into the delayed separation and compartmentalisation effects of wavy leading edges was provided in a recent LES by Pérez-Torró & Kim (2017). This study focused on a NACA0021 aerofoil at Reynolds number $Re_\infty = 1.2 \times 10^5$, focusing on 20 degrees angle of attack. It was shown how low pressure observed at the WLE troughs (Hansen *et al.* (2016); Skillen *et al.* (2015); Yoon *et al.* (2011)) is associated with laminar separation bubbles (LSBs). Unusually, the LSBs were shown to form in a collocated pattern (non-uniform and non-periodic) in the spanwise direction. A similar pattern has also been observed experimentally by Chong *et al.* (2015). It was speculated that the streamwise vortices stop the LSB bubbles from merging, resulting in compartmentalisation of the separated region, and a smaller wake volume. Additionally, the loss of spanwise coherence due to the streamwise structures resulted in reduced von Kármán shedding, and consequently less pressure drag in the stall regime. Similar to Skillen *et al.* (2015), they also showed a reduction of unsteady lift fluctuations caused by the WLE.

1.4.1.2 Previous experimental and numerical work on WLE noise reduction

One of the first investigations to specifically consider the aeroaocustic performance of WLEs was undertaken by Hansen *et al.* (2010), who performed experiments based on a NACA0021 aerofoil. They found that WLE cases provided large reductions to tonal noise, as well as significant reductions to broadband noise around the tonal peaks (between 1.5 kHz and 2.5 kHz). Hansen *et al.* (2010) theorised that the tonal noise reductions were related to the production of streamwise vortices at the leading edge troughs. These improve the stability of the boundary layer by mixing in higher momentum fluid from the freestream, which alters the shear layer and therefore the generation of vorticity near the trailing edge.

Lau *et al.* (2013) used a computational aeroacoustic approach based on high order compact finite differencing and filters to investigate the effect of wavy leading edge geometry on aerofoil-gust interaction (AGI) noise. They investigated a series of wavy leading edge profiles based on a NACA0015 aerofoil section at three gust frequencies at zero degrees angle of attack. They preserved

the same planform area and cross section throughout the span for fair comparison with straight leading edge counterparts. An upstream sinusoidal disturbance varying in both the streamwise and vertical direction was used as a gust model. It was concluded that the most effective method for reducing AGI was to increase the ratio between the leading edge amplitude and gust wavelength $2h/\lambda_g$. In particular, significant reductions were obtained once $2h/\lambda_g > 0.3$. Regarding the leading edge wavelength (λ) its influence was found to be much less significant, however they state that this could be due to the gust model lacking significant spanwise fluctuations. Examining the fluctuating pressure signals along of the LE, Lau *et al.* (2013) found that WLE cases produce a phase shift along the span resulting in a de-synchronised gust response, which they suggest is responsible for the noise reduction. Despite this the cause of the phase change was left unexplained, as well as whether this is the only reason for the reduced noise.

Clair *et al.* (2013) undertook both numerical and experimental investigations into the acoustic properties of wavy leading edges. Three serrated wings based on a NACA65-1210 aerofoil were tested in the University of Southampton ISVR anechoic wind tunnel. A square rod grid was implemented at the tunnel nozzle exit, designed to provide HIT. This was necessary in order to develop a scenario where ATI would be the dominant noise source over aerofoil self-noise (which is significant in a uniform flow). The WLE aerofoils where effective over a wide range of frequencies, broadening at lower mean flow speeds. Clair *et al.* (2013) describe the effect as similar to a low pass filter, attenuating sound above a certain cut of point (around 1 kHz at 60 m/s). Similar to Lau *et al.* (2013) they also found that performance was improved with increased leading edge amplitude, obtaining reductions as high as 6 dB for serrations of 15 mm (10% of the chord) in the mid-frequency range. Their CAA results also revealed reduced RMS surface pressure at the peak and hill regions of the WLE, compared to the SLE case. Since RMS surface pressure is usually correlated with radiated sound, this could be a reason for the lower noise generated by the WLE.

Narayanan *et al.* (2015) conducted a detailed parameter study into WLE amplitude ($2h$) and wavelength (λ). They performed experiments in the ISVR anechoic wind tunnel primarily for both flat plate aerofoils, validated with high-order CAA simulations. Inflow turbulence was generated using a HIT grid, which produced a velocity spectra very close to the von Kármán spectra. They found that sound power level reductions (ΔPWL) were primarily influenced by the LE amplitude, less so by LE wavelength, similar to Lau *et al.* (2013). The largest noise reductions were obtained with long (high $2h$) and wide (high λ) serrations. This finding agrees with the experimental results of Chong *et al.* (2015), but is incompatible with Hansen *et al.* (2010) where narrow serrations exhibited better performance. The noise reduction spectra obtained with a flat plate was also compared to a NACA-65 utilising the same serration profile. Larger noise reductions were obtained with the flat plate, 9 dB compared to 7 dB for the thick aerofoil. By plotting contour maps of ΔPWL vs frequency and flow speed (U_∞) Narayanan et al. also identified a minimum frequency f_0, above which significant noise reductions are achieved ($>$ 3dB). For all cases regardless of serration geometry and flow speed, they found that the minimum frequency was located at $f_0 = \alpha U_\infty/(2h)$, with $\alpha \approx 0.5$ (varying between $0.4-0.6$). This relation is consistent with the findings of Clair *et al.* (2013), who discovered that the frequency range where noise reduction are observed broadens as

U_∞ is reduced. However, it was unclear as to why noise reductions are restricted to $f > f_0$, as well as the cause for the variation in α.

Roger & Moreau (2016) carried out experimental investigations of two passive leading edge geometries wavy leading edges and porous leading edges, for a NACA0012 and flat plate aerofoils interacting with grid generated turbulence. For the NACA0012 experiments a spectral subtraction procedure was utilised to isolate the interaction noise from the self-noise contributions (where the self-noise was estimated by removing the upstream grid). For flat plate cases the interaction noise level was considered dominant enough at high frequencies for this process to be unnecessary. All geometries produced a 'hump-like' noise reduction profile which initially increases then drops off at higher frequencies. In the current work it is speculated that this drop-off could be caused by TEVS of the impinging disturbance. Generally better noise reductions were obtained by the wavy leading edges, with a maximum noise reduction of 10 dB vs. 6dB for the porous leading edge. Roger & Moreau (2016) also showed how the noise reduction spectra collapse when plot against the chord based Strouhal number (fL_c/U_∞), suggesting the results are self-similar for the flow speed.

More recently Kim *et al.* (2016) investigated the noise reduction mechanisms associated with WLEs with a CAA approach. Simulations were based on the 3D compressible Euler equations, effectively removing the influence of self-noise components generated at the TE. Flat plate aerofoils with various serration heights were positioned in a synthetically generated turbulence stream, based on the von Kármán velocity spectra, and generated by a synthetic eddy method (SEM) (Kim & Haeri, 2015). Kim *et al.* (2016) identified two mechanisms for noise reduction. The first is a source "cut-off" effect, which they attribute to the obliqueness of the LE hill regions. It was found that the mean squared surface pressure fluctuations at the hill regions and subsequently the source power are significantly reduced compared to a root and peak regions, which are more comparable to a SLE case. This effect is precipitated by the local increase in sweep angle at the LE hills, and hence is amplified with increased serration height (h). Correlations of surface pressure fluctuations along the LE also revealed a more rapid reduction for cases with higher h, suggesting a weaker radiation to the farfield. The source cut-off effect was further explored by analysing the surface pressure auto-spectrum along the LE, identifying that the hill regions are responsible for reducing the sound power across the whole range of frequencies. Interestingly analysis of the root and peak spectrum showed that relative to a SLE case the peak is a much weaker source of low frequency noise, while the root produces an approximately equal level. Alternatively at high frequencies the reverse trend is observed, all be it to a lesser degree. The second noise reduction mechanism put forward by Kim *et al.* (2016) is a phase interference effect. It was reported that WLE cases exhibit an increased out of phase shift between the LE peak and other locations along the LE, especially the hill regions. The relative phase spectra between straight and wavy cases matched well with the noise reduction spectra particularly at medium to high frequencies, thus demonstrating the importance of phase interference.

Following up from the work of Kim *et al.* (2016), Turner & Kim (2017*b*) conducted a canonical study based on CAA simulations of the interaction between at WLE and a single spanwise vortex. By simplifying the incoming disturbance they were able to identify fundamental features of the

flow which determine the source strength variation along the WLE. It was demonstrated that by increasing WLE height (h) the source strength at the hill is reduced throughout the frequency range (confirming the source cut-off effect identified by Kim *et al.* (2016)). At the peak, the source strength was shown to reduce, although saturate with continued increase to h. Alternatively at the root, the source strength was shown to remain almost constant regardless of the selected geometry. The differences observed between the peak and the root are particularly interesting as one would anticipate that they would maintain a similar pressure response since both are perpendicular to the incoming flow. The mechanisms behind these observations were explained in relation to a system of secondary horseshoe-like vortices which are generated on the aerofoil surface as the vortex passes over the LE. Through induced velocity contributions they alter the upstream field and consequently the unsteady pressure response on the surface. It should be noted that the streamwise vortices discussed here are separate from those discussed by (Rostamzadeh *et al.*, 2014) in that they are created by turning the impinging spanwise vorticity into the streamwise direction rather than the boundary layer vorticity. Full details of this study are included in this report under chapter 3.

Another important paper concerning the noise reduction mechanisms was recently introduced by Chaitanya *et al.* (2017) utilsing the same experimental setup as Narayanan *et al.* (2015). The main finding of this paper was the existence of an optimum WLE wavelength for a given impinging spanwise length scale. The optimum value occurs for $\lambda_{LE}/\Lambda = 4$, where Λ is the spanwise integral length scale of impinging turbulence. The discovery of an optimal serration explains the conflicting findings of Narayanan *et al.* (2015) and Hansen *et al.* (2010). Based on the findings of Kim *et al.* (2016) for the WLE root source strength, the authors of this paper speculated the optimum value corresponds to the point when the adjacent roots are first excited incoherently. Under this condition constructive interference of the high strength roots would be avoided, while simultaneously exciting enough of the edge to gain the benefits of reduced source strength and destructive interference. Another important discovery in this work is the existence of a Strouhal number dependence similar to Roger & Moreau (2016), this time based on the WLE amplitude (fh_{LE}/U_∞). This outcome highlights the importance of phase interference caused by the WLE as h_{LE}/U_∞ is proportional to the phase-shift between peak and root ($\phi = 4\pi f h_{LE}/U_\infty$). Plotting the noise reductions against the Strouhal number revealed an approximately linear trend when close to the optimum serration wavelength. Chaitanya *et al.* (2017) also hypothesised a noise reduction mechanism based on the variation of source characteristics along the LE. They proposed that the "effective length" of the sources near the root scale linearly with the hydrodynamic wavelength U/f, therefore resulting in a linear increase of noise reduction with frequency.

1.4.1.3 Analytical predictions for WLE noise reduction

There have also been recent developments in analytical approaches to predict ATI noise from WLEs. Roger *et al.* (2013) utilised a strip theory approach to model a semi-infinite chord WLE. The sinusoidal serration is separated into small spanwise strips each with a sweep angle corresponding to the local tangent of the edge. An extension to Amiet's method for swept blades is then utilised to

obtain the contribution from each strip (Roger & Carao, 2010). The limitation of this approach is that it neglects coupling between the spanwise strips. Regardless, it is useful for interpreting some of the fundamental mechanisms of the WLE. The study demonstrates how the radiated sound is highly dependent on whether the impinging gust is sub- or super-critical. Essentially a gust which is parallel to the SLE (super-critical) may be sub-critical at the WLE hills (where the local sweep angle is maximum) resulting in significantly reduced radiated sound. Similarly a sub-critical gust for the SLE may become super-critical for the WLE if parallel with the WLE hill slopes. This highlights a potential scenario where the WLE may under perform the baseline geometry. An additional Schwarzschild technique model was also introduced by in this paper taking into account the effect of LE curvature. This was accomplished by firstly transforming the problem into stretched coordinates by subtracting the WLE shape function from the x coordinate. As the aerofoil is semi-infinite, the now wavy TE can be considered sufficiently far downstream as to be ignored. Similar qualitative trends were observed with this new model as for the simple strip method.

An alternative approach to modelling the WLE noise reduction was carried out by Mathews & Peake (2015, 2018) based on a procedure introduced for self-noise predictions from serrated trailing edges (Howe, 1991). This study considered a flat plate semi-infinite chord WLE aerofoil interaction with a specific distribution of turbulent eddies. Uniquely the non-linear motion of the disturbances is captured analytically by determining the incident pressure field from the Euler momentum equation. The incident pressure field is then used in conjunction with an appropriate Green's function derived for a serrated half plane to approximate the far-field noise. Both single, and multiple eddy interactions are considered. It was found that in all cases a WLE exists which could effectively reduce the noise. However, similar to the findings of Roger *et al.* (2013), it was found that the WLE could increase the noise if the disturbances impinge at an oblique angle. Essentially, a priori knowledge of the disturbance field is required in order to select an optimum WLE profile for a given application.

A more recent attempt to extend the SLE flat plate theory of Amiet (1975) was carried out by Lyu & Azarpeyvand (2017) for saw-tooth type LE geometry. This innovative approach utilises a Fourier expansion method to eliminate the spanwise dependence of the boundary value problem. The resulting set of PDEs is then solved with an iterative Schwarzschild technique. This approach has also been applied with success to aerofoils with TE serrations (Lyu *et al.*, 2016). The predicted far field spectra showed good agreement with the experimental results produced by Narayanan *et al.* (2015), particularly at medium-high frequencies, while at low frequencies the model resulted in an over prediction. The predicted loss of noise reduction at low frequencies may be caused by not fully capturing the source mechanisms due to the frozen turbulence assumption. In particular the low frequency source strength reduction at hill and peak shown by Kim *et al.* (2016); Turner & Kim (2017*b*). Lyu & Azarpeyvand (2017) proposed that the noise reduction mechanism is mainly due to destructive interference occurring between points along the LE. This was demonstrated by plotting the scattered pressure over the surface at individual frequencies, revealing that the sign of the pressure response oscillates along the edge length. It was shown how increasing LE amplitude and

frequency both reduce the edge length spacing between opposite sign regions, effectively increasing the out-of-phase percentage of the LE, and the noise reductions. The destructive interference mechanism is investigated in more detail in §4, and compared to other proposed mechanisms, source strength reduction and effective source length.

Another attempt to analytically model the noise from serrations was carried out by Ayton (2017). This approach utilises the Wiener-Hopf technique in addition to a non-orthogonal co-ordinate transform to model the interaction of a sawtooth serration with semi-infinite chord length in a channel. Good agreement concerning the fundamental trends in the literature are obtained, such as the effect of increased frequency and LE amplitude. Additionally the surface response follows a similar pattern to Lyu & Azarpeyvand (2017), also implying destructive interference is one of the primary mechanisms.

1.4.1.4 Improved WLE geometries

Another recent development in the literature is the introduction of modified WLE geometries. Two interesting examples were presented in a recent paper by Chaitanya *et al.* (2016). In this study the WLE was modified with the aim of minimising the contribution from the root, which has been shown as the primary WLE noise source ((Kim *et al.*, 2016; Turner & Kim, 2017*b*)). The first geometry was a dual-frequency wavy leading edge (DWLE) consisting of two summed sine waves. The reasoning behind this was to introduce a streamwise displacement between consecutive roots in order to entice destructive interference. In experiments undertaken in the University of Southampton anechoic wind tunnel the DWLEs were successful in obtaining additional noise reductions of around 4 dB in a narrow frequency band. A simple estimate for the frequency where additional noise reduction occur is obtained by considering when half the hydrodynamic wavelength equals the streamwise root-root distance ($fd_{rr}/U_\infty = 0.5$). The second modified WLE was a slitted LE profile, obtained by cutting either rectangular or triangular streamwise slits at each WLE root. Overall better performance was obtained by the triangular slits which produced additional noise reductions from medium to high frequency. The largest noise reductions were obtained with greater slit lengths and smaller slit widths.

DWLEs have also been investigated through numerical simulations conducted by Turner *et al.* (2016*a*), utilising the same vortex-aerofoil interaction approach as outlined in Turner & Kim (2017*b*). The aim of this study was to precisely demonstrate the destructive interference mechanism by contrasting the DWLE acoustic sources with the resulting far field noise. It was shown that the root-root estimate for additional noise reductions is not entirely accurate as the two roots have different source strength. This is a consequence of differing local sweep angles at the adjacent hills, and therefore different strength horseshoe vortex structures (which determine the root wall pressure response). Further to this, it was shown that for cases with larger serration height additional noise reduction harmonics are observed at higher frequencies. It was speculated that this was not observed in the experimental procedure (Chaitanya *et al.*, 2016) due to them being

masked by viscous self noise from the TE. Some results from this study are presented in Appendix E.

Curved serrations which mimic owl feathers have also been investigated experimentally by Juknevicius *et al.* (2017). It was hypothesised that the LE curvature may block the flow impinging on the WLE root thereby increasing the noise reductions. The curved serrations outperformed undulated leading edges obtaining an additional 5dB maximum noise reduction. It was speculated that the LE curvature may increase the effective serration height, resulting in a stronger interference effect. So far no evidence has been obtained for the flow blocking mechanism which represents a possible future area of study.

1.5 Research aims and objectives

Despite rapid progress towards quantifying the extent of noise reductions from WLEs in recent years, there is still much unexplained regarding the physical noise reduction mechanisms. This includes fundamental aspects such as acoustic source generation and explanations for simple noise reduction trends. The principle aim of this research is therefore to develop a more comprehensive understanding of wavy leading edges as well as aerofoil interaction noise in general. The goal is broken into four major categories which are as follows:

1. Provide a physical interpretation of the acoustic source mechanisms for wavy leading edges during LEVS.
2. Investigate proposed noise reduction mechanisms in order to determine which is most fundamental to the WLE noise reduction trends, in particular source strength modification or destructive interference.
3. Quantify the extent of secondary interaction noise sources ABS and TEVS for aerofoil-vortex interaction.
4. Explore how the secondary interaction noise sources are effected by the WLE.

1.6 Original contributions

This work investigates the interaction noise generated by a spanwise vortex disturbance impinging on zero-thickness aerofoils with sinusoidal leading edge profiles. It employs a high fidelity computational aeroacoustic (CAA) approach based on the full 3D non-linear Euler/Navier-Stokes equations utilising high performance computing procedures.

1.6.1 Thesis outline

The work in this thesis is presented as a collection of four papers, each addressing one of the above objectives. Below are details of the work conducted for each paper:

§3-**Primary Leading Edge Source Mechanisms** contains the paper first presented in:

TURNER J.M. & KIM J.W. 2017 Aeroacoustic source mechanisms of an aerofoil with a wavy leading edge undergoing vortical disturbances. J. Fluid Mech. **811**, 582-611.

Abstract High-accuracy numerical simulations are performed to study aeroacoustic source mechanisms of wavy leading edges (WLEs) on a thin aerofoil undergoing vortical disturbances. This canonical study is based on a prescribed spanwise vortex travelling downstream and creating secondary vortices as it passes through the aerofoils leading edge. The primary aim of the study is to precisely understand the relationships between the vortex-induced velocity perturbation and the wall pressure fluctuation on the WLE geometry. It is observed that by increasing the size (amplitude) of the WLE the source strength at the peak region is reduced rapidly to a certain point, followed by a saturation stage, while at the root (trough) it remains fairly consistent regardless of the WLE size. This observation is demonstrated to be the consequence of three-dimensional vortex dynamics taking place along the WLE. One of the most profound features is that a system of horseshoe-like secondary vortices are created from the WLE peak region upon the impingement of the prescribed vortex. It is found that the horseshoe vortices produce a significantly non-uniform velocity perturbation in front of the WLE leading to the disparity in the source characteristics between the peak and root. The alterations to the impinging velocity perturbation are carefully analysed and related to the wall pressure fluctuation in this study. In addition, a semi-analytic model based on Biot-Savart's law is developed to better understand and explain the role of the horseshoe vortex systems and the source mechanisms.

§4-**Noise Reduction Modelling and Underlying Mechanisms** contains the paper:

TURNER J.M. & KIM J.W. 2019 On the universal trends in noise reduction due to wavy leading edges in aerofoil-vortex interaction, Under review J. Fluid Mech.

Abstract It is well established in existing literature that wavy leading edges may offer substantial broadband noise reductions for the problem of aerofoil interaction noise. However, despite rapid growth in the field there still exists fundamental questions regarding the physical mechanisms by which these reductions are made possible. In this paper two of the leading explanations – destructive interference and source strength reduction – are investigated in order to determine their contribution to the noise reductions. In particular the focus is on two universal properties of the observed WLE noise reduction spectra. 1. The increase of noise reduction with frequency. 2. Zero noise reduction at low frequency. The resulting findings have important consequences for future modelling approaches concerning which characteristics are critical for properly capturing the physics. Through application of a 1D LE model the interference mechanism is shown as the main driving force for the increasing noise reduction with frequency. However, it is found that this

approach based solely on the LE can lead to erroneous conclusions regarding the significance of source strength variation, which in fact requires a 2D representation. This is made apparent from the surface spectra, which shows the source strength downstream of the LE is far from negligible at high frequencies. As a consequence it is shown through application of the FW-H equation that the source variation over almost the entire surface is required to properly predict the noise reduction spectra. Regarding zero noise reduction at low frequency, it is found that despite previously observed reduced strength along the LE line, the percentage of the surface with similar strength is almost the same for SLE and WLE cases. This is caused by noise increase regions downstream of the LE, thus leading to net zero noise reduction for very low frequencies.

§5-**Secondary Noise Sources** contains the paper:

TURNER J.M. & KIM J.W. 2019 Secondary noise sources in the aerofoil-vortex interaction problem, Preprint

Abstract The noise generated by vortical disturbances impinging on an aerofoil has widely been studied in the past where the primary source mechanism is the vortical scattering at the leading edge (LE) of the aerofoil. In this paper the secondary source mechanisms – the subsequent vortical scattering at the trailing edge (TE) and the backscattering of the produced acoustic waves – are investigated in detail. The present study is performed by employing high-fidelity numerical simulations in which a prescribed spanwise vortex impinges on a non-lifting flat-plate aerofoil with zero thickness situated in an inviscid mean flow. One of the most profound observations made in this paper is that the vortical scattering at the TE is the dictating source of noise at high frequencies in almost all observer directions. This is demonstrated for both exactly parallel interactions, and interactions with vertical miss distances, even at distances where image vortex effects are expected to be negligible. This unique discovery has significant consequences for analytical approaches which typically neglect the TE scattering in aerofoil-vortex interaction. A series of two and three-dimensional laminar LES simulations are also conducted to determine the sensitivity of the TE event to the flow conditions. The resulting noise is found to be highly dependent on Reynolds number and vortex strength, existing only if the convective structures persist to through the boundary layer without being significantly dissipated.

§6-**The Effect of WLEs on Secondary Sources** contains the work first presented in:

TURNER J.M. & KIM J.W. 2019 Secondary noise sources in a vortical flow interacting with an undulated aerofoil, Preprint

Abstract

The current investigation provides new findings on the secondary sources and their influence on the noise reduction due to the LE undulation of the aerofoil. It is found that the secondary sources make substantial impacts on the acoustic power spectra and directivity profiles in the far field, which are not described by using the primary source only. The noise reduction directivity in particular can change by more than 10dB when the secondary effects are included. When an undulated LE is used the relative impact of the secondary sources is greater due to reduction of the primary LE noise.

For upstream angles the secondary TE scattering even exceeds the primary source for the majority of frequencies. The dominance of TE vortical scattering results in the noise reduction (a beneficial effect of using an undulated LE) disappeared in the high-frequency range. An effective means to regain the lost noise reduction is to also include a undulated TE, which results in superior high frequency performance than the semi-infinite WLE. Towards the end of the paper additional LES simulations are carried out in the laminar regime for $Re_\infty = 400,000$ in order to investigate if the observed noise reduction trends persist when the convective disturbances interact with a boundary layer. For the WLE aerofoil there is a sudden breakdown of the LE generated structures to tertiary 3D eddies on the aerofoil lower side. This phenomena is not observed for the SLE under the same flow conditions. The outcome is a large increase of the TE vortical scattered sound relative to the SLE, which raises a couple of critical questions to address in the future.

1.6.2 List of publications and conference proceedings

Journal papers-accepted

- TURNER J.M. & KIM J.W. 2017 Aeroacoustic source mechanisms of an aerofoil with a wavy leading edge undergoing vortical disturbances. J. Fluid Mech. **811**, 582-611.
- CHAITANYA, P., JOSEPH, P., NARAYANA, S., VANDERWEL, C., TURNER, J., KIM, J. W. & GANAPATHISUBRAMANI, B. 2017 Performance and mechanism of sinusoidal leading edge serrations for the reduction of turbulence-aerofoil interaction noise. J. Fluid Mech. **818**, 435-464.
- TURNER J.M., HAERI, S. & KIM J.W. 2016 Improving the boundary efficiency of a compact finite difference scheme through optimising its composite template. Comput. Fluids. **138**, 9-25.

Journal papers-in preparation

- TURNER J.M. & KIM J.W. 2019 On the universal trends in noise reduction due to wavy leading edges in aerofoil-vortex interaction. *In review J. Fluid Mech.*
- TURNER J.M. & KIM J.W. 2019 Secondary noise sources in the aerofoil-vortex interaction problem. *Preprint.*
- TURNER J.M. & KIM J.W. 2019 Secondary noise sources in a vortical flow interacting with an undulated aerofoil. *Preprint.*

Conference papers

- TURNER J.M. & KIM J.W. Aeroacoustic effects of the trailing edge of an undulated aerofoil subjected to impinging disturbances. In 23rd AIAA/CEAS Aeroacoustics Conference. AIAA Paper 2017-3494.

- TURNER J.M. & KIM J.W. Towards understanding aerofoils with wavy leading edges interacting with vortical disturbances. In 22nd AIAA/CEAS Aeroacoustics Conference. AIAA Paper 2016-2952.
- TURNER J.M., KIM J.W., CHAITANYA P. & JOSEPH P. Towards understanding aerofoils with dual-frequency wavy leading edges interacting with vortical disturbances. In 22nd AIAA/CEAS Aeroacoustics Conference. AIAA Paper 2016-2951.
- CHAITANYA, P., NARAYANA, S., JOSEPH, P., VANDERWEL, C., TURNER, J., KIM, J. W. & GANAPATHISUBRAMANI, B. 2015 Broadband noise reductions through leading edge serrations on realistic aerofoils. In 21st AIAA/CEAS Aeroacoustics Conference. AIAA Paper 2015-2202.

Chapter 2

Computational Methodology

2.1 Current computational approach

Previously synthetic turbulence approaches have been the primary basis for computational methodology used to model ATI noise. This approach has proved capable of capturing the underlying physics of ATI, which has been demonstrated through good agreement with experimental data. It has also yielded significant research findings with regards to the WLE noise reduction mechanisms (most notably the oblique cut-off and decorrelation effects identified by Kim *et al.* (2016)). Despite these successes there are some difficulties with this approach, particularly concerning the possible identification of any coherent structures which may be generated during the interaction. In addition, it is difficult to determine what extent of the spanwise variation in acoustic source strength is attributed to the LE geometry, opposed to a local inhomogeneity in the turbulent flow. In order to properly decipher the WLE interaction mechanisms a canonical study has been developed based on a single spanwise vortex disturbance. This approach offers a number of distinct advantages including:

- Simpler flow regime allows for easier identification of fundamental structures in the flow
- The use of a single disturbance means the resulting sound spectra is smooth and requires no additional filtering or averaging
- The spanwise vortex disturbance still maintains a reasonably large range of frequencies, unlike many other single disturbance approaches to modeling ATI (e.g. harmonic gusts).
- More control over the vortex dynamics, for example effects such as impingement angle and vertical offset can be predetermined.

The main limitation of this method is that we neglect spanwise length scale effects. A detailed study on this mechanism is provided by Chaitanya *et al.* (2017). This can result in larger oscillations in the spectra than an HIT approach as the LE interaction is coherent, and therefore promotes phase

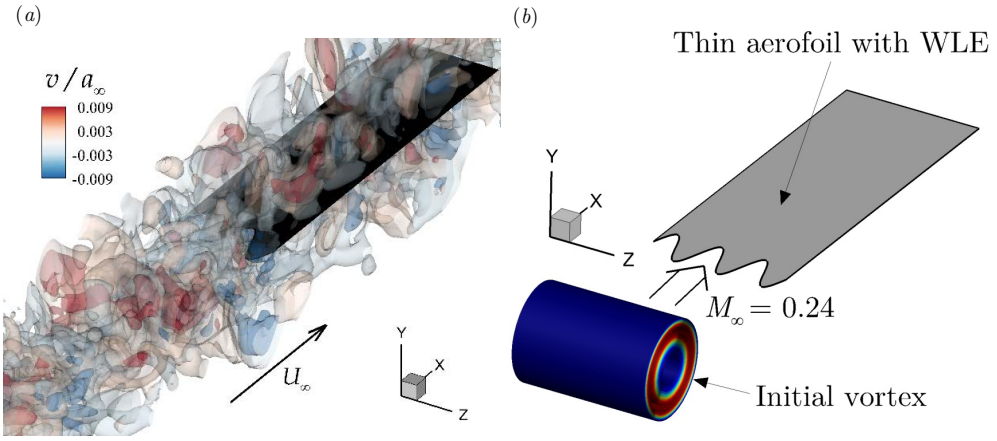

Figure 2.1: (a) Previous synthetic turbulence approach based on randomly distributed Gaussian eddies (Kim *et al.*, 2016). (b) Current aerofoil-vortex interaction approach.

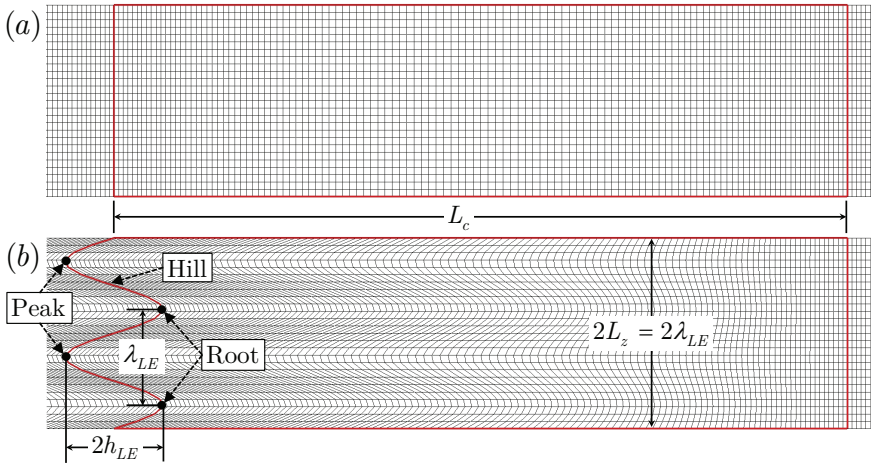

Figure 2.2: Surface meshes (coarsened for illustration purposes) on the flat-plate aerofoils used in the present study, with (a) straight and (b) wavy leading edges (SLE and WLE, respectively). The case of $h_{LE}/L_c = 1/15$ and $\lambda_{LE}/L_c = 2/15$ is shown in this figure. Specific details of the grid resolution are contained within the relevant results sections.

interference effects. Despite this limitations it is shown in later sections that the numerical results still follow similar underlying trends as experiments based on HIT (see figure 4.5).

The two inflow conditions are illustrated in figure 2.1. Two vortex shape functions are implemented in the current work, details are provided in the relevant results sections (§3 and §4). The remainder of this chapter provides details of the current computational setup and methodology.

2.1.1 Computational domain and aerofoil geometry

The computational domain is a rectangular cuboid which contains a flat-plate aerofoil at the centre with zero thickness and zero angle of attack. The zero-thickness aerofoil is modelled by using a

H-topology grid system where the central branch section represents the aerofoil's upper and lower surfaces with no gap between them. The longitudinal and vertical boundaries of the domain are surrounded by a sponge layer through which the flow is (gently) forced to maintain the potential mean flow condition. Any acoustic waves are attenuated and absorbed in the sponge layer to prevent numerical reflections at the outer boundaries. More details of this technique are provided in the following subsection and in Kim *et al.* (2010*a*,*b*). The lateral boundaries of the domain are interconnected via a periodic boundary condition. In §3 the entire computational domain; the inner region (physical domain) where meaningful simulation data are obtained; and, the sponge layer zone are defined as

$$\left.\begin{aligned} \Omega_{\infty} &= \{\boldsymbol{x} \,|\, x/L_c \in [-5,9], y/L_c \in [-7,7], z \in [-\tfrac{1}{2}L_z, \tfrac{1}{2}L_z]\}, \\ \Omega_{physical} &= \{\boldsymbol{x} \,|\, x/L_c \in [-3,3], y/L_c \in [-5,7], z \in [-\tfrac{1}{2}L_z, \tfrac{1}{2}L_z]\}, \\ \Omega_{sponge} &= \Omega_{\infty} - \Omega_{physical}, \end{aligned}\right\} \tag{2.1}$$

where L_z is the spanwise length of the domain. In the current simulations, L_z is set equal to the wavelength of the WLE profile while the periodic boundary condition is used to produce an essentially infinite span. This greatly reduces the cost of the simulation without having a significant effect on the validity of the results since the vortex has a uniform spanwise distribution.

The aerofoil WLE profile is based on the following sine function

$$x_{LE}(z) = -\frac{1}{2}L_c + h_{LE}\sin\left(\frac{2\pi z}{\lambda_{LE}}\right), \quad z \in \left[-\frac{1}{2}L_z, \frac{1}{2}L_z\right], \tag{2.2}$$

where the most protruded points are defined as "peak", the least as "root" and the middle as "hill" (see figure 2.2). Herein, h_{LE} is defined as the WLE amplitude/height, $2h_{LE}$ the peak-to-root amplitude, and λ_{LE} is the spanwise wavelength. The aerofoil centre chord point is located at $x = 0$, with the trailing edge (TE) and mean LE at $x_{TE} = \frac{1}{2}L_c$ and $\overline{x_{LE}} = -\frac{1}{2}L_c$ respectively. Amplitudes ranging from $h_{LE}/L_c = 1/40 - 1/10$ are investigated in this study with $h_{LE}/L_c = 1/15$ generally used as the default value. Unless explicitly stated the wavelength is fixed to $\lambda_{LE}/L_c = 2/15$ with one wavelength in the span. These values are selected for consistency with previous publications including (Chaitanya *et al.*, 2015; Kim *et al.*, 2016; Narayanan *et al.*, 2015; Turner & Kim, 2017*b*). Grid statistics and independence studies are contained within the relevant results chapters.

2.1.2 Sponge treatment

The primary function of the sponge zone forcing term on the RHS of (2.6) is to remove any non-physical numerical reflections experienced at the domain boundaries. The principle behind the technique is to force the flow to approach a desired reference solution within the sponge region. The current methodology uses the technique outlined by Kim *et al.* (2010*a*,*b*). This proposes the following forcing term for density, velocity and pressure in **S**

$$\mathbf{S} = \begin{cases} \mu_s(x,y)\,[\rho - \rho_\infty,\ \ \lambda_s(x)\rho(\mathbf{u}-\mathbf{u_t}),\ \ p - p_\infty] & \text{for } \mathbf{x} \in \Omega_{\text{sponge}} \\ \mathbf{0} & \text{for } \mathbf{x} \in \Omega_{\text{physical}} \end{cases} \tag{2.3}$$

where the sponge coefficient profile $\mu(x,y)$ is given by

$$\begin{aligned} \mu_s(x,y) &= \frac{\mu_0}{2}[1+\cos(\pi A(x)B(y))] \\ A(x) &= 1 - \max\left(\frac{x_a - x}{x_a - x_{min}}, 0\right) - \max\left(\frac{x - x_b}{x_{max} - x_b}, 0\right) \\ B(x) &= 1 - \max\left(\frac{y_a - y}{y_a - y_{min}}, 0\right) - \max\left(\frac{y - y_b}{y_{max} - y_b}, 0\right) \end{aligned} \tag{2.4}$$

and the weighting factor $\lambda_s(x)$ is

$$\lambda_s(x) = (1+\delta)[1 - \tanh(x/L_c)] + 1 \ \text{ and } \ \delta = \min[2M_\infty/(1+M_\infty), 1] \tag{2.5}$$

where the subscript ∞ represents freestream conditions, and the sponge strength parameter $\mu_0 = 1.5$. Within the sponge region ($\Omega_{sponge} = \Omega_\infty - \Omega_{physical}$), the density and pressure are forced to ambient conditions, while the velocities are forced to a target velocity $\mathbf{u_t}$, in this case mean flow U_∞. For pressure and density forcing the same sponge coefficient profile is employed in the upstream and downstream directions. This increases in strength closer to the domain boundaries, eventually reaching a maximum of μ_0. On the other hand the velocity forcing is reduced downstream of the aerofoil by use of the weighting factor $\lambda_s(x)$, varying from $3 + 2\delta$ at the inlet to 1 at the outlet. Since we do not need to enforce an inflow condition downstream of the aerofoil, a weaker constraint is applicable.

Additionally to reduce reflections at the domain exit boundary an increasingly stretched grid is employed in the sponge to help dissipate the disturbances. Visualisation of the sponge coefficient profiles is given in figures 2.3(a) for pressure and density and 2.3(b) for velocity.

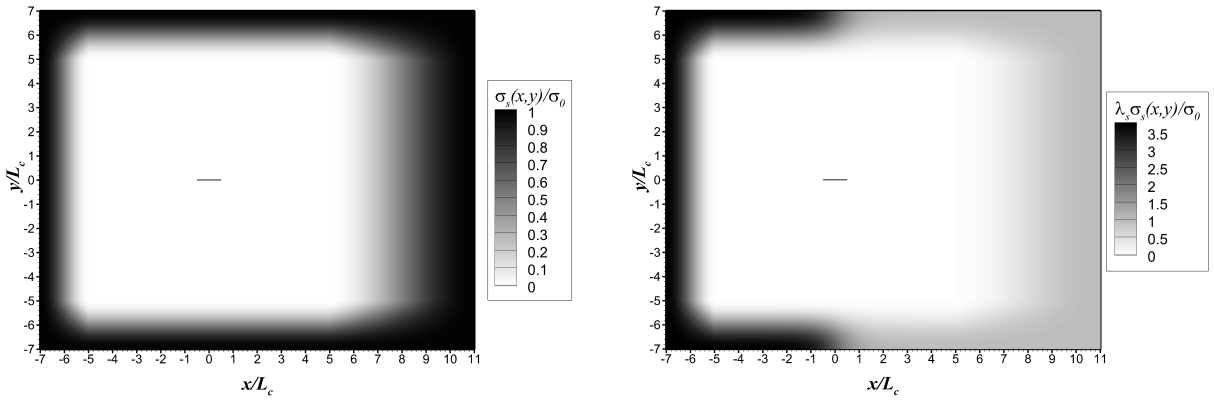

(a) Density and pressure forcing

(b) Velocity forcing

Figure 2.3: Sponge coefficient profiles

2.1.3 Governing equations

Aerofoil noise generated by interaction with vortical disturbances is largely considered an inviscid phenomenon and therefore exclusion of viscous terms is usually considered to be a reasonable simplification (Atassi *et al.*, 1990; Ayton & Peake, 2013; Evers & Peake, 2000; Gill *et al.*, 2015; Goldstein, 1978; Kim & Haeri, 2015; Lockard & Morris, 1998; Myers & Kerschen, 1995, 1997). In accordance with this historical approach we employ an inviscid approach throughout the majority of the current work, particularly when considering interaction with the LE. In chapters §5 and §6 focus switches to secondary sources of aerofoil-vorticity interaction noise, which primarily concern scattering of vortical structures at the TE. In these sections additional investigations are carried out to determine the role of viscosity on the vortex convection. We therefore employ the full three-dimensional compressible Euler/Navier-Stokes equations (with a source term for the sponge layer mentioned earlier) in a conservative form transformed onto a generalised coordinate system:

$$\frac{\partial}{\partial t}\left(\frac{\boldsymbol{Q}}{J}\right)+\frac{\partial}{\partial \xi_i}\left(\frac{\boldsymbol{E}_j}{J}\frac{\partial \xi_i}{\partial x_j}\right)=\frac{M_\infty}{Re_\infty}\frac{\partial}{\partial \xi_i}\left(\frac{\boldsymbol{F}_j}{J}\frac{\partial \xi_i}{\partial x_j}\right)-\frac{a_\infty}{L_c}\frac{\boldsymbol{S}}{J}, \tag{2.6}$$

where a_∞ is the ambient speed of sound; and, the indices $i=1,2,3$ and $j=1,2,3$ denote the three dimensions. In (2.6), $\boldsymbol{Q}$ represents the conservative variables, $\boldsymbol{E}$ the convective fluxes, and $\boldsymbol{F}$ the viscous and heat fluxes. $\boldsymbol{F}=0$ is employed for Euler calculations. The conservative variable and flux vectors are given by

$$\left.\begin{aligned}\boldsymbol{Q}&=[\rho,\rho u,\rho v,\rho w,\rho e_\mathrm{t}]^T,\\ \boldsymbol{E}_j&=[\rho u_j,(\rho u u_j+\delta_{1j}p),(\rho v u_j+\delta_{2j}p),(\rho w u_j+\delta_{3j}p),(\rho e_\mathrm{t}+p)u_j]^T,\\ \boldsymbol{F}_j&=[0,\tau_{1j},\tau_{2j},\tau_{3j},u_i\tau_{ji}+q_j]^T,\end{aligned}\right\} \tag{2.7}$$

with

$$\tau_{ij}=\mu\left(\frac{\partial u_i}{\partial x_j}+\frac{\partial u_j}{\partial x_i}-\frac{2}{3}\delta_{ij}\frac{\partial u_i}{\partial x_i}\right),\quad q_j=\frac{\mu}{(\gamma-1)Pr}\frac{\partial T}{\partial x_j}, \tag{2.8}$$

where $\xi_i=\{\xi,\eta,\zeta\}$ are the generalised coordinates, $x_j=\{x,y,z\}$ are the Cartesian coordinates, δ_{ij} is the Kronecker delta, $u_j=\{u,v,w\}$, $e_\mathrm{t}=p/[(\gamma-1)\rho]+u_ju_j/2$ and $\gamma=1.4$ for air. Furthermore τ_{ij} represents the stress tensor, the heat flux is given by q_j, and $Re_\infty=\rho_\infty U_\infty L_c/\mu_\infty$ is the Reynolds number. In the current setup, ξ, η and ζ are body fitted coordinates along the grid lines in the streamwise, vertical and lateral directions, respectively. The Jacobian determinant of the coordinate transformation (from Cartesian to the body fitted) is given by $J^{-1}=|\partial(x,y,z)/\partial(\xi,\eta,\zeta)|$ (Kim & Morris, 2002). The extra source term $\boldsymbol{S}$ on the right-hand side of (2.6) is non-zero within the sponge layer only, which is described in Kim *et al.* (2010*a*,*b*).

2.1.4 Numerical methods

2.1.4.1 Spatial discretisation

Spatial discretisation of the governing equations is achieved with use of the pentadiagonal matrix system of compact finite-differences schemes and filters outlined by Kim (2007, 2010), designed specifically for aeroacoustic simulations. This consists of one central interior scheme and three one-sided boundary closures, all of which achieve 4th order accuracy on seven point stencils. The interior scheme is expressed as follows:

$$\beta\bar{f}'_{i-2} + \alpha\bar{f}'_{i-1} + \bar{f}'_i + \alpha\bar{f}'_{i+1} + \beta\bar{f}'_{i+2} = \frac{1}{h}\sum_{m=1}^{3} a_m(f_{i+m} - f_{i-m}) \tag{2.9}$$

where f_i is a function evaluation at a nodal point i, $\bar{f}'_i$ is the numerical approximation to the exact derivative f'_i, and h is the grid spacing. In order to apply the same scheme as (2.9) to the boundary nodes $i = 0, 1, 2$ and $i = N, N-1, N-2$ extrapolation functions are required for the points outside of the boundary. The following spline function and its derivative are used as extrapolation functions for fi and $\bar{f}'_i$ beyond the boundaries:

$$g_i(x^*) = f_i + \sum_{m=1}^{N_A} p_m(x^*)^m + \sum_{m=1}^{N_B} [q_m \cos(\phi_m x^*) + r_m \sin(\phi_m x^*)] \tag{2.10}$$

$$g'_i(x^*) = \frac{1}{h}\left\{\sum_{m=1}^{N_A} m p_m(x^*)^{m-1} - \sum_{m=1}^{N_B} \phi_m[q_m \sin(\phi_m x^*) - r_m \cos(\phi_m x^*)]\right\} \tag{2.11}$$

where $x^* = (x - x_i)/h$ is the normalised coordinate of the target point, and p_m r_m and q_m are coefficients selected via constraints to match the interior solutions. The remaining parameters ϕ_m are used for resolution optimisation of the schemes. In order to maintain 4th order accuracy at the boundaries the polynomial terms are also set to fourth order ($N_A = 4$). Once the coefficients have been determined the extrapolation functions may be replaced by a linear combination of interior solutions. (2.9) may then be rearranged into the following set of one-sided differences for the three boundary nodes

$$i = 0: \quad \bar{f}'_0 + \gamma_{01}\bar{f}'_1 + \gamma_{02}\bar{f}'_2 = \frac{1}{h}\sum_{m=0,\neq 0}^{6} b_{0m}(f_m - f_0), \tag{2.12}$$

$$i = 1: \quad \gamma_{10}\bar{f}'_0 + \bar{f}'_1 + \gamma_{12}\bar{f}'_2 + \gamma_{13}\bar{f}'_3 = \frac{1}{h}\sum_{m=0,\neq 1}^{6} b_{1m}(f_m - f_1), \tag{2.13}$$

$$i = 2: \quad \gamma_{20}\bar{f}'_0 + \gamma_{21}\bar{f}'_1 + \bar{f}'_2 + \gamma_{23}\bar{f}'_3 + \gamma_{24}\bar{f}'_4 = \frac{1}{h}\sum_{m=0,\neq 2}^{6} b_{2m}(f_m - f_2) \tag{2.14}$$

Full details of the extrapolation procedure, and a complete list of the coefficients can be found in Kim (2007). In order to numerically evaluate the derivative using the above implicit schemes, the following matrix system of equations is solved:

$$\mathbf{P}\bar{\mathbf{f}}' = \frac{1}{h}\mathbf{Q}(\mathbf{f} + \mu\tilde{\Delta}\mathbf{f}) \tag{2.15}$$

with

$$\bar{\mathbf{f}}' = (\bar{f}'_0, \bar{f}'_1, \bar{f}'_2, \cdots, \bar{f}'_N)^T, \quad \mathbf{f} = (f_0, f_1, f_2, \cdots, f_N)^T, \quad \tilde{\Delta}\mathbf{f} = (\tilde{\Delta}f_0, \tilde{\Delta}f_1, \tilde{\Delta}f_2, \cdots, \tilde{\Delta}f_N)^T$$

The $(N+1)\times(N+1)$ matrices $\mathbf{P}$ and $\mathbf{Q}$ contain the finite-difference scheme coefficients, they may be expressed as follows.

$$\boldsymbol{P} = \begin{pmatrix} 1 & \gamma_{01} & \gamma_{02} & 0 & \cdots & 0 & 0 & 0 & 0 \\ \gamma_{10} & 1 & \gamma_{12} & \gamma_{13} & 0 & \cdots & 0 & 0 & 0 \\ \gamma_{20} & \gamma_{21} & 1 & \gamma_{23} & \gamma_{24} & 0 & \cdots & 0 & 0 \\ 0 & \beta & \alpha & 1 & \alpha & \beta & 0 & \cdots & 0 \\ \vdots & \ddots & \ddots & \ddots & \ddots & \ddots & \ddots & \ddots & \vdots \\ 0 & \cdots & 0 & \beta & \alpha & 1 & \alpha & \beta & 0 \\ 0 & 0 & \cdots & 0 & \gamma_{24} & \gamma_{23} & 1 & \gamma_{21} & \gamma_{20} \\ 0 & 0 & 0 & \cdots & 0 & \gamma_{13} & \gamma_{12} & 1 & \gamma_{10} \\ 0 & 0 & 0 & 0 & \cdots & 0 & \gamma_{02} & \gamma_{01} & 1 \end{pmatrix}$$

$$\boldsymbol{Q} = \begin{pmatrix} b_{00} & b_{01} & b_{02} & b_{03} & b_{04} & b_{05} & b_{06} & 0 & 0 & \cdots & 0 \\ b_{10} & b_{11} & b_{12} & b_{13} & b_{14} & b_{15} & b_{16} & 0 & 0 & \cdots & 0 \\ b_{20} & b_{21} & b_{22} & b_{23} & b_{24} & b_{25} & b_{26} & 0 & 0 & \cdots & 0 \\ -a_3 & -a_2 & -a_1 & 0 & a_1 & a_2 & a_3 & 0 & 0 & \cdots & 0 \\ 0 & -a_3 & -a_2 & -a_1 & 0 & a_1 & a_2 & a_3 & 0 & \cdots & 0 \\ \vdots & \ddots & \ddots & \ddots & \ddots & \ddots & \ddots & \ddots & \ddots & \ddots & \vdots \\ 0 & \cdots & 0 & -a_3 & -a_2 & -a_1 & 0 & a_1 & a_2 & a_3 & 0 \\ 0 & \cdots & 0 & 0 & -a_3 & -a_2 & -a_1 & 0 & a_1 & a_2 & a_3 \\ 0 & \cdots & 0 & 0 & -b_{26} & -b_{25} & -b_{24} & -b_{23} & -b_{22} & -b_{21} & -b_{20} \\ 0 & \cdots & 0 & 0 & -b_{16} & -b_{15} & -b_{14} & -b_{13} & -b_{12} & -b_{11} & -b_{10} \\ 0 & \cdots & 0 & 0 & -b_{06} & -b_{05} & -b_{04} & -b_{03} & -b_{02} & -b_{01} & -b_{00} \end{pmatrix}$$

As can be seen by the above matrices the three boundary closure schemes are administered at the boundary node $i = [0, N]$, and the first two interior nodes $[1, N-1]$ and $[2, N-2]$. The interior scheme is applied through the remainder of the domain $(3 \leq i \leq N-3)$. The parameter $\mu = 0||1$ is used to determine whether compact filters are applied to the finite-difference system. Filtered values are represented by $\tilde{f}_i = f_i + \tilde{\Delta}f_i$. $\tilde{\Delta}\mathbf{f}$. They are obtained in a similar manner, by solving

the following matrix system.

$$\mathbf{R}\tilde{\Delta}\mathbf{f} = \mathbf{T}\mathbf{f} \tag{2.16}$$

where the matrices $\mathbf{R}$ and $\mathbf{T}$ are the filter coefficient counterparts (superscripted F) of $\mathbf{P}$ and $\mathbf{Q}$, described as

$$\boldsymbol{R} = \begin{pmatrix} 1 & \gamma_{01}^F & \gamma_{02}^F & 0 & \cdots & 0 & 0 & 0 & 0 \\ \gamma_{10}^F & 1 & \gamma_{12}^F & \gamma_{13}^F & 0 & \cdots & 0 & 0 & 0 \\ \gamma_{20}^F & \gamma_{21}^F & 1 & \gamma_{23}^F & \gamma_{24}^F & 0 & \cdots & 0 & 0 \\ 0 & \beta^F & \alpha^F & 1 & \alpha^F & \beta^F & 0 & \cdots & 0 \\ \vdots & \ddots & \ddots & \ddots & \ddots & \ddots & \ddots & \ddots & \vdots \\ 0 & \cdots & 0 & \beta^F & \alpha^F & 1 & \alpha^F & \beta^F & 0 \\ 0 & 0 & \cdots & 0 & \gamma_{24}^F & \gamma_{23}^F & 1 & \gamma_{21}^F & \gamma_{20}^F \\ 0 & 0 & 0 & \cdots & 0 & \gamma_{13}^F & \gamma_{12}^F & 1 & \gamma_{10}^F \\ 0 & 0 & 0 & 0 & \cdots & 0 & \gamma_{02}^F & \gamma_{01}^F & 1 \end{pmatrix}$$

$$\boldsymbol{T} = \begin{pmatrix} b_{02}^F & b_{02}^F & b_{01}^F & b_{00}^F & b_{01}^F & b_{02}^F & b_{03}^F & 0 & 0 & 0 & 0 & 0 & \cdots & 0 & 0 & 0 & 0 \\ 0 & b_{13}^F & b_{12}^F & b_{11}^F & b_{10}^F & b_{11}^F & b_{12}^F & b_{13}^F & 0 & 0 & 0 & 0 & \cdots & 0 & 0 & 0 & 0 \\ 0 & 0 & b_{23}^F & b_{22}^F & b_{21}^F & b_{20}^F & b_{21}^F & b_{22}^F & b_{23}^F & 0 & 0 & 0 & \cdots & 0 & 0 & 0 & 0 \\ 0 & 0 & 0 & a_3^F & a_2^F & a_1^F & a_0^F & a_1^F & a_2^F & a_3^F & 0 & 0 & \cdots & 0 & 0 & 0 & 0 \\ 0 & 0 & 0 & 0 & a_3^F & a_2^F & a_1^F & a_0^F & a_1^F & a_2^F & a_3^F & 0 & \cdots & 0 & 0 & 0 & 0 \\ \vdots & \vdots & \vdots & \vdots & \ddots & \ddots & \ddots & \ddots & \ddots & \ddots & \ddots & \ddots & \ddots & \vdots & \vdots & \vdots & \vdots \\ 0 & 0 & 0 & 0 & \cdots & 0 & a_3^F & a_2^F & a_1^F & a_0^F & a_1^F & a_2^F & a_3^F & 0 & 0 & 0 & 0 \\ 0 & 0 & 0 & 0 & \cdots & 0 & 0 & a_3^F & a_2^F & a_1^F & a_0^F & a_1^F & a_2^F & a_3^F & 0 & 0 & 0 \\ 0 & 0 & 0 & 0 & \cdots & 0 & 0 & 0 & b_{23}^F & b_{22}^F & b_{21}^F & b_{20}^F & b_{21}^F & b_{22}^F & b_{23}^F & 0 & 0 \\ 0 & 0 & 0 & 0 & \cdots & 0 & 0 & 0 & 0 & b_{13}^F & b_{12}^F & b_{11}^F & b_{10}^F & b_{11}^F & b_{12}^F & b_{13}^F & 0 \\ 0 & 0 & 0 & 0 & \cdots & 0 & 0 & 0 & 0 & 0 & b_{03}^F & b_{02}^F & b_{01}^F & b_{00}^F & b_{01}^F & b_{02}^F & b_{03}^F \end{pmatrix}$$

where the terms $a_0^F = -2(a_1^F + a_2^F + a_3^F)$, and $b_{ii}^F = -2(b_{i0}^F + b_{i1}^F + b_{i3}^F)$. The function of the compact filters is to ensure a linearly stable matrix system of equations, determined through eigenvalue analysis. This is achieved by removing any unresolved scales from the solution at the end of each time step by introducing a cut-off frequency Ω_c. The filter coefficients offered in Kim (2010) are designed to maintain a sixth order accuracy, to avoid introducing additional errors into the domain which may be detrimental to the accuracy of the finite-difference schemes. Similarly to the boundary closures, the boundary filters apply extrapolation functions at the domain boundaries. The greyed out segments of the matrix $\mathbf{T}$ represent coefficients belonging to ghost points, which are determined via extrapolation of interior solutions as:

$$f_i = f_0 + \frac{i}{2}(f_3 - f_0) + \frac{i}{10}(f_6 - f_0) + \frac{i}{90}(f_9 - f_0), \quad \text{for} \quad i = \{-1, -2, -3\} \tag{2.17}$$

For the current study the filter coefficients are determined using a consistent normalised filter cut-off of $\Omega_c = 0.85\pi$ at both interior and boundary nodes. The order of accuracy of the numerical method, including finite-difference filters and non-reflecting boundary conditions (see §2.1.6), has been demonstrated for 2D vortex convection problems on Cartesian (Kim, 2007) and Curvilinear grids (Turner *et al.*, 2016*b*).

In addition to formal order of accuracy, numerical schemes are often judged based on their spectral resolution properties. These are typically quantified through Fourier analysis as dispersion and dissipation errors. The discrete Fourier series is given by

$$f(x) = \sum_{k=-N/2}^{N/2} \hat{f}(k) \exp\left(\frac{\jmath 2\pi k x}{L}\right) \tag{2.18}$$

where L is the length of the domain, k is a wavenumber, $\hat{f}(k)$ is a Fourier coefficient and $\jmath$ is the imaginary unit. Often the Fourier series will be simplified by converting to the scaled coordinate system $x^* = x/h$, and substituting for the scaled wavenumber $\omega = 2\pi k h/L$. This results in the following equation.

$$f(x) = \sum_{k=-N/2}^{N/2} \hat{f}(k) \exp\left(\jmath \omega x^*\right) \tag{2.19}$$

For a given wavenumber, the exact derivative of (2.19) is given by $f' = \jmath\omega f$. Errors introduced by the finite-difference approximation to the derivative may be expressed in terms of a modified wavenumber $\bar{\omega}$, such that $\bar{f}' = \jmath\bar{\omega} f$. An expression for $\bar{\omega}$ can be obtained in a relatively straightforward manner, simply by applying the Fourier transform to each term in the differencing scheme (taking into account that $f_{i\pm m} \equiv f(x^* \pm m)$). For optimal performance it is desired that $\bar{\omega} = \omega$, specifically $\mathrm{Re}(\bar{\omega}) \to \omega$ and $\mathrm{Im}(\bar{\omega}) \to 0$.

Compact schemes, such as those used in the current methodology are implicit based on a banded Hermitian matrix (in this case pentadiagonal). This means that they require a costly matrix inversion in order to evaluate the numerical derivative. However they offer a distinct advantage over more traditional explicit schemes due to their superior resolution properties for a given stencil size. This ultimately allows such a scheme to successfully resolve the desired scales with fewer grid points, leading to large savings in computational cost. This has made compact schemes very popular in the field of CAA.

By freeing up some of the coefficients constrained for formal order of accuracy, it is possible to improve the spectral properties of a compact scheme through optimisations. This was achieved by Kim (2007) by releasing three coefficients which were optimised by minimising an integral error measure defined between the exact and modified curves over a specified optimisation range $[0 - 0.8505\pi]$ (Kim, 2007). The improvement to spectral resolution is made apparent by figure 2.4, which compares the modified wavenumber curves of the interior scheme suggested in Kim

(2007), with those produced by explicit 2nd and 6th order central schemes. (N.B. there is no dissipation error produced by a central scheme, hence only the real part (dispersion) of the modified wavenumber is shown here). Figure 2.5 shows both the real and imaginary wavenumber curves produced by the boundary closure schemes at the $i = 0,\ 1$ and 2 nodes. The dispersion errors are very low, similar to that of the interior scheme, despite boundary closure schemes typically offering inferior performance. However due to their one-sided structure additional dissipation is inevitable, although low resolution errors are still maintained until a relatively high wavenumber.

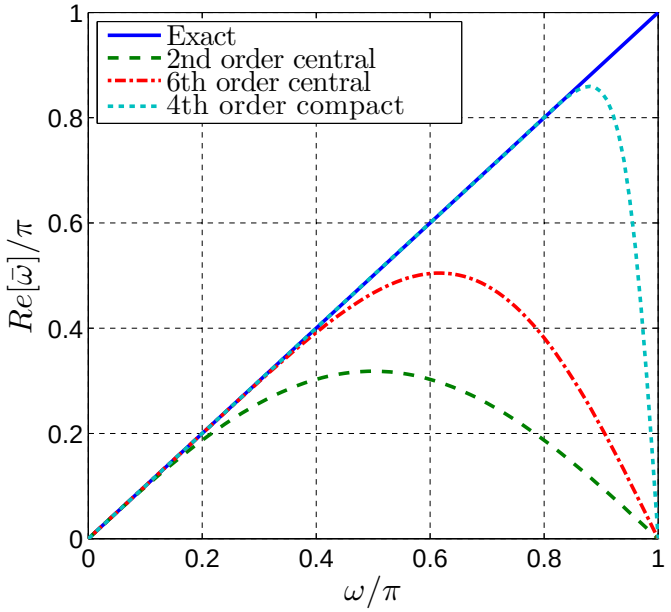

Figure 2.4: Modified wavenumber curves produced by a standard 2nd order central scheme, and 4th order compact used in the current methodology Kim (2007)

2.1.4.2 Temporal discretisation

Time marching schemes can be separated into to main categories, explicit and implicit. Explicit schemes obtain the solution for the next time step solely based on past solutions, while implicit schemes also require information at the current time step. The simplicity of explicit schemes generally means they are relatively cheap to implement, while implicit schemes require some kind of expensive matrix inversion or iterative procedure. On the other hand explicit schemes require strict constraints on their time step size for numerical stability, while implicit schemes are inherently stable. However for transient problems such as those considered here there is little advantage of implicit schemes, since time step requirement for accuracy is often less than that needed for stability in an explicit scheme (Pulliam & Zingg, 2014). In the current work time marching is achieved with an explicit 4th-order Runge-Kutta scheme. It involves integrating the following ODE.

$$\frac{\mathrm{d}\mathbf{Q}}{\mathrm{d}t} = \mathbf{G}(\mathbf{Q}, t) \tag{2.20}$$

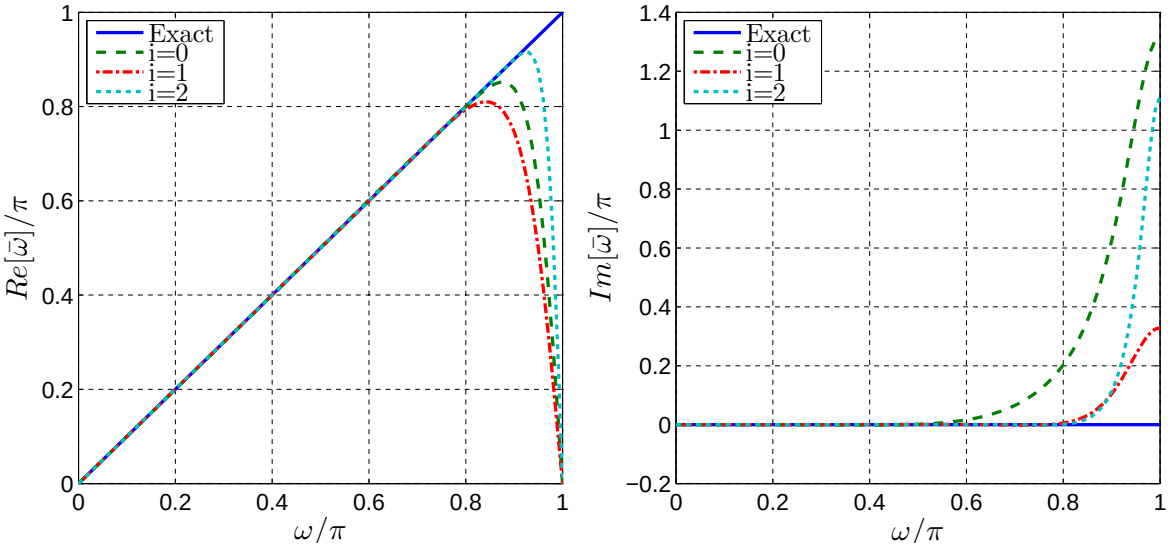

Figure 2.5: Real and imaginary modified wavenumber curves produced by boundary closure schemes used in the current methodology Kim (2007)

where $\mathbf{G}$ contains the flux derivatives and sponge forcing terms contained in (2.6), and $\mathbf{Q}$ contains the primitive variables. The procedure consists of four stages described as follows

$$\begin{aligned} \mathbf{K}_0 &= \mathbf{Q}_n \\ \mathbf{K}_i &= \mathbf{Q}_n + \frac{\Delta t}{4-i+1}\mathbf{G}(\mathbf{K}_{i-1}, t), \quad \text{for } i = \{1,2,3\} \\ \mathbf{Q}_{n+1} &= \mathbf{Q}_n + \Delta t \mathbf{G}(\mathbf{K}_3, t) \end{aligned} \tag{2.21}$$

where $\mathbf{Q}_n$ represents the solution at the current time step $n\Delta t$, $\mathbf{Q}_{n+1}$ represents the solution at the next time step $(n+1)\Delta t$, and K_i are temporary solutions produced at subsequent stages. In the current methodology we utilise an adaptive time stepping approach, where the time step Δt is determined by the Courant-Friedrichs-Lewy condition (CFL):

$$\Delta t = \frac{\text{CFL}}{u_\xi + u_\eta + u_\zeta} \tag{2.22}$$

where u_ξ, u_η, u_ζ represent the maximum speed with which information can propagate in the ξ, η and ζ directions respectively. For stability it is usually recommended that CFL ≤ 1 for explicit time marching schemes. For the current simulations CFL $= 0.95$ is used throughout.

2.1.5 Algorithm for compact schemes

In this section a description of the main algorithm used in the code is provided for a simple test case. An advection-diffusion equation in two-dimensions and Cartesian space can be expressed as:

$$\frac{\partial f}{\partial t}+\frac{\partial f}{\partial x}+\frac{\partial f}{\partial y}=\frac{\partial^2 f}{\partial x^2}+\frac{\partial^2 f}{\partial y^2} \tag{2.23}$$

where f is a primitive variable. All derivatives (1st and 2nd order) in the current setup are determined via the compact schemes provided in (2.1.4.1). (2.23) is therefore rewritten as follows:

$$\frac{\partial f}{\partial t}+\frac{\partial f}{\partial x}+\frac{\partial f}{\partial y}=\frac{\partial}{\partial x}\left(\frac{\partial f}{\partial x}\right)+\frac{\partial}{\partial y}\left(\frac{\partial f}{\partial y}\right) \tag{2.24}$$

combining the convection and diffusion terms then leads to:

$$\frac{\partial f}{\partial t}=-\frac{\partial}{\partial x}\left(f-\frac{\partial f}{\partial x}\right)-\frac{\partial}{\partial y}\left(f-\frac{\partial f}{\partial y}\right) \tag{2.25}$$

(2.25) can be solved through the following procedure:

1. The first step is to calculate the derivative $\partial f/\partial x$. Construct the matrices $\mathbf{P}_x$ and $\mathbf{Q}_x$ in (2.15) which contain the finite difference coefficients for the x direction.

2. Decompose the matrix $\mathbf{P}_x$ with Cholesky decomposition. $\mathbf{P}_x = \mathbf{L}\mathbf{L}^T$ where $\mathbf{L}$ is a lower triangular matrix.

3. Loop in the y direction solving the linear system of equations (2.15) for each line of the grid in the x-direction, i.e.:

   for $j = 0$ to ny, solve:

   $$\mathbf{P}_x\left(\frac{\partial f}{\partial x}\right)_{(:,j)}=\frac{1}{h}\mathbf{Q}_x\mathbf{f}_{(:,j)} \tag{2.26}$$

   where $\mathbf{f}_{(:,j)} = [f_{(0,j)}, f_{(1,j)}, \cdots, f_{(N,j)}]^T$, and $(\partial f/\partial x)_{(:,j)} = [f'_{(0,j)}, f'_{(1,j)}, \cdots, f'_{(N,j)}]^T$, with primes denoting a derivative. (2.26) is solved in two stages. Firstly solve

   $$\mathbf{L}\mathbf{y}=\frac{1}{h}\mathbf{Q}_x\mathbf{f}_{(:,j)} \tag{2.27}$$

   by forward substitution, then

   $$\mathbf{L}^T\left(\frac{\partial f}{\partial x}\right)_{(:,j)}=\mathbf{y} \tag{2.28}$$

   by back substitution.

4. Repeat steps 1-3 for the y derivative:

   for $i = 0$ to nx, solve:

   $$\mathbf{P}_y\left(\frac{\partial f}{\partial x}\right)_{(i,:)}=\frac{1}{h}\mathbf{Q}_y\mathbf{f}_{(i,:)} \tag{2.29}$$

   where $\mathbf{f}_{(i,:)} = [f_{(i,0)}, f_{(i,1)}, \cdots, f_{(i,N)}]^T$, and $(\partial f/\partial y)_{(i,:)} = [f'_{(i,0)}, f'_{(i,1)}, \cdots, f'_{(i,N)}]^T$.

5. The same process in steps 1-4 is then used to determine the derivatives on the R.H.S of (2.25), substituting the calculated values for $\partial f/\partial x$ and $\partial f/\partial y$.

6. With the R.H.S determined, (2.25) is now ready for time integration, which is achieved with 4 stage Runge-Kutta, described in (2.20) and (2.21)

2.1.6 Boundary conditions

The current methodology makes use of Generalised Characteristic Boundary Conditions (GCBC) for wall boundaries, domain boundaries and block interfaces. The principle behind this kind of boundary condition is to consider characteristic waves travelling normal to the boundary in consideration. They are derived by firstly considering the governing equations (2.6), which may be rewritten as:

$$\frac{\partial \widehat{\boldsymbol{Q}}}{\partial t} + \frac{\partial \widehat{\boldsymbol{E}}}{\partial \xi} + \frac{\partial \widehat{\boldsymbol{F}}}{\partial \eta} + \frac{\partial \widehat{\boldsymbol{G}}}{\partial \zeta} = \boldsymbol{S}_V \tag{2.30}$$

where

$$\widehat{\boldsymbol{Q}} = \boldsymbol{Q}/J \tag{2.31}$$

$$\widehat{\boldsymbol{E}} = (\xi_x \boldsymbol{E_1} + \xi_y \boldsymbol{E_2} + \xi_z \boldsymbol{E_3})/J \tag{2.32}$$

$$\widehat{\boldsymbol{F}} = (\eta_x \boldsymbol{E_1} + \eta_y \boldsymbol{E_2} + \eta_z \boldsymbol{E_3})/J \tag{2.33}$$

$$\widehat{\boldsymbol{G}} = (\zeta_x \boldsymbol{E_1} + \zeta_y \boldsymbol{E_2} + \zeta_z \boldsymbol{E_3})/J \tag{2.34}$$

where $\boldsymbol{S}_V$ represents the viscous flux terms, and $\boldsymbol{E}_j$ is defined as in (2.7). In the following derivation we will consider the case where the ξ direction is normal to the boundary. Moving all the transverse terms to the R.H.S, and expanding the normal terms (via chain rule) yields:

$$\frac{\partial \widehat{\boldsymbol{Q}}}{\partial t} + \frac{1}{J}\left(\xi_x \frac{\partial \boldsymbol{E_1}}{\partial \xi} + \xi_y \frac{\partial \boldsymbol{E_2}}{\partial \xi} + \xi_z \frac{\partial \boldsymbol{E_3}}{\partial \xi}\right) = \boldsymbol{S}_V - \left[\boldsymbol{E_1}\frac{\partial}{\partial \xi}\left(\frac{\xi_x}{J}\right) + \boldsymbol{E_2}\frac{\partial}{\partial \xi}\left(\frac{\xi_y}{J}\right) + \boldsymbol{E_3}\frac{\partial}{\partial \xi}\left(\frac{\xi_z}{J}\right) + \frac{\partial \widehat{\boldsymbol{F}}}{\partial \eta} + \frac{\partial \widehat{\boldsymbol{G}}}{\partial \zeta}\right] \tag{2.35}$$

After multiplying (2.35) by J, the entire R.H.S is combined as a single source term $\boldsymbol{S}_V^*$. (2.35) may then be expressed as:

$$\frac{\partial \boldsymbol{Q}}{\partial t} + \left(\xi_x \frac{\partial \boldsymbol{E_1}}{\partial \boldsymbol{Q}} + \xi_y \frac{\partial \boldsymbol{E_2}}{\partial \boldsymbol{Q}} + \xi_z \frac{\partial \boldsymbol{E_3}}{\partial \boldsymbol{Q}}\right)\frac{\partial \boldsymbol{Q}}{\partial \xi} = \boldsymbol{S}_V^* \tag{2.36}$$

Pre-multiplying by the transformation matrix P^{-1} between conservative and characteristic variables results in:

$$P^{-1}\frac{\partial \boldsymbol{Q}}{\partial t} + P^{-1}KPP^{-1}\frac{\partial \boldsymbol{Q}}{\partial \xi} = P^{-1}\boldsymbol{S}_V^* \tag{2.37}$$

where K is the term in brackets in (2.36), also known as the Flux Jacobian matrix. Full details of the transformation matrix P can be found in (Kim & Lee, 2000). This may then be expressed in

terms of the characteristic variables R by utilising the expression $\delta \boldsymbol{R} = P^{-1}\delta \boldsymbol{Q}$, resulting in:

$$\frac{\partial \boldsymbol{R}}{\partial t} + \boldsymbol{\Lambda}\frac{\partial \boldsymbol{R}}{\partial \xi} = \boldsymbol{S}_c \tag{2.38}$$

with $\boldsymbol{\Lambda} = P^{-1}KP$, and $\boldsymbol{S}_c = P^{-1}\boldsymbol{S}_V^*$. The GCBCs are applied by considering the convection term on the LHS of (2.38) defined as (Kim & Lee, 2000):

$$L_i = \lambda_i \frac{\partial R_i}{\partial \xi}, \quad \text{for} \quad i = \{1, \cdots, 5\} \tag{2.39}$$

There are five modes of L_i, the first representing entropy waves, the second and third vorticity waves, and the final two acoustic waves. The principle behind the characteristic boundary conditions is that waves coming into the domain through the boundary may be determined by the outgoing waves for which an interior solution exists, according to the chosen condition. The direction of the L_i terms is given by the eigenvalues of the system, that is the diagonal elements of the matrix $\boldsymbol{\Lambda}$.

$$\Lambda_{ii} = [U, U, U, U + a_\infty(\xi_x^2 + \xi_y^2 + \xi_z^2)^{\frac{1}{2}}, U - a_\infty(\xi_x^2 + \xi_y^2 + \xi_z^2)^{\frac{1}{2}}]^T, \quad \text{for} \quad i = \{1, \cdots, 5\} \tag{2.40}$$

where $U = \xi_x u + \xi_y v + \xi_z w$ is the contravariant velocity normal to the boundary. For a subsonic flow, this reveals that the first four characteristic waves travel in the mean flow direction, while the fifth travels in the opposite direction. For example in the case of a downstream outflow boundary, the terms L_{1-4} represent outgoing waves, and L_5 an incoming wave. In order to implement the GCBCs the following steps are taken:

1. Calculate the normal flux derivative $\partial \widehat{\boldsymbol{E}}/\partial \xi$ using the finite difference schemes and filters.
2. Calculate the five modes in (2.39) as

$$\boldsymbol{L} = \boldsymbol{\Lambda}\frac{\partial \boldsymbol{R}}{\partial \xi} = JP^{-1}\left(\frac{\partial \widehat{\boldsymbol{E}}}{\partial \xi} - \left[\boldsymbol{E_1}\frac{\partial}{\partial \xi}\left(\frac{\xi_x}{J}\right) + \boldsymbol{E_2}\frac{\partial}{\partial \xi}\left(\frac{\xi_y}{J}\right) + \boldsymbol{E_3}\frac{\partial}{\partial \xi}\left(\frac{\xi_z}{J}\right)\right]\right) \tag{2.41}$$

3. Next, update $\boldsymbol{L}$ based on the choice of boundary condition (e.g. outlet, no-slip wall etc.).
4. Finally, the normal flux derivative is recalculated based on $\boldsymbol{L}^*$, the corrected version of $\boldsymbol{L}$

$$\left(\frac{\partial \widehat{\boldsymbol{E}}}{\partial \xi}\right)^* = \frac{1}{J}P\boldsymbol{L}^* + \left[\boldsymbol{E_1}\frac{\partial}{\partial \xi}\left(\frac{\xi_x}{J}\right) + \boldsymbol{E_2}\frac{\partial}{\partial \xi}\left(\frac{\xi_y}{J}\right) + \boldsymbol{E_3}\frac{\partial}{\partial \xi}\left(\frac{\xi_z}{J}\right)\right] \tag{2.42}$$

5. The corrected flux derivative is then input into (2.30) for time integration. This procedure is carried out every Runge-Kutta step.

The present work utilises non-reflecting conditions at the far field boundaries (Kim & Lee, 2000), and as indicated earlier periodic boundary conditions are used in the spanwise direction. For the

aerofoil surface a no-slip/slip wall boundary condition is applied (Kim & Lee, 2004) (for Euler/-Navier Stokes equations respectively). Both finite (§5 and §6) and semi-infinite (§3 and §4) chord aerofoils are considered. For the later the wall boundary condition is extended downstream in the aerofoil xz-plane with the intention of removing any secondary interactions which takes place at the aerofoil TE. This allows the analysis to solely focus on the LE noise which is the primary source in ATI. A description of each GCBC used is provided as follows (Kim & Lee, 2004):

2.1.6.1 Inflow condition

Based on (2.40) at the inlet only the L_5 wave component is an outgoing wave which can be determined by the interior solution. The waves L_{1-4} must therefore be defined as follows:

$$L_1^* = 0 \tag{2.43}$$

$$L_2^* = \frac{K_{in}}{2}\left[\tilde{\xi}_x(w - w_\infty) - \tilde{\xi}_z(u - u_\infty)\right] \tag{2.44}$$

$$L_3^* = \frac{K_{in}}{2}\left[-\tilde{\xi}_x(v - v_\infty) + \tilde{\xi}_y(u - u_\infty)\right] \tag{2.45}$$

$$L_4^* = K_{in}\left[-\tilde{\xi}_x(u - u_\infty) + \tilde{\xi}_y(v - v_\infty) + \tilde{\xi}_z(w - w_\infty) + \frac{p - p_\infty}{\rho a_\infty}\right] \tag{2.46}$$

and

$$K_{in} = \sigma_{in}(1 - M_{max}^2)\frac{a_\infty}{l} \tag{2.47}$$

where $\sigma = 0.25$ is a parameter which controls the amount of reflectivity, l is the domain length, and $(\tilde{\xi}_x, \tilde{\xi}_y, \tilde{\xi}_z)$ is the unit normal vector. In addition for viscous flows tangential stresses and normal heat flux are set to zero.

$$\frac{\partial \tau_{12}}{\partial n} = \frac{\partial \tau_{23}}{\partial n} = \frac{\partial \tau_{31}}{\partial n} = \frac{\partial q_n}{\partial n} = 0 \tag{2.48}$$

2.1.6.2 Non-reflecting outflow

For an outflow condition the modes L_{1-4} are all outgoing waves, the only incoming wave which needs to be determined is L_5, where:

$$L_5^* = \frac{K_{out}(p - p_\infty)}{\rho a_\infty} \tag{2.49}$$

and

$$K_{out} = \sigma_{out}(1 - M_{max}^2)\frac{a_\infty}{l} \tag{2.50}$$

$\sigma_{out} = 0$ represents a perfect non-reflecting boundary condition, where the reflected waves have zero amplitude. However, as pointed out by Poinsot & Lele (1992) this condition causes inaccuracies for long time calculations. For this reason $\sigma_{out} = 0.25$ is selected. Condition (2.48) also applies if the flow is viscous.

2.1.6.3 Wall boundary conditions

There are two kinds of wall boundaries used in the current work, slip and no-slip (viscous) walls. For slip walls the normal velocity is zero, and the transverse velocities unspecified. For the case of a wall at the right boundary in the ξ direction the L_5 wave is incoming and the L_4 wave outgoing. If the wall is on the left boundary the reverse is true. Following this:

$$L_5^* = L_4 - S_{c4} + S_{c5} \quad \text{for r.h.s walls} \tag{2.51}$$

$$L_4^* = L_5 - S_{c5} + S_{c4} \quad \text{for l.h.s walls} \tag{2.52}$$

If the wall is viscous, each component of velocity is zero on the wall. In this case it is also required that:

$$L_2^* = L_3^* = 0 \tag{2.53}$$

$$S_{c2}^* = S_{c3}^* = 0 \tag{2.54}$$

The viscous source term in (2.30) is updated in a similar manner to the Euler terms via (2.54) and

$$\boldsymbol{S}_V^* = \frac{1}{J} P \boldsymbol{S}_c^* + \left[\boldsymbol{E_1} \frac{\partial}{\partial \xi} \left(\frac{\xi_x}{J} \right) + \boldsymbol{E_2} \frac{\partial}{\partial \xi} \left(\frac{\xi_y}{J} \right) + \boldsymbol{E_3} \frac{\partial}{\partial \xi} \left(\frac{\xi_z}{J} \right) + \frac{\partial \widehat{\boldsymbol{F}}}{\partial \eta} + \frac{\partial \widehat{\boldsymbol{G}}}{\partial \zeta} \right]. \tag{2.55}$$

2.1.6.4 Characteristic interface at block boundaries

In addition to physical boundaries a condition is also needed for computational boundaries due to the grid. As previously mentioned the current step up uses an H-grid topology. This consists of 6 blocks with the aerofoil as the central branch, 3 blocks above and 3 below the aerofoil. Since each block is meshed separately discontinuities may occur in the grid metrics at the block interfaces. In order to avoid the numerical errors arising from these discontinuities the one-sided boundary closure schemes are implemented. The consequence of this is that the solution for each block is independent from its neighbours, a condition is therefore required between the blocks to ensure the solution is identical at the interface.

Consider two blocks left and right. It is required that the privative variables and their time derivatives are identical. Similarly, the time derivatives of the characteristics variables should also be the same, i.e.: $\partial \boldsymbol{R}^L / \partial t = \partial \boldsymbol{R}^R / \partial t$. According to (2.38) and (2.39) it then follows that (Kim & Lee, 2003):

$$L_m^L - S_{cm}^L = L_m^R - S_{cm}^R \tag{2.56}$$

where $m = 1, \cdots, 5$ represents the five characteristic waves. At an interface the outgoing waves of one block represent the incoming waves of the adjacent block. The procedure is to update incoming

convection terms based on outgoing terms of the adjacent block. The block to update is therefore determined by the sign of the convection speed λ_m. The condition at the interface is expressed as:

$$L_m^L = L_m^R - S_{cm}^R + S_{cm}^L \quad \text{for} \quad \frac{\lambda_m^L}{|\lambda_m^L|} = \frac{\lambda_m^R}{|\lambda_m^R|} \leq 0 \tag{2.57}$$

$$L_m^R = L_m^L - S_{cm}^L + S_{cm}^R \quad \text{for} \quad \frac{\lambda_m^L}{|\lambda_m^L|} = \frac{\lambda_m^R}{|\lambda_m^R|} \geq 0 \tag{2.58}$$

2.1.7 Parallel routines

The compact finite difference system is parallelised through domain decompositions and MPI-routines. The most challenging aspect of this procedure is the parallisation of the spatial schemes which are implicit in space. This is accomplished through a recent quasi-disjoint pentadiagonal matrix system technique (Kim, 2013). The computational grid is split into small separate subdomains each of which is allocated one processor core. The pentadiagonal matrix systems for both differencing and filtering (outlined in (2.15) and (2.16)) are then modified through linear-algebraic transformations such that matrix inversions may be performed for each subdomain independently. The algebraic transformation produces a set of subdomain finite-differences and filters which require a three point halo exchange with neighbouring subdomains, achieved with MPI routines. These new schemes replace the original boundary closures when a subdomain boundary is present. The performance of the subdomain schemes is a trade off between accuracy and efficiency. Increasing their stencil size will increases their cohesion with the interior finite-difference scheme and filter, but at the cost of additional computations. Utilising stencil sizes of 11 for the subdomain boundary scheme, and 8 for the subdomain filters, ensures the wavenumber and amplification rate errors when compared to the interior remain less than 3%. These settings result in minimal artifact noise, as well as a superlinear speed-up.

Two cluster machines are used in the current research, Iridis4 the local super computer facility at the University of Southampton, and the national computing facility ARCHER. The distribution of processor cores and approximate run times is contained within table 2.1. The data is shown for the Iridis4 machine which has a processor limit of $NP = 512$. The settings are selected so that approximately an even number of points is distributed to each subdomain to avoid any load imbalance. The viscous cases are considerably more expensive due to the requirement of firstly obtaining a converged base-flow solution, in addition to the smaller grid spacings required.

Case	NP	NP_ξ	NP_η	NP_ζ	run time (hrs)
Low frequency vortex (WLE) §3	480	20	12	2	3
High frequency vortex (WLE) §4-6	512	32	16	1	7
High frequency vortex (SLE, $Re_\infty = 4.0 \times 10^5$, 3D) §5-6	512	32	16	1	35

Table 2.1: Number of processor cores and approximate run time for the simulations in the following sections. NP_ξ, NP_η and NP_ζ are the streamwise, vertical and spanwise number of processor cores respectively.

2.1.8 Definition of variables for post-processing

Data processing and analysis are carried out upon the completion of each simulation. The main property required in this study is the power spectral density (PSD) function of pressure fluctuations on the aerofoil surface and at the far-field observer locations. The far-field (acoustic) pressure and the surface (wall) pressure loading are defined as:

$$p_a(\boldsymbol{x},t) = p(\boldsymbol{x},t) - p_\infty, \quad \Delta p_w(\boldsymbol{x},t) = \lim_{y\to 0^+} p(\boldsymbol{x},t) - \lim_{y\to 0^-} p(\boldsymbol{x},t), \tag{2.59}$$

where superscripts '$y \to 0^+$' and '$y \to 0^-$' indicate the upper and lower surfaces of the flat-plate aerofoil, respectively. The PSD functions of the pressure fluctuations are then calculated by:

$$S_{ppa}(\boldsymbol{x},f) = \frac{2}{T}\widehat{p_a}(\boldsymbol{x},f)\widehat{p_a}^*(\boldsymbol{x},f), \quad S_{ppw}(\boldsymbol{x},f) = \frac{2}{T}\widehat{\Delta p_w}(\boldsymbol{x},f)\widehat{\Delta p_w}^*(\boldsymbol{x},f), \tag{2.60}$$

where '$\wedge$' represents a Fourier transformed variable and '$*$' denotes a complex conjugate. The multiplier '2' is introduced to consider the right-hand side of the spectra (positive frequencies) only. The noise reduction due to a WLE relative to the SLE case is then quantified by

$$\Delta\mathrm{SPL}(\boldsymbol{x},f) = 10\log_{10}\left[\frac{S_{ppa}(\boldsymbol{x},f)|_{\mathrm{SLE}}}{S_{ppa}(\boldsymbol{x},f)|_{\mathrm{WLE}}}\right]. \tag{2.61}$$

All of the results presented in this work are based on dimensionless variables. Length scales are normalised by the finite aerofoil chord length L_c, velocities are normalised by the speed of sound a_∞, density by the free-stream density ρ_∞, and acoustic pressure by the free-stream pressure p_∞.

2.1.9 Signal processing routines

The Fourier series can be used to obtain a frequency domain representation of a periodic time signal by decomposing it into a sum of simple sine and cosines waves. If the signal is non-periodic the Fourier transform may be used which represents the non-periodic signal as a periodic one with period $T \to \infty$:

$$\widehat{x}(f) = \int_{-\infty}^{\infty} x(t)\exp(-2\pi i f t)dt \tag{2.62}$$

In practice data measurements have finite length making the unbounded integration impossible. Alternatively the data is usually truncated by multiplication of a window function $w(t)$:

$$\widehat{x}(f) = \int_{-T/2}^{T/2} x(t)w(t)\exp(-2\pi i f t)dt \tag{2.63}$$

where T is the sample period. In practice signals recorded from experiments or simulations are sampled. A discrete approximation of the Fourier transform is therefore used where the integration

is replaced by a Riemann sum:

$$\widehat{x}[k] = \sum_{n=0}^{N-1} x[n]w[n]\exp(-2\pi ink/N)\Delta t \tag{2.64}$$

where the signal x is evaluated for $n = 0, 1, \cdots, N-1$ samples with constant spacing Δt. The spectra is calculated at $k = 0, 1, \cdots, N-1$ frequencies with spacing $k/(N\Delta t)$=k/T. Unlike the continuous form in (2.63), the minimum frequency which can be evaluated in (2.64) is linked to the sample period T. The discrete Fourier transform therefore interprets any non-periodic input signal as one with period equal to the sampling period T. The kinds of signals typically encountered in the current work are single pulses generated as an impinging vortex is chopped by the aerofoil LE. Although the LE-vortex interaction is an isolated event, the Fourier transform treats it as if it occurs periodicity (multiple LE-vortex collisions separated by the period).

It is desirable that the chosen sampling window is large enough to approximate the infinite integral in (2.62), so that the true Fourier transform is approximated. Figure 2.6 shows the time signals and the corresponding magnitude of the Fourier transform obtained for semi-infinite chord (*a*-*b*) and finite chord WLE aerofoils (*c*-*d*) based on the simulation settings of §4. The results are calculated using the MATLAB fft (Fast Fourier Transform) function. It shows that as the window is increased, the Fourier transform quickly converges. The window length also has an impact on the magnitude of the PSD as suggested by (2.60). For this reason the same window length must be used when comparing the spectra obtained by two simulations. The inviscid simulations carried out throughout this work use a window period $T^* = 10$ which ranges from 5 to 15 for the 90° observer angle. For longer simulations (viscous cases in §5 and 6) the PSD is scaled so that direct comparisons can be made to the inviscid cases.

In this work spectra are calculated using a MATLAB script provided in Appendix F. The code is based on the MATLAB CPSD function which returns cross power spectral density when the input signals are different, or power spectral density when they are equal. In the latter case the function is also equivalent to the MATLAB function PWELCH. Welch averaging is typically used to minimise variance in a PSD estimate. However, since the signals analysed in the current work are typically short single pulses averaging quickly leads to excessive smoothing of the key features in the spectra. For this reason spectra are calculated as a single periodogram estimate of the PSD as shown in the MATLAB script and described by (2.60). A Tukey (tapered cosine) window is utilised which ensures periodicity of the signal. This particular window is selected as it does not significantly attenuate the spectra amplitude while providing less spectral leakage at high frequency relative to a rectangular window. This is demonstrated in figure 2.7, which shows the spectra produced using three window shapes. Comparisons are made for a semi-infinite chord (*a*), and finite chord (*b*) WLE simulation (§4). The signals are also zero-padded by the CPSD function. Zero-padding increases the length of the Fourier transform, effectively providing a sinc interpolation between the k/T frequency samples. For the current results the number of samples is increased by a factor of two.

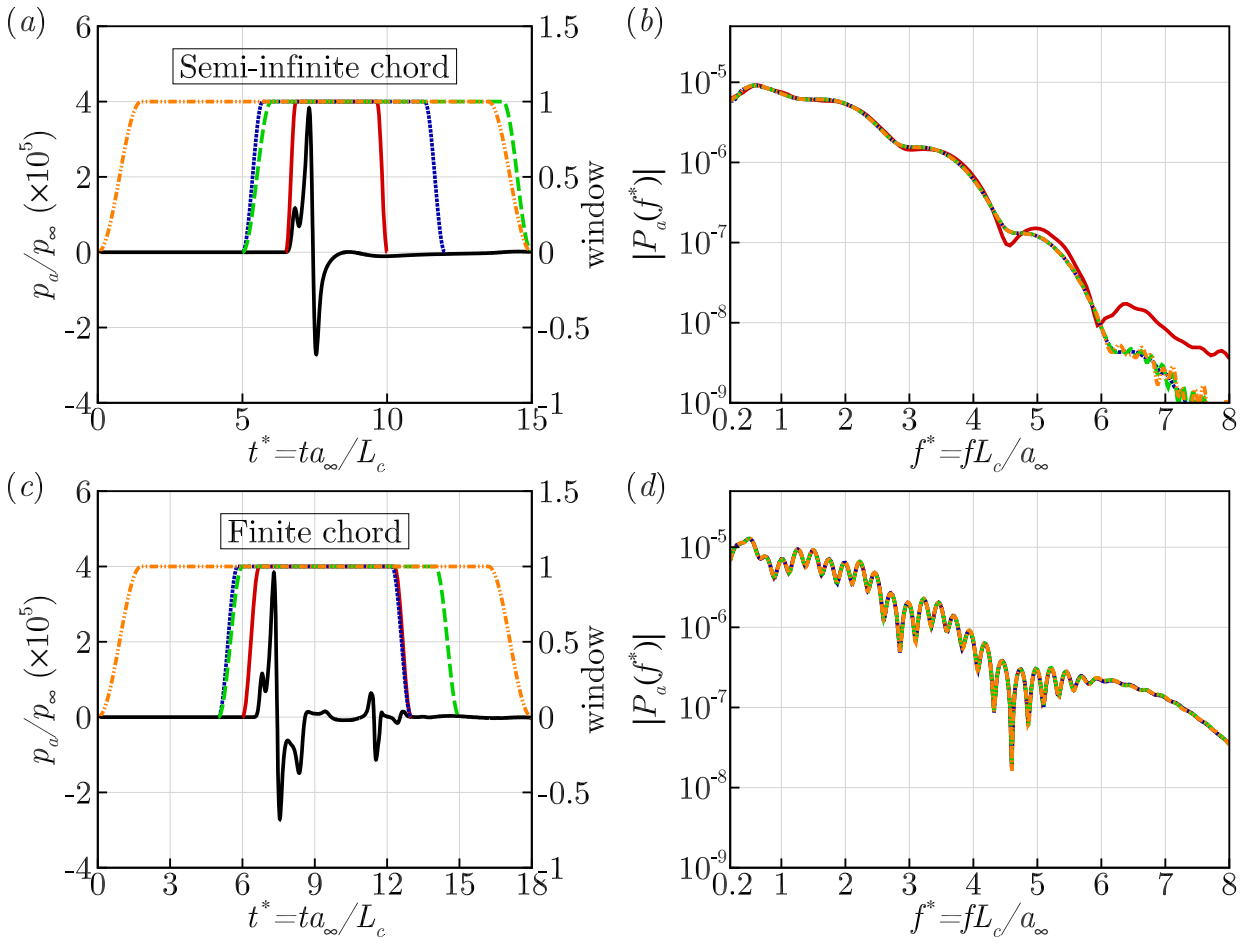

Figure 2.6: Effect of varying window length on the calculation of the Fourier transform. (a) Semi-infinite chord length WLE simulation. (a) Finite-infinite chord.

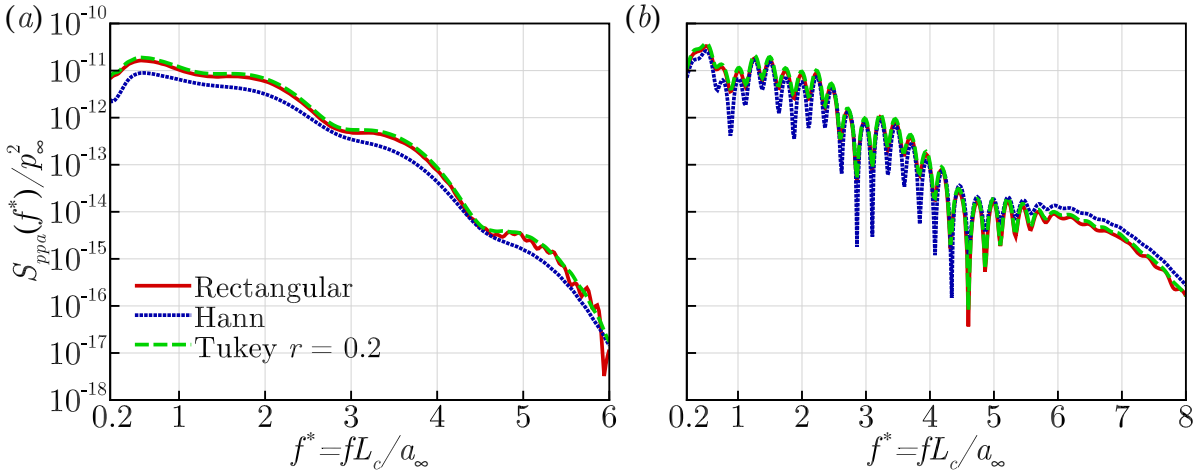

Figure 2.7: Effect of varying window shape on the calculation of the PSD (2.60). (a) Semi-infinite chord WLE simulation. (a) Finite-infinite chord.

Chapter 3

Primary Leading Edge Source Mechanisms

3.1 Problem description and computational set-up

3.1.1 Prescribed spanwise vortex model

The spanwise (two-dimensional) vortex model prescribed as an initial condition in this study is based on the Gaussian synthetic eddy profile used in previous publications (Kim & Haeri, 2015; Kim *et al.*, 2016). It provides a divergence-free velocity field via taking the curl of the following vector potential, i.e. $\boldsymbol{u}'(\boldsymbol{x}, t = 0) = \nabla \times [\Psi(\boldsymbol{x})\boldsymbol{e}_z]$:

$$\Psi(\boldsymbol{x}) = a_\infty L_c \frac{\epsilon}{\sqrt{\sigma}} \exp\{-[3\sigma r(\boldsymbol{x})]^2\}, \quad r(\boldsymbol{x}) = \frac{(x - x_0)^2 + y^2}{L_c^2}, \tag{3.1}$$

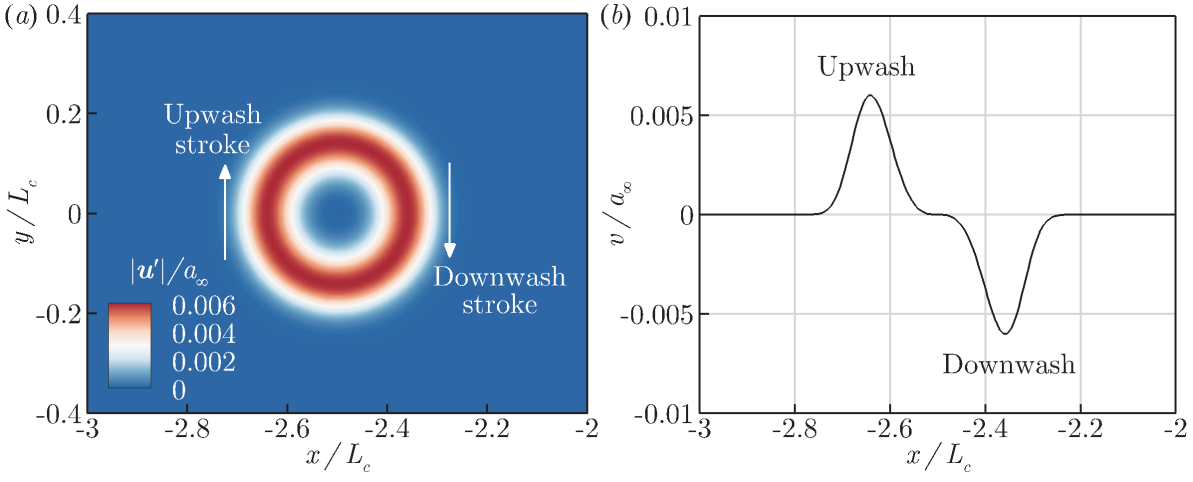

Figure 3.1: The initial velocity field induced by the spanwise vortex model given by (3.2): (a) induced velocity magnitude contours and (b) the vertical velocity profile along the centreline ($y = 0$).

where L_c is the mean chord length, ϵ and σ are control parameters for the vortex strength and size, $x_0 = -2.5L_c$ is the initial streamwise coordinate of the vortex core and $\boldsymbol{e}_z$ is the spanwise Cartesian unit vector. This results in the following formulae for the velocity field at $t = 0$:

$$u(\boldsymbol{x}) = u_\infty + 36\frac{\sigma^2}{L_c^2} yr(\boldsymbol{x})\Psi(\boldsymbol{x}), \quad v(\boldsymbol{x}) = -36\frac{\sigma^2}{L_c^2}(x - x_0)r(\boldsymbol{x})\Psi(\boldsymbol{x}), \tag{3.2}$$

while the pressure and the density are set to ambient/quiescent conditions (p_∞ and ρ_∞). The control parameters are set to $\epsilon = 0.00228$ and $\sigma = 14.4$. This produces a maximum velocity perturbation equivalent to the RMS perturbation obtained in the studies of Narayanan *et al.* (2015) and Chaitanya *et al.* (2015) ($u'/a_\infty = 0.006$). Furthermore, with the chosen parameters, the length scale of the vortex upwash/downwash stroke is similar to the radius of the largest eddies ($0.1L_c$) in the synthetic turbulence approach used by Kim *et al.* (2016), i.e.:

$$L_v = 0.1L_c = \frac{1}{\max|v(\boldsymbol{x})|}\int_{x_0}^{x_0+\infty} |v(\boldsymbol{x})|_{y=z=0}\mathrm{d}x. \tag{3.3}$$

The resulting velocity field is plotted in 3.1. The prescribed vortex induces clockwise rotating velocity components, firstly inducing a downwash stroke on to the aerofoil leading edge followed by an upwash stroke as the vortex travels downstream. Figure 3.2 shows the noise generation due to the interaction of the prescribed vortex and the LE. The initial downwash stroke creates a compression pressure wave on the aerofoil upper surface, quickly followed by an expansion wave produced by the subsequent downwash stroke. All of the simulations are conducted using a free-stream Mach number of $M_\infty = u_\infty/a_\infty = 0.24$, which is equivalent to that used in various previous studies (Kim *et al.*, 2016; Narayanan *et al.*, 2015). Comparison of the chosen vortex profile to classical models is provided in §A, while further discussion of the chosen vortex parameters, and their effect on the WLE noise reduction is provided in §C.1.

3.1.2 Computational grid

The simulations are carried out on a total of 43,760,640 grid cells (1036×660×64) in a H-block topology. The smallest cells are located at the aerofoil LE where the size is $\Delta x = \Delta y = 0.00625L_c$ and $\Delta z = 0.002083L_c$. The grid is stretched in the streamwise and vertical directions and kept uniform in the span. Nevertheless, it still maintains a high resolution at the far field in order to capture radiated high frequency components. The maximum Δx spacing is 0.01 which provides a minimum of 46 cells across the vortex diameter.

Figure 3.3 shows the results of a grid convergence test conducted with a WLE geometry: $h_{LE}/L_c = 1/15$ and $\lambda_{LE}/L_c = 2/15$ ($AR = 1$). Three different levels of grid resolution (coarse, medium and fine) were used. The medium level was used for all simulation data presented in this chapter. Subsequent levels are refined by 20% in all directions. The number of grid points and the min/max mesh sizes used for each resolution level are listed in table 3.1. Figures 3.3*a* and 3.3*b* demonstrates that there is effectively no difference in the resulting time signals and spectra between the three grids. Figure 3.3*d* also shows a comparison to the free-field solution obtained without the aerofoil in

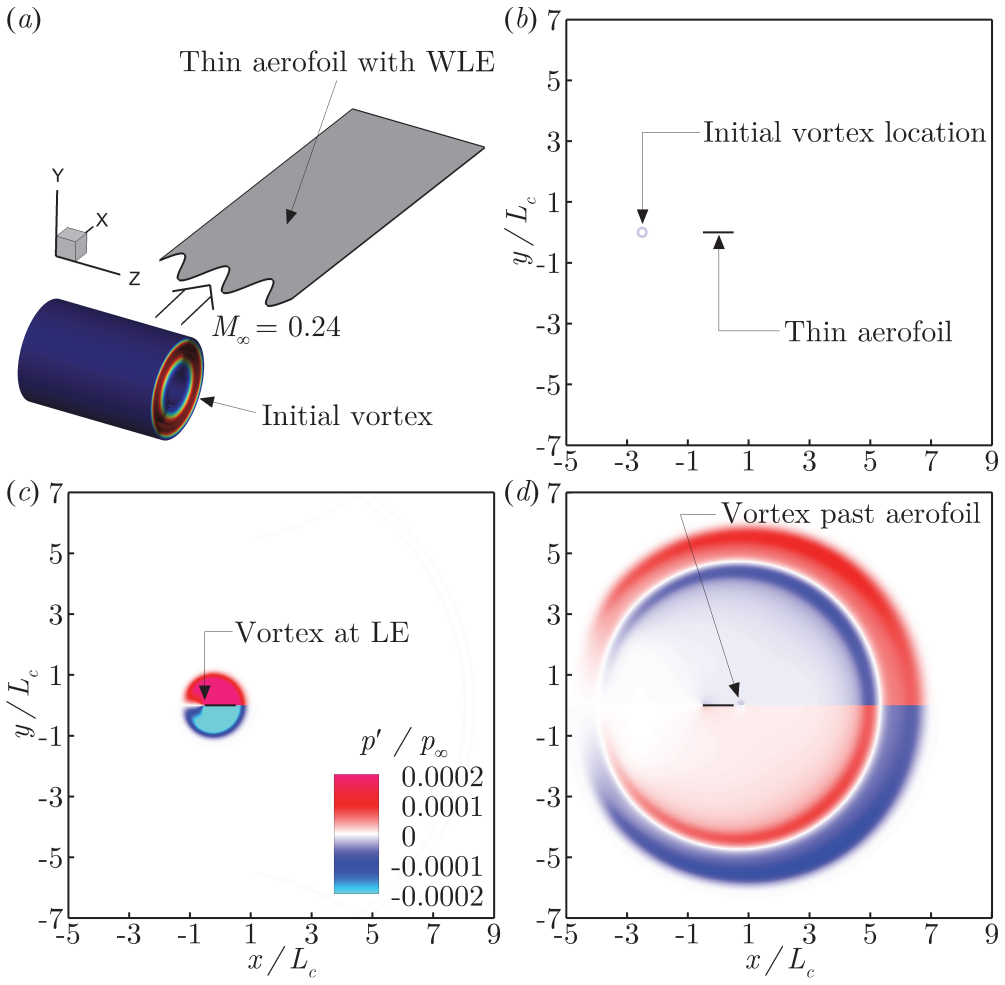

Figure 3.2: Description of the current problem: a prescribed spanwise vortex impinging on a thin aerofoil with a wavy leading edge: (*a*) schematic diagram, (*b*) initial condition, (*c*) during the interaction and (*d*) after the interaction.

place (using the medium grid). The level of background noise (numerical error residual) remained at least 40dB lower than the physical SPL throughout the entire frequency range, which demonstrates the quality of the current numerical solutions.

Resolution level	n_ξ	n_η	n_ζ	$\Delta x_{\max}/L_c$	$\Delta x_{\min}/L_c$
Coarse	836	528	52	0.012	0.0075
Medium	1036	660	64	0.01	0.00625
Fine	1254	792	78	0.008	0.005

Table 3.1: Supplementary information for the grid convergence test shown in figure 3.3, where n_ξ, n_η and n_ζ denote the number of grid cells in the ξ-, η- and ζ-directions, respectively – see (2.6) and (2.7).

Each simulations is run until a non-dimensional time of $ta_\infty/L_c = 20$, which is sufficient to capture both the fluctuating wall pressure signals and the far field sound.

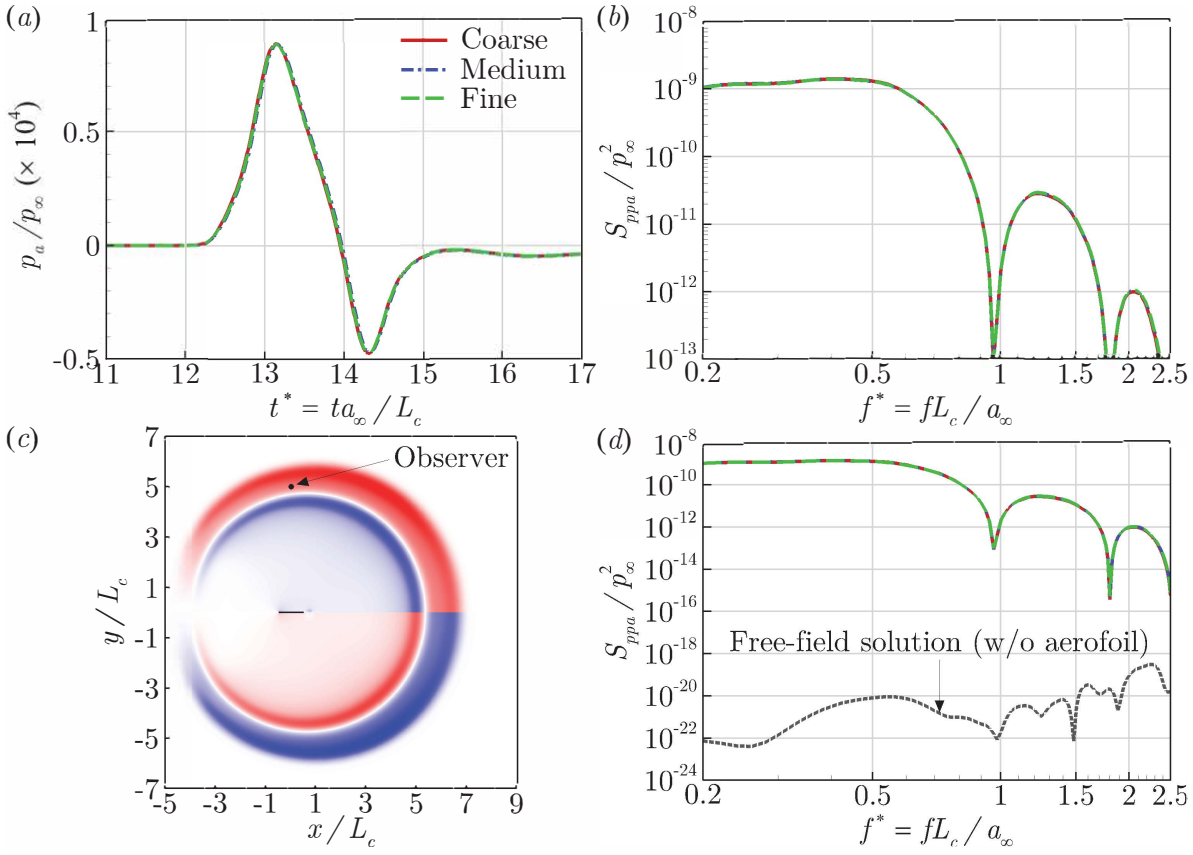

Figure 3.3: A grid convergence test of the current numerical simulation by using three different levels of grid resolution, based on the far-field acoustic pressure signal (p_a/p_∞) and its PSD (S_{ppa}/p_∞^2) obtained at the observer point $\boldsymbol{x}_0 = (0, 5L_c, 0)$ for $h_{LE}/L_c = 1/15$ and $\lambda_{LE}/L_c = 2/15$ (corresponding to figure 3.5).

3.2 Initial findings and the questions emerged

3.2.1 Wall and acoustic pressure fluctuations

As a result of the current simulations, figure 3.4 shows the time signals and corresponding PSD (power spectral density) of the wall pressure fluctuations (Δp_w) on the leading edge points for three different WLE geometries ($h_{LE}/L_c = 1/30$, $1/15$ and $1/10$) compared with the SLE baseline case. First, it is apparent in the figure that the level of wall pressure fluctuations (acoustic source strength) at the hill location constantly decreases with increasing h_{LE} (WLE amplitude) across the entire frequency range. This is directly related to the "source cutoff" effect due to the geometric obliqueness as suggested by Kim *et al.* (2016), i.e. $\Delta p_w \propto \cos\theta$ where θ is the local sweep angle of the leading edge. Figure 3.4 also shows that the source strength at the root does not seem to change much with h_{LE} (maintained at the level of the SLE case apart from the high frequency range), which might be rather simply anticipated because the sweep angle is locally zero at the root. However, at the peak where the sweep angle is also zero, the source strength does change with h_{LE} although it does not drop as consistently as the hill case and seems to converge towards

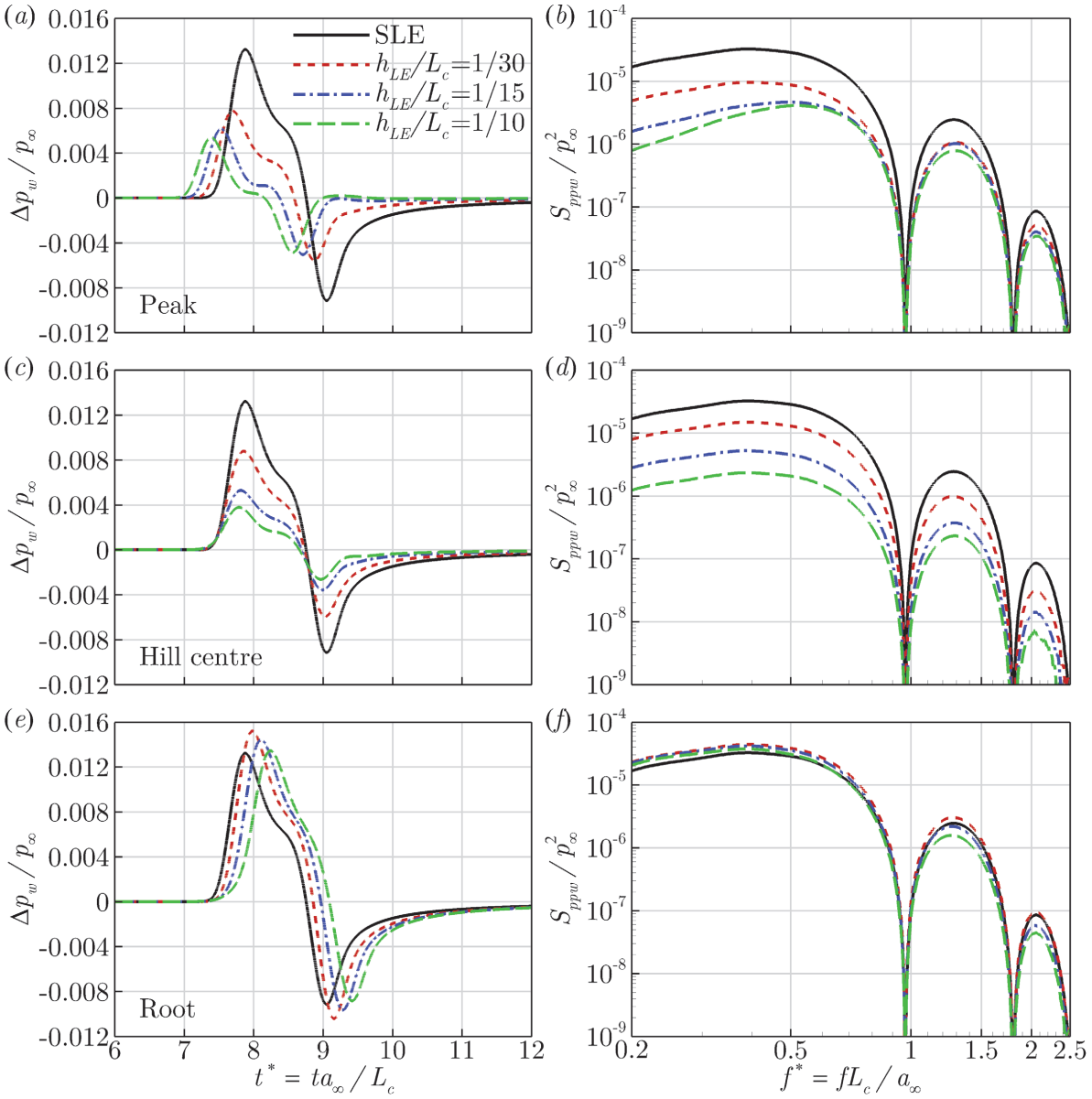

Figure 3.4: Fluctuating wall pressure time signals, $\Delta p_w(t^*)/p_\infty$, and the corresponding power spectral density (PSD), $S_{ppw}(f^*)/p_\infty^2$, obtained at three different locations on the WLE (peak, hill centre and the root) for three different values of the WLE amplitude (h_{LE}/L_c = 1/30, 1/15 and 1/10) with its wavelength fixed (λ_{LE}/L_c = 2/15), compared with the SLE baseline case.

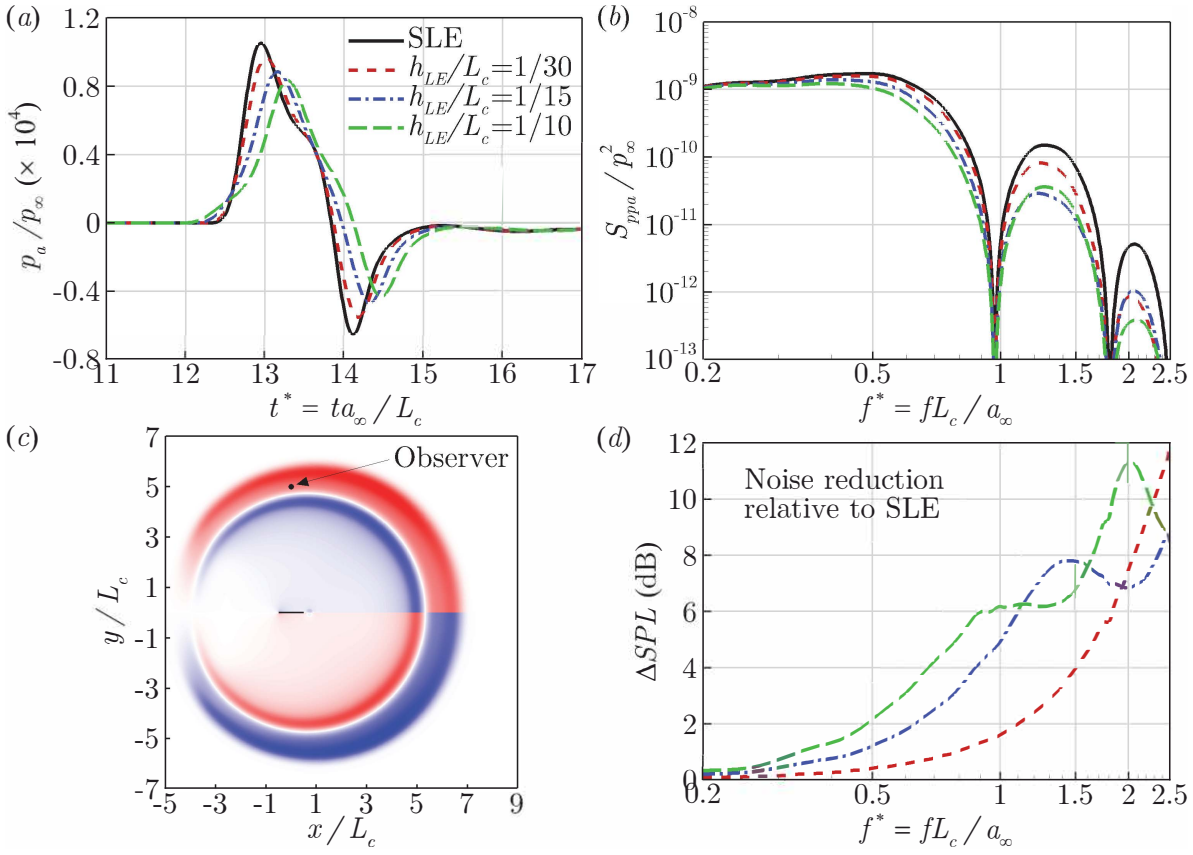

Figure 3.5: Far-field acoustic pressure time signals, $p'_a(t^*)/p_\infty$, the corresponding PSD, $S_{ppa}(f^*)/p^2_\infty$, and the relative noise reduction spectra, $\Delta SPL(f^*)$, obtained at an observer location, $\boldsymbol{x}_o = (0, 5L_c, 0)$, from three different WLE geometries ($h_{LE}/L_c = 1/30$, $1/15$ and $1/10$ with $\lambda_{LE}/L_c = 2/15$), compared with the SLE baseline case.

a constant level. The distinction in source strength between the peak and root was also reported by Kim *et al.* (2016) with little understood about its cause. Consequently, the main aim of this chapter is to provide an explanation for the different source behaviours at the peak and root.

Figure 3.5 shows the far-field radiated acoustic pressure signals, their PSDs and the relative noise reduction spectra for the three different WLE amplitudes as tested in figure 3.4. The reduction of the sound pressure level in the WLE cases is clear in this figure. It is apparent that the noise reduction increases with the WLE amplitude (h_{LE}) and with the frequency as well. The same observations have also been made in previous studies with different upstream flow conditions as mentioned in §1. The current vortex flow condition adds another example in which the WLE successfully achieves noise reductions. However, it is still unknown as to how the radiated sound field achieves such a large reduction in the high frequency range (figure 3.5*b*) when the source at the peak and root does not generate as much reduction in the same frequency range (figure 3.4*b* and 3.4*f*). In addition, the weakened source strength in the low frequency range at the peak and hill (figure 3.4*b* and 3.4*d*) does not seem to reflect in the radiated sound field at all (figure 3.5*b*). It is speculated that these controversial results are due to crucial overlooked propagation mechanisms which will be explored in the following chapter.

3.2.2 Horseshoe vortex systems induced by WLE

As mentioned above, the distinction between the peak and root source behaviours seems contradictory to some extent, as one would assume that both interact with the impinging vortex in a parallel fashion (zero geometric obliqueness). It is found that the distinction is mainly attributed to the dynamics of secondary vortices induced along the WLE. The impinging vortex (rotating clockwise viewed from the xy-plane) induces a downwash ($v < 0$) downstream of its core and consequently an upwash ($v > 0$) upstream of it as indicated in figure 3.1. As the vortex nears the aerofoil the preceding downwash is rapidly forced to zero on the wall due to the no-penetration condition. The upshot of this is that a high velocity gradient ($\partial v/\partial x \gg 0$ while $\partial u/\partial y \approx 0$) is created at the leading edge, which results in counter-clockwise (positive) vorticity there ($\omega_z = \partial v/\partial x - \partial u/\partial y \gg 0$). This is a typical example of vortex-body interaction (Rockwell, 1998). In the SLE case the induced spanwise vorticity is uniform along the span. However, for a WLE the vorticity varies along the span in both the magnitude and the orientation (now consisting of both spanwise and streamwise components).

Figure 3.6 shows snapshots of the WLE-vortex interaction taken as time elapses from the first contact until the vortex completely detaches from the WLE. The vortex travelling through the aerofoil is shown by the spanwise vorticity contour surfaces ($\omega_z L_c/a_\infty$) and the induced secondary vortices on the wall are visualised by using the Q-criterion contour surfaces. In addition, the plots of p'_a/p_∞ in the xy-plane show the dipole sound pulses with an alternating sign being generated when the downwash and upwash strokes of the travelling vortex impact the leading edge.

One of the most critical features shown in figure 3.6 is the creation of horseshoe-like vortex systems emanating from the WLE as shown from the Q-criterion plots. The horseshoe vortex system consists of a bound vortex sitting at the WLE around the peak and two counter-rotating streamwise vortices trailing from the bound vortex as depicted in figure 3.6*b*. The horseshoe vortex systems are created twice, firstly during the downwash, and then the upwash stroke, with the direction of rotation reversed between them. The spanwise distance between a pair of the streamwise vortices becomes larger as the initial vortex moves further downstream. However, this results in a decreasing gap between two neighbouring streamwise vortices from two adjacent horseshoe vortex systems. These are significantly different vortex dynamics, which do not appear in the SLE case.

In figure 3.7 the Q-criterion contour surfaces shown in figures 3.6*b* and 3.6*e* are recoloured by the streamwise vorticity ($\omega_x L_c/a_\infty$) indicating the direction of rotation about the x-axis. A schematic diagram of this event is provided in figure 3.8 depicting the WLE-induced horseshoe vortex systems at a single instant of time during the downwash stroke of the impinging vortex. In particular the induced streamwise vorticity distribution is sketched in figure 3.8*b*. It is explained in the figure that, during the downwash stroke of the impinging vortex, the WLE-induced streamwise vortices create an additional downwash at the root but a counteracting upwash at the peak (figure 3.8*b*). For the upwash stroke the opposite trend takes place. On a minor note, the streamwise vorticity distribution observed from the simulation data is almost symmetrical across both sides of the aerofoil with a small difference in magnitudes.

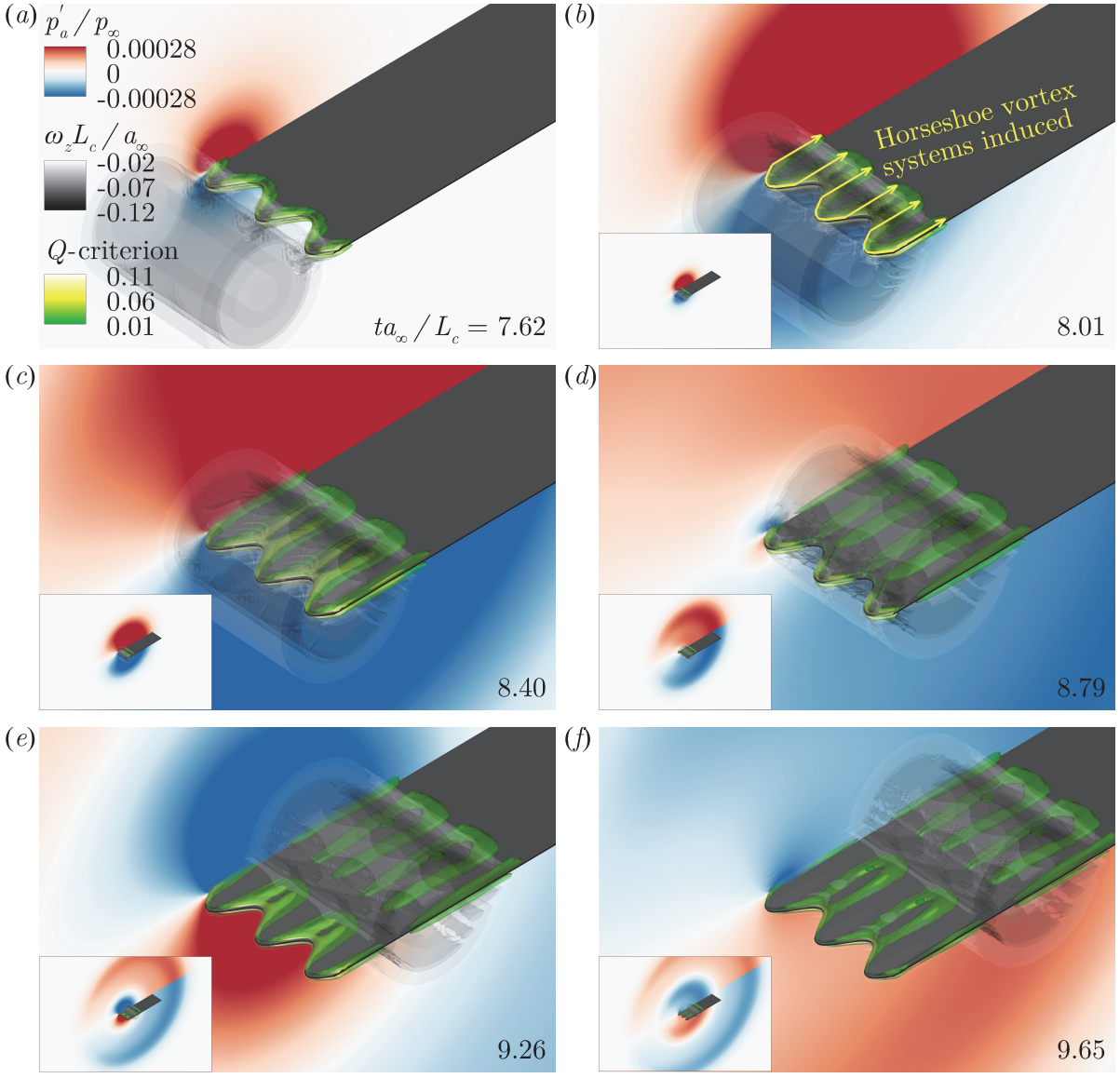

Figure 3.6: Snapshots of WLE-vortex interaction in temporal order: contour plots for perturbed acoustic pressure (p'_a/p_∞), spanwise vorticity ($\omega_z L_c/a_\infty$) and the Q-criterion ($||\Omega_{ij}L_c/a_\infty||^2 - ||S_{ij}L_c/a_\infty||^2$ where Ω_{ij} and S_{ij} are the vorticity and rate-of-strain tensors, respectively). The figures show secondary vortices (Q-criterion) and sound waves (p'_a/p_∞) generated at the leading edge during the interaction. The bottom left corner of images (b)–(f) provides a zoomed out perspective visualising the radiating sound waves. $h_{LE}/L_c = 1/30$.

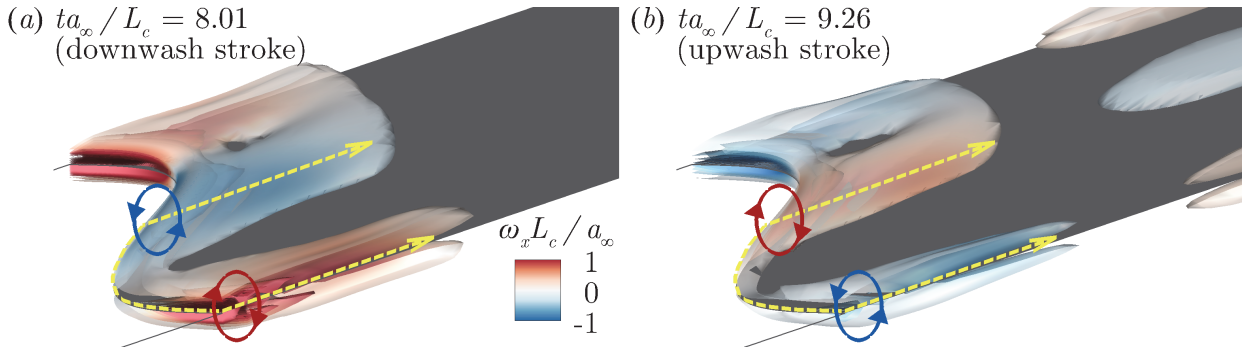

Figure 3.7: Q-criterion iso-surfaces coloured by streamwise vorticity ($\omega_x L_c/a_\infty$) taken at two different points in time during (a) the downwash and (b) upwash strokes of the impinging vortex. The red and blue surfaces indicate positive (clockwise) and negative (anti-clockwise) rotations around the x-axis, respectively. The dashed yellow curves indicate the WLE-induced horseshoe vortex systems.

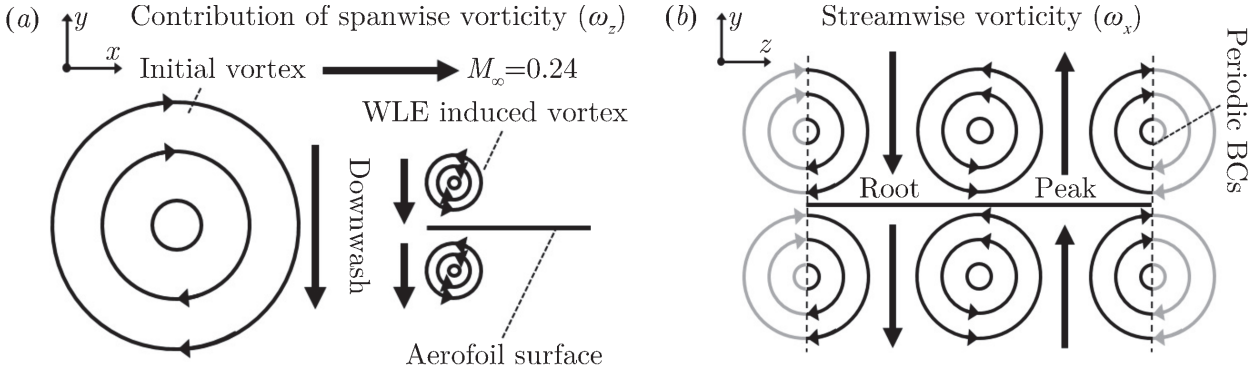

Figure 3.8: Simplified illustration of the WLE-induced vorticity distribution exhibited in Figures 3.6 and 3.7: (a) the sideview on the WLE showing the contribution of spanwise vorticity components induced during the downwash stroke of the impinging vortex; and, (b) the frontview on the WLE describing the streamwise vorticity contribution creating an upwash at the peak and a downwash at the root as a result.

It is reasonable to assume that the acoustic source is almost purely driven by the vertical velocity component (downwash and upwash) impinging on the leading edge since the current aerofoil geometry is completely horizontal with zero thickness and no viscosity. Based on this assumption, it is suggested that the uneven spanwise distribution of the induced vertical velocity illustrated in figure 3.8b is mainly responsible for the disparity in source behaviours between the peak and root observed in §3.2.1. It is apparent in the figure 3.8b that the peak is experiencing a reduced level of vertical velocity perturbation due to the counteracting effect of the streamwise vortices, hence a weaker source strength at the peak as seen in figures 3.4a and 3.4b. On the other hand, the root experiences an amplified level of the vertical velocity perturbation and therefore a reinforced source strength, which is also manifested to a certain extent in figures 3.4e and 3.4f. However, the relative difference to the baseline case is much smaller at the root compared to that taking place at the peak. This requires further investigation. Furthermore, this in no way explains how the root source strength remains almost consistent as the serration height is increase, nor how the saturation event at the peak occurs. Additional quantitative investigations provided in the

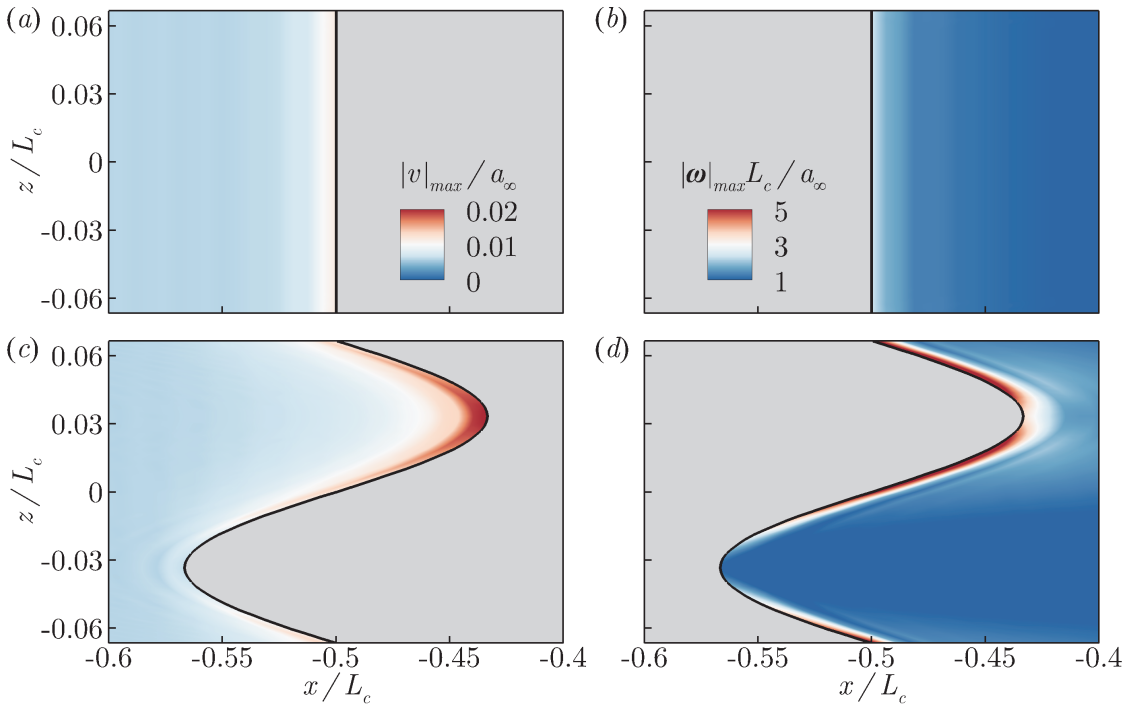

Figure 3.9: The distribution of maximum values (taken from time signals) of the perturbed vertical velocity ($|v|_{max}/a_\infty$) and the vorticity magnitude ($|\boldsymbol{\omega}|_{max}L_c/a_\infty$) on the horizontal plane ($y = 0$): (a/b) for a SLE baseline case and (c/d) for a WLE case with $h_{LE}/L_c = 1/15$. The vertical velocity plots are shown in the flow field only, and the vorticity magnitude plots on the aerofoil's upper surface only.

following sections reveal further details on these matters.

3.3 Consistent source strength at the root

Figure 3.9 shows the distribution of maximum values of the net induced vertical velocity ($|v|_{max}/a_\infty$) and vorticity magnitude ($|\boldsymbol{\omega}|_{max}L_c/a_\infty$) on the horizontal plane ($y = 0$) where the aerofoil is located, obtained from their time signals at each and every point in space:

$$|v|_{max}(\boldsymbol{x}) = \max_{t=0}^{\infty} |v(\boldsymbol{x},t)|, \quad |\boldsymbol{\omega}|_{max}(\boldsymbol{x}) = \max_{t=0}^{\infty} |\boldsymbol{\omega}(\boldsymbol{x},t)|. \tag{3.4}$$

It can be seen in figure 3.9*c* that the amplitude of the induced vertical velocity is highest around the WLE root area as expected. It is also indicated in figure 3.9*d* that the streamwise vortices once created at the peak become amplified as they are moving downstream along the hill towards the root, which results in the highly concentrated vertical velocity spot around the root. These are, surprisingly, much higher (by a factor of two) than those of the SLE baseline cases, which leads to a question how such a highly amplified level of velocity perturbation at the root settles down with a minor increase in the acoustic source strength (wall pressure fluctuation) as seen in figures 3.4*e* and 3.4*f*. A discussion on this follows below.

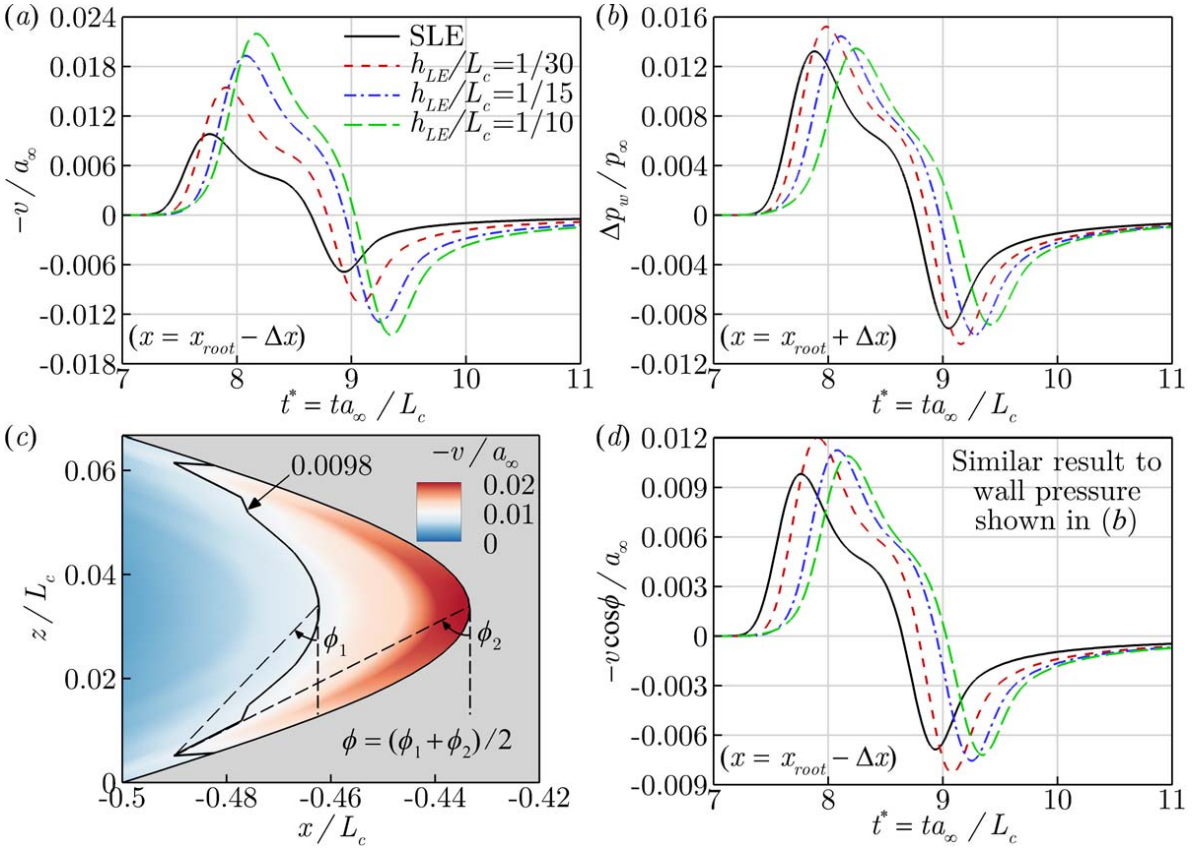

Figure 3.10: A comparison between the induced vertical velocity and wall pressure fluctuation (v/a_∞ and $\Delta p_w/p_\infty$) at the WLE root for various WLE amplitudes (h_{LE}/L_c): (a) time signals of v/a_∞ obtained one grid point upstream of the root; (b) time signals of $\Delta p_w/p_\infty$ obtained one grid point downstream of the root; (c) an instantaneous contour plot of v/a_∞ taken at $t^* = 8.08$ (when the induced vertical velocity reaches its maximum, for $h_{LE}/L_c = 1/15$) indicating an oblique interaction with the root, where the value 0.0098 is the maximum of the SLE baseline case; and, (d) time signals of $v\cos[(\phi_1 + \phi_2)/2]/a_\infty$ which includes the obliqueness effect. The values of ϕ_1 and ϕ_2 are listed in table 3.2.

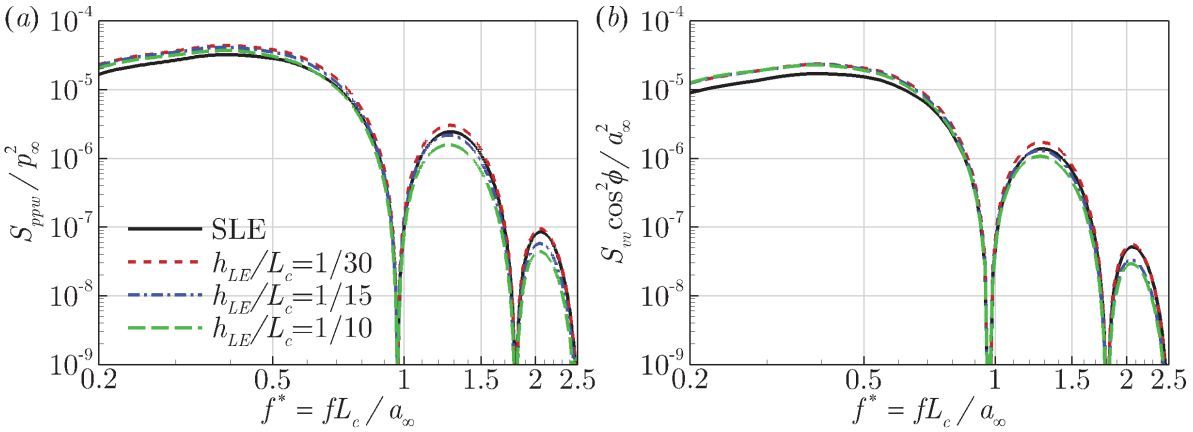

Figure 3.11: Spectral similarity at the root between the wall pressure fluctuation and the induced vertical velocity including the obliqueness effect: (a) PSD of $\Delta p_w/p_\infty$ and (b) PSD of $v\cos\phi/a_\infty$ from figure 3.10b and 3.10d, respectively.

h_{LE}/L_c	ϕ_1	ϕ_2	$\phi = \frac{\phi_1+\phi_2}{2}$
1/30	30.13°	47.72°	38.93°
1/15	45.37°	63.33°	54.35°
1/10	50.76°	69.76°	60.26°

Table 3.2: The cosine angles representing the oblique interaction between the induced vertical velocity and the WLE shown in figure 3.10*c*.

The time signals of the induced vertical velocity impinging at the root are provided in figure 3.10*a* for various values of h_{LE}, where it is clear that the velocity fluctuation increases significantly and steadily with h_{LE} (linked with the streamwise vorticity intensifying as the WLE becomes slender). On the contrary, the wall pressure fluctuation at the root shown in figure 3.10*b* does not vary as much, and even slightly decreases with increasing h_{LE}. One of the possible answers to this paradoxical event might be related to the fact that the vertical velocity perturbation approaches the root area in an oblique fashion as can be seen from figure 3.10*c*. The iso-contours of vertical velocity are skewed and bent around the root area exhibiting the oblique interaction. In order to quantify the obliqueness of the interaction, as shown in figure 3.10*c*, two cosine angles (ϕ_1 and ϕ_2) are measured from the slender *crescent*-shaped high-intensity area in which the vertical velocity perturbation is stronger than the maximum value of the SLE baseline case ($-v/a_\infty = 0.0098$). The angles ϕ_1 and ϕ_2 are defined between the tip and the two inflection points of the crescent. The average of the two measures is then taken to represent the overall obliqueness, i.e. $\phi = (\phi_1 + \phi_2)/2$. This measure is only used as a rough estimate in order to determine the plausibility of the current hypothesis, a more precise measurement for the obliqueness may be possible. The estimated angles for each of the WLE cases ($h_{LE}/L_c = 1/30$, 1/15 and 1/10) are listed in table 3.2. Figure 3.10*d* reveals that the vertical velocity signals multiplied by the obliqueness factor ($\cos\phi$) are remarkably similar to the wall pressure fluctuation signals ($\Delta p_w/p_\infty$) given in figure 3.10*b*. They even show the same trend of changes with respect to increasing h_{LE}. The remarkable similarity is also demonstrated in the spectral domain in figure 3.11 where the agreement is consistent throughout the entire frequency range. A sensitivity test of ϕ for various threshold values (up to ±20% from 0.0098) is also carried out with no significant changes found, this is shown in Appendix A. The result here therefore strongly suggests that the oblique interaction is a possible explanation for the consistent source strength at the root.

An additional investigation is performed in this section to find out if there is a certain normalisation applicable to the vertical velocity perturbation which leads to a meaningful correlation with the wall pressure fluctuation at the root. In this regard, an area-averaged norm of the vertical velocity perturbations is defined around the root as a function of time as follows:

$$\left.\begin{aligned} v_{mean}(t) &= \frac{1}{\mathcal{A}} \int_0^{\frac{1}{2}\lambda_{LE}} \int_{-\frac{1}{2}L_c}^{x_{LE}} v(x, y=0, z, t)\mathrm{d}x\mathrm{d}z, \\ \mathcal{A} &= \int_0^{\frac{1}{2}\lambda_{LE}} \int_{-\frac{1}{2}L_c}^{x_{LE}} \mathrm{d}x\mathrm{d}z = \frac{\lambda_{LE} h_{LE}}{\pi}, \end{aligned}\right\} \tag{3.5}$$

where $\mathcal{A}$ is the area of integration enclosed by the concave part of the WLE (near the root) and

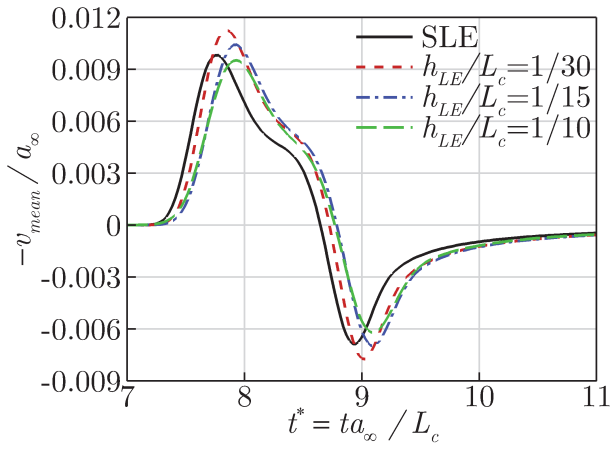

Figure 3.12: Mean vertical velocity signals calculated from (3.5) around the root area for various values of h_{LE}/L_c (WLE amplitude), in relation to the consistent source strength at the root irrespective of h_{LE}.

a straight line at $x = -0.5L_c$ in the xz-plane. The expression for x_{LE} as a function of z is given in (2.2). The calculated mean vertical velocity signals are presented in figure 3.12. It is shown that the mean vertical velocity perturbation remains relatively unchanged despite the substantial variation in h_{LE}. This might indicate that the overall vertical momentum (created by the initial vortex) is conserved although the vertical velocity tends to surge locally around the root area. The v_{mean}/a_∞ signals also exhibit a good similarity with the $\Delta p_w/p_\infty$ (wall pressure fluctuation) signals at the root shown in figure 3.10*b*. Therefore, it may be concluded here that the source strength at the root is better correlated with the mean vertical velocity signal than with the local one nearest to it. This outcome is analogous to the theoretical consideration based on a Poisson equation, i.e. $\nabla^2 p = -\rho(\partial u_i/\partial x_j)(\partial u_j/\partial x_i)$ – see Tsuji *et al.* (2007) – indicating that pressure at a certain location is determined by integrating velocity properties surrounding it.

3.4 Variations in source strength at the peak

The focus is now moved on to the WLE peak in this section. It has been observed earlier in §3.2 that the acoustic source characteristics at the peak are considerably different to those at the root. The source strength at the peak decreases significantly with increasing WLE amplitude (h_{LE}) as shown in figure 3.4*a* and 3.4*b*. It seemed rather straightforward from figure 3.8 that this was due to the attenuating vertical velocity contribution created at the peak by the streamwise vorticity components that are growing with h_{LE} as can be seen in figures 3.13 and 3.14. The time signals of the induced vertical velocity (v) and the corresponding wall pressure fluctuation (Δp_w) at the peak for different values of h_{LE} are shown in figure 3.15. It is apparent in the figure that the vertical velocity perturbation decreases with increasing h_{LE} and it results in the reduction of the source strength at the peak. One thing to note is that for the downwash stroke the flow near the LE has not necessarily had sufficient time to return to ambient conditions. For this reason we observe that the vertical velocity plateau caused by the spacing between the up and downwash

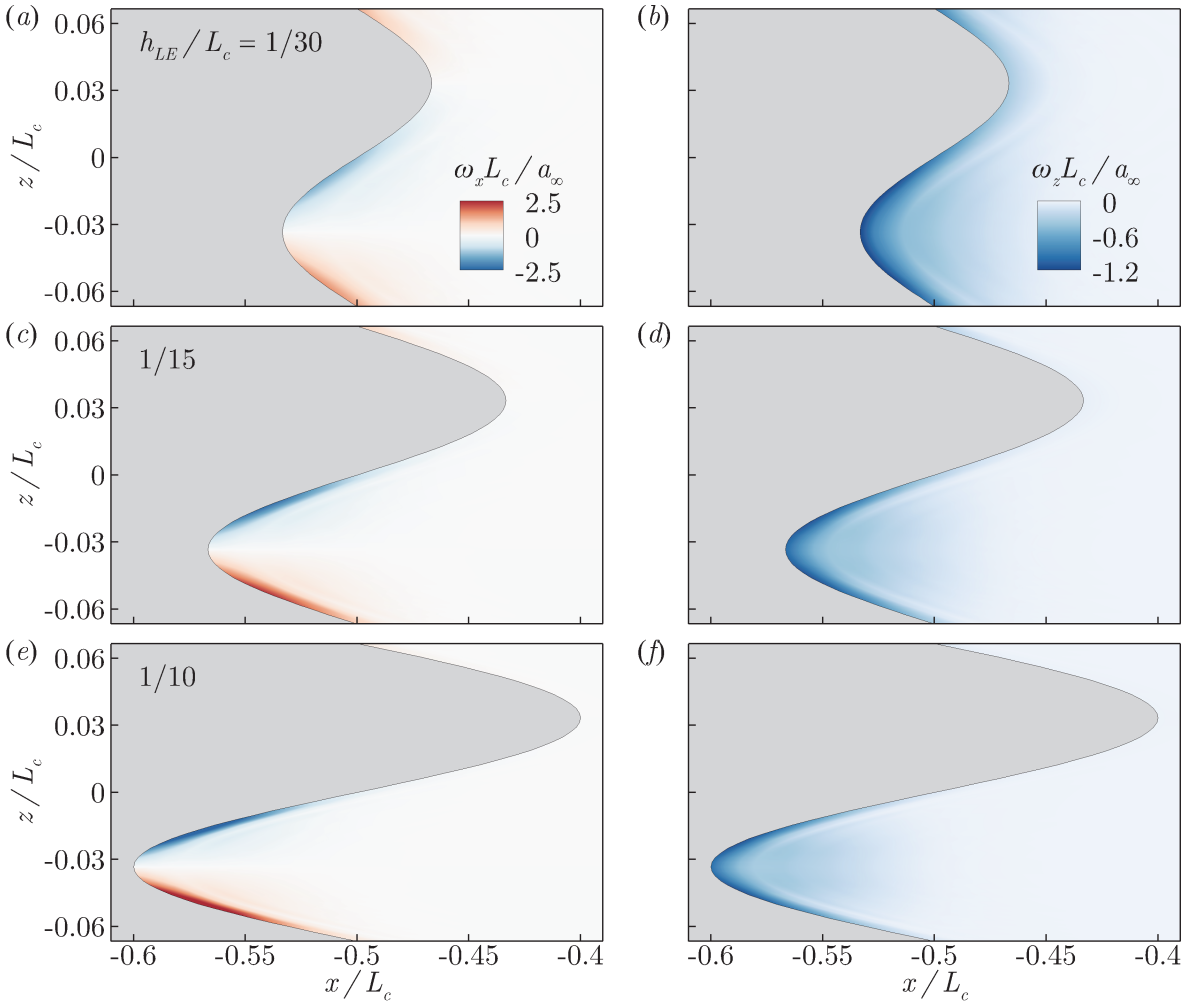

Figure 3.13: Instantaneous contour plots of streamwise vorticity ($\omega_x L_c/a_\infty$: left) and spanwise vorticity ($\omega_z L_c/a_\infty$: right) on the upper surface of the aerofoil for three different WLE amplitudes, obtained when the induced vertical velocity in front of the peak reaches its maximum amplitude: (a/b) $ta_\infty/L_c = 7.540$, (c/d) 7.461 and (e/f) 7.305 – see figure 3.15*a*.

strokes is non-zero. Once this is taken into account the same trend is observed for both upwash and downwash strokes.

A more interesting observation is that both v and Δp_w become significantly less sensitive to increasing h_{LE} after a certain point. In particular the v signal seems to converge towards that of the free-field solution generated without the aerofoil in place. This section is focused on explaining the mechanism of the convergence/saturation phenomenon taking place at the peak.

Considering the horseshoe vortex (HV) system identified in §3.2, a semi-analytic approach based on Biot-Savart's law is proposed in order to obtain more information on the induced velocity components from the HV system. The general form of Biot-Savart's law is expressed by

$$\mathrm{d}\boldsymbol{v}(\boldsymbol{x}_0, \boldsymbol{l}) = \frac{\Gamma}{4\pi} \frac{\boldsymbol{r} \times \mathrm{d}\boldsymbol{l}}{|\boldsymbol{r}|^3}, \quad \boldsymbol{r} = \boldsymbol{l} - \boldsymbol{x}_0, \tag{3.6}$$

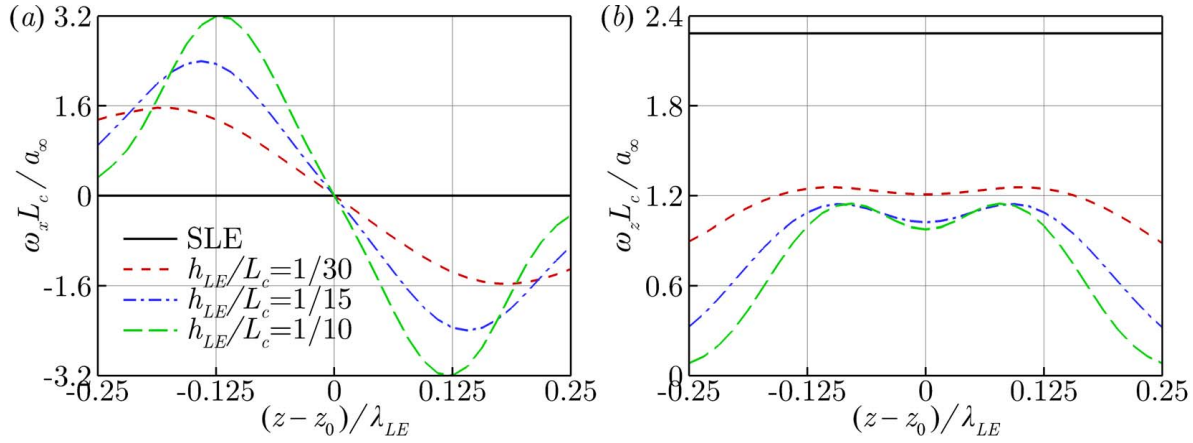

Figure 3.14: Vorticity distributions in span along the leading edge for various values of h_{LE}/L_c obtained when the induced vertical velocity in front ot the peak reaches its maximum amplitude: (a) streamwise vorticity ($\omega_x L_c/a_\infty$) and (b) spanwise vorticity ($\omega_z L_c/a_\infty$) on the upper surface of the aerofoil – see figure 3.13. The spanwise coordinate of the peak is denoted by z_0 in the x-axis labels.

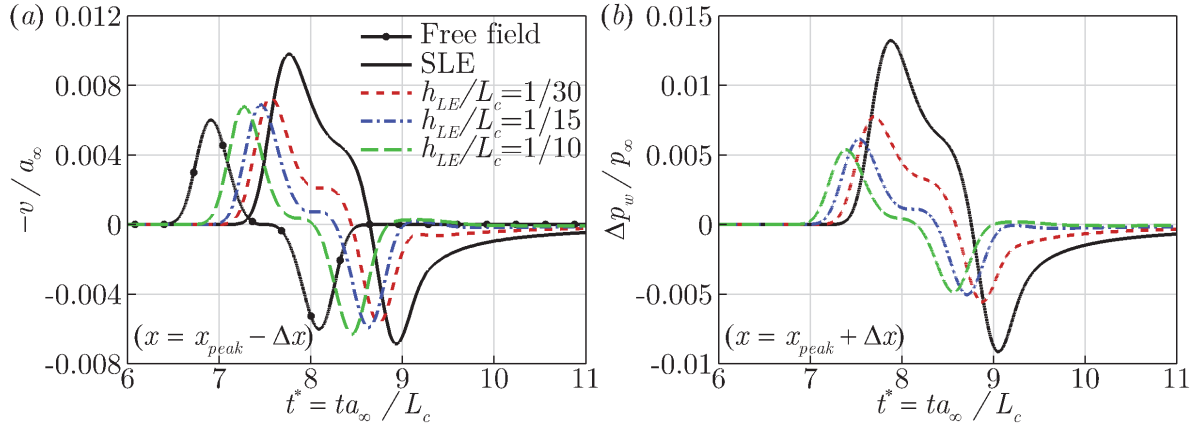

Figure 3.15: A comparison between the induced vertical velocity and wall pressure fluctuation (v/a_∞ and $\Delta p_w/p_\infty$) at the WLE peak for various WLE amplitudes (h_{LE}/L_c): (a) time signals of v/a_∞ obtained one grid point upstream of the peak; and, (b) time signals of $\Delta p_w/p_\infty$ obtained one grid point downstream of the peak. The case with "Free field" indicates a free-field solution (without the aerofoil) recorded at $(x, y) = (-0.7L_c, 0)$.

where $\boldsymbol{x}_0$ and $\boldsymbol{l}$ are position vectors of the observer and a certain point on the vortex filament, respectively; and, Γ is the cross-sectional circulation induced by the vortex. Since the current HV (horseshoe vortex) system is on a horizontal plane, the above equation with the observer position fixed at the peak can be simplified as

$$\mathrm{d}v^{HV}_{peak} = \frac{\Gamma}{4\pi}\frac{(r_3\mathrm{d}x - r_1\mathrm{d}z)}{(r_1^2 + r_3^2)^{\frac{3}{2}}}, \tag{3.7}$$

where the subscripts "1" and "3" denote the streamwise and spanwise coordinates, respectively. Integrating all contributions from the bound vortex and the two trailing vortices lead to the following

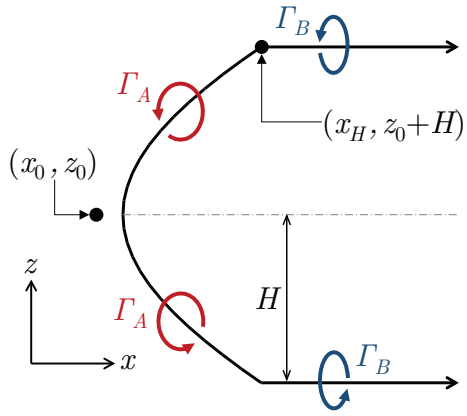

Figure 3.16: Schematic of the horseshoe vortex (HV) system used to estimate the WLE-induced vertical velocity in front of the peak, in relation to (3.8).

formula (see figure 3.16):

$$\left.\begin{aligned} v_{peak}^{HV} &= v_A + v_B, \\ v_A = \frac{1}{4\pi}\int_{z_0-H}^{z_0+H} &\frac{\Gamma_A}{[(x_{LE}-x_0)^2+(z-z_0)^2]^{\frac{3}{2}}}\left[(z-z_0)\frac{\mathrm{d}x_{LE}}{\mathrm{d}z}-(x_{LE}-x_0)\right]\mathrm{d}z, \\ v_B = \frac{H}{2\pi}\int_{x_H}^{\infty} &\frac{\Gamma_B \mathrm{d}x}{[(x-x_0)^2+H^2]^{\frac{3}{2}}}, \end{aligned}\right\} \tag{3.8}$$

where the subscripts "A" and "B" represent contributions from the bound and trailing vortices, respectively; $(x_0, z_0) = (-L_c/2 - h_{LE} - \Delta x, -\lambda_{LE}/4)$ is the observer position one grid cell ahead of the peak point; and, H is the half width of the HV. The bound vortex is located along the WLE ($x = x_{LE}(z)$) that is given by (2.2) and $x_H = x_{LE}(z_0 + H)$ is the starting x-coordinate of the trailing vortices. Here, x_H is selected at the position where the largest streamwise vorticity ($|\omega_x|$) is obtained.

In (3.8), the cross-sectional circulations Γ_A and Γ_B are calculated at each grid point along the HV based on the simulation data by using the Stokes' theorem with a constraint for the Q-criterion as

$$\Gamma = \int_{\mathcal{A}} \omega_n \mathrm{d}\mathcal{A}\Big|_{Q>\max(Q)/100}, \tag{3.9}$$

where $\mathcal{A}$ is the integration area on a plane that is perpendicular to the WLE curve and accordingly ω_n is the vorticity component normal to the plane. The Q-criterion constraint is used to eliminate the circulation produced by the initial upstream vortex in the current evaluation. Since the upstream disturbance has a significantly lower strength, a value blanking method can be adopted for this purpose. This is achieved by restricting $\mathcal{A}$ to the region where the Q-criterion remains above 1% of the global maximum value. Since the HV structure exists on both the upper and lower surfaces of the aerofoil, the calculation is repeated for both and added together to obtain the total induced velocity.

The result of the semi-analytic prediction by using (3.8) for the HV-induced vertical velocity in

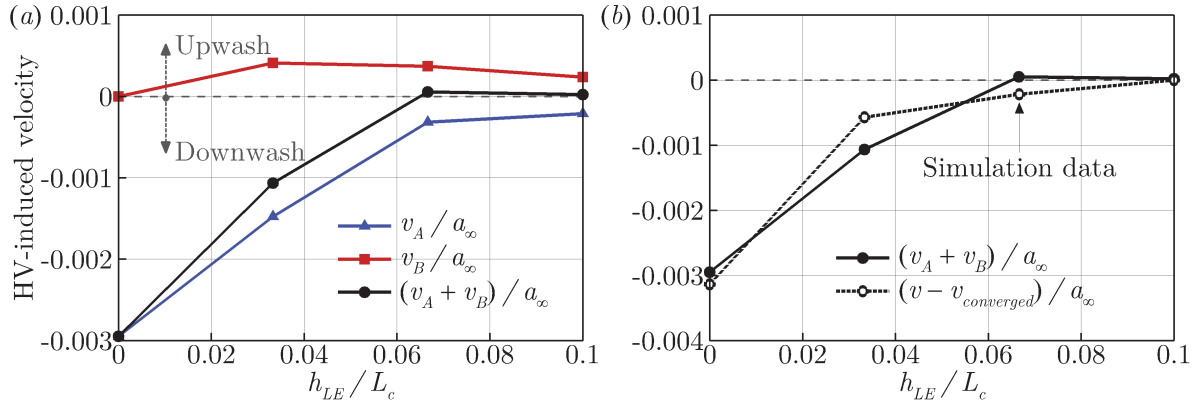

Figure 3.17: Semi-analytic predictions of the HV-induced vertical velocity components in front of the peak, obtained by using (3.8) for various values of h_{LE}/L_c. The predictions are made at $ta_\infty/L_c = 7.770$, 7.540, 7.461 and 7.305 for $h_{LE}/L_c = 0$, 1/30, 1/15 and 1/10, respectively, when the vertical velocity reaches its maximum amplitude (see figure 3.15).

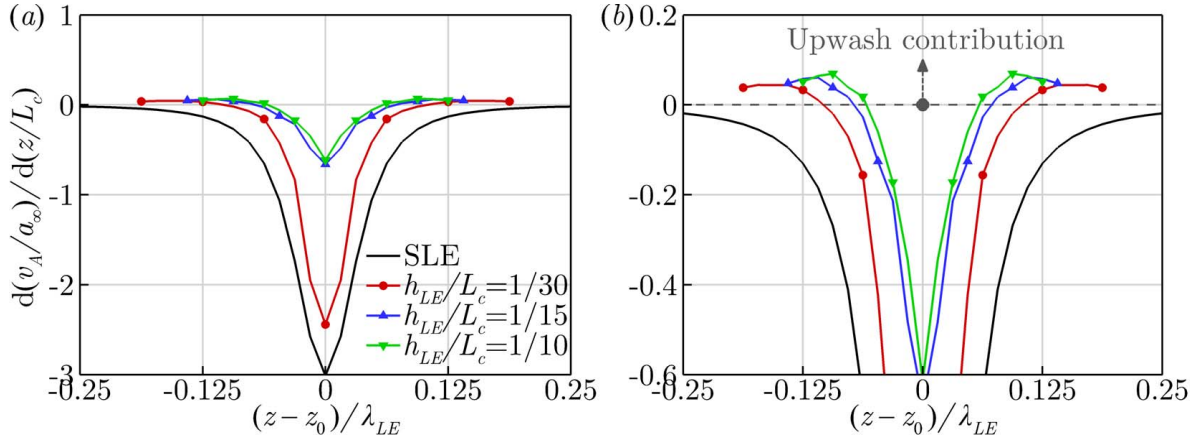

Figure 3.18: Profiles of $\mathrm{d}v_A/\mathrm{d}z$ (normalised by a_∞ and L_c) from (3.8): (*a*) entire and (*b*) zoomed-up views, showing local piecewise contributions of the bound vortex to the overall induced vertical velocity in front of the peak resulted in figure 3.17.

front of the peak is presented in figure 3.17. It is clearly shown in the figure that the net HV-induced vertical velocity diminishes with increasing h_{LE}. It is due to the contributions from the bound and trailing vortices (v_A and v_B) cancelling out each other. The cancellation is almost perfect resulting in a zero sum when $h_{LE}/L_c = 1/15$ or higher, in which case the overall vertical velocity is effectively maintained by the initial vortex approaching (free-field solution). This explains the convergence/saturation of the vertical velocity signal at the peak for high h_{LE}/L_c, which was questioned in the beginning of the section.

Some more information can be found from the semi-analytic prediction data. In figure 3.17 the contribution of the trailing vortices (v_B) seems to gradually decreases with increasing h_{LE}, although the streamwise vorticity (ω_x) grows with h_{LE} as shown in figures 3.13 and 3.14. It may be explained by using (3.8) where v_B is proportional to H and asymptotically to $(x_H - x_0)^{-3}$. For a higher h_{LE}, H decreases and x_H increases (as shown in figures 3.14 and 3.16), which may result in a reduced v_B despite a higher ω_x or Γ_B.

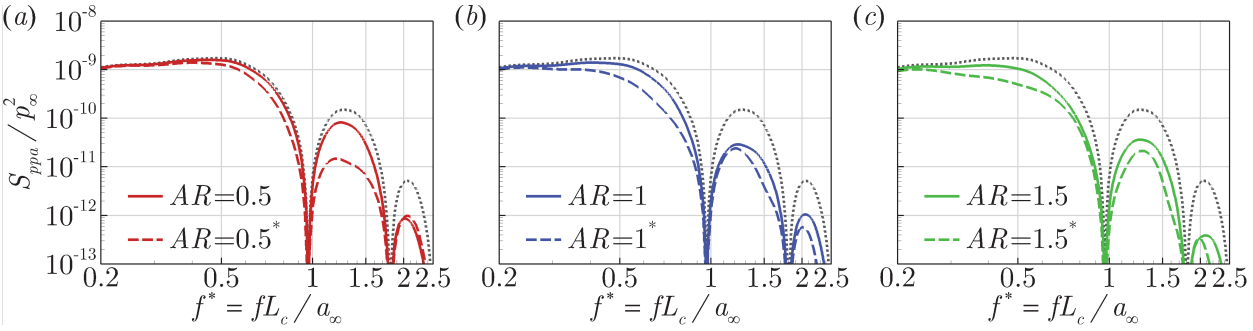

Figure 3.19: Far-field acoustic pressure PSD profiles, $S_{ppa}(f^*)/p_\infty^2$, obtained at an observer location, $\boldsymbol{x}_o = (0, 5L_c, 0)$, for three different WLE aspect ratios ($AR = 2h_{LE}/\lambda_{LE} = 0.5$, 1 and 1.5). The aspect ratios with "$*$" indicate that the size of the WLE is doubled ($AR^* = 2h^*_{LE}/\lambda^*_{LE}$ where $h^*_{LE} = 2h_{LE}$ and $\lambda^*_{LE} = 2\lambda_{LE}$). The dotted curves are from the SLE baseline case.

In the meantime, in figure 3.17, the contribution of the bound vortex (v_A) decreases rapidly and converges towards zero with increasing h_{LE}. This may be explained in three steps. First, between $h_{LE} = 0$ (SLE) and 1/30, there is a large drop in the spanwise vorticity (ω_z) and the appearance of ω_x, which are shown in figure 3.14. Secondly, between $h_{LE} = 1/30$ and 1/15, there is a moderate drop in ω_z and a further growth in ω_x leading to a continued reduction of v_A up to this point. Lastly, between $h_{LE} = 1/15$ and 1/10, ω_x still grows consistently (with very little change in ω_z); however, this does not reflect efficiently on v_A due to the fact that the term $[(z - z_0)\mathrm{d}x_{LE}/\mathrm{d}z - (x_{LE} - x_0)]$ in (3.8) tends to zero or a very small number (except for the area nearest to the peak where ω_z prevails) as the WLE profile becomes substantially slender. These trends can also be found in figure 3.18 which provides local piecewise contributions of the bound vortex ($\mathrm{d}v_A/\mathrm{d}z$ as a function of z) showing the rapid decrease of the bound vortex contribution and its convergence at high h_{LE}/L_c. The figure also shows a certain amount of upwash generated by the bound vortex indicating the influence of the streamwise vorticity component prevalent around the edges of the bound vortex.

3.5 Additional findings and discussions

This section briefly presents additional findings made with regard to two different aspects based on the current simulation framework: 1) the relationship between the aeroacoustic source strength and the WLE aspect ratio; and, 2) the effect of a three-dimensional profile introduced in the impinging vortex on the interaction with the leading-edge geometries.

3.5.1 WLE aspect ratio and source strength

A parametric study is carried out to find a relationship between the aeroacoustic source strength and the WLE aspect ratio ($AR = 2h_{LE}/\lambda_{LE}$). Three different values of $AR = 0.5$, 1 and 1.5 have been studied in §3.2 to §3.4 with the wavelength fixed at $\lambda_{LE}/L_c = 2/15$. In this section, additional simulations are performed with both h_{LE} and λ_{LE} doubled (hence, the aspect ratios

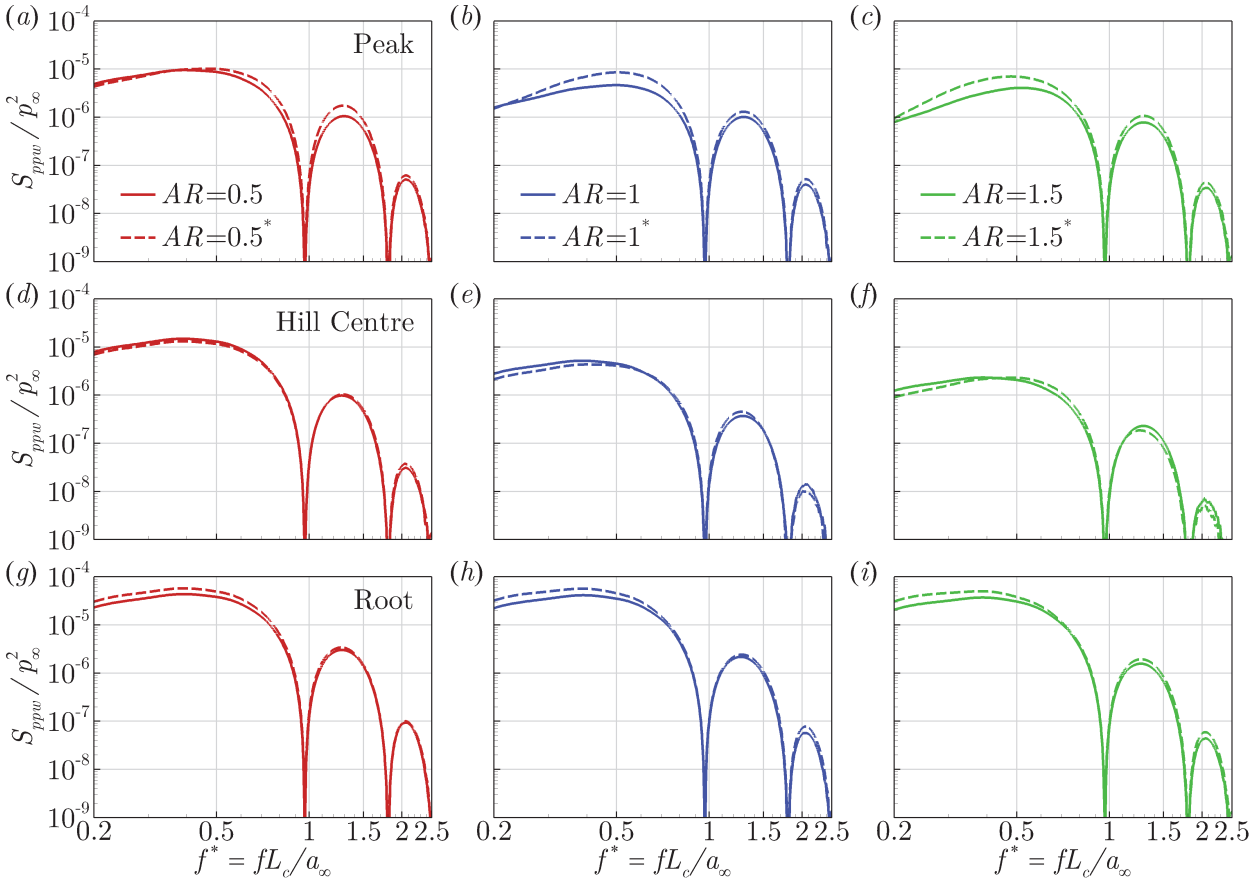

Figure 3.20: Wall pressure PSD profiles, $S_{ppw}(f^*)/p_\infty^2$, obtained at three different locations on the WLE (peak, hill centre and the root) for three different WLE aspect ratios ($AR = 2h_{LE}/\lambda_{LE} = 0.5$, 1 and 1.5). The aspect ratios with "$*$" indicate that the size of the WLE is doubled ($AR^* = 2h^*_{LE}/\lambda^*_{LE}$ where $h^*_{LE} = 2h_{LE}$ and $\lambda^*_{LE} = 2\lambda_{LE}$).

remain the same) in order to investigate the differences in the source characteristics. In terms of the radiated sound pressure level (SPL), it is well known that the SPL is dependent largely on h_{LE} with secondary contributions from λ_{LE} (Chaitanya *et al.*, 2015; Kim *et al.*, 2016; Lau *et al.*, 2013; Narayanan *et al.*, 2015). This means that the SPL would be further reduced in the cases of doubled h_{LE} for the same aspect ratio, which is also true in the current study as shown in figure 3.19 ($AR^* = 0.5$, 1 and 1.5). The further reduction of sound is apparent across the whole frequency range. However, the reduced sound does not necessarily relate to a reduced source strength as far as the current results are concerned.

Figure 3.20 shows the source strength (wall pressure spectra) at the peak, hill centre and root, obtained from the additional simulations with double sized WLEs, compared with the earlier original cases of the same aspect ratios. It is noticeable that the source strength remains relatively unchanged by doubling the size of the WLE as far as the aspect ratio is maintained. Although moderate deviations are seen at the peak at some frequencies, a remarkable level of similarities can be found at the root and the hill. The result might suggest that the WLE aspect ratio is a similarity parameter which dictates the source strength and characteristics, despite the radiated sound being influenced mainly by the WLE amplitude. It also suggests that there exist imperative mechanisms

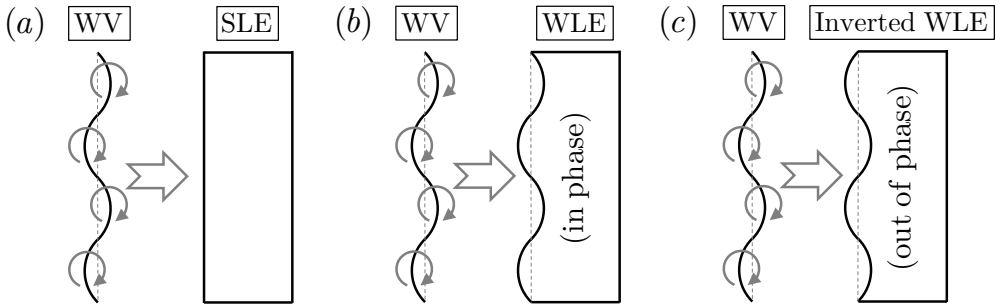

Figure 3.21: Schematics of a wavy vortex (WV) interacting with three different leading-edge geometries: (*a*) SLE, (*b*) WLE and (*c*) the WLE inverted. The centreline of the wavy vortex is undulated along the span in the same fashion applied to the WLE profile – based on (2.2). The inverted WLE (IWLE) has an out-of-phase formation against the prescribed WV.

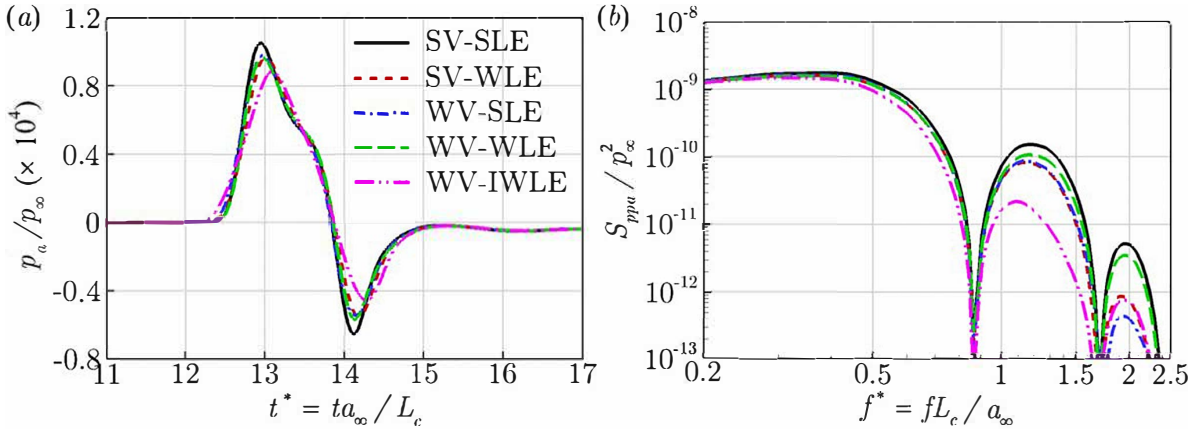

Figure 3.22: Far-field acoustic pressure time signals and the corresponding PSD: (*a*) $p_a(t^*)/p_\infty$ and (*b*) $S_{ppa}(f^*)/p_\infty^2$ obtained at an observer location, $\boldsymbol{x}_o = (0, 5L_c, 0)$, from the additional simulations described in figure 3.21. The new results are compared with the earlier cases (SV-SLE and SV-WLE) that used a straight vortex. The WLE and WV profiles are based on $h_{LE}/L_c = 1/30$ and $\lambda_{LE}/L_c = 2/15$.

contributing to the noise reduction purely associated with the propagation of the sound waves. Most likely destructive interference as outlined in §1. Regardless, there is little known about the propagation mechanisms regarding the discrepancies between the source spectra and the radiated sound spectrum as highlighted towards the end of §3.2.1. An explanation of this observation is one of the key outcomes of the following chapter on the noise reduction mechanisms (§4).

3.5.2 The effect of a three-dimensional profile in the impinging vortex

A miscellaneous test has been performed in order to briefly demonstrate the effect of three-dimensionality introduced in the impinging vortex on the interaction with the leading-edge geometries. The schematics of the additional test cases are described in figure 3.21. The centreline of the impinging vortex no longer remains straight but forms a wavy profile in the same fashion as the WLE considered in this work. Three additional cases of aerofoil-vortex interaction are considered

as depicted in figure 3.21: (*a*) WV-SLE, (*b*) WV-WLE and (*c*) WV-IWLE, where WV and IWLE stand for wavy vortex and inverted WLE, respectively. The WV and WLE profiles are identical but the IWLE (inverted WLE) has an 180° phase-shift against the WV. The WV profile is created simply by changing the centre coordinate (x_0) of the vortex used in (3.1) and (3.2) as follows:

$$x_0 = -2.5L_c + h_{LE}\sin\left(\frac{2\pi z}{\lambda_{LE}}\right), \quad z \in \left[-\frac{1}{2}L_z, \frac{1}{2}L_z\right]. \tag{3.10}$$

The result of the additional simulations is presented in figure 3.22 in comparison with the earlier cases (SV-SLE and SV-WLE) that was based on a straight vortex (SV). It is shown that the WV-WLE case yields an almost identical sound pressure spectrum to that of the SV-SLE case. Also, the WV-SLE and SV-WLE cases are remarkably similar to each other except a marginal difference at high frequencies. In comparison, the WV-IWLE case exhibits a substantial noise reduction across a wide range of frequencies. These results could be explained by looking at the streamwise distance between the impinging vortex and the leading edge. First, the WV-WLE and SV-SLE cases have the same relative distance that is constant along the span. Therefore the impact takes place synchronously (with no time delay) across the span. The WV-SLE and SV-WLE cases also have the same relative distance but varying along the span, which results in an asynchronous interaction over the span, hence a reduced noise level. Finally, the WV-IWLE case is effectively comparable to the SV-WLE case with the WLE amplitude doubled ($h_{LE}/L_c = 1/15$ instead of $1/30$) and therefore resulting in a significantly increased noise reduction (see figure 3.5).

It is also possible to consider more complex cases such as a wavy vortex with different wavelength, amplitude or phase-shift to those of the wavy leading edge geometry. Also, the impinging vortex can be finite in span (similar to an individual eddy) as explored in Mathews & Peake (2015, 2018). Studying these increasingly complex cases may enhance the understanding of the noise generation/reduction mechanisms in more details later on.

3.6 Concluding remarks

Detailed understandings of the aeroacoustic source mechanisms of a thin aerofoil with a WLE interacting with a prescribed impinging vortex have been achieved by using high-order accurate aeroacoustics simulations in this chapter. The numerical flow visualisation showed that the WLE upon interaction with the impinging vortex created a horseshoe vortex (HV) system stemming from the peak area. The HV-induced vorticity and velocity fields around the WLE provided key information to quantify and understand the changes in the wall pressure fluctuations compared to the SLE baseline cases. Two distinctive source behaviours were observed and questioned during the initial analysis of the simulation data. Some scientific explanations to the questions have emerged after investigating into the role of the HV system and the induced velocity field induced by it.

The aeroacoustic source strength at the root remained consistent (similar to that of the SLE counterpart) irrespective of the WLE amplitude (h_{LE}). This initially seemed incompatible with the

growing contribution of the HVs substantially amplifying the vertical velocity perturbation around the root with increasing h_{LE}. The current investigation showed that the oblique interaction between the vertical velocity perturbation and the root area could be one of the mechanisms to explain the paradoxical event. From another point of view, it was demonstrated that the area-averaged vertical velocity remained at a constant level irrespective of h_{LE} (indicating the conservation of vertical momentum), which might suggest that the source strength at the root was determined mainly by the overall amount of vertical momentum possessed in the upstream of the root.

Unlike the root, the source strength at the peak was significantly reduced with increasing h_{LE} up to a certain point. The reduction of source strength at the peak was well correlated with the growth in streamwise vorticity and the decay in the spanwise vorticity along the HV which efficiently attenuated the vertical velocity perturbation. However, the source strength at the peak ceased to decrease further when h_{LE} was sufficiently large. The source convergence/saturation event was explained by using a semi-analytic model of the HV (a curved bound vortex connected with two straight trailing vortices) based on Biot-Savart's law. The semi-analytic model showed that the HV-induced downwash and upwash components eventually led to a complete mutual cancellation as h_{LE} becomes large, and therefore the net vertical velocity in front of the peak converged to that of the free-field solution with no aerofoil in place. It was also found that the highly slender WLE geometry made the HV effectively non-responsive to the source strength at the peak despite the intensified streamwise vorticity components surrounding it.

It appeared that there was a strong similarity rule existing in the source characteristics between two different WLE geometries with the same aspect ratio. The level of similarity viewed from the wall pressure spectra was maintained at all frequencies and all probing points (peak, hill centre and root). This might suggest that the source mechanisms explained in this chapter have a certain level of universality applicable to a wide range of WLE geometries. This hypothesis also highlights the importance of investigating the "propagation" mechanisms such as destructive interference since there is a significant disagreement between the source power spectra at the wall and the noise reduction spectrum at the far field, as addressed in §3.2.1. Also, the linear growth of noise reduction with frequency – reported repeatedly by Chaitanya *et al.* (2015); Kim *et al.* (2016); Narayanan *et al.* (2015) – is unexplained solely by the source mechanisms.

The current study was focused on the most basic scenario where the impinging vortex was kept two-dimensional and only the leading-edge geometry was changed from 2D to 3D such that it was straightforward to identify the differences that the geometric modification made to the flow and sound. It would be necessary afterwards to consider a more complex case where the impinging vortex has a three-dimensional profile as briefly demonstrated in §3.5.2. It will aid better understanding of the realistic aerofoil-turbulence interaction that has a certain spanwise length scale and coherence. However, the size of the parametric space to explore will become substantial.

Chapter 4

Noise Reduction Modelling and Underlying Mechanisms

4.1 Motivation

It is now well established how undulated leading edges are an effective means to reduce broadband noise caused by interaction of aerofoils with unsteady vortical disturbances. However despite the rapid progress obtained by the research community in the last few years, there are still various gaps to fill in order to complete the understanding of the core mechanisms. In particular there are two explanations for the noise reductions offered by undulated leading edges which are most prevalent in the literature: 1. Spanwise destructive interference; 2. Source strength magnitude reduction. There are compelling arguments for both mechanisms, however to date there is no comprehensive study detailing the relative significance of the two mechanisms.

Both source cut-off and spanwise decorrelation effects were suggested as potential noise reduction mechanisms by Kim *et al.* (2016). It was demonstrated how the WLE hill region reduces the source strength (wall pressure spectra) throughout the frequency range, while the WLE peak has a reduced magnitude at low frequencies. Reduced wall pressure magnitude at the hill has also been observed numerically by Clair *et al.* (2013) and Tong *et al.* (2018*a*). Additionally, both two point correlation and phase spectra showed an increasingly out-of-phase shift between the LE peak and points across the span. The LE source mechanisms were later investigated in detail by Turner & Kim (2017*b*) (§3), who revealed secondary hydrodynamic structures (most notably streamwise vortices) were responsible for the variation in strength along the span. This work also noted that the low frequency source reductions reported at the hill were not perceived at the far-field, revealing a significant gap in our understanding of the noise reduction mechanisms.

An approximately linear noise reduction trend was demonstrated by Chaitanya *et al.* (2017) after realising their experimental results were self-similar based on the LE amplitude Strouhal number (fh_{LE}/U_∞). A simplified model was introduced based on the integral of the LE phase variation

($\omega \cos(\theta) h_{LE}/U_\infty$) across one LE cycle. Although the result produces large overshoots, its stationary points match well with the experimental data and linear noise reduction trend, indicating that the noise reductions are determined primarily by destructive interference. Simultaneously, a conflicting theory for the Strouhal number dependence was proposed based on the hypothesis that the effective source length of the WLE scales with the impinging streamwise hydrodynamic wavelength (U/f).

Strong evidence for the destructive interference mechanism was also provided by Lyu & Azarpeyvand (2017), who extended the Amiet approach to applications with saw-tooth type serrations. Lyu & Azarpeyvand (2017) demonstrated how the predicted scattered surface pressure along the edge exhibits more phase difference at a fixed frequency as LE amplitude is increased. They suggested two geometric criteria for noise reduction $\omega h_{LE}/U\infty >> 1$, which is required to provide sufficient phase variation along the span; and $\omega h_e/U\infty >> 1$ ($h_e = ARl_y$, where l_y is the spanwise correlation lengths scale) which ensures the impinging disturbance is wide enough to excite with multiple in/out-phase regions. Predictions obtained by the model were compared to the experimental data of Narayanan *et al.* (2015) with good in the medium-high frequency range. However, at low frequency the WLE obtained a noise increase which was not observed in the experiment. Lyu & Azarpeyvand (2017) suggested this is caused by a larger wetted edge length for the WLE compared to the SLE case. In the present work it is shown that inclusion of the complete source strength reduction mechanisms negates the increased wetted length of the WLE.

As a response to the previous work there are two main objectives in this chapter. Firstly, to establish the relative contributions from the source reduction and phase interference mechanisms respectively, and to establish which is responsible for the linear noise reduction trend. To that end, also to investigate the proposed effective edge length hypothesis of Chaitanya *et al.* (2017). Secondly, to answer the question proposed by Turner & Kim (2017*b*), explaining why the far-field noise does not reflect the low frequency reductions observed on the surface. The same methodology is continued here as in the previous chapter. This approach neglects spanwise lengths scale effects, which can result in exaggerated interference peaks relative to a HIT approach. Despite this the underlying linear noise reduction trend suggested is still similar to the experiments.

Firstly this chapter extends the work of Chaitanya *et al.* (2017) by introducing a similar 1D LE line model for predicting the noise reductions. The model is primarily based on the spanwise phase variation, but also accounts for the difference in edge length between straight and wavy cases, spanwise periodic boundary conditions, retarded time effects, and source reduction at the hill. This approach provides strong evidence for the phase interference mechanisms being the primary reason for the noise reduction frequency trend. However one of the main findings of this work is that such an approach provides erroneous conclusions regarding the significance of source strength variation, which in fact requires 2D surface information to be properly captured. This is made apparent by analysing the 2D surface spectra which shows the source is non-compact at high frequencies. This is speculated to be a response of high frequency content contained within the convected secondary vortex structures generated at the LE. A FW-H propagation model is applied to incrementally increasing portions of the surface, revealing approximately 4 vortex diameters are

required in the streamwise direction to obtain a reasonable prediction. Regarding the low frequency surface vs far-field disparity, it is found that despite reduced low frequency source strength on the LE line, the percentage of the surface with similar magnitude wall pressure spectra is comparable. It is also revealed that the effective source area (rather than length) reduces with frequency to a significant extent. Finally an attempt is made to isolate the two mechanisms by modifying the source input to the FW-H model. The work raises some concerns for models based solely on the destructive interference mechanism, which can produce misleading results regarding the physics. It is shown that both mechanisms increase the noise reduction with frequency. However, it is also important to remember the mechanisms are coupled, meaning variation in source strength reduces the effectiveness of destructive interference.

4.2 Problem description and computational set-up

4.2.1 Prescribed spanwise vortex model

The current study employs a spanwise (two-dimensional) vortex model prescribed as an initial condition. The vortex model is based on a Gaussian shape function suggested by Yee *et al.* (1999), which provides a divergence-free velocity field:

$$\{u(\boldsymbol{x})\,,\,v(\boldsymbol{x})\,,\,w(\boldsymbol{x})\} = a_\infty \psi(\boldsymbol{x}) \left\{ M_\infty + \sigma \frac{y}{L_c}\,,\; -\sigma \frac{x-x_0}{L_c}\,,\; 0 \right\}, \tag{4.1}$$

where x_0 is the initial location of the vortex. The Gaussian shape function is defined as

$$\psi(\boldsymbol{x}) = \frac{\epsilon}{2\pi} \sqrt{\exp\left[1 - \sigma^2 \frac{(x-x_0)^2 + y^2}{L_c^2}\right]}. \tag{4.2}$$

The pressure and density are determined by assuming an isentropic initial flow condition:

$$\rho(\boldsymbol{x}) = \rho_\infty \left[1 - \frac{\gamma - 1}{2} \psi^2(\boldsymbol{x})\right]^{\frac{1}{\gamma - 1}}, \quad p(\boldsymbol{x}) = p_\infty \left(\frac{\rho}{\rho_\infty}\right)^\gamma. \tag{4.3}$$

The subscript '∞' denotes the free-stream condition. The free parameters σ and ϵ in (4.2) determine the size and strength of the vortex. In the following chapters the default parameters are set to $\epsilon = 0.0377$ and $\sigma = 44.25$. This set of parameters results in the largest vertical velocity perturbation to reach 2.5% of the free-stream velocity, i.e. $v_{\max} = 0.025 u_\infty$. The size (diameter) of the vortex is about 16% of the aerofoil chord, defined by the locations where the velocity perturbation drops down to 1% of the maximum value, i.e. $|v(x)|_{y=0} = 0.01 v_{\max}$.

The vortex diameter is reduced from the previous section in order to analyse a larger range of frequencies. Although the previous vortex produces a broadband spectra most of it's energy is contained at low frequencies. In addition, the smaller diameter makes it easier to distinguish secondary source effects such as ABS and TEVS in the acoustic pressure signals, which is the subject of chapter §5. With regards to the shape function, the current vortex provides a spectra

without lobes, which is particularly helpful for identifying interference peaks shown in the following chapters. It is important to note that changing the vortex shape function only has a small effect on the WLE noise reduction spectra, suggesting the previous results are still applicable to the following chapters. Further discussion of the vortex parameters, and their effect on the noise reduction is provided in appendix C.1.

In all cases the vortex is positioned $0.5L_c$ upstream of the aerofoil LE ($x_0 = -1.0L_c$). Simulations are run for 15 non-dimensional time units ($t^* = ta_\infty/L_c = 15$) which sufficiently captures the acoustic pressure signals in all observer directions.

4.2.2 Computational grid and domain

As in the previous chapter the cases presented here are based on semi-infinite chord length, the following chapter which utilises the same grid settings additionally presents finite chord simulations. The total grid cell count is $N_\xi \times N_\eta \times N_\zeta = 1600 \times 960 \times 64 = 98,304,000$ where N_ξ, N_η and N_ζ are the number of cells in the streamwise, vertical and lateral/spanwise directions, respectively. The smallest cells are positioned at the LE and TE where $\Delta \mathrm{x_{min}} = \Delta \mathrm{y_{min}} = 0.002\mathrm{L_c}$ and $\Delta \mathrm{z_{min}} = 0.002083\mathrm{L_c}$. The aerofoil surface (for the finite-chord case) is covered by $N_\xi \times N_\zeta = 400 \times 64 = 25,600$ cells to keep a high resolution across the vortices while they are travelling over the aerofoil. The dense grid is maintained in the far field as well in order to capture the high-frequency components of the radiated acoustic waves. The domain is also extended in the following work so that the noise directivity may be analysed five chord lengths from the aerofoil centre.

$$\left.\begin{aligned} \mathcal{D}_\infty &= \{\boldsymbol{x} \,|\, x/L_c \in [-7, 11],\ y/L_c \in [-7, 7],\ z/L_z \in [-\frac{1}{2}, \frac{1}{2}]\} \\ \mathcal{D}_{\text{physical}} &= \{\boldsymbol{x} \,|\, x/L_c \in [-5, 5],\ y/L_c \in [-5, 5],\ z/L_z \in [-\frac{1}{2}, \frac{1}{2}]\} \\ \mathcal{D}_{\text{sponge}} &= \mathcal{D}_\infty - \mathcal{D}_{\text{physical}} \end{aligned}\right\}, \tag{4.4}$$

The outcome of a grid-dependency test based on a finite-chord aerofoil is provided in figure 4.1. The grid information is given in table 4.1, where level 2 represents the resolution of choice selected for all inviscid simulations in the remainder of the work (unless otherwise stated). It is shown that the resolution levels 2 and 3 produce almost identical acoustic power spectra for both SLE and WLE cases whereas level 1 exhibits noticeable numerical dissipation at high frequencies. Figure 4.1(b) and (d) compare the measured spectra to the background noise level for SLE and WLE cases respectively. The background noise is approximated by convecting the vortex on the same grid without the aerofoil present. For all frequencies the background noise remains at least two orders of magnitude below the physical level, therby confirming that it has no significant influence on the analysis. Acoustic directivity profiles are also presented in figure 4.2 for both low and high frequencies ($f^* = 2$ and 6), which further verifies that levels 2 and 3 are produce sufficiently converged results.

Grid resolution level	N_ξ	N_η	N_ζ	Total	$\Delta x_{min}/L_c$	CPW at $\boldsymbol{x}_o$
Level 1	1280	768	52	51,118,080	0.0024	3.93
Level 2	1600	960	64	98,304,000	0.0020	5.71
Level 3	1760	1056	70	130,099,200	0.0018	6.74

Table 4.1: Three different levels of grid resolution used for the current grid-dependency tests shown in figures 4.1 and 4.2. N_ξ, N_η and N_ζ denote the number of grid cells used in the streamwise, vertical and spanwise directions, respectively. Δx_{min} is the smallest cell size used at LE and TE of the aerofoil. CPW (cells per wavelength) indicates the minimum number of grid cells used across the acoustic wavelength. CPW is measured at the far-field observer location $\boldsymbol{x}_o/L_c = (0, 5, 0)$.

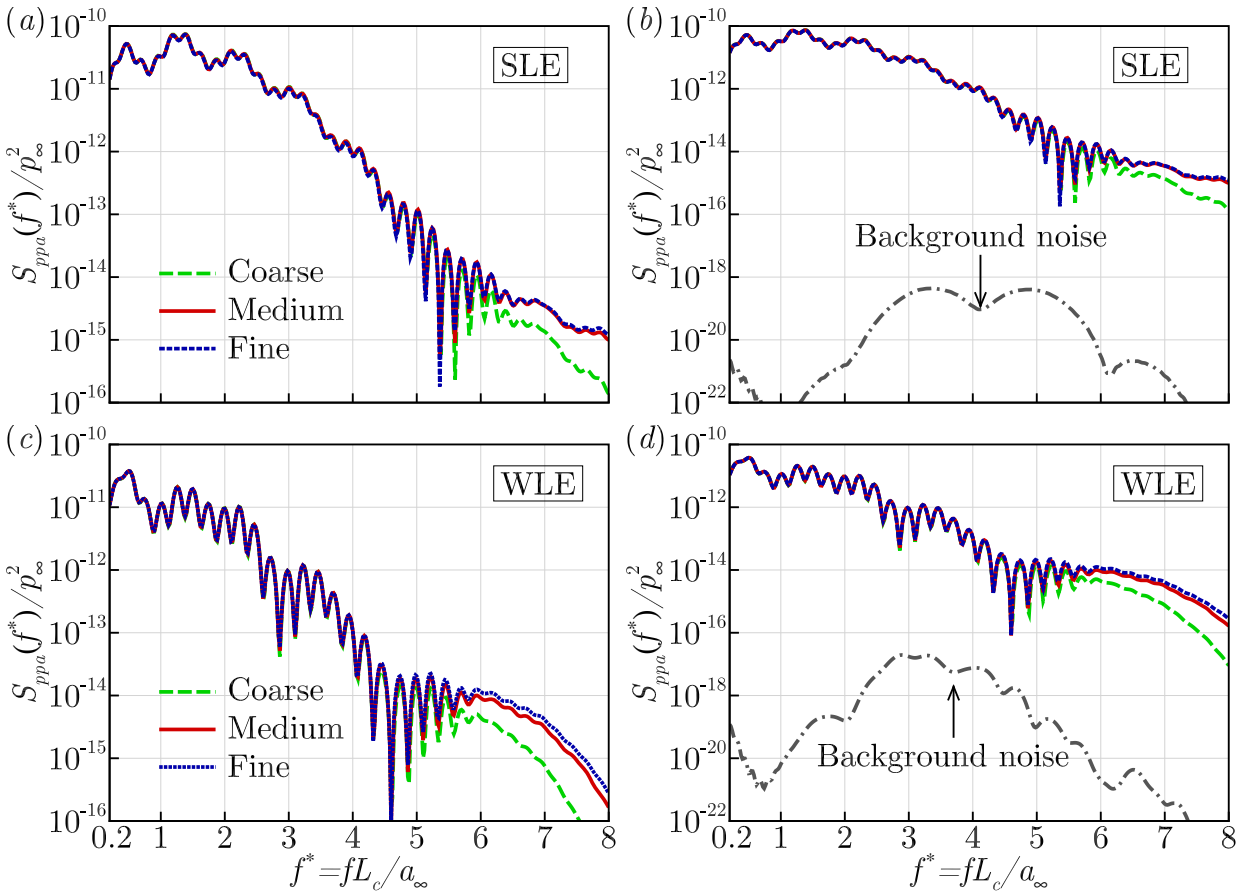

Figure 4.1: Grid-dependency test for the acoustic power spectra obtained at $\boldsymbol{x}_o/L_c = (0, 5, 0)$ based a finite chord aerofoil using three different levels of grid resolution described in table 4.1: (a) SLE; (b) a comparison to the background noise level produced on the SLE grid; (c) WLE $h_{LE}/L_c = 1/15$ and $\lambda_{LE}/L_c = 2/15$; (d) comparison to the background noise level produced on the WLE grid.

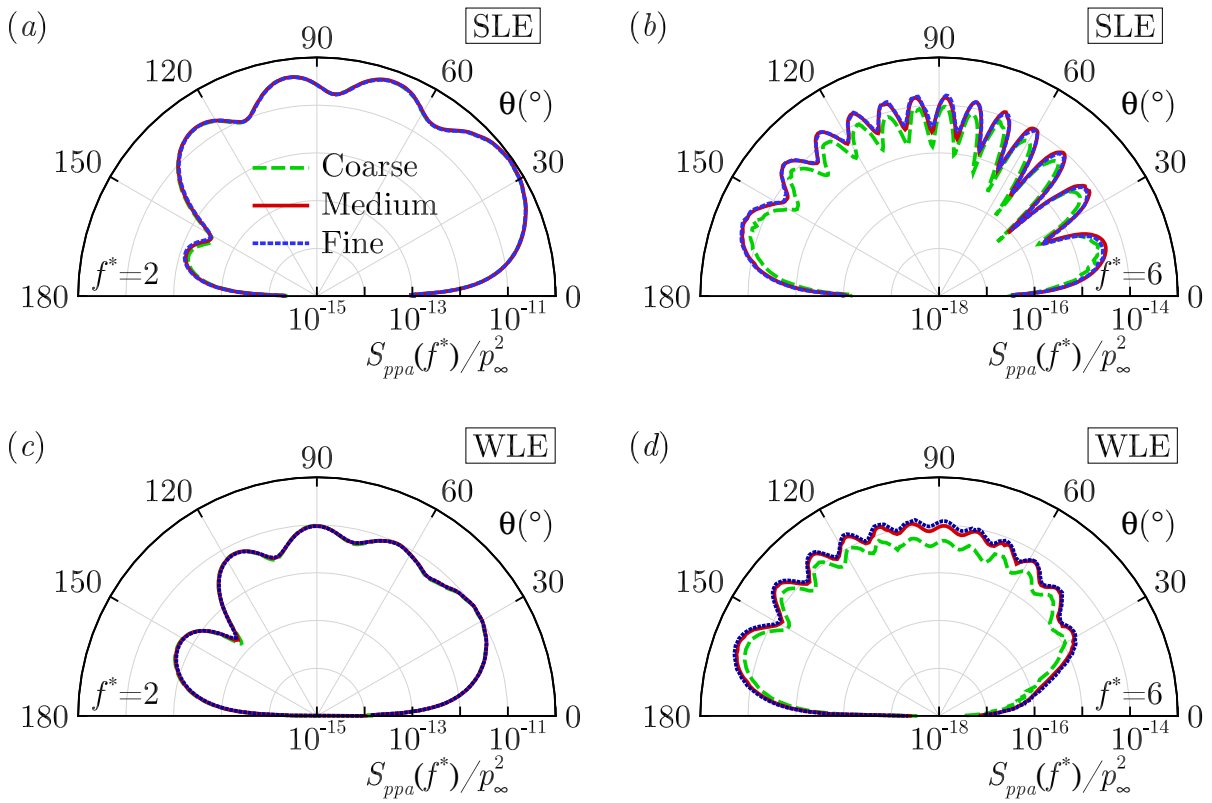

Figure 4.2: Grid dependence test for the acoustic directivity based a finite chord aerofoil. (a) and (b) SLE $f^* = 2$ and 6. (c) and (d) WLE ($h_{LE}/L_c = 1/15$ and $\lambda_{LE}/L_c = 2/15$) $f^* = 2$ and 6.

In addition to the grid dependency study, the maximum feasible length of the simulation is estimated by running an additional simulation of a stationary vortex on the skewed grid (WLE case). The simulation is run with no flow for 30 non-dimensional time units with the vortex is initialised at $x_0 = -0.5L_c$ on the $AR_{LE} = 1$ WLE grid (the location of maximum grid skewness). Figure 4.3(a) shows the vertical velocity profile of the vortex taken at the mid-span at times $t^* = 0, 6, 15, 21$ and 30, while figure 4.3(b) shows the corresponding wavenumber spectrum calculated in the x-direction (based on the spatial equivalent of (2.60)). For reference $kL_c = 157$ corresponds to a normalised frequency $f^* = 6$ for $u_\infty = 0.24$. The solution remains consistent until approximately $t^* = 24$, where errors begin to accumulate at high wavenumbers. In the current work the vortex reaches the aerofoil TE at approximately $t^* = 6$, and the maximum simulation times are $t* = 15$ and 20 for inviscid and viscous cases respectively. This therefore confirms that the skewed grid near the LE (for wavy cases) does not introduce significant errors during the simulations.

4.3 Observed noise reduction trends

Figure 4.4 shows the acoustic pressure data at an observer $\boldsymbol{x} = (0, 5L_c, 0)$ for SLE and three WLE geometries with amplitudes $h_{LE}/L_c = 1/20$, $1/15$ and $1/10$. This figure demonstrates the aforementioned trends associated with the WLE, identifying the key questions we aim to answer

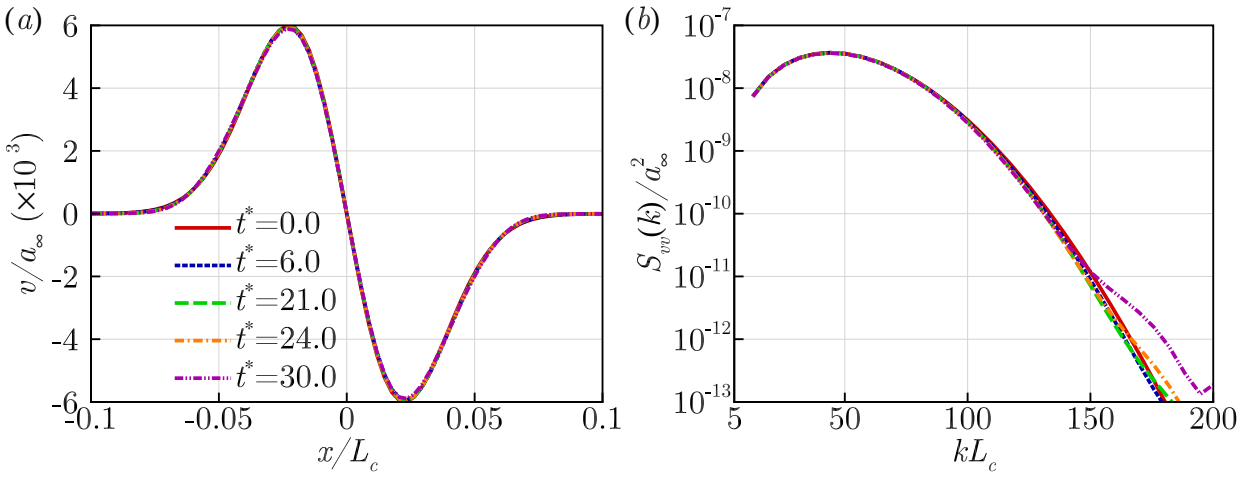

Figure 4.3: (a) Vertical velocity profile produced by stationary vortex in the centre of the skewed grid (aerofoil LE) at various times. (b) Corresponding wavenumber spectrum.

in this chapter. Figure 4.4(a) shows the acoustic pressure time signals, while figure 4.4(b) shows the corresponding PSD. The resulting noise reduction (obtained by subtracting the WLE from the SLE PSD) is shown in figure 4.5(a). The WLE amplitude is typically considered to be the defining parameter for the WLE noise reduction, and it is clear here how it improves the noise reduction for the majority of frequencies.

Meanwhile, figure 4.5(b) shows the noise reduction vs. the Strouhal number calculated from the WLE amplitude and mean flow speed fh_{LE}/U_∞. This clearly demonstrates the approximately linear increase of noise reduction with frequency, which highlights the first main question of this chapter. The collapse of the noise reduction curves to the linear trend line $10\log_{10}(10fh_{LE}/U_\infty)$ (Chaitanya *et al.*, 2017) highlights the importance of destructive interference for the noise reduction. For the current spanwise uniform flow condition the phase difference at a far-field observer for sound emitted by two source locations can be approximated by:

$$\phi_{A|B} = 2\pi f \left[\frac{\boldsymbol{x}_A - \boldsymbol{x}_B}{u_\infty} + r(\boldsymbol{x}_A) - r(\boldsymbol{x}_B)\right] \tag{4.5}$$

where r is the distance to the observer. It is worth noting how the noise reduction minima/maxima occur at almost exact intervals of $\Delta f^* = nU_\infty/4h_{LE}$ ($\Delta f^* h_{LE}/U_\infty = n/4$), which according to (4.5) approximates a peak-root $n\pi$ phase shift. Contrasting figure 4.5(a) and (b) it is clear that for a given dimensional frequency the noise reduction offered by a larger amplitude WLE is usually greater, however corresponding destructive interference peaks are smaller. It is therefore likely that WLE amplitude increases the noise reduction by forcing destructive interference to begin earlier, effectively shifting the spectra to the left as shown in figure 4.5(a). An explanation for the reduced interference peaks with larger amplitude may be due to the variation of source strength along the LE. Typically a larger amplitude WLE will have greatly reduced strength near the WLE hill and peak regions due to oblique cut-off and streamwise vortex effects respectively Kim *et al.* (2016); Turner & Kim (2017*b*). This disparity in strength along the span (in contrast with small amplitude WLEs which will be almost uniform) will result in less complete interference. In this

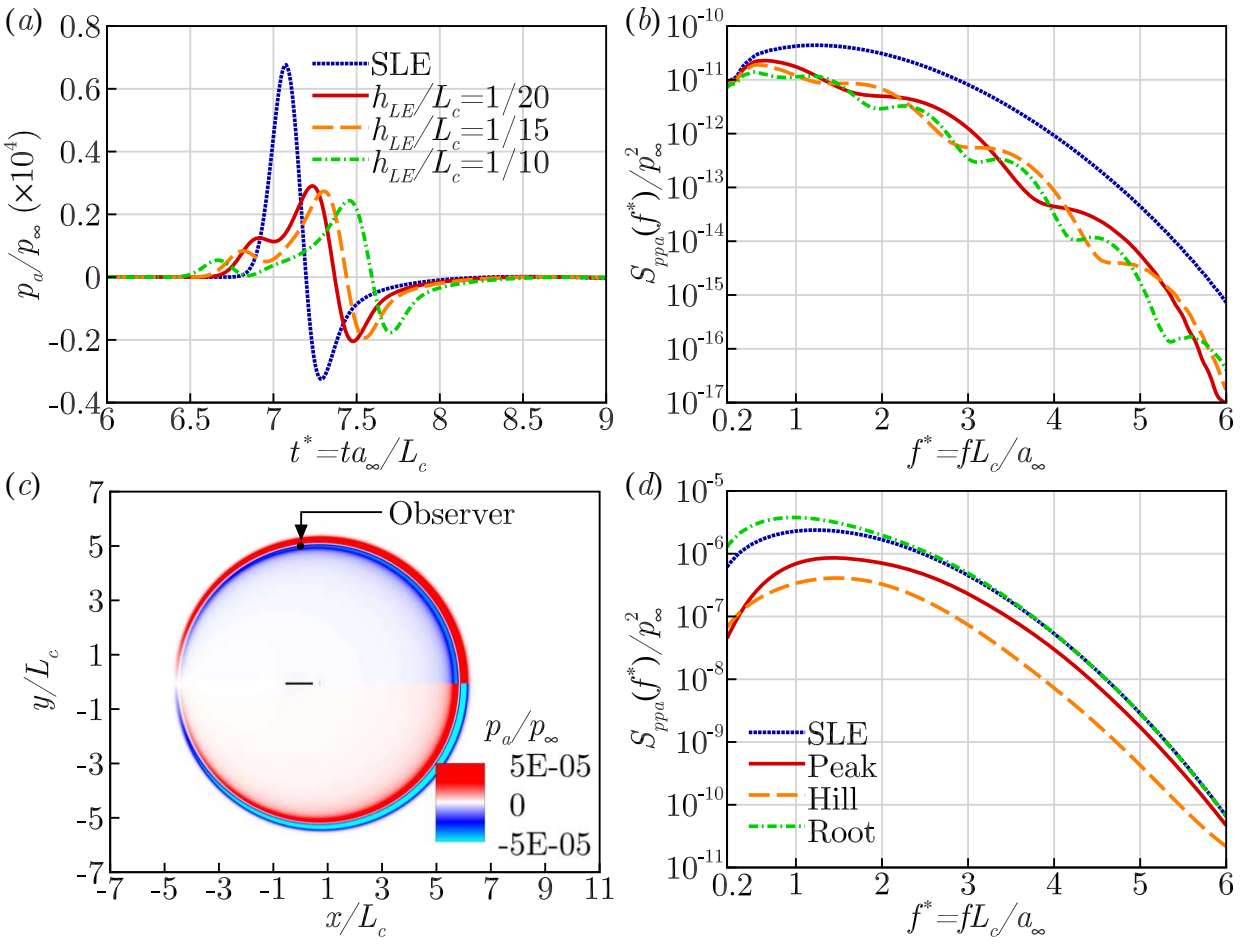

Figure 4.4: Acoustic pressure data obtained at observer $\boldsymbol{x}_o/L_c = (0, 5, 0)$ for SLE and three WLE geometries with differing amplitude (h_{LE}/L_c = 1/20, 1/15 & 1/10, λ/L_c = 2/15). (a) time signals of $p_a(\boldsymbol{x}_o, t)/p_\infty$; (b) the corresponding power spectra; (c) an instantaneous contour plot of $p_a(\boldsymbol{x}_o, t^* = 7.34)/p_\infty$ taken at mid-span ($z = 0$) for the SLE case; and, (d) LE source strength (wall power spectra) for the SLE, WLE Peak, Hill centre and Root, taken one grid point downstream of the LE with $h_{LE}/L_c = 1/15$.

chapter we show that both destructive interference and reduced source strength contribute to the noise reduction when considered individually. However in relativity they are coupled and to some extent may contradict each other as proposed here. Similar conclusions are also drawn for the LE wavelength in Appendix C.2.

The next most prominent trend in literature concerns the WLE source characteristics. Figure 4.4(d) shows the surface pressure spectra obtained one point aft of the LE for SLE and WLE peak, hill and root (default amplitude $h_{LE}/L_c = 1/15$). There is significant source strength reduction obtained by the WLE hill throughout the frequency range. As previously discussed the source strength reduction increases proportionally with WLE aspect ratio (or amplitude for a fixed λ_{LE}) (Turner & Kim, 2017*b*). Source reduction therefore represents the other possible noise reduction mechanism responsible for the linear noise reduction trend in addition to destructive interference. However, questions arise regarding the low frequency source reductions of the peak and hill, which are not echoed in the far-field spectra. The confusion comes from only considering the source along

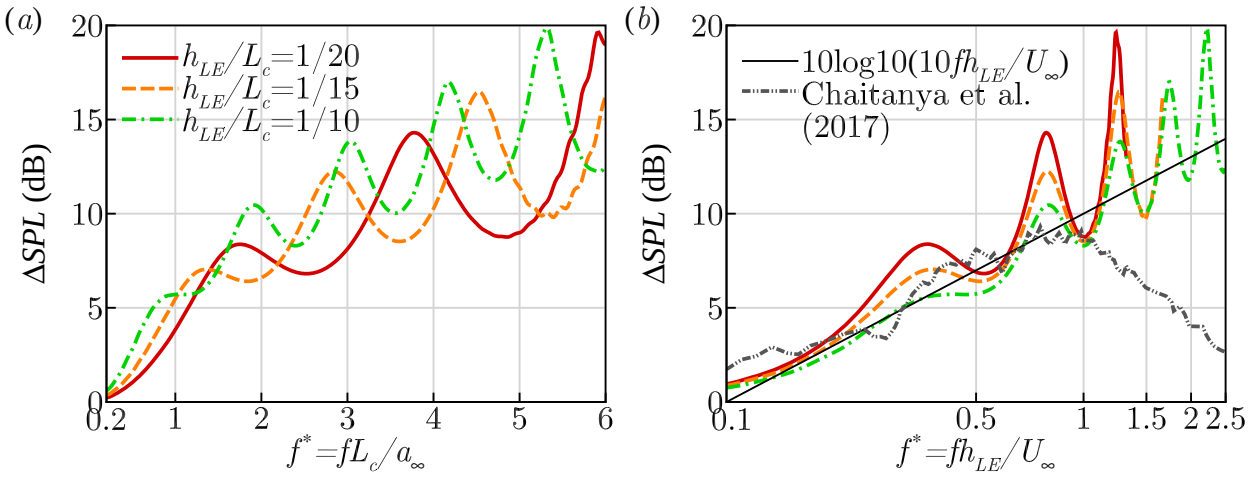

Figure 4.5: (*a*) Noise reduction spectra ($\Delta SPL(\boldsymbol{x}_o, f^*_{h_{LE}})$) obtained for the three WLE amplitudes at observer $\boldsymbol{x}_o/L_c = (0, 5, 0)$. (*b*) Noise reduction re-plot vs Strouhal number (based on WLE amplitude) $f^* = fh_{LE}/U_\infty$ demonstrating the linear trend in question. Comparison is also made to the experimental data obtained by Chaitanya *et al.* (2017) for $h_{LE}/L_c = 1/10$ at the optimum wavelength $\lambda/\Lambda = 4$.

the leading edge. In this chapter we show that if the source area is considered, the percentage of the surface with similar strength is comparable at low frequencies.

4.4 One-dimensional modelling of the leading edge

4.4.1 Effective source length

In this we aim to investigate the speculations made by Chaitanya *et al.* (2017), regarding the root source length theory for the linear noise reduction trend. The basis for this theory is that the root represents the dominant portion of the WLE source and radiates with similar strength to the SLE baseline. This has been observed for both synthetic turbulence and spanwise vortex flows (Kim *et al.*, 2016; Turner & Kim, 2017*b*). If the root region may be considered to be the only significant radiator of sound then, it follows that $\Delta SPL \sim L_z/\mathcal{L}(f)$ where L_z is the SLE span, and $\mathcal{L}$ represents the effective root source length. It is speculated that $\mathcal{L}$ should scale linearly with the hydrodynamic wavelength (U/f) interacting with the root, and therefore is inversely proportional to the frequency. To validate this theory the WLE source length is approximated from the numerical data as follows:

$$\mathcal{L} = \mathcal{L}_{peak} + \mathcal{L}_{root} = \int_0^{\lambda_{LE}/2} \frac{S^{WLE}_{ppw}(x_{LE}, z, f^*)}{S^{SLE}_{ppw}(-0.5L_c, f^*)} dz + \int_{-\lambda_{LE}/2}^{0} \frac{S^{WLE}_{ppw}(x_{LE}, z, f^*)}{S^{SLE}_{ppw}(-0.5L_c, f^*)} \mathrm{d}z \tag{4.6}$$

Figure 4.6 shows the calculated effective root and peak source lengths as a function of frequency compared to the expected source length. The expected length is calculated as the ratio of WLE to SLE far-field sound spectra:

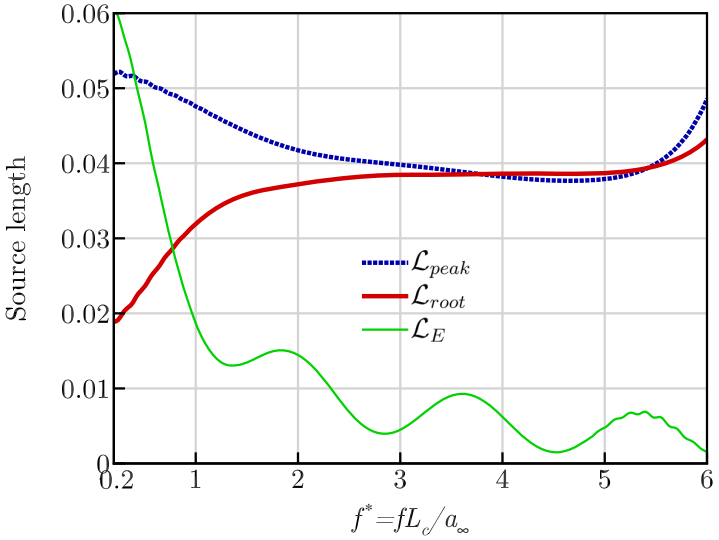

Figure 4.6: Effective source edge lengths $\mathcal{L}$ (peak and root regions) as predicted by (4.6). For comparison the change in length required to constitute the far field noise reduction is also included as $(S_{ppa}^{WLE}/S_{ppa}^{SLE})\mathcal{L}(f^*=0)$.

$$\mathcal{L}_E = \frac{\lambda_{LE}}{2}\frac{Spp_a^{WLE}(\boldsymbol{x}, f^*)}{Spp_a^{SLE}(\boldsymbol{x}, f^*)} \tag{4.7}$$

(4.7) is scaled by $\lambda_{LE}/2$, which represents the source length of either the peak or root region when the strength is the same as the SLE. Although the root source length decreases with frequency in an approximately linear fashion, the rate of change is insufficient when compared to the expected source length. Furthermore, as frequency is increased the effective peak source length actually increases rapidly. This is expected from figure 4.4(d) which shows the peak source strength begins to approach that of the root for high frequency. It is therefore unlikely that effective LE source length is the primary noise reduction mechanism, however it may play a secondary role which contributes to the noise reduction-frequency trend.

4.4.2 LE phase interference modelling

In this section a semi-analytical model for the noise reduction of the WLE is introduced in order to gain insight into the contribution of LE phase on the noise reduction vs. frequency relationship. The model takes inspiration from the work of Chaitanya *et al.* (2017) who considered the integrated LE phase-shift along one cycle of the WLE. In addition to the LE phase we consider the LE source strength variation, the retarded time caused by varying effective acoustic distance in span, the WLE arc length, and the influence of the simulation infinite span caused by the lateral periodic boundary condition. Firstly, assuming that the aerofoil aeroacoustic source is concentrated at the LE, we consider a single frequency sinusoidal response from a single element of the LE arc. (The validity of this assumption is investigated in detail in §4.5.):

$$p_{LE} = p_m(\theta) sin\left[2\pi f\left(t - \frac{h_{LE}\sin(\theta)}{U_\infty}\right)\right] \tag{4.8}$$

where p_m is the pressure based source strength of the element, and $2\pi f h_{LE}\sin(\theta)/U_\infty$ is the spanwise LE phase-shift caused by convection of the vortex with the mean flow. Assuming the signals originating along the LE are coherent, the total far field response is then modelled by integrating (4.8) along the LE curve:

$$F(x_o, y_o, f, t) = \int_C \frac{p_m(\theta)}{r} \sin\left[2\pi f\left(\tau(\mathbf{x}) - \frac{h_{LE}\sin(\theta)}{U_\infty}\right)\right] \mathrm{d}l \tag{4.9}$$

where $\mathrm{d}l = \sqrt{1 + (\mathrm{d}x/\mathrm{d}z)^2}\mathrm{d}z$ indicates integration along the LE arc length, $\theta = 2\pi z/\lambda$ is the phase of the sinusoidal LE geometry, and $\tau(\boldsymbol{x}) = t - \Delta t_o(\boldsymbol{x})$ is the retarded time due to radiation of the sound in a mean flow, with $\Delta t_o(\boldsymbol{x})$ given by Garrick & Watkins (1953):

$$\Delta \mathrm{t_o}(\boldsymbol{x}) = \frac{\mathrm{M_\infty(x - x_o)} + \sqrt{\mathrm{M_\infty^2(x - x_o)^2} + (1 - \mathrm{M_\infty^2})|\boldsymbol{x} - \boldsymbol{x}_\mathrm{o}|^2}}{\mathrm{a_\infty}(1 - \mathrm{M_\infty^2})}. \tag{4.10}$$

Spherical radiation of the propagating acoustic waves from each LE element is considered via the $1/r$ term in (4.9), where $r = \Delta \mathrm{t_o}(\boldsymbol{x})/\mathrm{a_\infty}$. Finally substituting for $\mathrm{d}l = \sqrt{(\mathrm{d}x/\mathrm{d}\theta)^2 + (\mathrm{d}z/\mathrm{d}\theta)^2}\mathrm{d}\theta$ in (4.9) allows the integral to be expressed in terms of θ, then evaluated over m cycles:

$$F(x_o, y_o, f, t) = \int_{-m\pi}^{m\pi} \frac{p_m(\theta)}{r} \sin\left[2\pi f\left(t - \Delta \mathrm{t_o}(\theta) - \frac{\mathrm{h_{LE}}\sin(\theta)}{\mathrm{U_\infty}}\right)\right] \sqrt{h_{LE}^2\cos^2(\theta) + \left(\frac{\lambda_{LE}}{2\pi}\right)^2}\mathrm{d}\theta \tag{4.11}$$

The current results are based on $m = 15$ LE cycles, although it was found that this parameter has little to no influence on the result. Since F represents the pressure time response for a given frequency, the noise reduction spectra can be approximated by simply calculating the relative difference between the maximum values in time obtained by both SLE and WLE cases, resulting in the following:

$$\Delta SPL(x_o, y_o, f) = 20\log_{10}\left(\frac{\max_i[F_{SLE}(x_o, y_o, f, t_i)]}{\max_i[F_{WLE}(x_o, y_o, f, t_i)]}\right) \tag{4.12}$$

There are a number of simplifications made in the derivation of (4.12). This includes: coherent LE excitation, source concentrated at the LE, and that the disturbance is parallel to the SLE. Figure 4.7(a) shows a comparison between the numerically predicted noise reduction spectra for $h_{LE}/L_c = 1/15$, and that predicted by (4.11) based on different expressions for the LE source term ($p_m(\theta)$). Three models for the source strength are considered with increasing complexity. The

simplest, Model **A**, utilises $p_m = 1$, and therefore only considers the LE phase shift and retarded time effects.

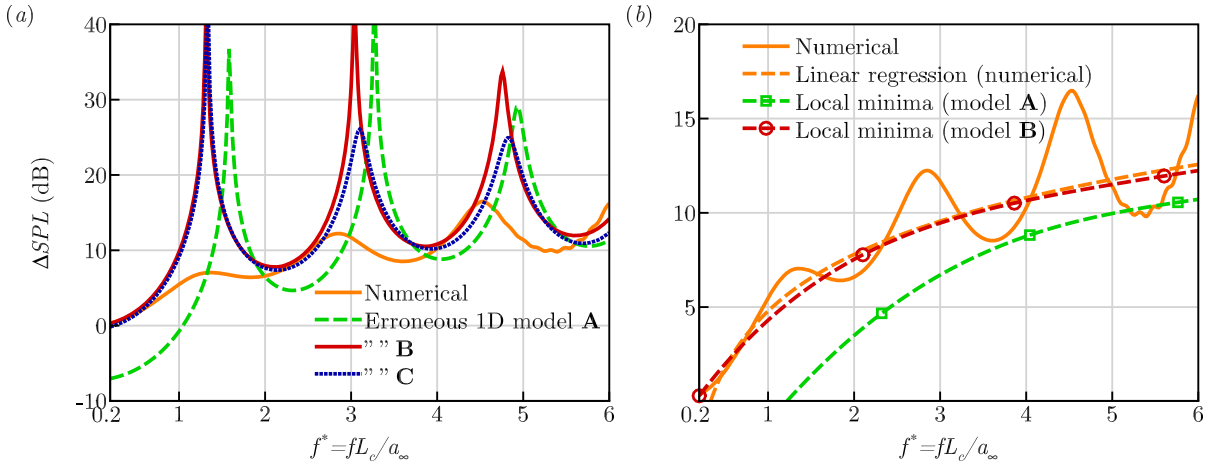

Figure 4.7: (a) Comparison between numerical noise reduction spectra ($\Delta SPL(\boldsymbol{x}_o, f^*)$) and that predicted by the erroneous 1D semi-analytical model of (4.12). Models **A**-**C** provide different representations of the LE source characteristics. **A**: constant source along the edge (equivalent to SLE). **B**: cosine of local sweep angle ($\cos(\Phi)$). **C**: realistic phase and source obtained from numerical data. For all cases the WLE geometry is constant at $h_{LE}/L_c = 1/15$ and $\lambda/L_c = 2/15$.

The accuracy of this model is fairly poor, the local maximums represent large overshoots and are offset in frequency from those obtained by the numerical result. Moreover at low frequency a negative noise reduction is predicted, which contradicts previous experimental observations Chaitanya *et al.* (2017). We note here that low frequency under prediction is also observed by the Amiet approach adopted by Lyu & Azarpeyvand (2017). This is a consequence of the increased edge length for the WLE case, which especially influences the low frequencies due to the LE elements being relatively in-phase. Figure 4.7(b) compares the local minima of model **A** to the far-field noise reduction. Despite the exaggerated peaks and poor low frequency prediction, the stationary points of model **A** seem to capture the correct noise reduction slope at medium-high frequency.

4.4.3 Influence of realistic source on leading-edge model

An immediate improvement to the LE line model of Figure 4.7 can be made by modelling the variation in source strength along the span. A simple analytical expression for the LE source is to consider the LE sweep angle as suggested by Kim *et al.* (2016). This follows from the the work of Roger & Carao (2010), who showed that the acoustic pressure response due to a aerofoil swept from the mean flow direction follows $\overline{p'} \propto \cos(\Phi)$. $p_m(\theta) = \cos(\Phi)$ is therefore implemented as model **B** in figure 4.7. Inclusion of this simple source term rectifies the low frequency under prediction, and improves the location of the peaks (particularly at low frequencies). Furthermore, comparison between the model stationary points, and a linear regression of the simulation data shows a near perfect agreement.

A more complete description of the source may be implemented by adopting a semi-analytical approach which incorporates data extracted directly from the simulation. The source wall pressure and phase spectra are included as $p_m(\theta) = \sqrt{S_{ppw}(\theta, f)}$ ($S_{ppw} \propto p^2$), and $2\pi f h_{LE} \sin(\theta)/U_\infty = \phi_{ppw}(\boldsymbol{x}_{Hill}, \boldsymbol{x}, f)$ respectively in (4.11). Surprisingly, inclusion of these more realistic terms only offers minor improvements compared to the sweep angle source prediction mainly in terms of reduced magnitude overshoots for medium-high frequency.

An explanation for the improved accuracy of models **B** and **C** at low frequency is made apparent by considering the following:

$$\sqrt{S^{Hill}_{ppw}(\boldsymbol{x}, f^*)} \sim \cos(\Phi) = \cos\left(atan\left(\frac{\mathrm{d}x}{\mathrm{d}z}\right)\right) = \frac{1}{\sqrt{1 + \left(\frac{\mathrm{d}x}{\mathrm{d}z}\right)^2}} = \frac{\mathrm{d}z}{\mathrm{d}l} \tag{4.13}$$

This implies a cancellation effect between the increased edge length of the WLE and the reduced source strength of the hill region. A comparison between the source strength along the span at three frequencies is compared to the cosine sweep angle prediction in figure 4.8(a). The local sweep angle is revealed to accurately predict the source strength near the WLE root and nearby hill region for medium and high frequencies. However, the peak strength is generally over predicted, while the peak adjacent hill region is under predicted. The asymmetry about the hill centre consequently influences the destructive interference mechanism which results in the shifted peaks produced by model **C** relative to **B**. As previously mentioned the source strength reduction at the peak actually conflicts with the destructive interference mechanisms. However, the full impact of this effect is not captured in one-dimension, and therefore requires further investigation in the following section. It should be noted here that the model result is completely independent of WLE wavelength (λ_{LE}). As is shown in Appendix C.2 better agreement for the noise reduction peaks is possible when the wavelength is increase, which is believed to be caused by more compatible peak-root source strengths.

In figure 4.8(b) the LE source ratio is scaled by $\mathrm{d}l/\mathrm{d}z$, revealing the extent of the cancellation between edge length and source strength. Integration of the curves w.r.t. z/λ_{LE} results in values of 1.215, 1.210 and 1.172 for $f^* = 1$, 3 and 5, indicating a near perfect cancellation which improves with frequency. It will be shown in the following section that this turns out to be an erroneous conclusion, reached by imposing that the source is located very close to the LE. In reality the aerofoil surface is two-dimensional, and the radiation area for SLE and WLE cases is equivalent. Therefore the loss of noise reduction at low frequency must be caused by noise increase regions aft of the LE. Consequently this chapter highlights the danger of neglecting the complex source characteristics when describing the physical mechanisms of noise reduction, although doing so may yield reasonable predictions.

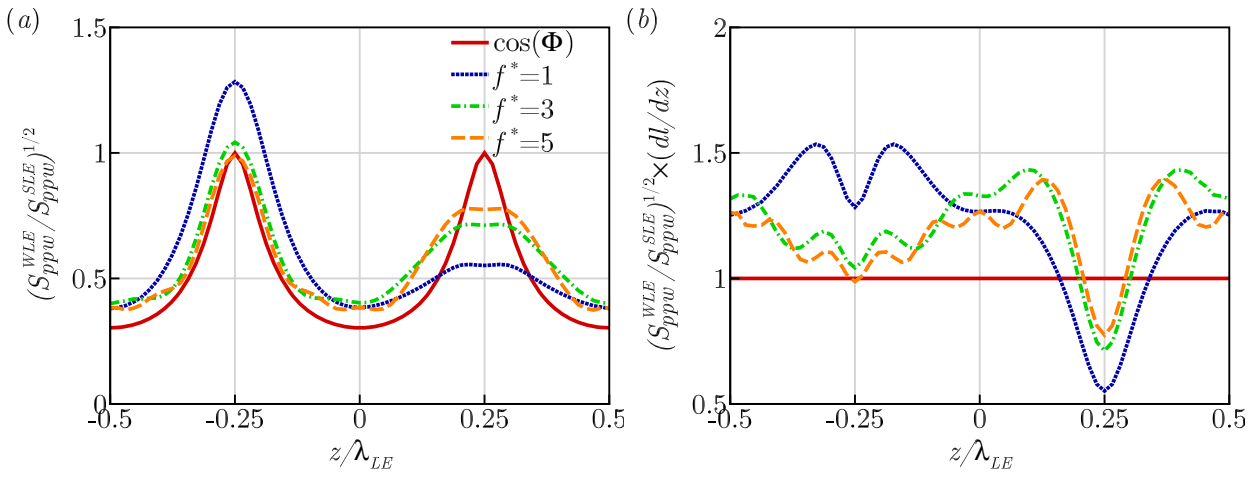

Figure 4.8: (a) WLE-SLE source strength ratio at three selected frequencies $f^* = 1$, 3 and 5, compared to the cosine of the local LE sweep angle Φ. (b) Source strength ratio scaled by dl/dz

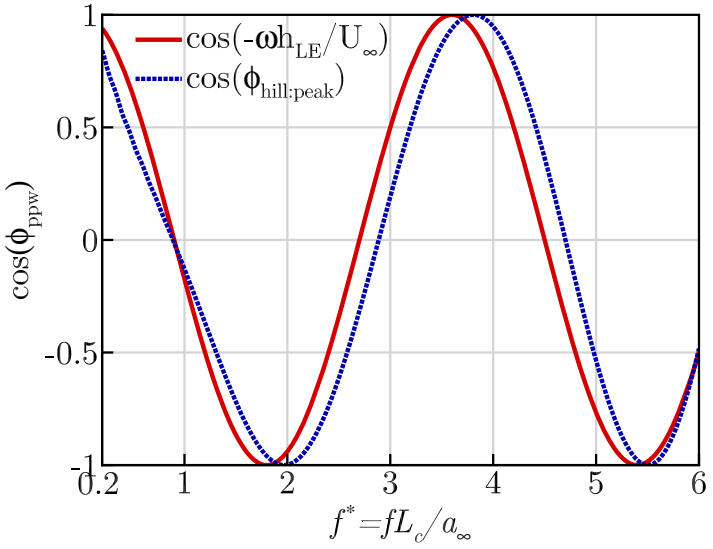

Figure 4.9: Comparison of numerical and modelled two-point phase spectra taken between LE hill and peak.

4.5 Consideration of distributed source

4.5.1 Surface source distribution

Figure 4.10 and 4.11 show the wall pressure spectra distribution over the aerofoil surface for SLE and WLE cases at frequencies 0.2, 1, and 4, 6 respectively. The results are plot in decibel scale, as $SPL = 10\log_{10}(Sppw/p_{ref}^2)$, where $p_ref = 2 \times 10^5$ Pa. At the lowest frequency ($f^* = 0.2$) the source is highly concentrated near the leading edge, and rapidly reduces downstream. This agrees with observations made by Kim *et al.* (2016) regarding the RMS surface pressure distribution. At a more moderate frequency of $f^* = 1$ the source is more spread in the streamwise direction. It

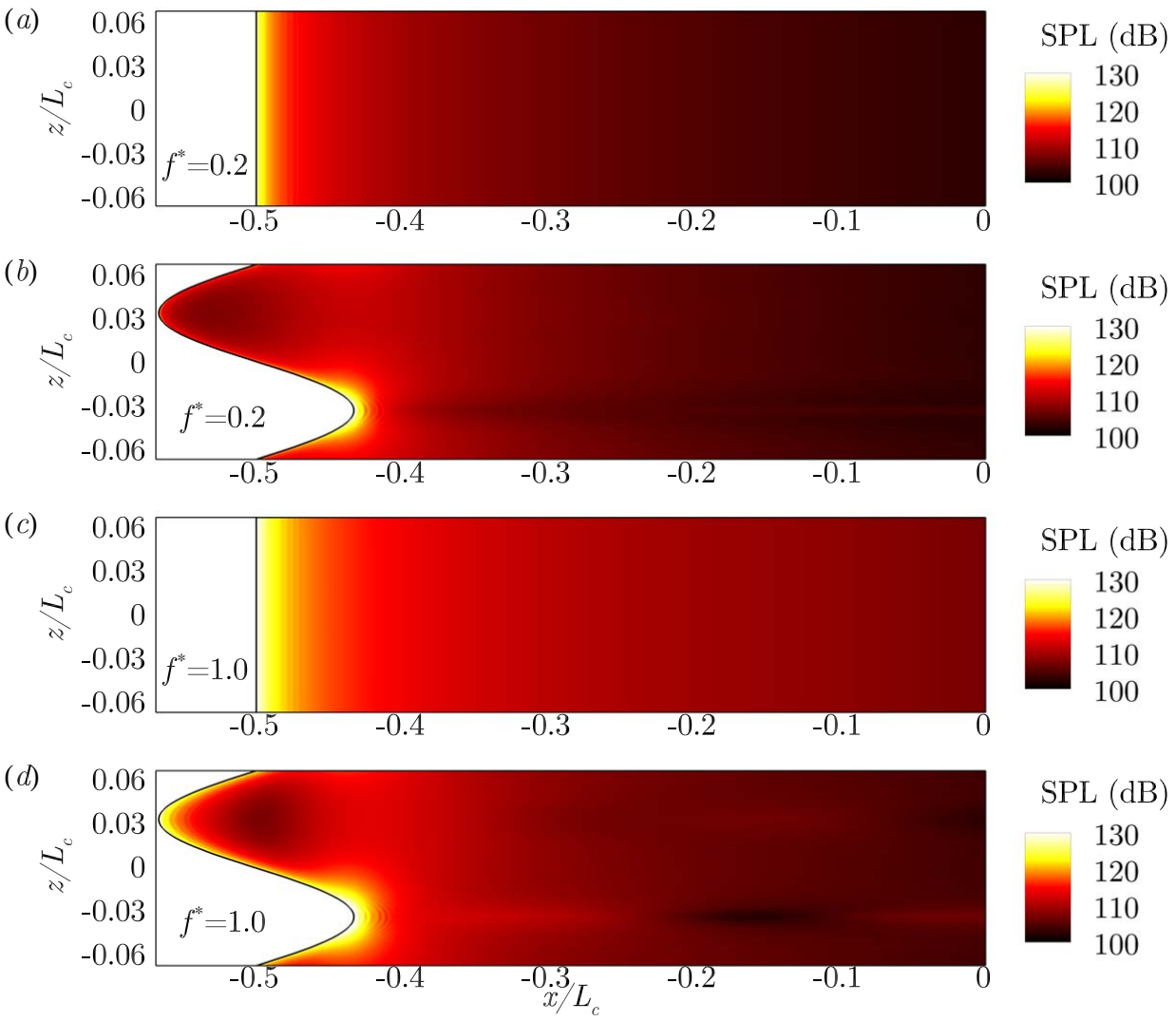

Figure 4.10: Surface source strength distribution $S_{ppw}(x, z, f^*)$ for SLE and WLE geometries plot as SPL (dB scale). (a) SLE $f^* = 0.2$; (b) WLE $f^* = 0.2$; (c) SLE $f^* = 1$; (d) WLE $f^* = 1$.

was also noted by Agrawal & Sharma (2016) that the source was radiated from a surprisingly large portion of the surface for $f^* = 0.456$ and 0.84. For the WLE case there is also significant spread of the high intensity source near the LE root. Table 4.2 shows the percentage of the aerofoil surface (within $1L_c$ of the LE) radiating noise within various magnitude bandwidths at four frequencies, $f^* = 0.2$, 1, 4 and 6. Despite the reduced low frequency source strength on the LE line (figure 4.4), the total surface percentage within each magnitude bandwidth is almost the same for SLE and WLE cases at $f^* = 0.2$. It is worth noting that each magnitude bandwidth is 10 times weaker than the previous but possesses approximately 10 times more surface area, and therefore contributes comparably to the radiated sound. It is therefore reasonable to conclude that the lack of WLE noise reduction at low frequency occurs due to the source characteristics being comparable over the full surface, albeit modified very locally at the LE.

At high frequency ($f^* = 4$) the SLE exhibits moderate-high source strength over the majority of the

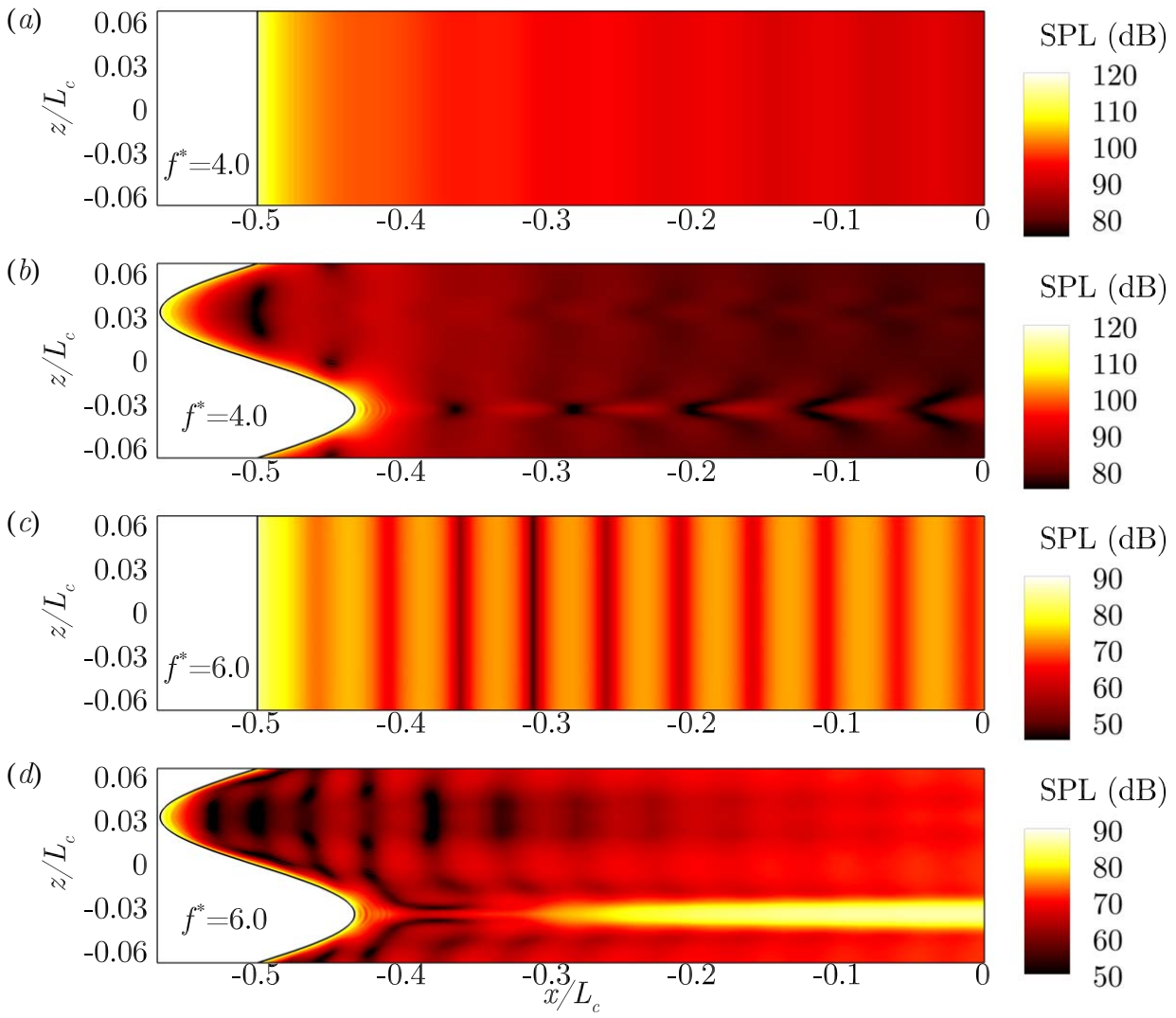

Figure 4.11: Surface source strength distribution $S_{ppw}(x, z, f^*)$ for SLE and WLE geometries plot as SPL (dB scale). (a) SLE $f^* = 4$; (b) WLE $f^* = 4$; (c) SLE $f^* = 6$; (d) WLE $f^* = 6$.

surface. Comparatively the WLE source is still concentrated near the LE, highlighting the source reduction mechanism and how it becomes more prominent with frequency. This is also highlighted by table 4.2, which shows the majority of the WLE aerofoil surface is contained within a smaller magnitude band than the SLE case. There are also different patterns observed downstream of the leading edge root, which alternate between high and low strength in the streamwise direction. The author speculates that these patterns are related to the propagation of secondary vorticity over the aerofoil surface which results in a small pressure jump as it propagates downstream. The generation of the secondary vorticity is discussed in detail in Turner & Kim (2017*b*), and its influence on the high frequency noise is demonstrated in Turner & Kim (2017*a*) and the following chapter.

The unusual observations made at $f^* = 4$ are even more prominent at $f^* = 6$. For the SLE aerofoil the wall pressure spectra over the majority of the surface remains within approximately 20 dB of the LE maximum. For both cases the downstream source regions associated with secondary

Geometry	f^*	$SPL \geq 120$	$110 \leq SPL < 120$	$100 \leq SPL < 110$	$SPL < 100$
SLE	0.2	0.800	9.32	89.5	0.38
WLE	0.2	0.720	12.1	84.3	2.88
SLE	1	2.41	22.1	75.0	0.490
WLE	1	0.891	13.2	81.9	4.01
		$SPL \geq 110$	$100 \leq SPL < 110$	$90 \leq SPL < 100$	$SPL < 90$
SLE	4	0.400	4.67	56.6	38.3
WLE	4	0.0438	0.962	2.67	96.3
		$SPL \geq 80$	$70 \leq SPL < 80$	$60 \leq SPL < 70$	$SPL < 60$
SLE	6	0.804	55.8	30.2	13.2
WLE	6	5.90	53.1	27.2	13.8

Table 4.2: Percentage of source surface area satisfying various magnitude constraints at frequencies $f^* = 0.2$, 1, 4 and 6. Only the first $1L_c$ of the surface is considered.

vorticity convection are apparent. In particular the WLE aerofoil possesses a streamwise strip downstream of the root which represents the maximum strength region. At this frequency table 4.2 shows the strongest source magnitude bandwidth contains a larger surface area for the WLE than the SLE, while the lower magnitude bandwidths contain similar area proportions. Therefore implies any noise reduction at this frequency must be generated by destructive interference.

In order to verify that the unusual surface spectra patterns observed at high frequencies are not artefacts of the grid the WLE simulation is repeated with a finer surface mesh. The new grid consists of $1920 \times 960 \times 128 = 236M$ grid cells which represents a factor 1.5 refinement in the streamwise direction over the surface of the flat plate, and a factor 2 refinement in the spanwise direction. The minimum spacings at the LE and TE are also reduced to $\Delta x_{min} = \Delta y_{min} = 0.0015L_c$. A comparison of the wall pressure spectra distribution obtained by the baseline and refined grids is shown for $f^* = 4$ and 6 in 4.12. Overall there is good agreement between the baseline and refined solutions at both frequencies. The two grid levels obtain nearly identical patterns at the lower frequency, while at the higher frequency the finer grid obtains a slightly smoother distribution particularly in regions with low source strength. The key feature (high strength streak downstream of the root) is present at both levels with only subtle magnitude differences. Based on these findings it is reasonable to conclude that the downstream sources are not artefacts of poor grid resolution.

The above analysis is repeated in figure 4.13 and table 4.3 for the maximum noise reduction frequencies ($f^* = 1.32$, 3.04 and 4.76) of the LE line model described in §4.4 (model **B**). In all three cases there are contributions made to the source away from the LE line. For the lowest frequency case the second magnitude band has similar significance to the upper band by containing approximately 10 times more surface area despite reduced magnitude. This band mainly includes the region located laterally from the root. This region is highlighted more clearly for the second frequency peak ($f^* = 3.04$) which generally shows similar results. Meanwhile for the third peak, downstream contributions start to gain some significance.

The previous discussions highlight that in order to progress further it is important to verify exactly what extent of the aerofoil surface is required to correctly predict the far-field noise reduction. To this end, a Ffowcs-Williams and Hawkings (FW-H) propagation solver based on the Farassat 1A

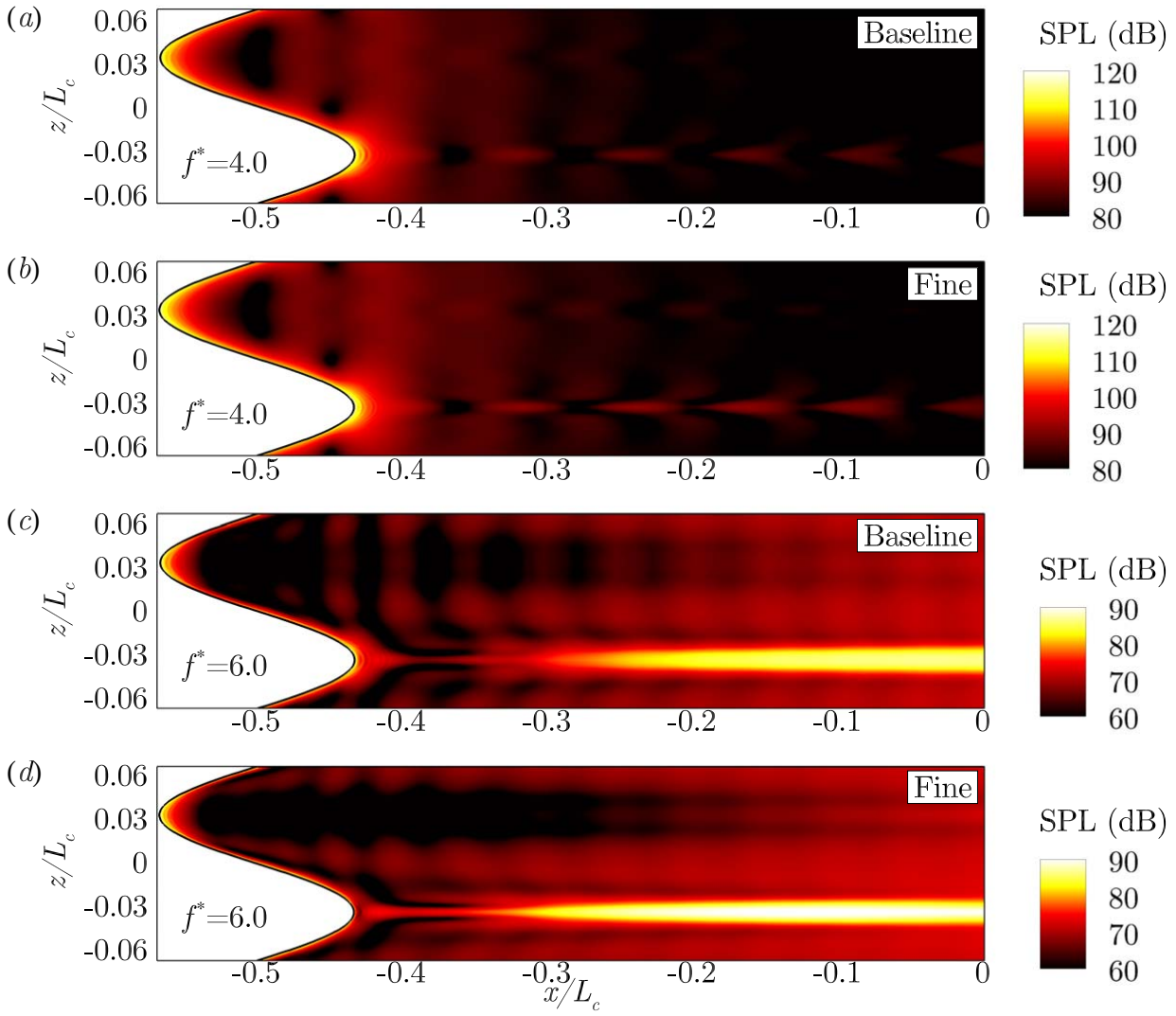

Figure 4.12: Comparison of wall pressure spectra distribution ($S_{ppw}(x, z, f^*)$) plot as SPL (dB scale) obtained by baseline and refined grids. (a-b) $f^* = 4$; (c-d) $f = 6$. The refined grid contains $1920 \times 960 \times 128 = 236M$ grid cells (factor 1.5 refinement in the streamwise directions, and factor 2 in span).

Geometry	f^*	$SPL \geq 120$	$110 \leq SPL < 120$	$100 \leq SPL < 110$	$SPL < 100$
SLE	1.32	2.41	24.8	72.8	0
WLE	1.32	0.838	8.9	53.8	36.5
SLE	3.04	0.400	4.04	42.9	52.7
WLE	3.04	0.0250	0.951	4.38	94.6
		$SPL \geq 100$	$90 \leq SPL < 100$	$80 \leq SPL < 90$	$SPL < 80$
SLE	4.76	0.600	7.38	64.9	27.1
WLE	4.76	0.0500	0.953	7.35	91.6

Table 4.3: Percentage of source surface area satisfying various magnitude constraints at frequencies $f^* = 1.26, 3.04, 4.76$. Only the first $1L_c$ of the surface is considered.

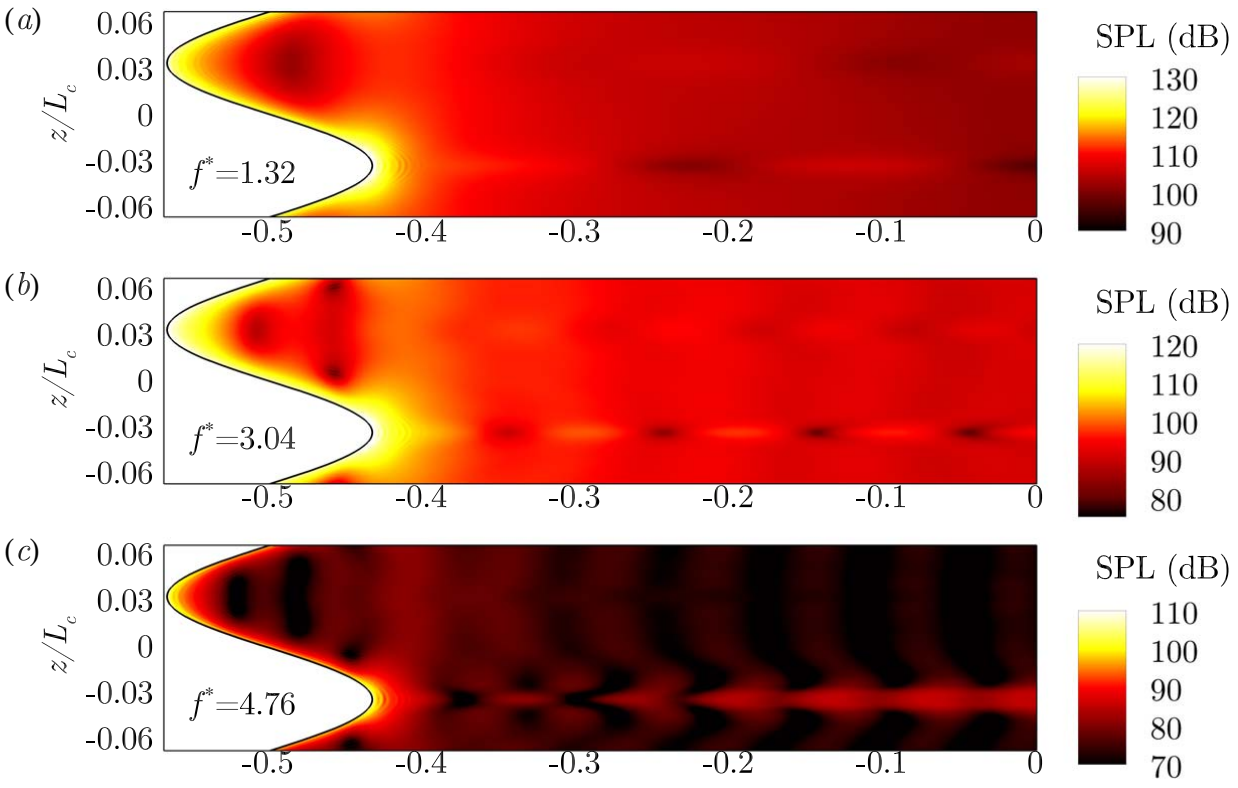

Figure 4.13: Surface source strength distribution $S_{ppw}(x, z, f^*)2$ for WLE geometry plot as SPL (dB scale) at the maximum interference frequencies of the LE line model. (a) $f^* = 1.32$; (b) $f^* = 3.04$; (c) $f^* = 4.76$.

formulation is implemented taking the aerofoil geometry as the integration surface (Farassat, 2007; Ffowcs Williams & Hawkings, 1969):

$$4\pi p_a(\boldsymbol{x}, t) = \int \left[\frac{\dot{p}\cos(\theta)}{cr(1-M_r)^2} + \frac{p\cos(\theta)}{r^2(1-M_r)^2} + \frac{(M_r - M^2)p\cos(\theta)}{r^2(1-M_r)^3} \right]_{ret} \mathrm{d}S \qquad (4.14)$$

where subscript ret indicates variables are analysed at the retarded time, dotted variables indicate the time derivative, $M_r = \mathbf{M} \cdot \hat{\mathbf{r}}$ and r is the acoustic distance. The periodic boundary condition is accounted for by performing the surface integral iteratively in span, typically around 200 span lengths are required to reach the converged solution. Figure 4.14 compares the predicted far-field acoustic pressure time signals and spectra for SLE and WLE cases to that obtained by the implemented FW-H solver. There is good agreement for both cases throughout the desired frequency range.

In the current procedure we incrementally increase the surface integral region as described by the schematic diagram in figure 4.15(a). The various FW-H predictions are shown in figure 4.15(b)-(e). Additionally the one-to-one source strength difference based on (4.15) is shown for frequencies $f^* = 0.2$, 1, 4 and 6 in figure 4.16.

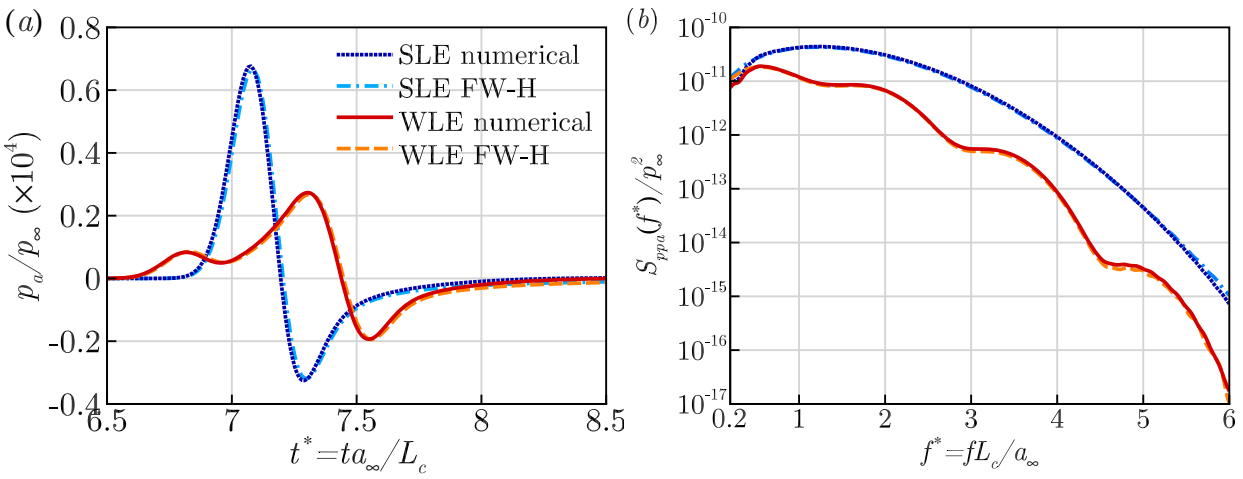

Figure 4.14: Validation of FW-H solver for predicted (a) far field acoustic pressure for SLE and WLE cases; (b) corresponding power spectra.

$$\Delta S_{ppw}(x,z,f^*) = 10\log_{10}\left(\frac{S_{ppw}^{SLE}(x,z,f^*)}{S_{ppw}^{WLE}(x,z,f^*)}\right) \tag{4.15}$$

Figure 4.15(b) shows the result for the first 3 integration surfaces. The prediction is massively improved by including the source region downstream of the LE peak/hill in the third integration surface. The overshot peaks are greatly reduced and occur at approximately correct frequencies. Additionally the low frequency noise reduction is reduced towards 0. As was previously shown by table 4.2 it is apparent that the 2D source distribution is responsible for the lack of low frequency noise reduction, and therefore a significant percentage of the source must be included to capture this effect. The noise increase regions at low frequency are shown by figure 4.16(a), revealing they are mainly located near the LE root, although a large proportion of the downstream surface also represents a small noise increase. Figure 4.15(c) and (d) shows gradual convergence of the FW-H prediction as the integration region is increased to include 12 LE amplitudes ($\approx$ 5 vortex diameters). The integration surface is extended further to 30 LE amplitudes ($\approx$ 12.5 vortex diameters) in figure 4.15(e). It is apparent that an exact match is not possible unless the full surface is included, although it could be argued a reasonable match is observed from around 9 LE amplitudes ($\approx$ 3.75 vortex diameters) onwards.

4.5.2 Quantification of destructive interference and source reduction mechanisms

A 2D interpretation of the effective source region (§4.4.1) is provided by (4.16):

$$\mathcal{A} = \int_{-\lambda_{LE}/2}^{\lambda_{LE}/2}\int_{-0.5L_c}^{x_{TE}-h_{LE}} \mathcal{W}\frac{S_{ppw}^{WLE}(x',z,f^*)}{S_{ppw}^{SLE}(x',z,f^*)}\mathrm{d}x'\mathrm{d}z \tag{4.16}$$

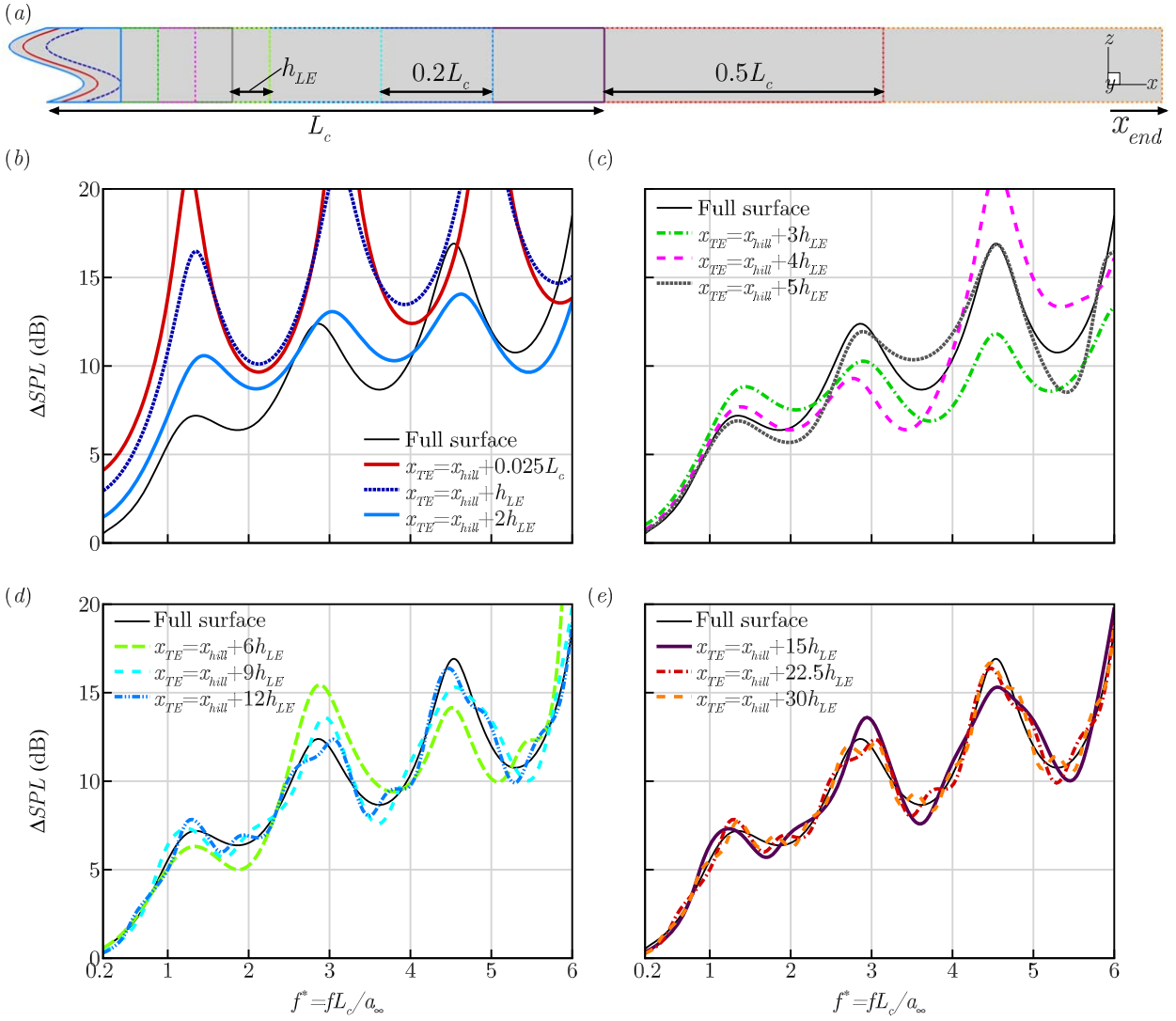

Figure 4.15: FW-H predicted noise reduction spectra obtained by integrating incrementally increasing proportions of the aerofoil surface. (*a*) Schematic diagram indicating the incrementally increasing surface integration region. (*b*) three integration regions starting from the LE and extending to $x = x_{LE} + 0.025L_c$, $x = x_{LE} + h_{LE}$ and $x = x_{hill} + 2h_{LE}$ respectively. (*c*) further extensions to the integration region increasing in increments of h_{LE} until $x_{hill} + 5h_{LE}$; (*d*) extensions increasing by $2h_{LE}$ until $x_{hill} + 12h_{LE}$; (*e*) extensions increasing by $7.5h_{LE}$ until $x_{hill} + 30h_{LE}$. Comparison is consistently made to the full surface integration.

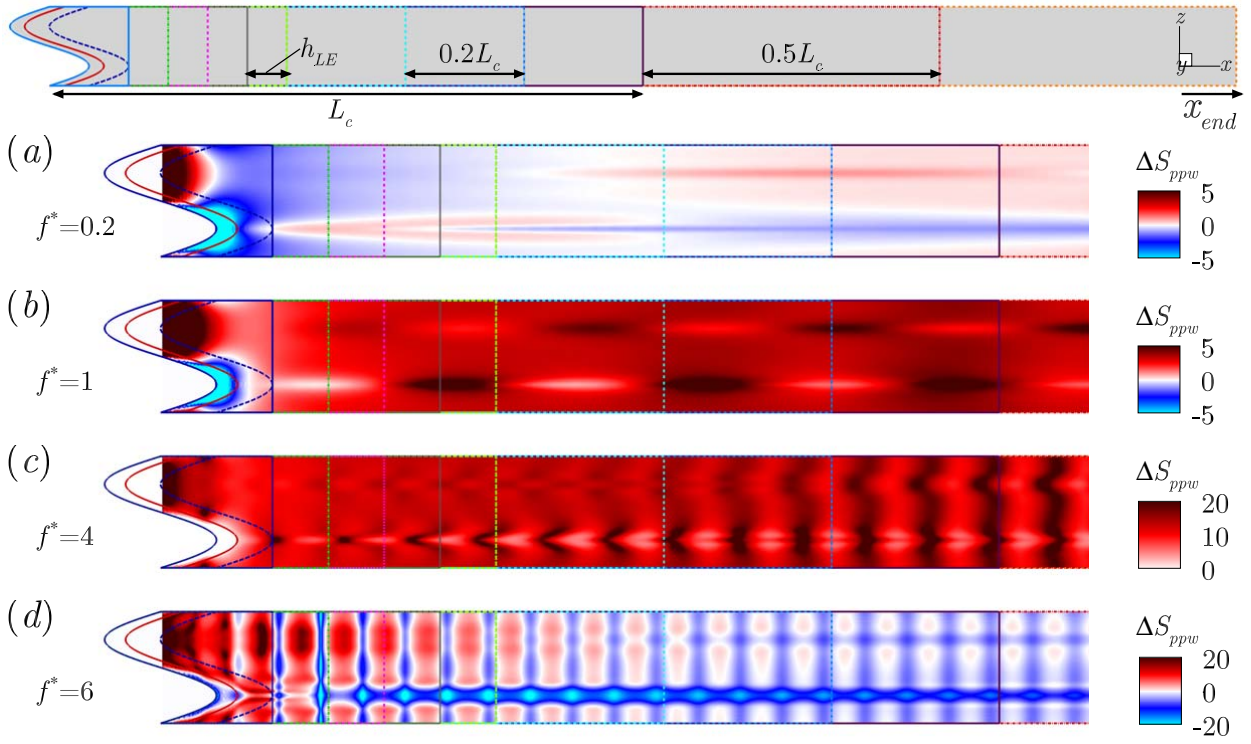

Figure 4.16: One-to-one source strength difference spectra (4.15). (a) $f^* = 0.2$; (b) $f^* = 1$; (c) $f^* = 2$; (d) $f^* = 6$.

where $x' = x - x_{LE} - 0.5L_c$. The above formulation is based on the ratio between WLE and SLE source at a given distance from the LE line. The change of coordinates maps the WLE to a SLE with a wavy trailing edge (similar to the stretched coordinates used in Roger *et al.* (2013)). The inner integral is therefore calculated over the range $-0.5L_c \leq x' \leq x_{TE} - h_{LE}$, which represents the range where the SLE and stretched WLE geometries overlap. In the following analysis we use $x_{TE} = 15h_{LE}$, which was shown previously to represent enough of the surface to capture the underlying noise reduction vs. frequency relationship. An optional weighting term:

$$\mathcal{W} = S^{SLE}_{ppw}(x', z, f^*)/S^{SLE}_{ppw}(-0.5L_c, z, f^*), \tag{4.17}$$

is also included to avoid bias from surface regions with a comparatively weaker source magnitude. The result is plot in figure 4.17. Remarkably the un-weighted effective source area agrees very well with the noise reduction spectra until $f^* \approx 4$. At this point the source downstream of the LE which is comparable for SLE and WLE aerofoils begins to dominate, causing the source area to increase rapidly. Inclusion of the weighting term results in a less accurate prediction, although possibly a fairer representation of the source strength contribution to the noise reduction mechanisms. Regardless, this result highlights that source strength reductions may contribute to the increasing noise reduction with frequency trend at least to moderate frequencies (despite the misleading information obtained by only modelling the LE line).

Another simple quantification of the LE source strength noise reduction can be obtained by simply

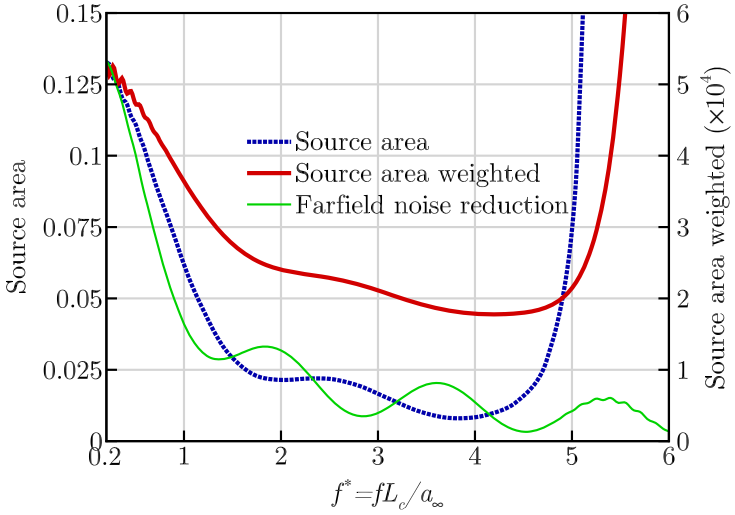

Figure 4.17: Effective source area $\mathcal{A}$ as predicted by (4.16). As in figure 4.6, the required reduction with frequency is also plot for comparison, showing a good match until $f^* = 4$.

integrating the source along the LE curve or surface. One and two-dimension representations of the 'integrated source strength' (ISS) are calculated as:

$$ISS_{1D} = \frac{1}{\lambda_{LE}} \int \frac{S_{ppw}(\boldsymbol{x}_{LE}, f^*)\mathrm{d}l}{p_\infty^2} \tag{4.18}$$

and

$$ISS_{2D} = \frac{1}{\lambda_{LE} L_c} \int\int \frac{S_{ppw}(x, z, f^*)\mathrm{d}S}{p_\infty^2} \tag{4.19}$$

Figure 4.18 compares the LE integrated source strength as described by (4.18) with the surface integrated source strength (4.19). It is clear that the WLE source characteristics make a non-negligible contribution to the noise reduction for frequencies below $f^* = 5$. It is also apparent how a LE-only representation of the WLE source characteristics can lead to misleading results. It is worth noting that the current quantification of source based noise reduction excludes retarded time effects due to different chord wise location, which is considered in the following analysis.

A more sophisticated approximation of the source and phase based noise reduction contributions is achieved by modifying the input to the FW-H solver. The two mechanisms are decoupled by altering the source characteristics over the surface. The interference only prediction is obtained by transforming the SLE to a WLE and introducing a spanwise phase shift. Firstly the x coordinates are stretched by adding the WLE profile to the SLE geometry $x' = x_{SLE} + h_{LE}\sin(2\pi z/\lambda)$, then surface pressure signals are evaluated at the retarded time $\tau = t - h_{LE}\sin(2\pi z/\lambda)/U_\infty$. Meanwhile, the source only prediction is obtained by transforming the WLE to a SLE and eliminating the spanwise variation in sound emission time from the WLE case. This is the reverse procedure of the previous case. The WLE coordinates are stretched as $x' = x_{WLE} - h_{LE}\sin(2\pi z/\lambda)$, and the time signals evaluated at $\tau = t + h_{LE}\sin(2\pi z/\lambda)/U_\infty$. In both cases the coordinate transformation introduces a wavy trailing edge. However, since this occurs at the domain exit boundary ($x/L_c =$

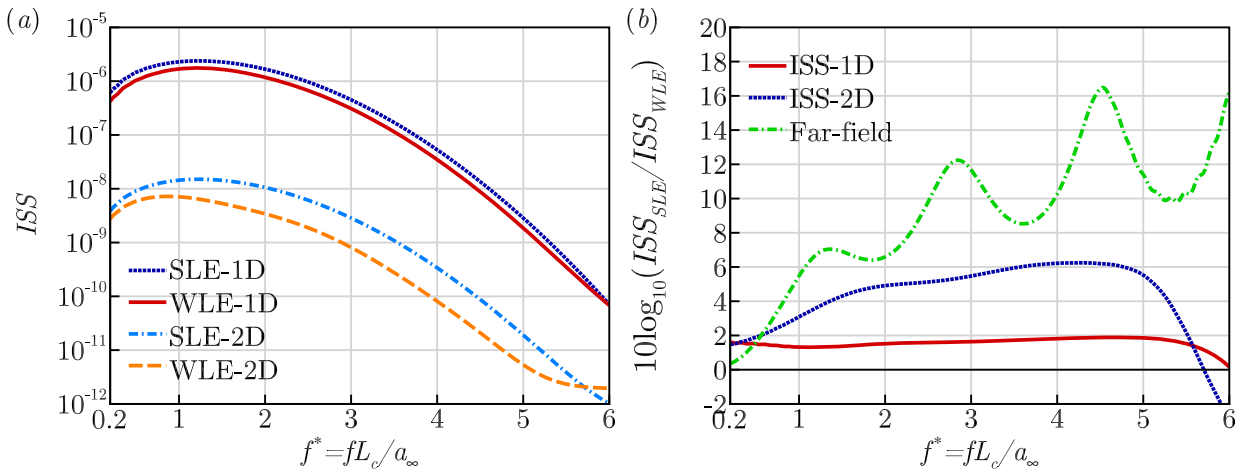

Figure 4.18: (*a*) Source strength integrated along the LE line as in (4.18) compared with surface integrated source strength (4.19). (*b*) Corresponding ISS difference spectra $10\log_{10}[ISS_{SLE}(\boldsymbol{x}_o, f^*)/ISS_{WLE}(\boldsymbol{x}_o, f^*)]$.

11), it is assumed to be sufficiently far downstream to not effect the result. Figure 4.19 shows the results of the two FW-H calculations, in addition comparison is made to the LE line model **B** from §4.4.

We immediately notice that the interference FW-H prediction exceeds the source prediction except at low frequency ($f^* < 1$). The interference prediction generally overestimates the actual far-field noise reduction, while the source prediction underestimates. (Note: the source prediction still has streamwise interference effects, which may allow the noise reduction to continue beyond the drop off point $f^* = 5$ shown in figure 4.18.) We may therefore conclude that individually interference has a stronger influence on noise reduction at high frequencies. Although, in reality the two effects are coupled, and therefore the source variation may actually weaken the phase interference effect resulting in a more comparable level from the two mechanisms (imperfect cancellation due to different strengths). The net results is then somewhere in between the two predictions. As we have previously stated the LE line approximation leads to false conclusions regarding the impact of source variation, however it is clear from this figure that it accurately capture the phase interference effect.

4.6 Concluding remarks

The noise reduction mechanisms of a WLE aerofoil have been investigated in detail utilising a high resolution numerical approach. The problem considers a flat plate aerofoil interacting with a spanwise vortex disturbance which allows for easy identification of noise reduction trends associated with spanwise destructive interference and source strength modification. This chapter makes an attempt to quantify the contribution of these two mechanisms to the far-field noise reduction, particularly the source reduction which has been largely overlooked by literature.

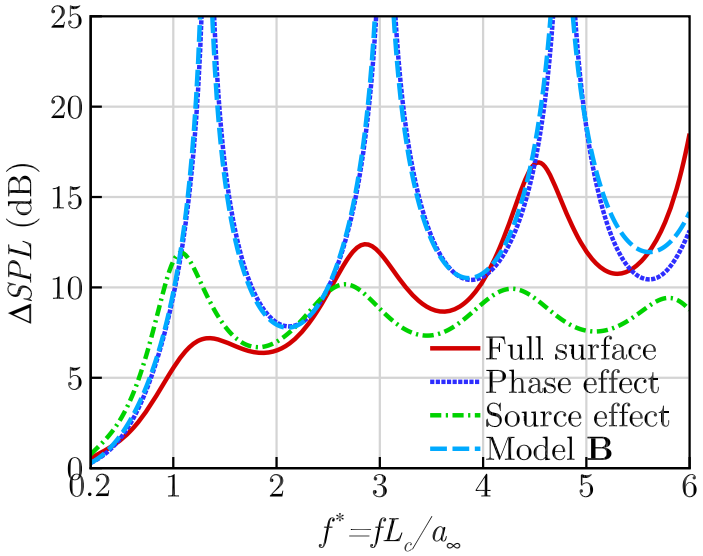

Figure 4.19: Modified FW-H noise reduction predictions highlighting contributions from destructive interference and source strength variation respectively. The phase effect prediction is obtained by mapping the SLE surface pressure data onto the WLE geometry. Meanwhile the source alone prediction is obtained by eliminating the spanwise variation in retarded time from the WLE case. Comparison is also made to the 1D model **B** outlined in §4.4.

Firstly a simple noise reduction prediction model based on the aerofoil LE line is introduced. The model considers the destructive interference mechanism due to the WLE geometry and takes into account the variation of source strength along the LE. The model is capable of predicting the general noise reduction relationship with frequency with good accuracy.

Despite its capability to provide reasonable predictions, it is later demonstrated that the LE approach leads to misleading conclusions regarding the physics. In particular the importance of the source characteristics on the noise reduction trend. This realisation comes from analysing the wall pressure spectra over the full surface, which reveals downstream regions which make significant contributions to the source (particularly at higher frequencies). The importance of considering the full source characteristics is ultimately demonstrated by performing FW-H calculations with progressively larger surface areas. It is shown that approximately 3-4 vortex diameters in the streamwise direction is required to produce adequate results. Analysis of the wall pressure spectra also provides an explanation for the lack of noise reduction offered at low frequency. A question proposed due to the large low frequency surface pressure reductions exhibited locally at the LE hill. It is found that despite these previous observations the percentage of the surface with similar strength is almost the same for SLE and WLE cases. Around 1 vortex diameter in the streamwise direction is required to capture this effect.

Although it is difficult to determine which mechanism is most significant (as they are coupled). Attempts are made to quantify their contributions to the noise reduction independently. The source mechanism contribution is estimated by considering the effective surface area which radiates sound with same strength as the SLE baseline. It is shown that this quantity reduces with frequency and

approximately follows the far-field noise reduction trend. Source and interference only predictions are also made by modifying the input to the FW-H solver to eliminate spanwise differences in strength and retarded time respectively. Generally noise reduction predictions based solely on destructive interference over predict the noise reduction, while source only predictions under predict at high frequencies. The results indicating that destructive interference is likely the more dominant mechanism at high frequencies where the source actually produces a noise increase. At low frequencies on the other hand source reduction is a crucial mechanism for the noise reduction. It is also important to consider that the variation of source will reduce the effectiveness of destructive interference due to incomplete cancellations.

Chapter 5

Secondary Noise Sources

5.1 Problem background

It is well established that the majority of the aerofoil noise due to upstream vortical disturbances emanates from the leading edge (LE) where the impinging vortices scatter into acoustic waves, which is the primary source mechanism. The secondary source mechanisms on the other hand are associated with the existence of a trailing edge (TE) and are twofold: (a) the backscattering of the acoustic waves produced earlier (travelling back and forth between the LE and TE); and, (b) the scattering of the vortices at the TE (after being bisected and modified at the LE).

The acoustic back scattering event is a well known physical phenomena in classical acoustics, and we refer to the work of Ayton & Peake (2013); Rienstra (1981); Roger *et al.* (2016) on the matter. TE vortical scattering event on the other hand is significantly less studied. The well known theoretical work of Howe (1976, 2002) investigated the parallel aerofoil-vortex interaction problem for a point vortex convected above a flat plate aerofoil. It was found that the generation of sound is highly dependent on application of the Kutta condition at the trailing edge. Remarkably if it is included Howe shows that shed vorticity from the TE effectively cancels the scattered sound caused by the impinging vortex. These results were later reiterated by Glegg & Devenport (2009) and extended to aerofoils of arbitrary thickness. Despite this there is plenty of speculative experimental and numerical evidence supporting vortical TE scattered sound through analysis of unsteady lift data. Straus *et al.* (1990) compared experimental pressure coefficient data with the linear theory of Sears (1941), noting a major departure from theory approximately when the vortex passed the TE. A later study by Horner *et al.* (1992) specifically focused on convective events in aerofoil-vortex interaction experiments. The vortex position was correlated with force and moment data, revealing a relationship between passage of the vortex over the TE and magnitude changes. Furthermore pressure transducer experiments by Kitaplioglu *et al.* (1997) identified convective disturbances propagating at approximately the mean flow speed followed by secondary BVI events. The findings of Kitaplioglu *et al.* (1997) were later reiterated by Thom & Duraisamy (2010) who conducted Euler simulations of the same configuration. The failure of the analytical approaches to

capture the sound generated by the vortex at the TE is likely due to linearity or rapid distortion theory (RDT) assumptions. Therefore treating unsteady disturbances as mean flow perturbations which only change strength due to mean flow gradients and solid boundaries. These kind of assumptions are usually considered reasonable if the vortex is weak, or far from the wall, such that its strength and trajectory is not significantly influenced by image vortices. It is worth noting that these studies all consider high strength vortex disturbances, however the results of Straus *et al.* (1990) fit the requirements for linear assumptions suggested by Grace (2001) (induced velocity n% of the mean flow passing within n% of the aerofoil half chord).

There is insufficient investigation into the validity of linearised analytical theory, and the extend of the secondary TE sound when it breaks down. This chapter therefore aims to provide comprehensive understandings of the secondary noise sources present in the event of vortical disturbances impinging on an aerofoil. The current work follows directly from Turner & Kim (2017*b*) where the primary noise source was investigated in detail. The earlier work employed semi-infinite aerofoils only and therefore did not involve any of the secondary sources. In contrast this work focuses on the secondary sources, which is achieved by eliminating the semi-infinite-chord solution (primary source) from the finite-chord one. The decomposed solutions reveal various characteristics of the secondary sources that contrast with those of the primary source.

One of the most significant findings captured in this study is that the TE vortical scattering is the dictating source of noise at high frequencies in almost all observer directions. This is particularly true for exactly parallel interactions, but also significant for moderate vertical miss distances (well beyond the RDT validity range suggested by Grace (2001)). The generation of the TE vortical scattered sound is linked to the interaction of LE generated bound vorticity with the impinging vortex which results in an asymmetric vorticity distribution between upper and lower sides. This phenomena has been neglected in historical analytical approaches as the bound vorticity is believed to make no direct contribution to the LE sound (Howe, 2002). Although this study primarily concerns the inviscid flow considered by the analytical theory, the effects of viscosity are investigated towards the end of the chapter and found to play a significant role. Effectively secondary TE noise can only exist if the vortex is strong enough (or dissipative effects weak enough) to survive travel through the boundary layer. The inviscid case therefore represents the limiting case where TE vortical scattering is most severe.

The chapter is organised into the followings sections. In §5.2 the significance of the secondary noise sources is revealed by analysing their acoustic power spectra obtained at a certain observer location. In §5.3 the effect of vertical miss distance during the leading edge interaction is investigated primarily concerning the cut-off where non-linear TE effects are negligible. Additional discussions are then provided in §5.4 with regard to the provision of existing analytical prediction models based on the major findings achieved in this chapter. Penultimately §5.5 investigates the significance of viscous effects on the presented findings. In particular the importance of viscous dissipation is discussed. Finally some concluding remarks are made in §5.6.

5.1.1 Description of problem and the computational set-up

The current problem of aerofoil noise generation due to interaction with a prescribed spanwise vortex impinging on the leading edge is depicted in figure 5.1(*a* and *b*). Instantaneous contour plots of the acoustic pressure generated as a result of the interaction are shown in figure 5.1(*c* to *f*) for the aerofoil with a semi-infinite chord and with a finite chord compared against each other. The aerofoil is a flat plate with zero thickness and zero angle of attack against the mean flow. The semi-infinite-chord case shows the LE vortical scattering (LEVS) that is the primary source (denoted by S1) of the interaction noise generation. In the meantime the finite-chord case reveals additional acoustic waves generated due to the presence of a TE, which are herein referred to as the secondary source (denoted by S2). In this work the secondary source is subdivided into two: (1) the scattering of the vortex at the TE (after being bisected and modified at the LE); and, (2) the backscattering of the acoustic waves produced earlier (travelling back and forth between the LE and TE). The former is referred to as "TE vortical scattering" (TEVS) and the latter is "acoustic backscattering" (ABS) in this thesis.

The computational domain is constructed in the same manner as the previous section, although only the SLE geometry is considered in this section. Towards the end of this chapter we consider viscous flow simulations for which we employ the full three-dimensional compressible Navier-Stokes equations. The computational approach implements no turbulence modelling, and is in essence an implicit LES calculation utilising the filter technique highlighting in §2.1.4 to remove the unresolved scales.

As mentioned earlier, we focus on the secondary sources of the aerofoil-vortex interaction in this chapter. The secondary sources are obtained by eliminating the primary source from the full solution. In order to do this, two different simulations are carried out where one is based on a semi-infinite chord aerofoil (containing the primary source only) and the other based on a finite-chord aerofoil (containing both the primary and secondary sources), and the difference is calculated:

$$p_{\mathrm{S2}}(\boldsymbol{x}, t) = p(\boldsymbol{x}, t) - p_{\mathrm{S1}}(\boldsymbol{x}, t), \tag{5.1}$$

where p_{S1} is the solution from the semi-infinite-chord aerofoil and p is from the finite-chord one.

5.2 The secondary sources associated with aerofoil vortex interaction

The acoustic pressure data obtained at the far field as a result of the simulations are provided in figure 5.2. The data are collected at a single observer location $\boldsymbol{x}_o/L_c = (0, 5, 0)$ that is five chords above the aerofoil's centre (in terms of the finite-chord case). Figures 5.2*a* and *b* show the time signals of the acoustic pressure and the corresponding power spectra for a finite and a semi-infinite

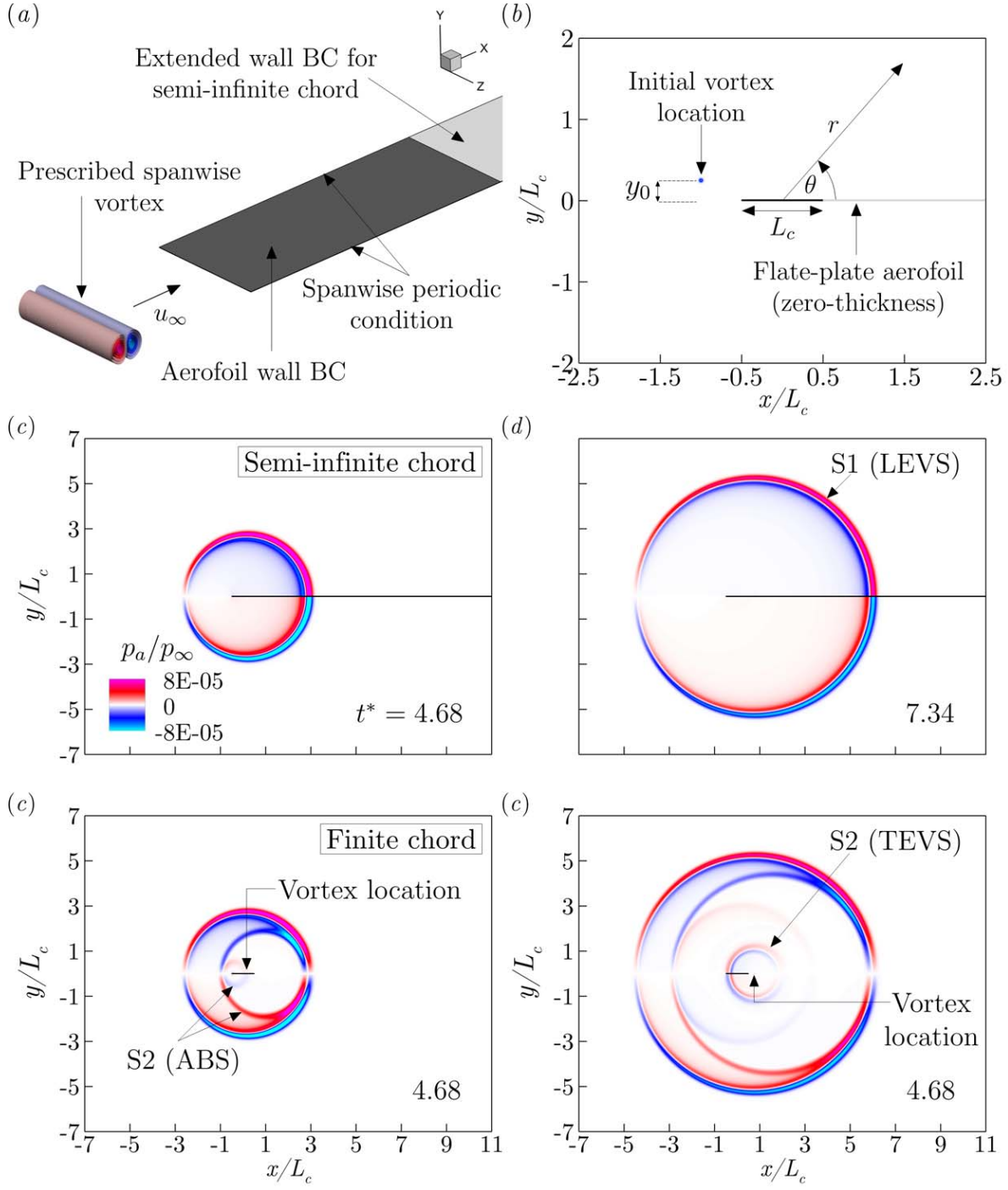

Figure 5.1: The current numerical simulation of aerofoil noise due to an impinging vortex: (a) the initial and boundary conditions where the prescribed vortex is visualised by iso-contour surfaces of vertical velocity; (b) the initial condition viewed from the mid span ($z = 0$) in the xy-plane where the origin of the coordinates is located at the mid chord; (c & d) instantaneous contour plots of acoustic pressure (p_a/p_∞) in the case of a semi-infinite-chord aerofoil at the dimensionless time of $t^* = ta_\infty/L_c = 4.68$ and 7.34; and, (e & f) equivalent plots in the case of a finite-chord aerofoil. The aerofoil has a SLE in (c to f). The acronyms are defined as follows: S1 = primary source; S2 = secondary source; LEVS = leading-edge vortical scattering; TEVS = trailing-edge vortical scattering; and, ABS = acoustic backscattering.

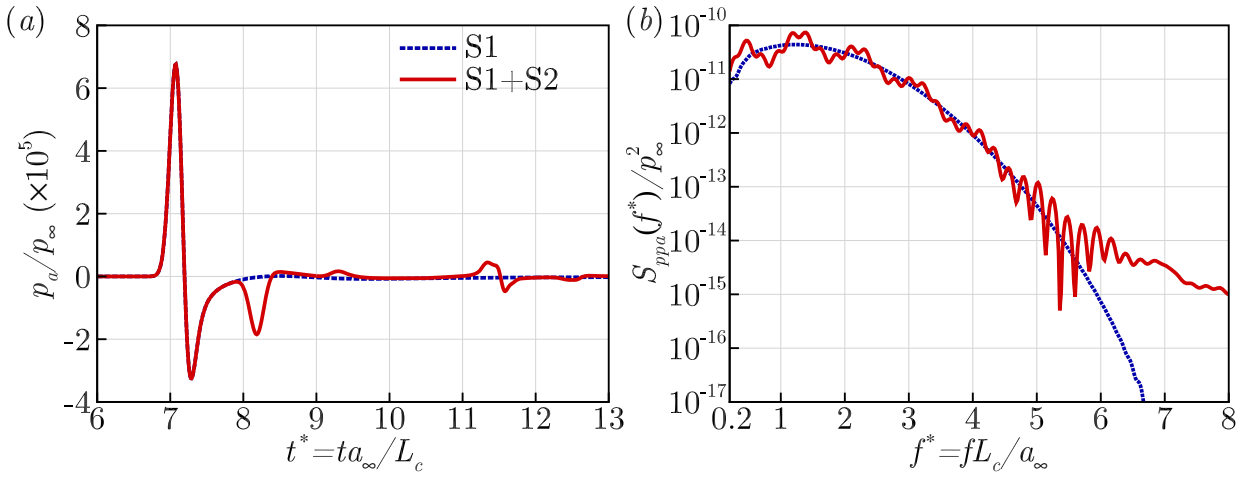

Figure 5.2: Acoustic pressure data obtained at an observer location from the current simulations with two different chord lengths (finite and semi-infinite, where the former includes all noise sources and the latter contains S1 only): (a) time signals of $p_a(\boldsymbol{x}_o, t)/p_\infty$ where $\boldsymbol{x}_o/L_c = (0, 5, 0)$; (b) the corresponding power spectra. It is worth noting here that S1 = LEVS and S2 = TEVS+ABS.

chord length of the flat-plate aerofoil. As indicated earlier the semi-infinite-chord case shows the primary source only whereas the finite-chord case includes both the primary and secondary sources.

5.2.1 Initial findings

The first thing that can be observed in figure 5.2a is that the pressure response generated by the TEVS (approx $t^* = 11.5$) is significantly weaker than that from the LEVS (approx $t^* = 7$). This is anticipated by the theory of Howe (Howe, 1988) who quotes "sound produced by vorticity shed from the trailing edge in order to satisfy the Kutta condition, interferes destructively with the 'direct' sound generated by the impinging vorticity". This effect can be observed in figure 5.3 which shows the development of spanwise vorticity ($\omega_z L_c/a_\infty$) during the aerofoil-vortex interaction. Figure 5.3 (c) and (d) show the vorticity as the vortex passes x_{TE} for semi-infinite and finite chord cases respectively. It is clear how the finite chord case generates secondary vorticity at the TE which is of opposite sign to the impinging vorticity. According to Howe, the far-field radiated pressure may be determined through the following equation:

$$p_a(\boldsymbol{x}, t) = -\rho_0 \int (\boldsymbol{\omega} \times \boldsymbol{u})(\boldsymbol{y}, \tau) \cdot \frac{\partial G}{\partial \boldsymbol{y}}(\boldsymbol{x}, \boldsymbol{y}; t - \tau) \mathrm{d}^3\boldsymbol{y}\mathrm{d}\tau \tag{5.2}$$

where G is an appropriate Green's function for the geometry and τ is the retarded time. Based on (5.2) it is easy to see how the opposite signed TE generated vorticity will reduce the overall pressure response.

One of the principle finding of this chapter is that unlike analytical approaches (Glegg & Devenport, 2009; Howe, 1988) the cancellation of the two sources at the TE is not complete. Relative to the LEVS, the TEVS acoustic pressure magnitude is reduced by approximately 93%, however we

find that the residual response acts as a major source of sound under certain conditions. The discrepancy is caused by non-linear effects captured in the current Euler approach which are not present under RDT assumptions or linearised theory. The first non-linear effect is the interaction of the vortex with its image as it convects over the wall. This effect is particularly significant if the vortex is strong or if the interaction is exactly parallel, and will influence the trajectory of the vorticity. Additionally in a full non-linear approach secondary vorticity will be generated at the LE which will convect with the impinging disturbance. The generation of the secondary LE vorticity has been discussed in detail in Turner & Kim (2017*b*), and is also shown in figure 5.3(*b*). This phenomena is usually omitted on application of (5.2) as ∇G is parallel to the surface and therefore $(\boldsymbol{\omega} \times \boldsymbol{u}) \cdot \nabla G = 0$ (Howe, 2002). Consequently there will be no cancellation between generated and impinging vorticity at the LE (as with the TE). However, it is clear from figure 5.3(*c*) that the LE vorticity will interact with the impinging disturbance, drastically changing the vorticity distribution which arrives at the TE. Effectively, once the vortex reaches the TE its upper/lower halves are no longer symmetric and represent a small pressure jump which is scattered by the TE. Furthermore it is apparent how the TE shed vorticity changes sign as the convective secondary structures pass the TE, see figure 5.3(*d*), further indicating it plays a major role in the TEVS mechanism.

Turning to the the acoustic power spectra in figure 5.2*b* the first thing we observe is that there is a drastic change in the slope of the spectra at high frequencies ($f^* > 5$) when the secondary sources are included. It is shown later in this chapter that the increased high-frequency noise associated with the finite chord case is related with the dominance of TEVS over the other sources.

In order to focus on the secondary sources, the equation (5.1) is implemented to remove the primary source from the full solution as mentioned earlier. The remaining secondary solution $p_{a\text{-S2}}$ is shown in figure 5.4. Five sub-components of the secondary sources are detailed in figure 5.4*a*. The figure shows that 1) the first sub-component (labelled A) is due to the ABS (acoustic backscattering) of the initial wave that was created by the primary source (LEVS) shown in figure 5.1; 2) B is the subsequent ABS of A; 3) TEVS is the vortical scattering at the TE as defined earlier; 4) C is the ABS of the TEVS; and, 5) D is the subsequent ABS of C. In this chapter, the ABS represents the sum of A, B, C and D, where the contribution of D is insignificant compared to others.

Perhaps the most striking feature displayed in figure 5.4*c* (as well as figure 5.2*b*) is that there is a remarkable change in the spectral shape and slope at around $f^* \approx 4.5$. It should also be noted that the spectral oscillations disappear after the critical frequency indicating that the phase interference between the LE and TE sources becomes insignificant. In other words one of the secondary sources (either TEVS or ABS) dominates over the other and therefore there is no longer a meaningful competition taking place between them after the critical frequency. The next logical step in this investigation is to figure out which one of them is responsible for the high-frequency events and how the phase relationship between the LE and TE sources changes with frequency.

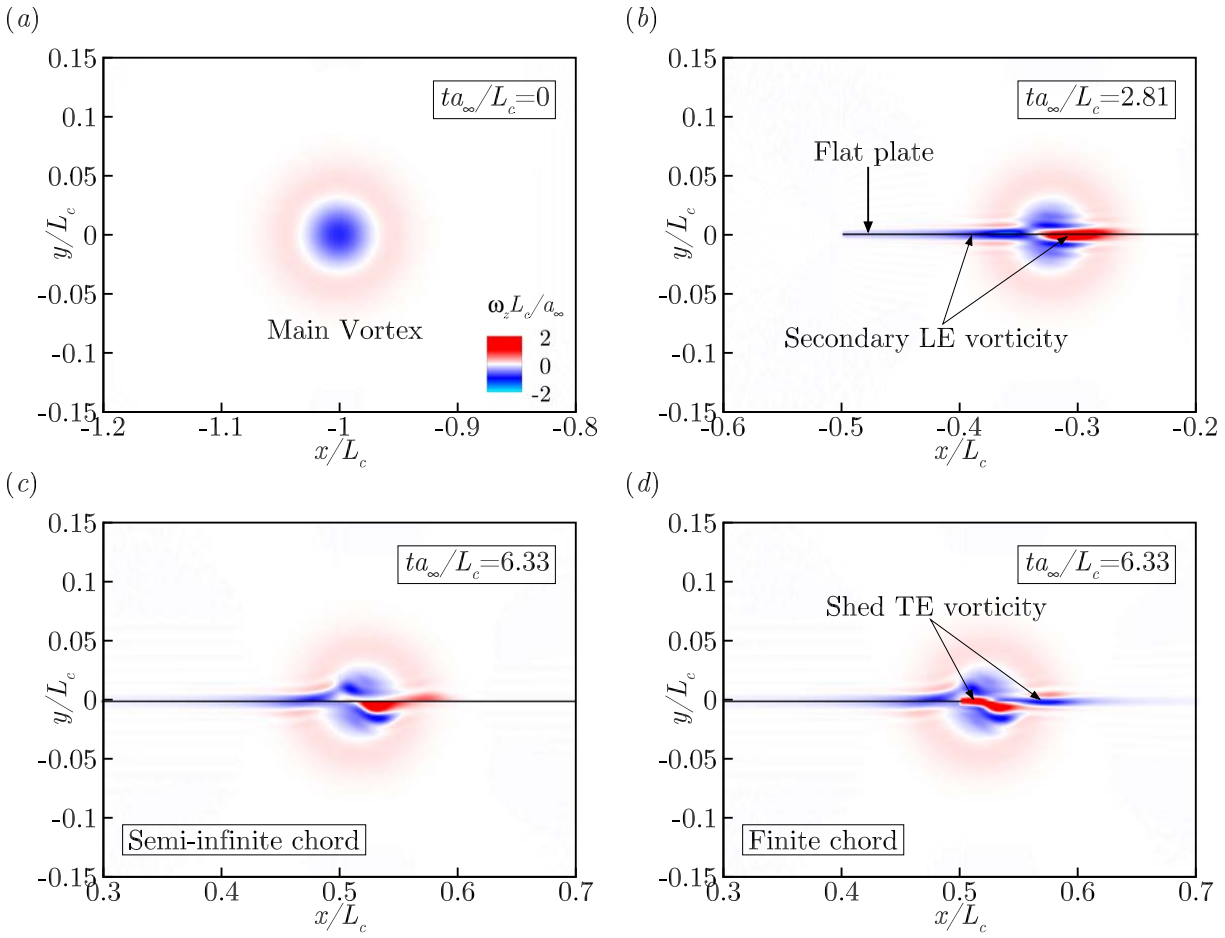

Figure 5.3: Contours of spanwise vorticity ($\omega_z L_c/a_\infty$) in the xy-plane at initial condition (a), after LE interaction $ta_\infty/L_c = 2.81$ (b), and at $ta_\infty/L_c = 6.33$ for semi-infinite chord (c), and finite chord cases (d).

5.2.2 Dominance of TE vortical scattering at high frequencies

In order to find an answer to the questions emerged above, an additional simulation is carried out. The aim of the new simulation is to extract isolated TEVS that is separated from ABS. The detailed procedure of the new simulation is described in figure 5.5. Firstly the finite chord simulation is run until a non-dimensional time of $ta_\infty/L_c = 25/6$ where the solution for the primitive variables is saved. At this time the vortex has convected $1L_c$ and is now at the aerofoil mid-chord. Next the freestream condition is restored away from the vortex by applying a window with radius $r/L_c = 1/4$ about the vortex mid-point. This is achieved with a hyperbolic tangent function $0.5(\tanh(25(0.25 - r)) + 1)$. Following this the LE is removed by extending the slip-wall boundary condition upstream to the domain inlet (resulting in an inverse semi-infinite-chord aerofoil). The simulation is then restarted and run for an additional 10 time units. The resulting time signal is then windowed to the range $10 \leq t^* \leq 13$ where the TEVS occurs.

The main assumption of this approach is the principle of superposition. This should be a reasonable assumption if the different wave components (LEVS, ABS and TEVS) interfere linearly. For this reason it may not be applicable for higher vortex strengths. The current vortex strength based

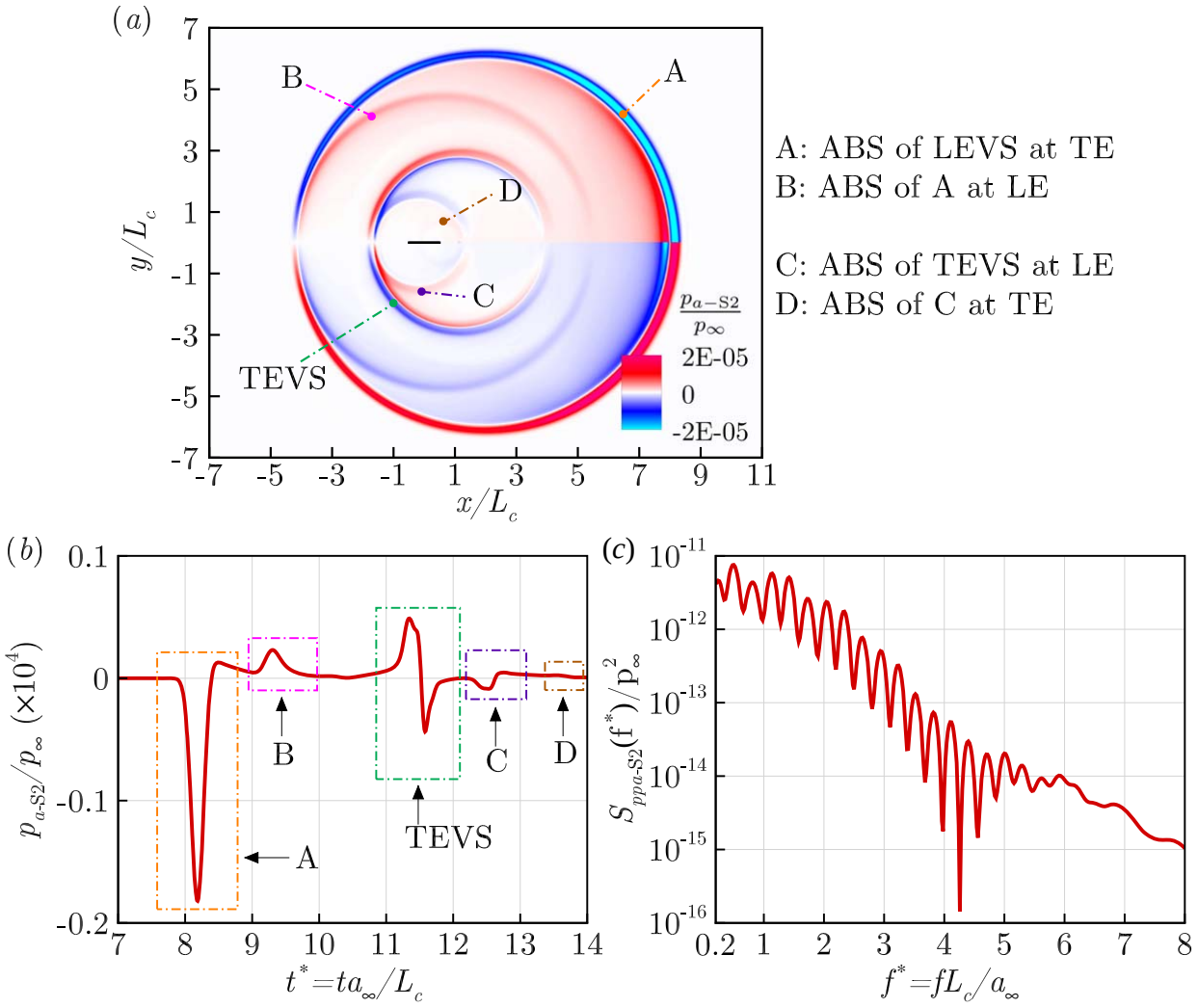

Figure 5.4: Acoustic pressure generated by the secondary sources (with the primary source excluded) obtained by using (5.1): (*a*) instantaneous contours of the acoustic pressure $p_{a\text{-}S2}/p_\infty$ at $t^* = 9.0$; (*b*) the time signals of $p_{a\text{-}S2}/p_\infty$ obtained at the observer location $\boldsymbol{x}_o/L_c = (0, 5, 0)$; and, (*c*) the corresponding power spectra. The acronyms are defined in figure 5.1 (as well as in the text).

on $\epsilon = 0.0377$, produces a linear response, as is demonstrated in appendix C. The application of this assumption is further supported by considering that based on the current vortex size the LEVS and TEVS waves are emitted distinctly with no overlap (as shown in figure 5.2). Despite this, it is possible that the ABS waves travelling back and forth between the LE and TE may have an impact on the vortex as it convects over the surface (which would not be captured in the above procedure). In order to verify that this is not a concern, the isolated TEVS signal determined through the procedure outlined above is compared to the original acoustic pressure signal obtained by the finite chord simulation in figure 5.6. The two signals are identical in the range $11 \leq ta_\infty/L_c \leq 12$ where the TEVS interaction takes place. This confirms that the above approach accurately captures the required portion of the signal.

Once the solution for isolated TEVS is obtained the other solution for isolated ABS can be evaluated

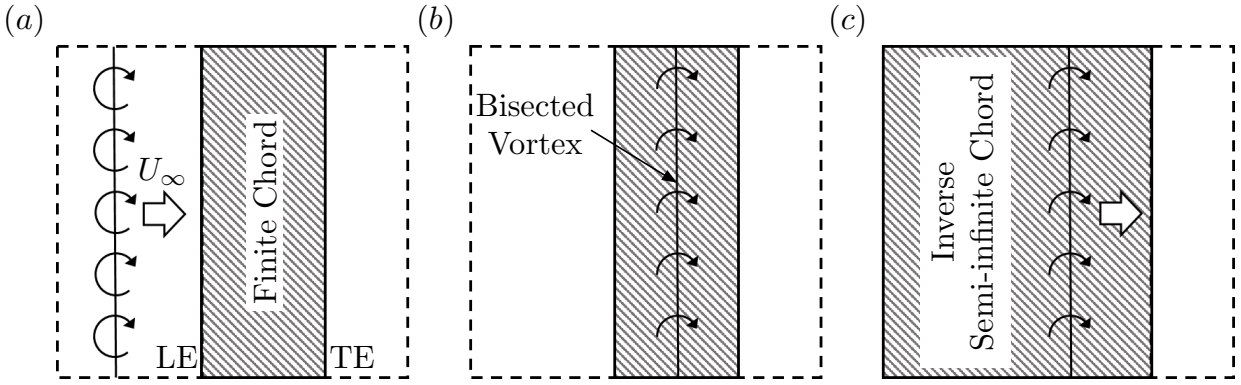

Figure 5.5: An additional simulation procedure in order to isolate the TEVS event: (a) continue the original simulation with the finite-chord aerofoil until $ta_\infty/L_c = 25/6$ by which time the upstream vortex is bisected and convected down to the mid-chord location $(x = 0)$; (b) restore the unperturbed freestream condition outside a radius of $r/L_c = 1/4$ from the mid-chord location to remove all the acoustic waves that have propagated but keep the bisected vortices contained inside the radius (on both the upper and lower sides of the aerofoil); and, (c) extend the wall boundary condition upstream to create an inverse semi-infinite-chord aerofoil (with no LE) and restart the simulation with the filtered solution in (b) as the initial condition.

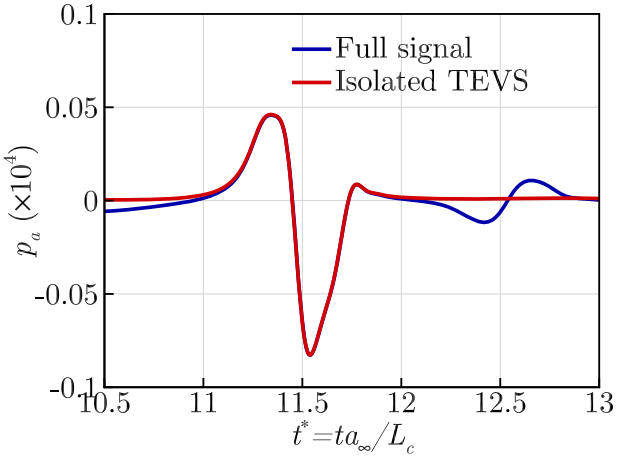

Figure 5.6: Far-field acoustic pressure signal obtained through the procedure outlined in figure 5.5 compared to the original signal produced by the finite-chord length WLE.

by subtracting the new solution from the entire secondary solution that was already made available via (5.1):

$$p_{\mathrm{ABS}}(\boldsymbol{x}, t) = p_{\mathrm{S2}}(\boldsymbol{x}, t) - p_{\mathrm{TEVS}}(\boldsymbol{x}, t). \tag{5.3}$$

The resulting acoustic power spectra obtained at the observer location $\boldsymbol{x}_o/L_c = (0, 5, 0)$ from each of the split solutions p_{TEVS} and p_{ABS} are presented in figure 5.7. The figure clearly shows that TEVS is the dominating source responsible for the high-frequency noise. It also reveals here that TEVS even exceeds the primary source (LEVS) in the high-frequency range as indicated in figure 5.2*b*. The starting frequency of the TEVS dominance over ABS is $f^* \approx 4.5$. On another note, it

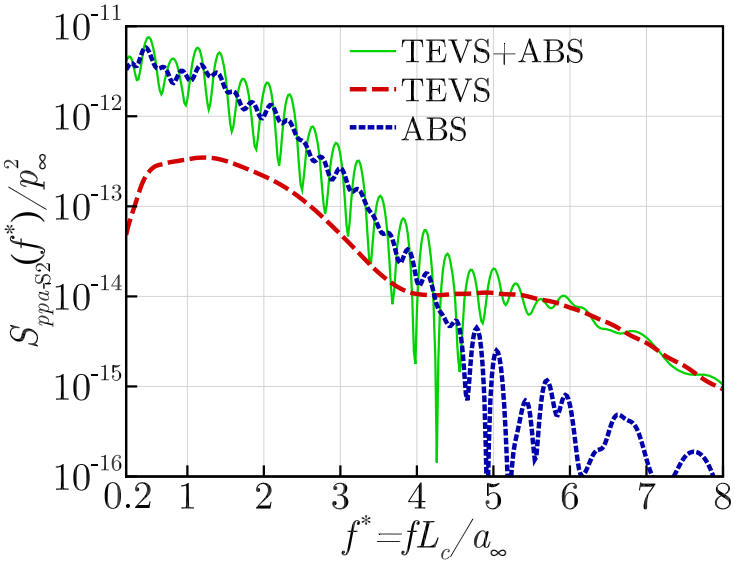

Figure 5.7: Acoustic power spectra for each individual TEVS and ABS components of the secondary source. The observer location is $\boldsymbol{x}_o/L_c = (0, 5, 0)$. The curve denoted by TEVS+ABS is that presented in figure 5.4*c*.

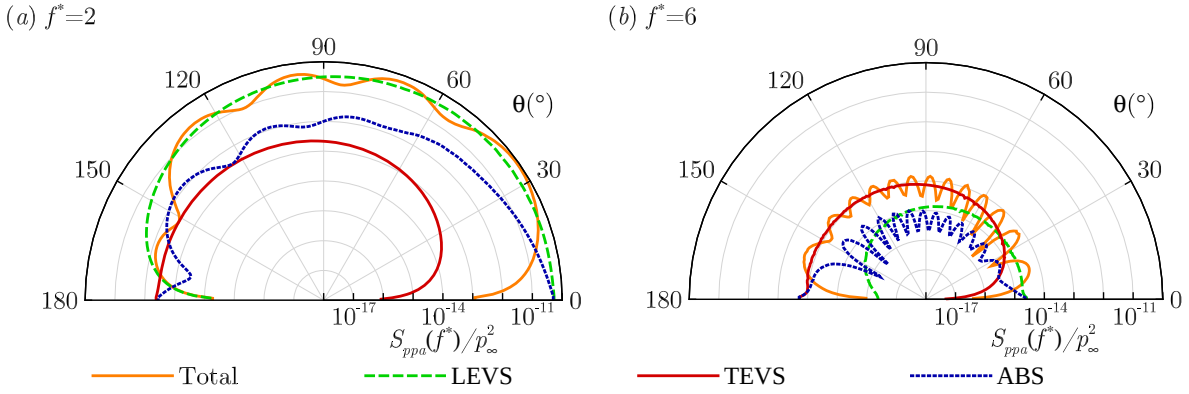

Figure 5.8: Directivity profiles (on a logarithmic scale) of $S_{ppa}(f^*)/p_\infty^2$ at two different frequencies: (*a*) $f^* = 2$ and (*b*) $f^* = 6$, around a circle of $\boldsymbol{x}_o/L_c = (5\cos\theta, 5\sin\theta, 0)$, obtained from each individual noise source and also from all sources combined (S1+S2). Lower half planes are not repeated due to symmetry.

is shown in figure 5.7 that the spectral oscillations in the spectra for TEVS+ABS intensify when the amplitudes of TEVS and ABS are similar, but disappear when one of them is superior to the other. This is a strong indication of the phase relationship existing between the two secondary sources (which is investigated in more detail in the following §6). The high frequency dominance of TEVS is also confirmed by the directivity patterns of $S_{ppa}(f^*)/p_\infty^2$ for two different (low and high) frequencies shown in figure 5.8. LEVS is the dominant noise source at $f^* = 2$, while TEVS is at $f^* = 6$. The only exception is for far upstream/downstream directions where there is a changeover. The directivity patterns of the secondary sources are covered in more detail in the following chapter §6 including comparison with WLE cases.

In order to verify the peculiar characteristics of TEVS, the wall pressure loading fluctuations

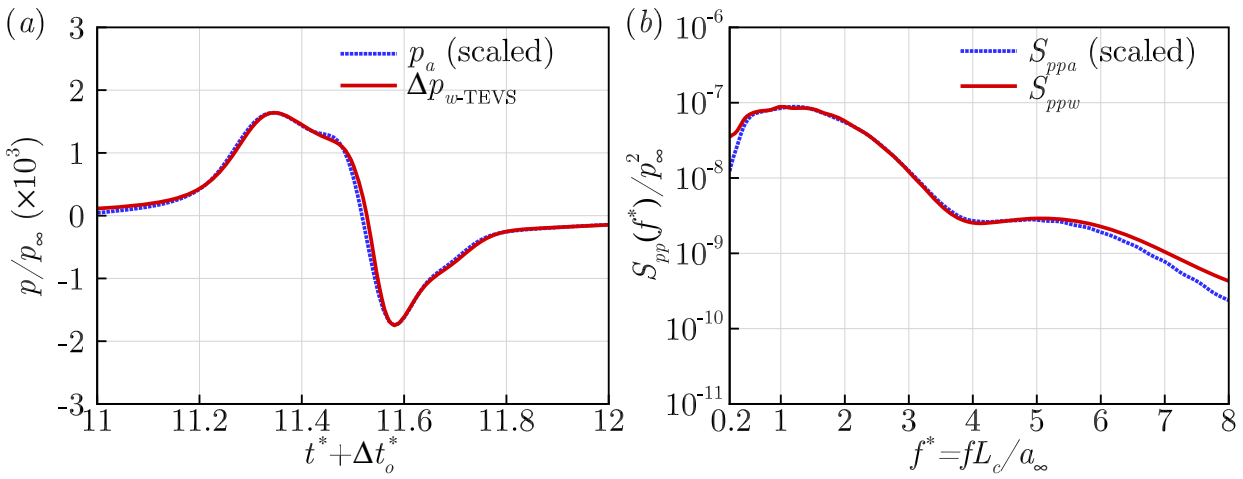

Figure 5.9: Comparison of the far-field acoustic pressure and wall pressure loading fluctuations at the TE due to the TEVS, averaged over the span: (a) the time signals of $\Delta p_{\text{w-TEVS}}/p_\infty$ and p_a/p_∞ scaled to the wall pressure fluctuation magnitude. (b) the corresponding power spectra.

$\Delta p_{w\text{-TEVS}}$ collected at the TE (averaged over the span) are examined as shown in figure 5.9. The results shows that the wall pressure loading PSD (figure 5.9b) at the TE matches almost perfectly with the far-field acoustic PSD (figure 5.7c) based purely on the TEVS event. This means that the peculiar characteristics of TEVS are a direct projection of what has happened at the wall, i.e. the vortex dynamics and evolution processes taking place across the aerofoil surface.

Interestingly work conducted by Howe (2001) indicates the TE shed vorticity response is mainly limited to low frequency. The author therefore speculates that the high frequency contribution from the TEVS is caused by the scattering of the convective LE generated vorticity at the TE, which is naturally of a smaller length scale than the main impinging disturbance.

5.3 The effect of vertical miss distance

In this section the findings discussed thus far are extended to account for a vertical offset between the aerofoil and impinging disturbance. This is particularly useful for evaluating the validity cut-off of linear assumptions by determining at which point the contribution from TEVS becomes negligible. This also provides a fairer comparison with models based on point or line vortices, which are incapable of predicting perfectly parallel interactions due to LE singularities. Figure 5.10 shows the far-field acoustic pressure data for three vortex vertical miss distances, $y_0 = 0$, $y_0 = 0.03$ and $y_0 = 0.06$. The latter is larger than the vortex core radius (see figure 5.3). The pressure and spectral data are scaled by $\max p_a$ and $(\max p_a)^2$ respectively so that direct comparisons may be made. It is apparent that the LEVS, ABS-A and ABS-B portions of the time signal scale linearly with the vertical wall distance. The TEVS signal on the other hand changes both shape and relative magnitude suggesting non-linear effects are present. Looking at the frequency distribution in figure 5.10(b) we find that the spectra collapse for $f^* < 3.5$, although there are significant differences

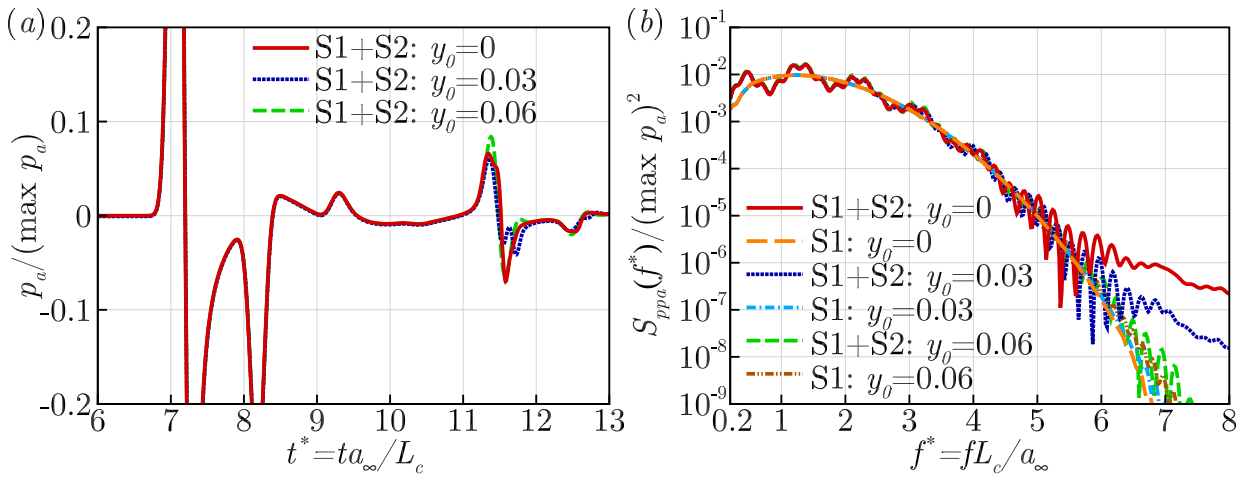

Figure 5.10: Magnitude scaled acoustic pressure data obtained at an observer location from the current simulations with three different vertical miss distances ($y_0 = 0$ (exactly parallel), $y_0 = 0.03$ and $y_0 = 0.06$): (a) time signals of $p_a(\boldsymbol{x}_o, t)/(\max p_a)$ where $\boldsymbol{x}_o/L_c = (0, 5, 0)$; (b) the corresponding power spectra.

at higher frequencies where TEVS begins to dominate. As the vertical miss distance is increased the high frequency content of the S1+S2 spectra becomes comparatively weaker eventually tending towards the S1 only solution. This is good news for RDT based models which typically consider cases with non-zero miss distances. However, care must still be taken with moderate miss distances as we observe no relative reduction in the TEVS acoustic pressure amplitude, and oscillations due to phase interaction with TEVS may still exist at high frequency (as for the $y_0 = 0.06$ cases).

Similar findings are made by Grace (2001), who suggested that RDT approaches may be invalid if the non-linear interactions at the wall are significant, i.e. the vortex strength is high or the miss distance is small. Grace (2001) suggested an approximate validity cut-off for RDT assumptions as a vortex of strength n% passing within n% of the aerofoil half chord. For the current example ($u' = 0.025U_\infty$) this would equate to a validity limit of $y_0 = 0.0125$. Despite this we still observer strong differences between the $y_0 = 0.03$ and $y_0 = 0.06$ cases at very high frequency suggesting non-linear effects still play some role. The discrepancy here likely emerges from the very large range of frequencies considered in the current study, approximately 5 time higher than in Grace (2001). If the high frequency sound produced during TEVS is a consequence of the convective LE generated disturbances then it is easy to explain the loss of high frequency power. Simply increasing miss distance results in weaker LE secondary vorticity due to a less severe vertical velocity field impinging at the LE.

5.4 Provision for analytical predictions

One of the main findings in this chapter is the dominance of TEVS at high frequencies that is even exceeding the primary source (LEVS). It is therefore imperative to take the effect of TEVS into account when an analytical prediction model is considered. One of the most favoured analytical

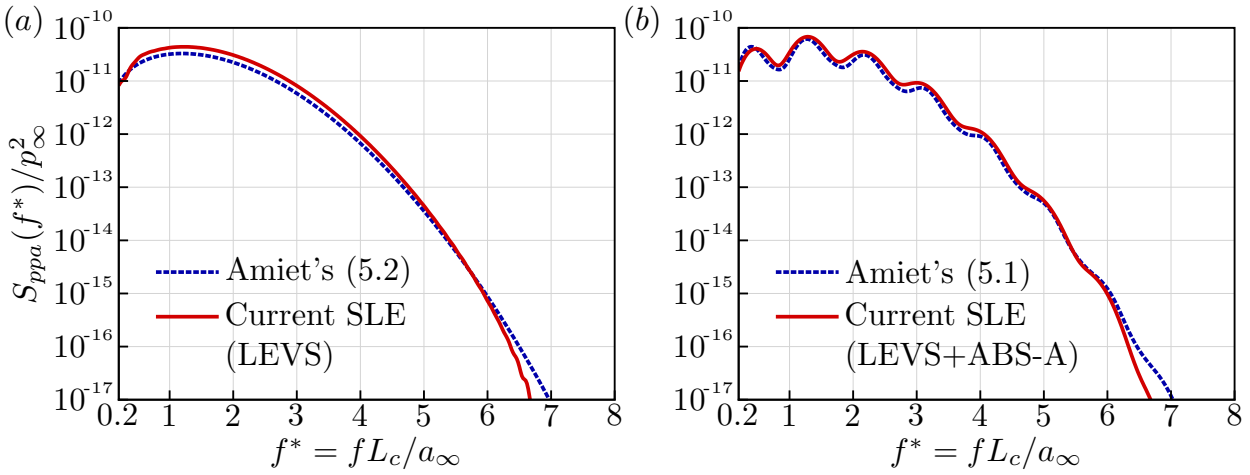

Figure 5.11: Amiet's model predictions of the acoustic power spectra at $\boldsymbol{x}_o/L_c = (0, 5, 0)$ given by (5.4) and (5.5) compared with the current SLE simulation results, with respect to two different source scenarios: (*a*) LEVS only; and, (*b*) LEVS and ABS-A combined. The velocity power spectrum (Φ_{vv}) required in the Amiet's models is given by (4.1).

models for aerofoil noise prediction was proposed by Amiet (1975, 1976). The Amiet's model is basically split into two independent models where one is for LE interaction noise due to upstream velocity disturbances and the other for TE self-noise due to boundary-layer turbulence. The first one (Amiet, 1975) naturally has a direct relevance to the current work. Blandeau *et al.* (2011) recently derived a two-dimensional version (for an infinite span) of the original model which can directly be compared to the current results. The two-dimensional model is written as

$$S_{ppa\text{-Amiet1}}(k_x) = \frac{\pi k_x M_\infty \rho_\infty^2 u_\infty^2 L_c^2 \sin^2\theta}{8 r_o A^3(\theta)} \Phi_{vv}(k_x) \left|\mathcal{L}(k_x)\right|^2, \tag{5.4}$$

where $k_x = 2\pi f/u_\infty$; $A(\theta) = (1 - M_\infty^2 \sin^2\theta)^{1/2}$; r_o is the observer distance from the mid-chord of the aerofoil; $\Phi_{vv}(k_x)$ is the PSD of the vertical velocity fluctuations impinging on the LE of the aerofoil; and, $\mathcal{L}(k_x)$ describes the unsteady loading on the aerofoil – see Blandeau *et al.* (2011) for full details. This model accommodates the primary source (LEVS) and the first acoustic backscattering component (ABS-A in figure 5.4). However, this means that the model omits TEVS and the rest of the acoustic backscattering components (ABS-B, C and D). In this section we apply a semi-infinite-chord approximation ($L_c \to \infty$) to (5.4) and remove the acoustic backscattering term in $\mathcal{L}(k_x)$ in order to obtain the pure LEVS solution (after some algebraic manipulations):

$$S_{ppa\text{-Amiet1-LEVS}}(k_x) = \frac{\rho_\infty^2 u_\infty^2 (1 - M_\infty) \sin^2\theta}{2\pi r_o k_x A(\theta)^2 [A(\theta) - \cos\theta]} \Phi_{vv}(k_x). \tag{5.5}$$

A comparison of the analytical predictions and the current simulation results is provided in figure 5.11. It is shown that there is a very good agreement between them (except at the very high frequencies), which confirms the validity of both approaches. However, the current work also suggests that the prediction model needs to be extended and improved in order to accommodate the rest of the sources (ABS-B to D and TEVS) that are excluded in this model. In particular

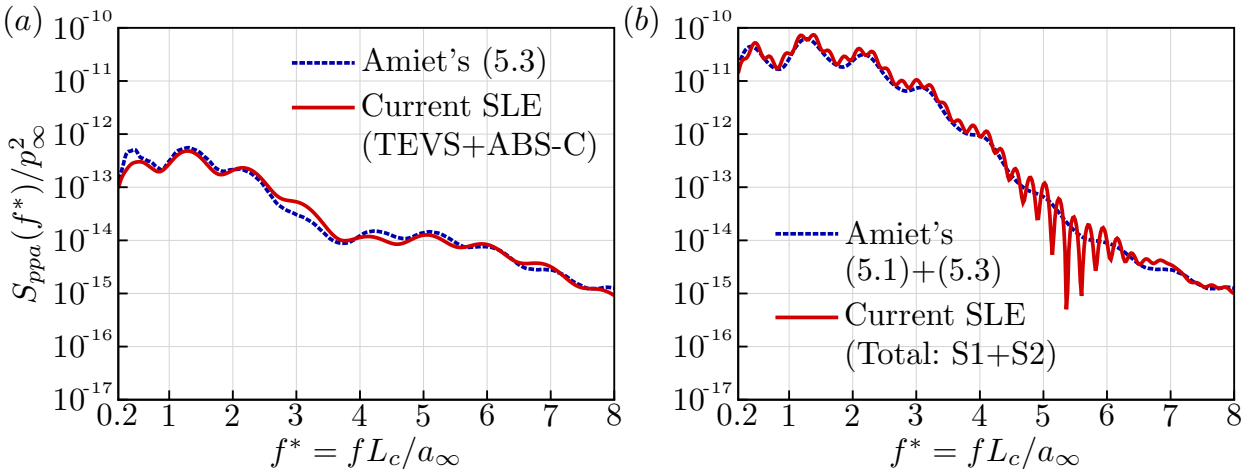

Figure 5.12: Amiet's model predictions of the acoustic power spectra at $\boldsymbol{x}_o/L_c = (0, 5, 0)$: (a) by using (5.6) for TEVS and ABS-C; and, (b) by adding (5.4) and (5.6) to represent a combination of LEVS, TEVS, ABS-A and ABS-C (without complete phase interactions between them). The current simulation result (Total: S1+S2) includes all noise sources (LEVS, TEVS and ABS-A to D) and their phase interactions. The S_{QQ} term required in (5.6) is calculated by using the simulation data (Δp_w) consisting of TEVS and ABS-C.

the dominance of TEVS at high frequencies should be addressed as a matter of priority. In this regard we suggest employing Amiet's second prediction model (Amiet, 1976) developed for TE scattering of boundary-layer turbulence (self-noise) and its acoustic backscattering at LE. The two-dimensional version (for an infinite span) of the self-noise model has been derived by Sandberg & Sandham (2007) as

$$\left.\begin{aligned} S_{ppa\text{-Amiet2}}(k_x) = -\frac{\beta^2\mu_0^2}{16}(y_{TE}-y_o)^2 \iint \frac{S_{QQ}(x_1,x_2,k_x)}{R(x_1)R(x_2)} \times \\ H_1^{(2)}(S(x_1))H_1^{(1)}(S(x_2))\mathrm{d}x_1\mathrm{d}x_2 \\ R(x) = \sqrt{(x-x_o)^2+\beta^2(y_{TE}-y_o)^2}, \quad S(x) = \mu_0[M_\infty(x-x_o)+R(x)] \end{aligned}\right\}, \tag{5.6}$$

where $\mu_0 = M_\infty L_c k_x/(2\beta^2)$; $\beta = (1-M_\infty^2)^{1/2}$; $H_1^{(1)}$ and $H_1^{(2)}$ are the first-order Hankel functions of the first and second kinds, respectively; and, S_{QQ} is the cross-PSD of Δp_w over the aerofoil surface. This model is able to accommodate TEVS and ABS-C (via S_{QQ}) although they are not produced by a turbulent boundary layer. The calculated values of (5.6) are presented in figure 5.12 compared with the current simulation data. Again it is demonstrated that the analytical predictions and the simulation data agree very well each other. However, a more important message delivered here is that the Amiet's interaction-noise model (5.4) is in fact incomplete without an additional term to describe the dominance of TEVS at high frequencies. The self-noise model (5.6) used here for this purpose, however, relies on the term S_{QQ} that is not given/known a priori (unlike Φ_{vv}), which poses significant limitations in practice. Also, additional capability to model the impact of WLE on the secondary sources is an additional challenge.

The result shown above also implies that some of the previous experimental measurements (Chaitanya *et al.*, 2017; Narayanan *et al.*, 2015) might contain a noticeable signature of the TEVS

Grid resolution level	N_ξ	N_η	N_ζ	$\Delta x_{min}/L_c$	$\Delta y_{min}/L_c$	CPW at $\boldsymbol{x}_o$
$Re_\infty = 40,000$, $\epsilon = 0.0377$, two-dimensional						
Level 1	1600	960	-	0.0020	0.0020	5.71
Level 2	1760	1056	-	0.0020	0.0010	6.55
Level 3	1920	1152	-	0.0018	0.0008	7.64
$Re_\infty = 400,000$, $\epsilon = 0.0377$, two-dimensional						
Level 1	1600	1120	-	0.0020	0.000350	7.13
Level 2	1920	1232	-	0.0018	0.000315	8.52
Level 3	2240	1344	-	0.0016	0.000280	10.02
$Re_\infty = 400,000$, $\epsilon = 0.377$, three-dimensional						
Level 1	1600	1120	32	0.0020	0.000350	7.13
Level 2	1920	1232	35	0.0018	0.000315	8.52
Level 3	2240	1344	38	0.0016	0.000280	10.02
$Re_\infty = 800,000$, $\epsilon = 0.377$, two-dimensional						
Level 1	1600	1120	-	0.0020	0.000200	7.08
Level 2	1920	1232	-	0.0010	0.000180	8.46
Level 3	2240	1344	-	0.0008	0.000120	9.98

Table 5.1: Grid resolution levels used for the four grid-dependency tests shown in figure 5.13. N_ξ, N_η and N_ζ denote the number of grid cells used in the streamwise, vertical and spanwise directions, respectively. Δx_{min} is the smallest cell size used at LE and TE of the aerofoil. CPW (cells per wavelength) indicates the number of grid cells used across the acoustic wavelength at the frequency of $f^* = 8$. CPW is measured at the far-field observer location $\boldsymbol{x}_o/L_c = (0, 5, 0)$.

dominance at high frequencies. The earlier experimental work consistently speculated that the high-frequency range of their aerofoil-turbulence interaction noise spectra was masked by the contribution of self-noise. While this is a reasonable speculation, the current study reveals that the high-frequency range may still be dominated by the TEVS event due to the freestream turbulence rather than the boundary-layer turbulence. Therefore it is suggested that the experimental data should be carefully re-examined to clarify whether the self-noise was truly the major contributor to the high-frequency range (or not).

5.5 The effect of flow viscosity on TE vortex scattering

In this section we move beyond the inviscid theory to investigate the effects of viscous dissipation and vortex-boundary layer interaction on the AVI problem. In particular how it affects the contribution from TEVS. We consider viscous flow at three Reynolds numbers, $Re_\infty = 4.0 \times 10^4$, 4.0×10^5 and 8.0×10^5. The majority of the simulations are two-dimensional which significantly saves computation cost while also ensuring boundary layer transition effects are avoided at the higher Reynolds number. It is preferable to avoid boundary layer turbulence as the resulting self-noise will interfere with the TEVS event. The aim here is not to investigate how secondary vortices interact with turbulence altering the self-noise, but rather to determine if TEVS is significant in a viscous flow.

5.5.1 Grid independence study for viscous simulations

This section provides the validation of the set-up used for viscous simulations. Three different levels of grid resolution are considered for four cases the details of which are given in table 5.1. Level 3 is selected as the chosen resolution for each of the cases. The far-field acoustic spectra ($S_{ppw}(x, z, f^*)/p_\infty^2$) is compared for the three grid levels at the observer $\boldsymbol{x}_o/L_c = (0, 5, 0)$ in figure 5.13. Each case considers a finite chord flat plate with a SLE. Two vortex strengths and three Reynolds numbers are investigated. Figure 5.13(a) considers a two dimensional flow at $Re_\infty = 4{\times}10^4$ with low impinging vortex strength $u_{max} = 0.025u_\infty$. There is very good agreement for all three grid levels until approximately $f^* = 7$. Beyond this point the coarser grids over predict the sound level, and fail to detect the peak at $f^* = 7.8$ associated with shedding at the TE. The low magnitude (approx 10^{-17}) suggests this may be caused by an increased level of spurious noise on the coarser grids. Figure 5.13(b) considers the same vortex at increased Reynolds number $Re_\infty = 4{\times}10^5$. The medium and fine grid levels show some disagreement in terms of the size of oscillations especially at high frequency. However, generally there is a good match for the shape and magnitude of the spectra. The coarse grid on the other hand significantly under resolves frequencies beyond $f^* = 8$. Figure 5.13(c) considers a three-dimensional flow at the same Reynolds number and with higher vortex strength ($u_{max} = 0.25u_\infty$). A similar result is obtained for all three levels of grid resolution, albeit with some variation in the phase oscillations occurring at high frequencies. As demonstrated in §6.2 the phase oscillations are determined primarily by the emission time of sound at the TE. In order for this aspect to fully converge the full range of scales exhibited by the secondary disturbances needs to be resolved which is a challenging task at such high Reynolds numbers. Despite this, it is clear from figure 5.13(c) that the current grids are capable of capturing at least the general acoustic trends (e.g. which source is dominant) by obtaining the correct magnitude and shape of the spectra. Finally, in figure 5.13(d) the grid is tested for a strong vortex interaction in a two-dimensional flow at $Re_\infty = 8{\times}10^5$. The outcome is similar to the previous case, although the differences in LE-TE phase oscillations are more apparent since TEVS is comparable to the LEVS over a wider frequency range. The current grid (level 3) is sufficient to compare the effect of Reynolds number on the approximate magnitude of the high frequency sources. Comparing the current results to higher resolution simulations where the full range of scales is captured would be useful (particularly in 3D), but this is beyond the scope of the current work.

5.5.2 Weak vortex interactions

Firstly the boundary layer u-velocity and skin friction coefficient profiles (C_f) are compared to the Blasius solution in figure 5.14. Generally there is good agreement except very close to the TE where the Blasius solution begins to break down. In figure 5.15(a-b) the acoustic pressure signals and spectra are shown for the default observer $\boldsymbol{x} = (0, 5L_c, 0)$ under inviscid, $Re_\infty = 4.0 \times 10^4$, and 4.0×10^5 flow conditions. It is clear from figure 5.15(b) how the high frequencies begin to converge towards the inviscid case as the Reynolds number is increased. For the lowest Reynolds number

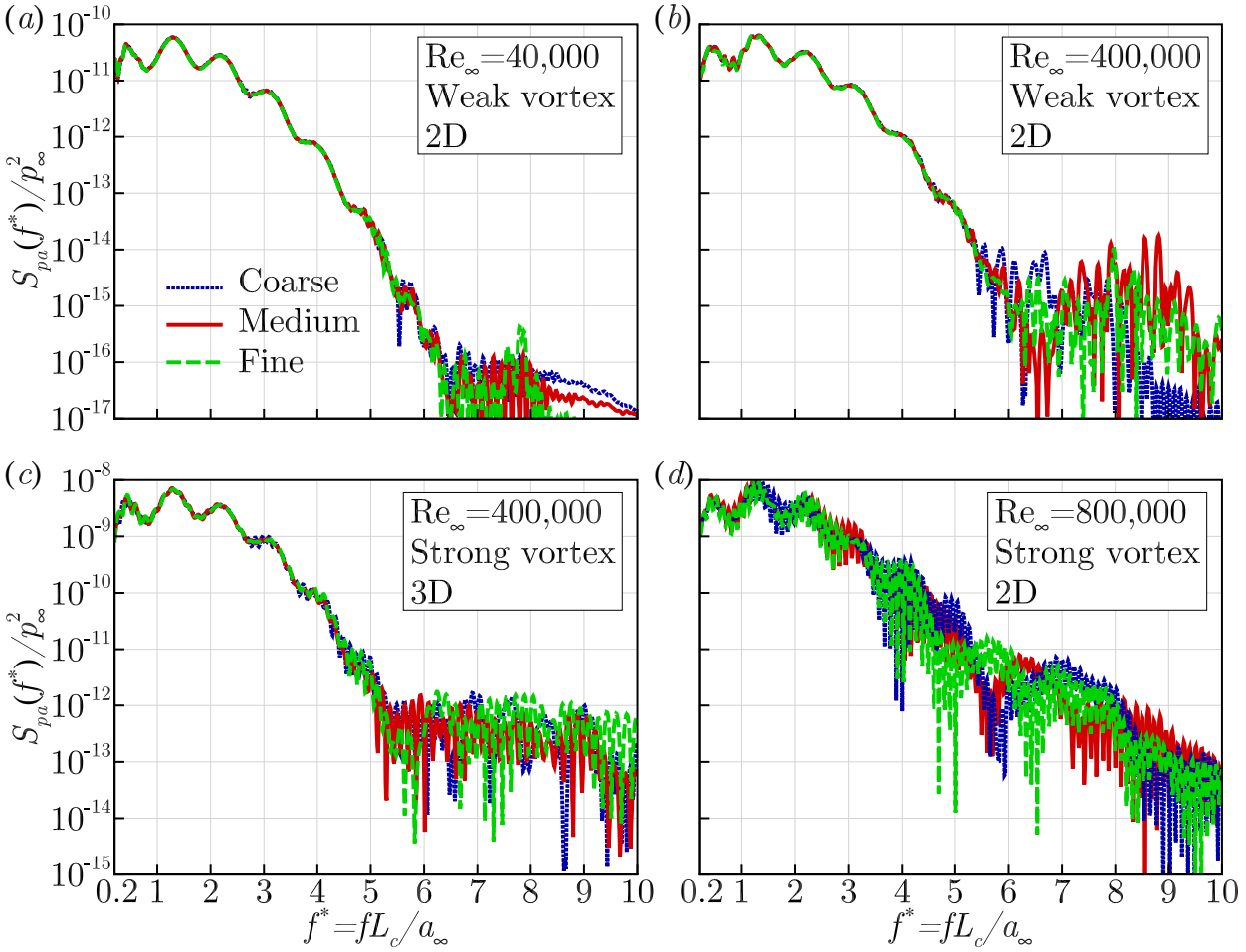

Figure 5.13: Results of the current grid-dependency test by using three different levels of grid resolution described in table 5.1: (*a*) acoustic power spectra obtained at $\boldsymbol{x}_o/L_c = (0, 5, 0)$ for $Re_\infty = 4{\times}10^4$ weak vortex interaction 2D; (*b*) $Re_\infty = 4{\times}10^5$ weak vortex interaction 2D; (*c*) $Re_\infty = 4{\times}10^5$ strong vortex interaction 3D; (*d*) $Re_\infty = 8{\times}10^5$ strong vortex interaction 2D.

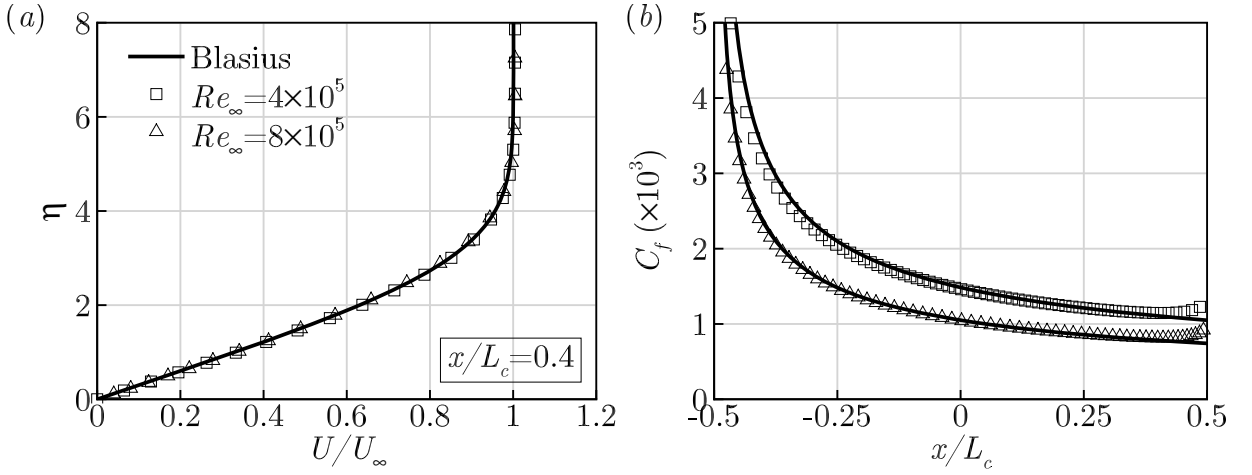

Figure 5.14: Boundary layer profiles obtained two Reynolds numbers $Re_\infty = 4.0 \times 10^5$ and 8.0×10^5: (*a*) streamwise velocity profile at $x/L_c = 0.4$; (*b*) skin friction coefficient $C_f = 2\tau_w/(\rho U_\infty^2)$.

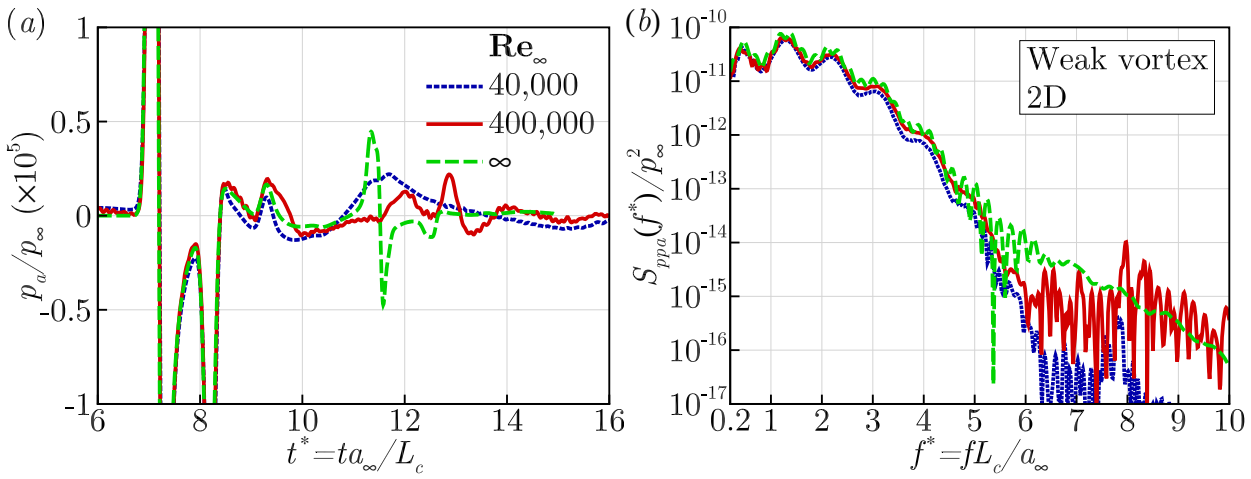

Figure 5.15: Comparison of the acoustic pressure data obtained at the observer location $\boldsymbol{x}_o/L_c = (0, 5, 0)$ for a weak vortex interaction (2.5% strength) at Reynolds numbers 40,000, 400,000 and ∞. (a) time signals, (b) corresponding PSD.

and most dissipative case the high frequency components of the vortex (and associated convective disturbances) are almost entirely eliminated before they can reach the TE, resulting in reduced magnitude low-frequency pressure signature from TEVS. As a result the spectra is reminiscent of the LEVS+ABS-A solution figure 5.11(b), with exception of additional phase oscillations observed at very high frequency. As the Reynolds number is increased to 4.0×10^5 the acoustic pressure time signal displays a clear compression-expansion pulse at around $ta_\infty/L_c = 13$ as well as an increased level of broadband noise for frequencies $f^* > 6$. Both of these observations are consistent with trends observed for TEVS in inviscid flow. Additionally the time signal contains small oscillations of consistent period ≈ 0.125. These oscillations are caused by vortex shedding in the wake which is triggered by the passing of the LEVS wave past the TE. The wake shedding manifests as a tone at $f^* \approx 8$ corresponding to the observed shedding period.

5.5.3 Impact of high vortex strength

The previous results demonstrate how increasing the Reynolds number increases the significance of TEVS due to weaker dissipative effects. This suggests that altering the vortex strength will also increase the TEVS response. Additional simulations are carried out based on a stronger vortex disturbance using the same shape function. The maximum velocity perturbation of the high strength vortex is $|u'| = 0.25U_\infty$, which is obtained with $\sigma = 0.377$. This is more comparable to that encountered in helicopter rotor noise than turbomachinery applications. The strength parameter used here is selected to match the experimental work of Straus *et al.* (1990).

The development of the impinging vortex and secondary structures is shown in figure 5.16(a) which plots spanwise vorticity at four instances for $Re_\infty = 4.0 \times 10^5$: (i) the generation of secondary vortices after the impinging vortex is chopped by the LE; (ii) the vortex near the mid-chord; (iii) scattering of the vortex at the TE; (iv) scattering of secondary disturbances at the TE. As

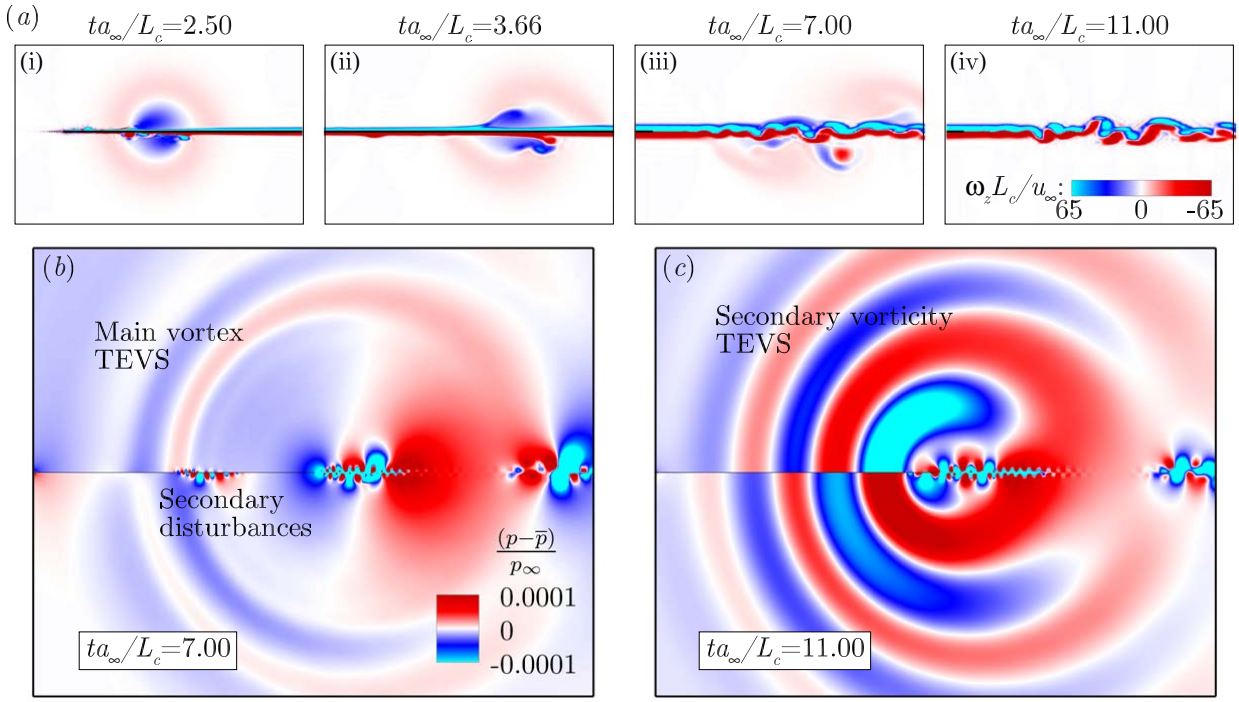

Figure 5.16: (*a*) Spanwise vorticity $\omega_z L_c/u_\infty$ contours obtained at four instances for $Re_\infty = 4 \times 10^5$ and $\sigma = 0.377$: (i) after the vortex is bisected by the LE; (ii) vortex near the mid-chord; (iii) vortex interacting with the wake; (iv) secondary vorticity interacting with the wake. (*b*-*c*) Corresponding acoustic pressure contours obtained during the last two vorticity snapshots.

the vortex convects the upper and lower halves begin to separate due to reversed image vortex induced velocities (this is particularly severe due to the high vortex strength). The main vortex and upwash stroke secondary vorticity convect more quickly on the aerofoil lower side, while the downwash vorticity convects at a lower speed causing it to collide with the main vortex. There is also a strong disparity between the secondary vortices on either half, which are significantly stronger on the lower side. The disturbances are primarily contained within the boundary layer but can be clearly observed by their acoustic pressure signature in 5.16(*b*). For high vortex strength viscous cases the TEVS can be clearly separated into two categories: TEVS-1, caused by scattering of the bisected vortex which resides outside of the boundary layer; TEVS-2 caused by scattering of disturbances inside the boundary layer including secondary vortices generated at the LE. Both events are present in figure 5.16(*b*) and (*c*) which show acoustic pressure contours near the TE at time instances $ta_\infty/L_c = 7.0$ and 11.0 respectively.

Figure 5.17(*a*-*b*) shows similar analysis as figure 5.15 for the high strength vortex case at Reynolds numbers $Re_\infty = 4.0 \times 10^5$, and 8.0×10^5. The TEVS-2 fluctuations are substantially larger relative to TEVS-1 with comparable magnitude to ABS-A. In terms of spectra, a similar level is obtained at both Reynolds numbers for most of the frequency range. Relative to the weak vortex cases (figure 5.15) phase oscillations are more severe, suggesting competing sources exist over a wider range of frequencies. The phase oscillations also have shorter wavelength due to a larger time lag between LEVS:TEVS-2, relative to LEVS:TEVS-1. This is a consequence of slower convection speeds in

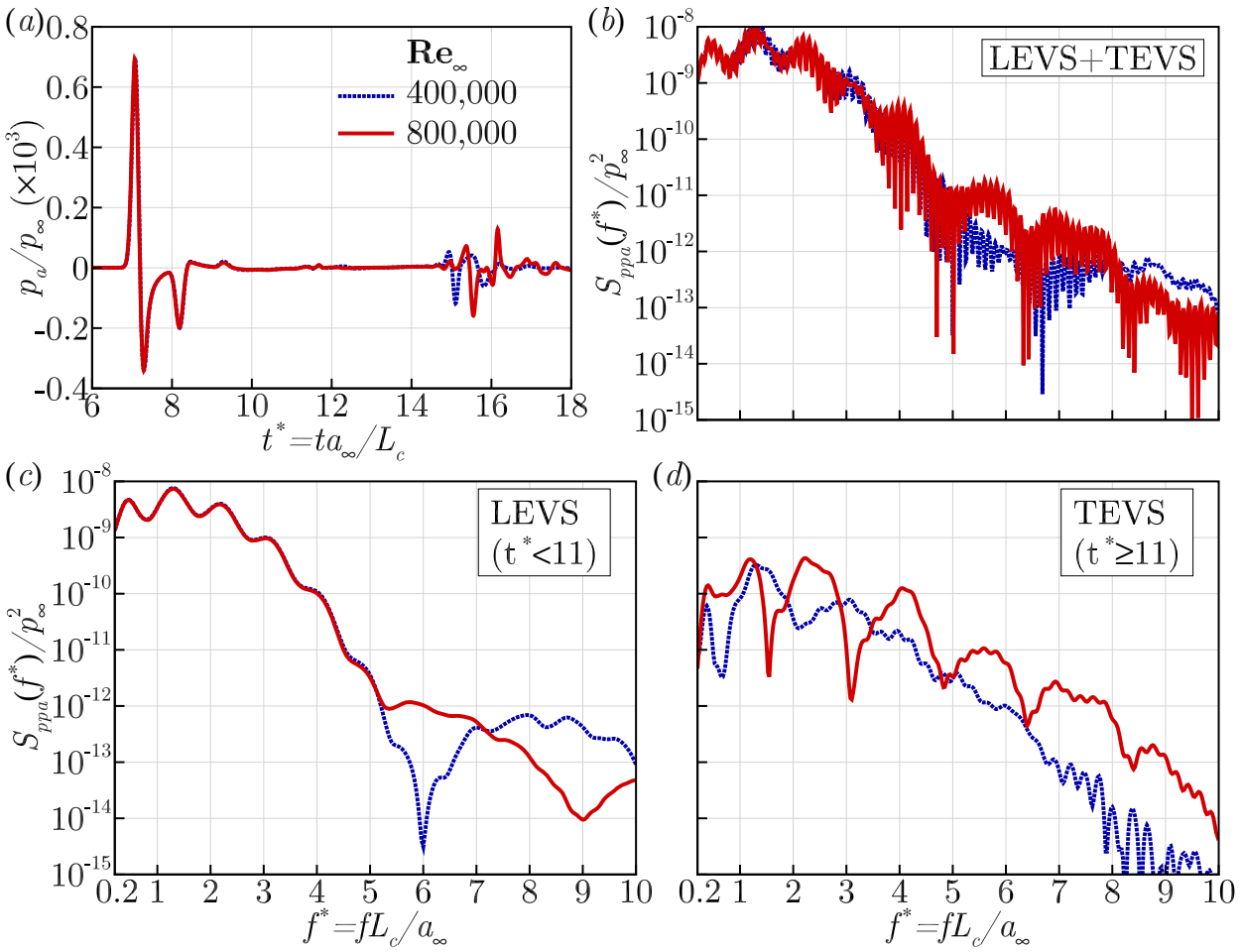

Figure 5.17: Comparison of the acoustic pressure data obtained at the observer location $\boldsymbol{x}_o/L_c = (0, 5, 0)$ for a strong vortex interaction (25% strength) at Reynolds numbers 4×10^5 and 8×10^5. (a) time signals of $p_a(\boldsymbol{x}_o, t)/p_\infty$; (b) the corresponding power spectra; (c) Power spectra obtained for $t^* < 11$ (approximate LEVS contribution + ABS A+B); (c) Power spectra obtained for $t^* \geq 11$ (approximate TEVS contribution + ABS C+D).

the boundary layer. Figure 5.17$(c$-$d)$ shows a comparison of the LEVS and TEVS noise produced at the two Reynolds numbers. It is not possible to extract the isolated TEVS signal through the same procedure as the inviscid cases as the approach will interfere with boundary layer profile. Additionally, the principle of linear superposition is no longer a reasonable assumption due to non-linear effects caused by high vortex strengths. Alternatively in figure 5.17 the LEVS and TEVS contributions are approximated by a simple windowing procedure. The LEVS solution is obtained by considering $t^* < 11$, whereas TEVS is obtained for $t^* \geq 11$. A tapered cosine window is applied before taking the Fourier transform to ensure the signals are periodic. This interpretation of the sources also contains contributions from relevant ABS events (ABS-A & B for LEVS, ABS-C & D for TEVS). The approach is therefore a way to quantify the total impact of TEVS concurrently (since ABS-C & D are outcomes of TEVS). Comparatively the $Re_\infty = 8.0 \times 10^5$ case displays significantly increased levels of TEVS for $f^* \gtrapprox 5$. This result is consistent with the weak vortex trend and suggests as viscosity is reduced TEVS becomes stronger at high frequencies.

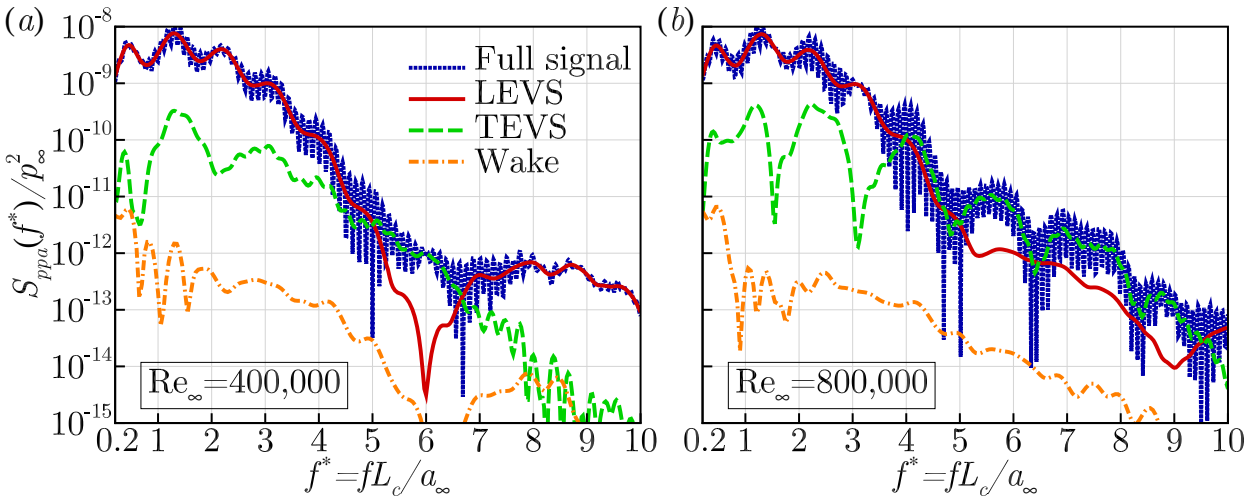

Figure 5.18: Comparison of approximate LEVS, TEVS and wake noise contributions to the overall acoustic spectra. Each component is obtained by windowing the time signal $t^* < 11$ for LEVS, $t^* \geq 11$ for TEVS, $10 \geq t^* \leq 14$ for wake. LEVS and TEVS solutions also contain ABS A+B, and C+D components respectively. (a) $Re_\infty = 4.0 \times 10^5$; (b) $Re_\infty = 8.0 \times 10^5$.

In figure 5.18 LEVS, TEVS and wake contributions are re-plot and compared against each other. For the lower Reynolds number the TEVS component becomes dominant in the range $5 \leq fL_c/a_\infty \leq 6.6$. TEVS dominance does not persist beyond this upper band due to an increase in the high frequency content of the LEVS noise. The high frequency LEVS contribution is not registered in the weaker vortex case, and is likely associated with non-linear effects at the LE due to the high vortex strength. Much more strikingly for $Re_\infty = 8.0 \times 10^5$ the TEVS shows levels typically around 10 dB higher than LEVS from $fL_c/a_\infty = 4$ onwards. Approximate contributions from the wake shedding are made by considering the time signals in the range $10 \leq t^* \leq 14$, where there is no significant LEVS, ABS or TEVS sound. In both cases the wake noise is at least two orders of magnitude lower than the TEVS for the majority of frequencies.

5.5.4 Three-dimensional effects

The next logical step in the current investigation is to extend the analysis to account for three-dimensional effects on the development of the convective vortical structures. To this end the $Re_\infty = 4.0 \times 10^5$ strong vortex simulation is rerun with a finite span $L_z = 0.05L_c$. It is expected that the results will be sensitive to the chosen span, however the current set-up should be sufficient to demonstrate some of the differences with the two-dimensional flow presented in the previous section.

Figure 5.19(a) and (b) shows of the flow structures generated by the three-dimensional case at time instants $ta_\infty/L_c = 4.33$ and 8.66 respectively. The plots show iso-surfaces of spanwise vorticity $\omega_z L_c/u_\infty$ with 50 contour levels as well as the acoustic pressure in the xy-plane. Spanwise vorticity is selected as it is directly linked to the TE noise (5.2).

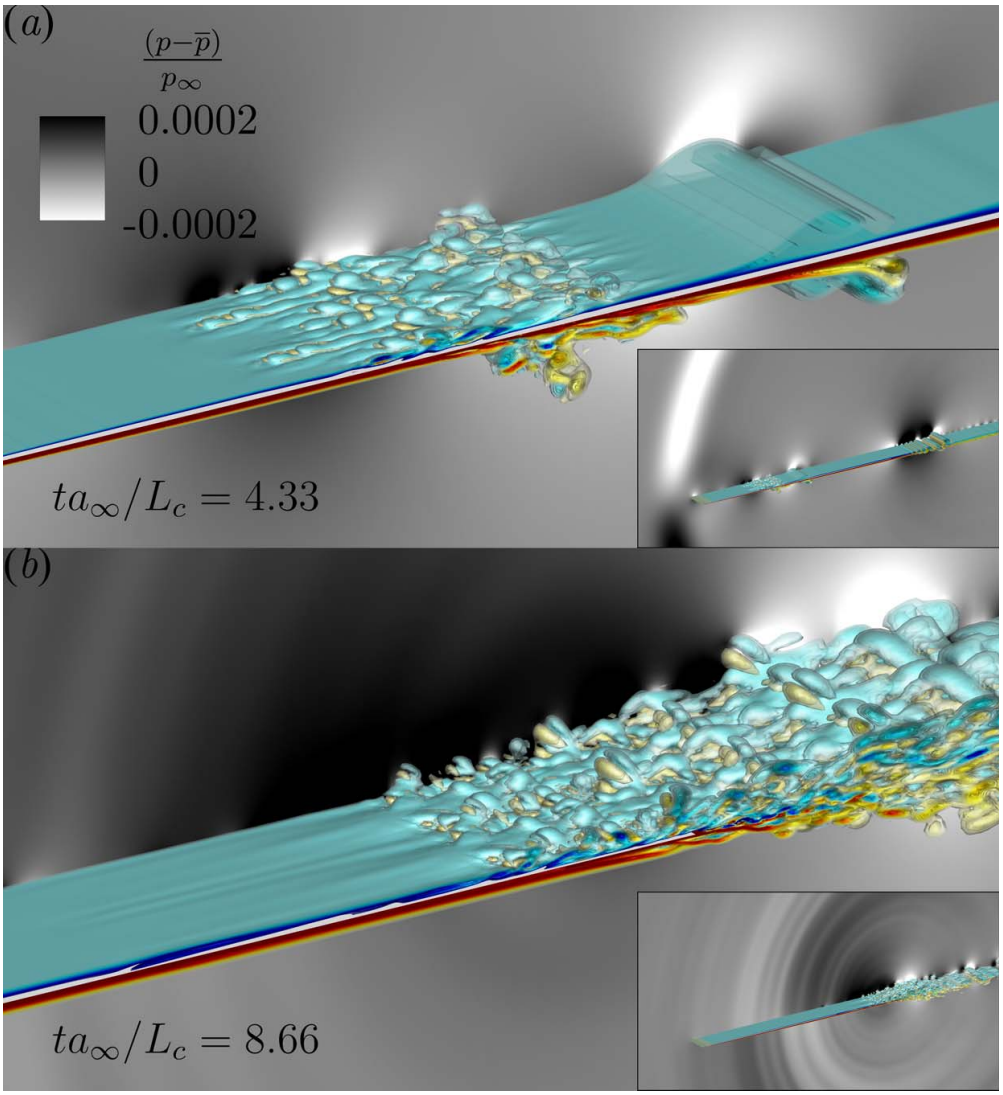

Figure 5.19: Iso-surfaces of spanwise vorticity $\omega_z L_c/u_\infty$ (50 levels shown) and contours of acoustic pressure p_a/p_∞ obtained for the 3D $Re_\infty = 4.0 \times 10^5$ ($\epsilon = 0.377$) case shortly after the vortex has convected past the LE at $ta_\infty/L_c = 4.33$ (a). $ta_\infty/L_c = 8.66$, as the secondary vorticity passes the TE (b). Solution repeated in span for visualisation.

In figure 5.19(a) the chopped vortex is shown near the mid-chord. The trailing secondary structures (which are initially uniform in span) have been broken down into smaller three-dimensional eddies (which are referred to as tertiary structures in this work). Spanwise non-uniformity of the secondary structures occurs rapidly near the LE particularly for the structures generated during the upwash (second) stroke. Comparatively the downwash stroke structures show some similarity to the two-dimensional flow in figure 5.16(a)(i)-(ii) until a later time. Unlike the two-dimensional flow the secondary structures protrude significantly from the BL due to the increased mixing caused by streamwise components of vorticity. This results in an earlier interaction at the TE due to higher convection speeds. It should be noted that the three-dimensional flow behaviour is not observed for the weak vortex interaction (not presented here).

Figure 5.19(b) shows the scattering of the secondary structures at the TE. It is clear how the

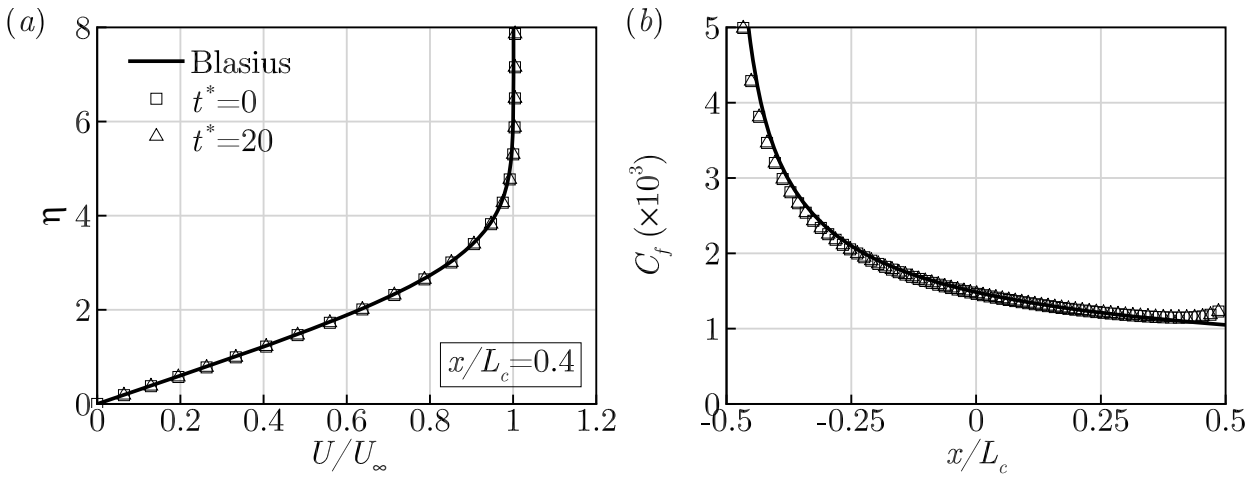

Figure 5.20: Boundary layer profiles taken at $t^* = 0$ and $t^* = 20$ (before and after the aerofoil-vortex interaction) for the 3D $Re_\infty = 4.0 \times 10^5$ simulation ($\epsilon = 0.377$): (a) streamwise velocity profile for $x/L_c = 0.4$; (b) skin friction coefficient $C_f = 2\tau_w/(\rho U_\infty^2)$.

radiated sound field contains smaller lengths scales relative to the two-dimensional case in figure 5.16. It is also worth noting that the three-dimensional flow is entirely transient meaning the boundary layer profile returns to the laminar solution after the vortex has passed the TE, see figure 5.20. Categorising the noise in this case is somewhat of a grey area. As previously demonstrated TEVS is also observed in inviscid flow, however development of the secondary eddies relies on interaction within the boundary layer. Arguments could therefore be made for either interaction noise or boundary layer self-noise.

A comparison of the TEVS noise with the two-dimensional solution is shown in figure 5.21(a) for a 90 degree observer angle. The 3D flow produces more noise in the high frequency range $6 \leq f^* \leq 8$ and less at low frequencies which is indicative of the reduced lengths scales of the secondary structures. Figure 5.21(b) compares the directivity pattern for $f^* = 7$. There is some asymmetry between upper and lower half planes especially for the the three-dimensional solution. Increased TEVS noise is exhibited for all observer angles in the lower half and for angles less than 120 degrees on the upper half plane.

Figure 5.22 compares LEVS and TEVS sources obtained in the three-dimensional simulation based on the windowing procedure outlined in section 5.5.3. The acoustic spectra at a 90 degree observer is shown in figure 5.22 (a). The LEVS source is comparable to that demonstrated in the two-dimensional flow at the same Reynolds number. The TEVS also becomes dominant in a similar range $5.7 \leq f^* \leq 6.7$, but also remains comparable to LEVS for larger frequencies. Directivity patterns of LEVS and TEVS are shown at three frequencies $f^* = 6.0, 6.5$ and 7.5 in figure 5.22 (a-c). For $f^* = 6.0$ the LEVS solution radiates more significantly in the lower half plane which allows TEVS to dominate in the upper halve. TEVS also makes a significant contribution for upstream angles in the lower half plane. A similar trend is observed for $f^* = 6.5$ where TEVS is the largest source for $44 \leq \theta \leq 169$ and $190 \leq \theta \leq 244$ by up to 10.5 dB. Finally for $f^* = 7.5$ the TEVS dominance is restricted to upstream angles approximately in the range $130 \leq \theta \leq 240$.

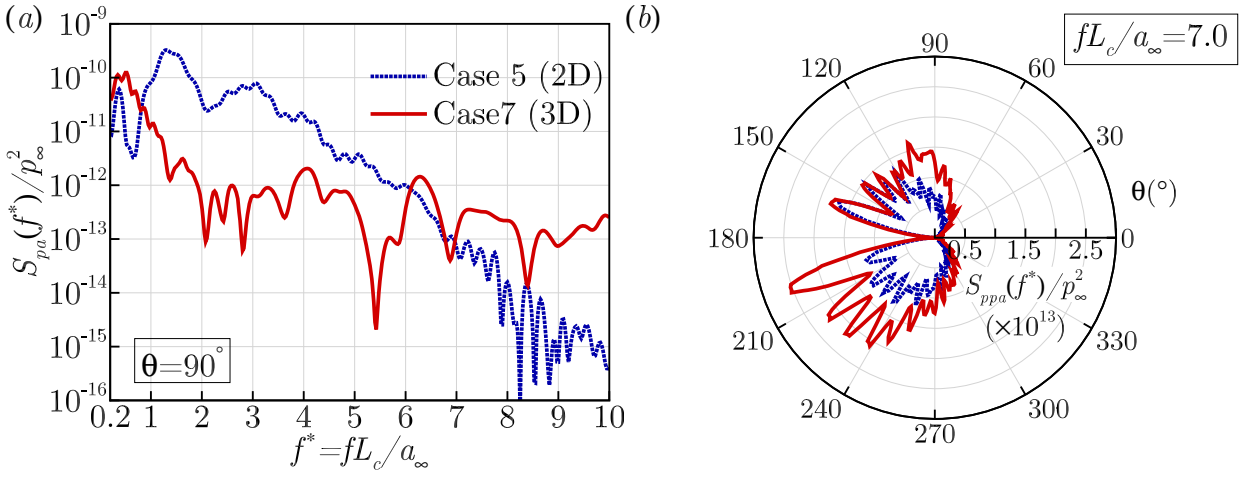

Figure 5.21: Comparison of acoustic pressure data obtained for 2D and 3D simulations for $Re_\infty = 4.0 \times 10^5$ and $\epsilon = 0.377$. The TEVS signals are obtained through the windowing procedure outlined in section 5.5.3: (a) power spectra of acoustic pressure at $\boldsymbol{x}_o/L_c = (0, 5, 0)$;; (b) directivity profiles for $fL_c/a_\infty = 7.0$.

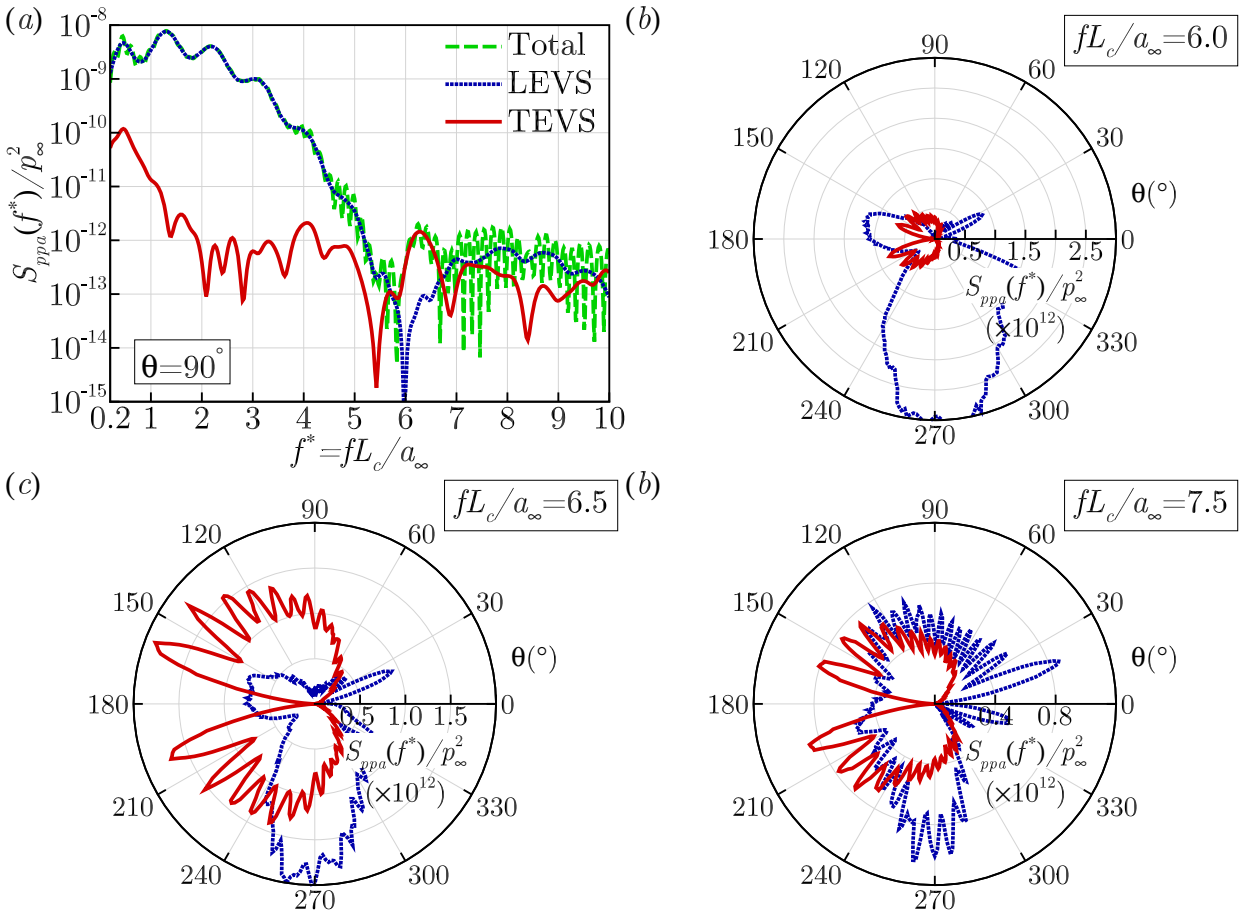

Figure 5.22: Power spectra comparison for LEVS and TEVS obtained for the 3D $Re_\infty = 4.0 \times 10^5$ simulation at $\boldsymbol{x}_o/L_c = (0, 5, 0)$ (a). Directivity profiles (linear scale) at frequencies $fL_c/a_\infty = 6.0, 6.5$ and 7.5 where TEVS is the dominant source of noise $(b\text{-}d)$. The TEVS and LEVS components are obtained through the windowing procedure outlined in section 5.5.3 which also includes ABS components.

5.6 Concluding remarks

Detailed high-resolution numerical simulations have successfully been conducted to study the secondary noise sources that are generated in the event of interaction between a vortical flow and a flat-plate aerofoil. The identified secondary noise sources are TEVS (TE vortical scattering) and ABS (acoustic backscattering) as opposed to the primary source, LEVS (LE vortical scattering). In-depth investigations have been made on each of the individual sources by accurately splitting the numerical solutions for each. This is achieved by manipulating the time signals of finite chord (total noise), downstream semi-infinite chord (primary noise), and upstream semi-infinite chord (vortex-trailing edge noise) aerofoil simulations.

Linearised analytical theory predicts a complete cancellation of vortex scattered sound at the TE with Kutta condition shed vorticity. However, if non-linear effects are included the cancellation is not complete, and noise may radiate from the TE during AVI. It is suspected by the author that the secondary vorticity generated at the LE plays an important role in the generation of TEVS. The secondary vorticity is nearest to the wall, and therefore is most severely effected by image vorticity induced velocity. The interaction between the two sources of vorticity results in asymmetric vortex distribution and therefore a pressure jump which near the TE.

At low frequencies the ABS is the more prominent secondary effect (particularly in the downstream direction), while at high frequencies the TEVS scattering takes over. The power spectrum relating to the TEVS decays at a lower rate relative to the LEVS, predicted by Amiet's TE and LE analytical models respectively (Amiet, 1975, 1976)). As a consequence TEVS dominates all the other sources beyond a certain threshold, despite significant reduced acoustic pressure magnitude due to TE cancellation. This means that TEVS was effectively the primary source at high frequencies, contrary to historical analytical approaches.

The effect of vertical offset during the interaction is also investigated concerning the validity cut-off for linear approaches (where TEVS effects become negligible). The TEVS is found to make a significant contribution to the acoustic pressure signal even for relatively large miss distances. The high frequency contribution to the noise is shown to decrease with offset, however it extends well beyond the expected range where image vortex effects are anticipated to be negligible.

Finally a series of viscous laminar simulations are conducted in order to verify the existence of TEVS in a viscous flow. It is demonstrated how TEVS depends heavily on the Reynolds number and vortex strength. Essentially for a TEVS event to occur the secondary vorticity must convect through the boundary layer without being significantly dissipated at high frequencies. Somewhat ironically, this means analytical methods which typically neglect the boundary layer are most effective when the flow is highly viscous.

Chapter 6

The Effect of WLEs on Secondary Sources

Following directly from the previous chapter on secondary interaction noise mechanisms, this chapter aims to investigate the impact of secondary sources on WLE noise reduction. In depth analysis is provided in the following sections concerning the time signals and noise reduction spectra in §6.1, secondary source phase relationships in §6.2, and acoustic directivity in §6.3. Following this in §6.4 results are presented for undulated trailing edges, with the purpose of reducing the TEVS noise. As was shown in the previous section the secondary mechanisms (particularly TEVS) are highly susceptible to flow conditions including vortex strength and Reynolds number. For this reason we choose to focus primarily on the most sever case, an inviscid flow. This may also provides insight for analytical modelling of WLEs which typically follows an inviscid approach Ayton (2017); Lyu & Azarpeyvand (2017); Mathews & Peake (2018). Regardless, in §6.5 a viscous study is conducted and contrasted to the results in §5.5. The outcome highlights some concerns for the WLE geometry which represents the principle future work of this study.

6.1 The secondary sources associated with a wavy leading edge

Acoustic pressure data for both SLE and WLE cases is shown in figure 6.1. As in the previous section the data is collected at a single observer location $\boldsymbol{x}_o/L_c = (0, 5, 0)$ that is five chords above the finite-chord aerofoil's centre (as highlighted in figure 6.1*c*). The time signals and the corresponding power spectral density are shown in figures 6.1*a* and *b* respectively for all four cases (semi-infinite + finite chord length, SLE and WLE). Figure 6.1*d* shows the noise reduction – a beneficial effect of using a WLE – varying with frequency, where the semi-infinite-chord case has been studied in detail in chapters §3 to §4. The new result of the finite-chord case reveal significant differences to the earlier semi-infinite-chord case, which indicates profound effects of the secondary sources due to the presence of TE. Detailed investigations into the secondary sources in relation with the WLE are followed below.

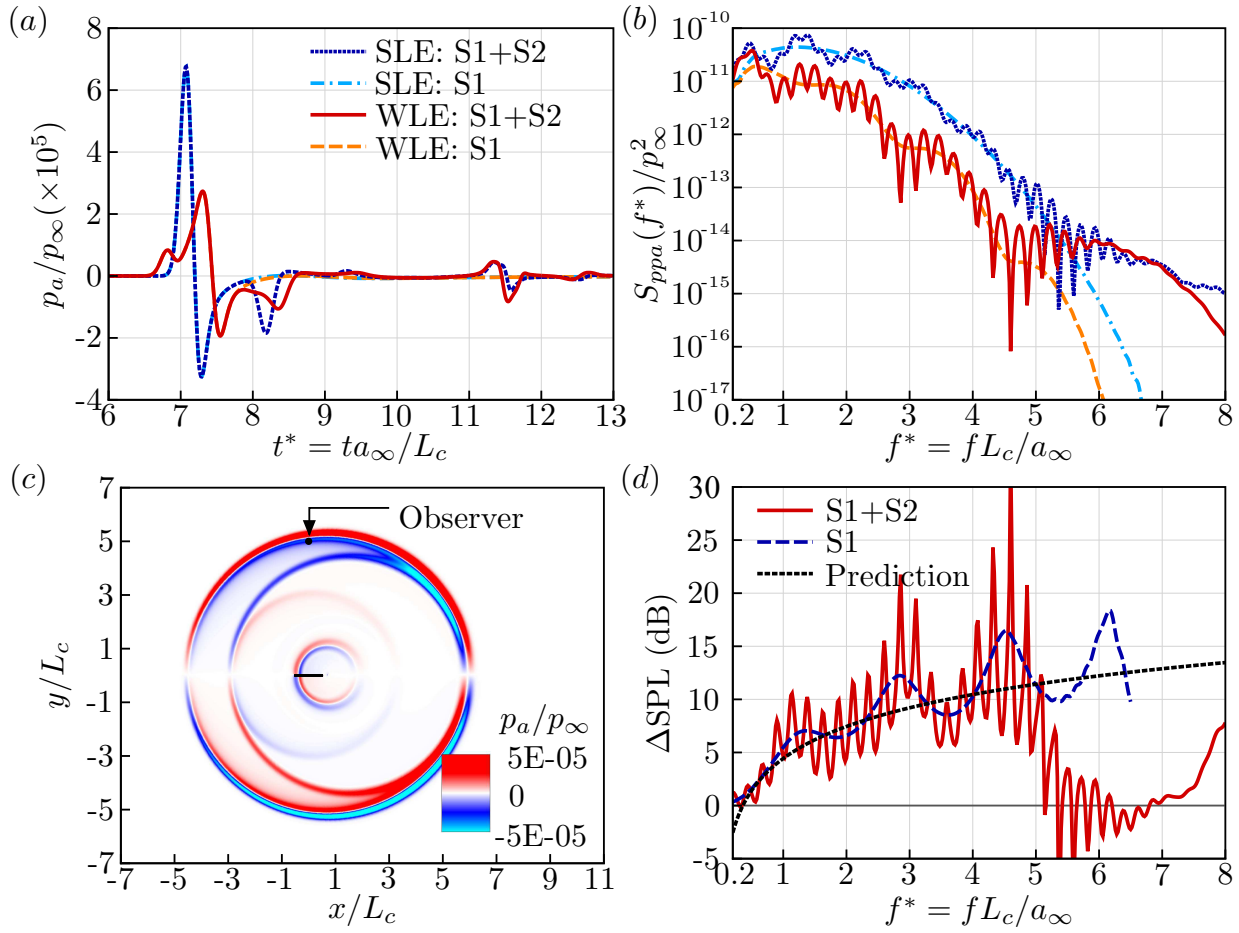

Figure 6.1: Acoustic pressure data obtained at an observer location from the current simulations with two different LE geometries (SLE and WLE) and two different chord lengths (finite and semi-infinite, where the former includes all noise sources and the latter contains S1 only): (a) time signals of $p_a(\boldsymbol{x}_o, t)/p_\infty$ where $\boldsymbol{x}_o/L_c = (0, 5, 0)$; (b) the corresponding power spectra; (c) an instantaneous contour plot of $p_a(\boldsymbol{x}, t^* = 7.34)/p_\infty$ taken at the mid-span ($z = 0$) for the SLE finite-chord case; and, (d) the spectra of the noise reduction due to the WLE defined by (2.61) in comparison with a semi-empirical prediction by Chaitanya *et al.* (2017) ($\Delta\text{SPL} = 10\log_{10}(fh_{LE}/u_\infty) + 10$). It should be noted that the plot in (d) for the S1-only case is terminated at $f^* = 6.5$ due to the value of $S_{ppa}(f^*)/p_\infty^2$ for WLE falling below the lower bound of the machine accuracy (double precision used).

6.1.1 Initial findings

The first thing that can be observed in figure 6.1*b* is that the SLE and WLE cases produce almost identical spectra at the high frequencies ($f^* > 5$) when the secondary sources are involved. This leads to a loss of the noise reduction in the high-frequency range shown in figure 6.1*d*, which is a big contrast to the primary-source-only case where the noise reduction continues to increase with frequency. Additionally we notice that there are significant differences between the spectral oscillation for SLE and WLE cases. It is shown later in this section that the spectral oscillations are due to phase relationships between the noise sources (LEVS, TEVS and ABS), which involves the retarded source time difference between LE and TE. As can be anticipated from the previous

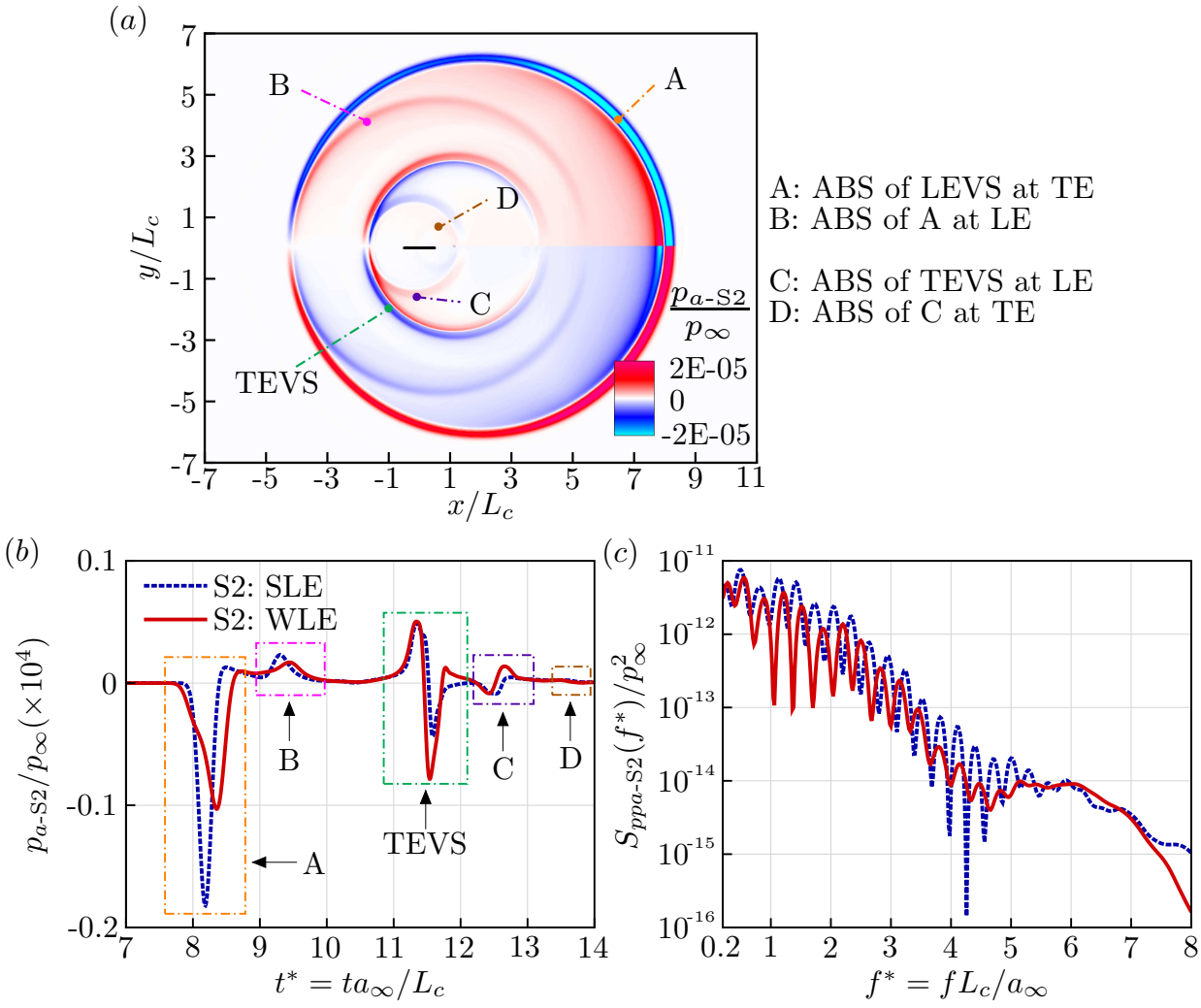

Figure 6.2: Acoustic pressure generated by the secondary sources (with the primary source excluded) obtained by using (5.1): (*a*) instantaneous contours of the acoustic pressure $p_{a\text{-S2}}/p_\infty$ at $t^* = 9.0$ from the SLE case; (*b*) the time signals of $p_{a\text{-S2}}/p_\infty$ obtained at the observer location $\boldsymbol{x}_o/L_c = (0, 5, 0)$ for the SLE and WLE cases; and, (*c*) the corresponding power spectra. The acronyms are defined in figure 5.1 (as well as in the text).

chapter, it is also shown later that the loss of noise reduction in the high-frequency range is related with the dominance of TEVS over the other sources at the high frequencies.

As in the previous section the equation (5.1) is implemented in order to focus on the secondary sources. Comparing the SLE and WLE cases in figure 6.2*b*, the acoustic waves A and B that are by-products of the LEVS are weaker in the WLE case and this is an expected result since the LEVS has already been weakened due to the WLE (see figure 6.1*a*). On the contrary, the later events that are caused by the TEVS exhibit a slightly amplified level of acoustic waves in the WLE case, which was not expected earlier. This finding suggests that the secondary source (TEVS) may have a negative impact on the noise reduction effect of WLE. It also implies that the vortex bisected and modified by the WLE, when it reaches TE, may produce stronger wall pressure fluctuations compared to the SLE counterpart. As a consequence, the noise reduction contributed from the

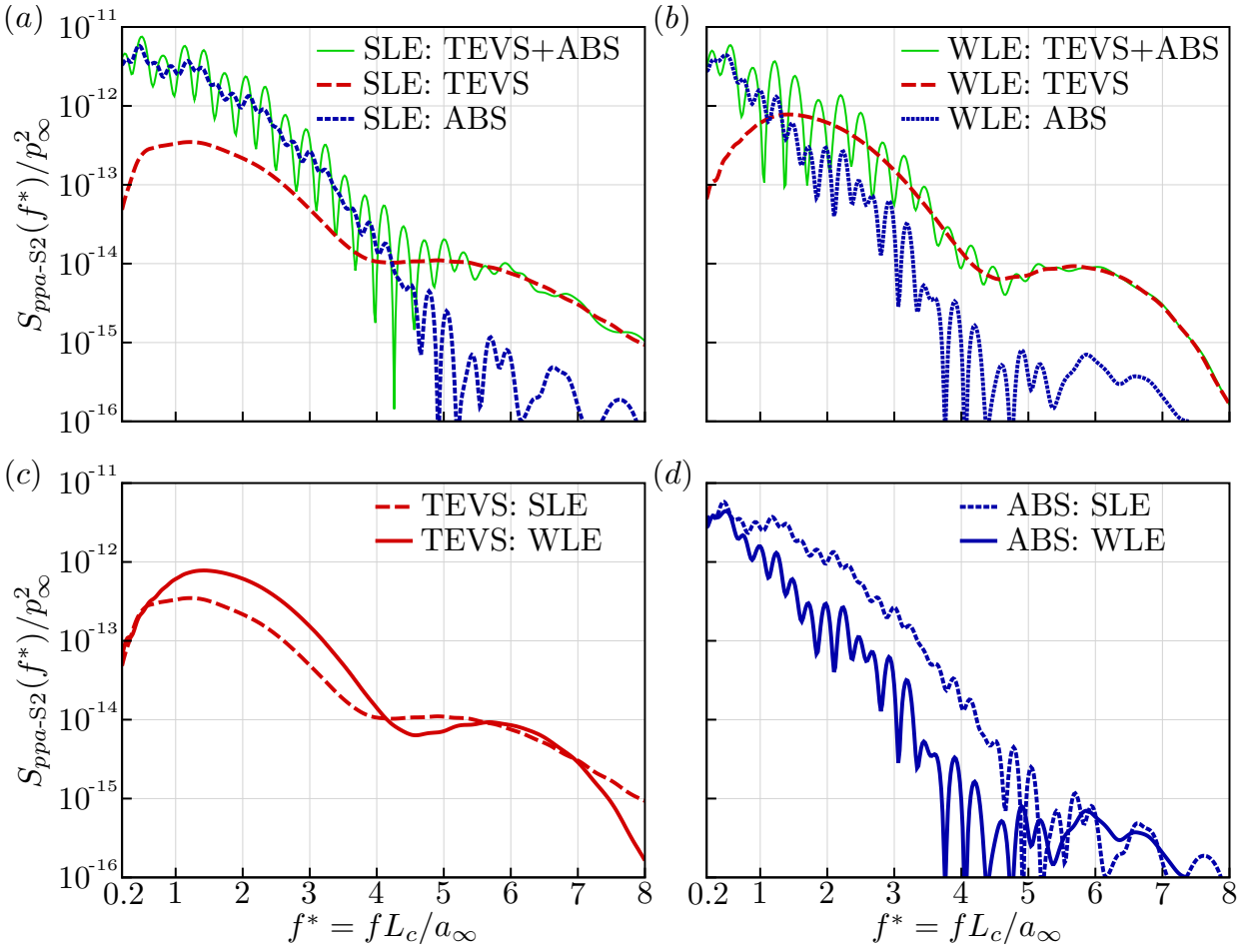

Figure 6.3: Acoustic power spectra for each individual component of the secondary sources: (a & b) comparing S2-TEVS and S2-ABS in each of the SLE and WLE cases; and, (c & d) comparing the SLE and WLE cases for each of the individual components. The observer location is $\boldsymbol{x}_o = (0, 5L_c, 0)$. The curves denoted by S2 (all) in (a) and (b) are those presented in figure 6.2c.

secondary sources is significantly smaller than that from the primary source as shown in figure 6.2c compared to figure 6.1b (looking at the gaps between the SLE and WLE cases).

6.1.2 Dominance of TE vortical scattering at high frequencies

Continuing the same procedure an additional semi-infinite (no LE) simulation is conducted in order to isolate the ABS from the TEVS components. The resulting acoustic power spectra obtained from the individual secondary source components is presented in figure 6.3. The starting frequency of the TEVS dominance over ABS is much earlier for the WLE case at $f^* \approx 1.5$ (figure 6.3b), compared to $f^* \approx 4.5$ in the SLE case (figure 6.3a). The early dominance of TEVS in the WLE case is attributed to the fact that LEVS is already weaker compared to the SLE case and therefore its subsequent acoustic backscattering is also reduced.

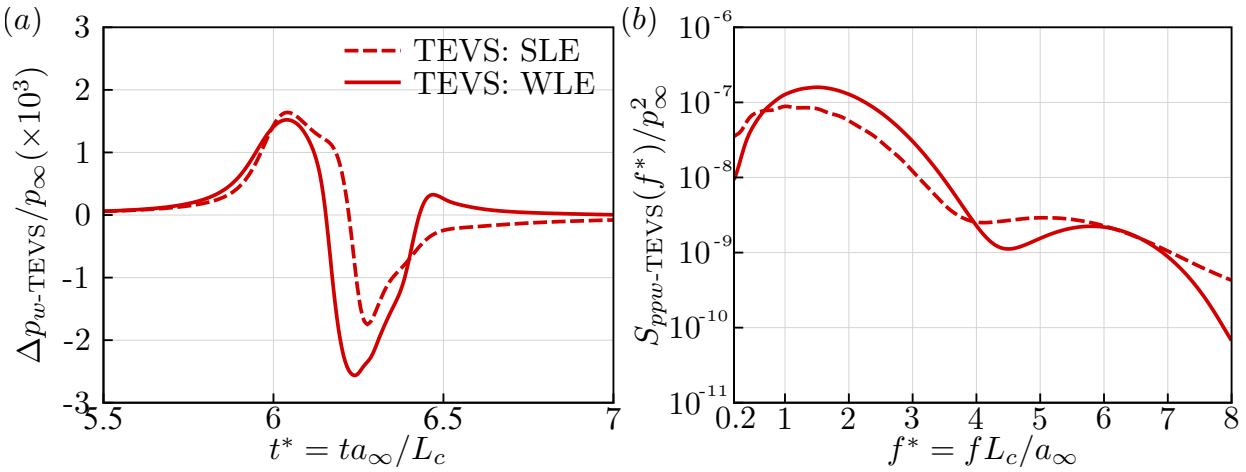

Figure 6.4: Wall pressure loading fluctuations at the TE due to the TEVS, averaged over the span: (*a*) the time signals of $\Delta p_{w\text{-TEVS}}/p_\infty$ and (*b*) the corresponding power spectra, comparing the SLE and WLE cases.

Figures 6.3*c* and *d* show the comparison of the acoustic power spectra between the SLE and WLE cases for each of the secondary sources (TEVS and ABS). They both show that the spectral gap between the SLE and WLE cases is noticeably smaller at high frequencies than that at the low-to-mid frequencies. It is evident now that the collapse of the spectral gap at the high frequencies particularly in TEVS is responsible for the loss of noise reduction identified from figure 6.1*d*. Another interesting outcome captured in figures 6.3*c* and *d* is that TEVS is amplified at low frequencies when the WLE is used, whereas ABS (at low-to-mid frequencies) and LEVS (at all frequencies) are reduced by using WLE. As before we compare the wall pressure loading fluctuations $\Delta p_{w\text{-TEVS}}$ collected at TE (averaged over the span) shown in figure 6.4, to the far-field TEVS spectra figure 6.3(*c*). The wall pressure spectra successfully captures the trend observed at the far-field. This indicates that unlike the LE interaction spanwise phase interference does not play a major role in the TEVS. This comes as some surprise as one may anticipate significant deformation of the impinging vortex as it interacts with the WLE. It is necessary to understand the fluid dynamics of the bisected vortices travelling downstream in order to find out how they evolve and produce a similar high frequency response for SLE and WLE cases at the TE. This is investigated in more detail in Appendix D.

6.2 Phase relationships between noise sources

As mentioned earlier there exist phase relationships between the noise sources which lead to the oscillatory patterns appearing in some of the acoustic power spectra presented above. This is mainly due to the different emission times of acoustic waves at the LE and TE, and also due to the difference in the effective distance they travel to reach an observer location. It is a well known classical theory in acoustics and therefore not needed to reiterate in this work. However, it is worth having a look at the phase relationships in this work since there are multiple sources (and

Period of Spectral Oscillations	SLE	WLE
$\Delta f^*_{\text{LEVS\|ABS-A}}$	0.9424	1.0029
$\Delta f^*_{\text{LEVS\|TEVS}}$	0.2262	0.2419
$\Delta f^*_{\text{ABS-A\|TEVS}}$	0.2976	0.3189

Table 6.1: The calculated values of (6.1) and (6.3) for the periods of spectral oscillations (due to phase interactions between the noise sources) that appear in figures 6.1*b* and 6.2*c* with the observer location given at $\boldsymbol{x}_o/L_c = (0, 5, 0)$.

therefore multiple relationships) involved. For any two different sources, the phase relationship may be expressed by $\Delta\phi = 2\pi f \Delta t$ where Δt is the difference in the time taken for their acoustic waves to arrive at a given observer location. The relationship is most constructive when $\Delta\phi = 2m\pi$ and most destructive when $\Delta\phi = (2m \pm 1)\pi$ where m is an integer. The spectral oscillations will form local maxima when the phase relationship is most constructive and local minima when most destructive. Therefore the period of oscillations in the acoustic power spectra is expected to be $\Delta f = 1/\Delta t$.

First, the phase relationships of LEVS against the others (TEVS and ABS) are considered. Based on the findings from figure 6.3, it is deduced that LEVS interacts mainly with ABS at low frequencies and with TEVS at high frequencies. Also, given the information from figures 6.2*a* and *b*, it is expected that up to five separate interactions exist for LEVS against the sub-components of S2 (ABS-A to D and TEVS). Among the S2 sub-components we consider the strongest two (ABS-A and TEVS) from which the dimensionless periods of the oscillations to appear in the total acoustic power spectra (figure 6.1*b*) are predicted to be

$$\left.\begin{aligned} \Delta f^*_{\text{LEVS|ABS-A}} &= \frac{L_c}{a_\infty}\left[\frac{x_{TE} - \hat{x}_{LE}}{a_\infty + u_\infty} + \Delta t_o(\boldsymbol{x}_{TE}) - \Delta t_o(\hat{\boldsymbol{x}}_{LE})\right]^{-1} \\ \Delta f^*_{\text{LEVS|TEVS}} &= \frac{L_c}{a_\infty}\left[\frac{x_{TE} - \hat{x}_{LE}}{u_\infty} + \Delta t_o(\boldsymbol{x}_{TE}) - \Delta t_o(\hat{\boldsymbol{x}}_{LE})\right]^{-1} \end{aligned}\right\}, \tag{6.1}$$

where Δt_o is the time taken for an acoustic wave to travel from its source location ($\boldsymbol{x}$) to the observer ($\boldsymbol{x}_o$) (Garrick & Watkins, 1953):

$$\Delta t_o(\boldsymbol{x}) = \frac{M_\infty(x - x_o) + \sqrt{M_\infty^2(x - x_o)^2 + (1 - M_\infty^2)|\boldsymbol{x} - \boldsymbol{x}_o|^2}}{a_\infty(1 - M_\infty^2)}. \tag{6.2}$$

In (6.1), $\hat{x}_{LE} = -L_c/2 + h_{LE}$ (the root position) is used for the WLE case since the source is strongest at the root as reported by Kim *et al.* (2016) and Turner & Kim (2017*b*), whereas $\hat{x}_{LE} = -L_c/2$ for the SLE case. The calculated values of $\Delta f^*_{\text{LEVS|ABS-A}}$ and $\Delta f^*_{\text{LEVS|TEVS}}$ are listed in table 6.1. The predicted periods of the spectral oscillations are compared with the actual simulation data in figure 6.5. The result shows that the prediction is correct and accurate. It is also displayed that $\Delta f^*_{\text{LEVS|ABS-A}}$ is prevalent at low frequencies but subsequently taken over by $\Delta f^*_{\text{LEVS|TEVS}}$ when the dominance of S2-TEVS begins to appear at $f^* \approx 4.5$ and 1.5 for SLE and WLE, respectively.

Another phase relationship can be found amongst the secondary sources (excluding the primary

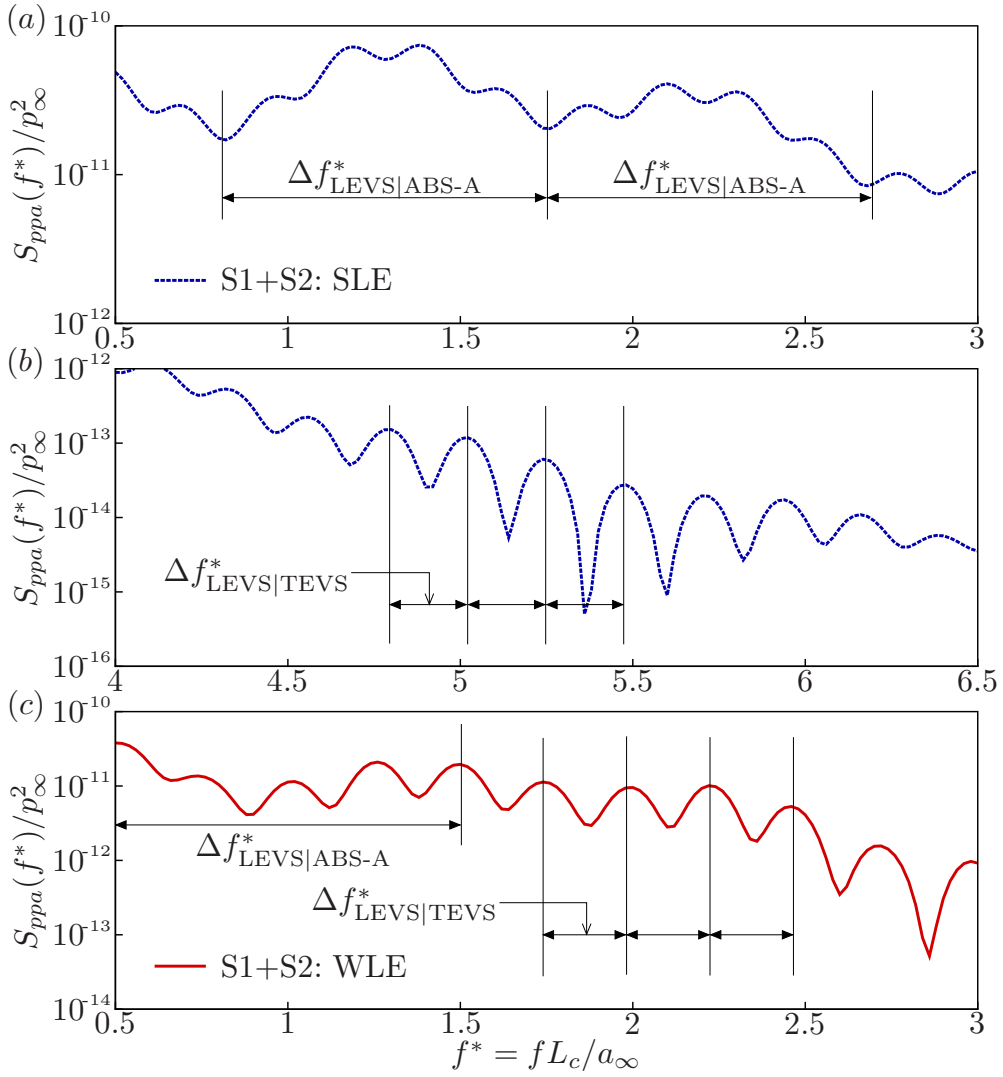

Figure 6.5: Spectral oscillations appeared in the overall acoustic power spectra (S1+S2 in figure 6.1*b*) due to the phase relationships between S1 and S2: (*a*) the SLE case at low frequencies, (b) the SLE case at high frequencies and (c) the WLE case. The values of $\Delta f^*_{\text{LEVS|ABS-A}}$ and $\Delta f^*_{\text{LEVS|TEVS}}$ are calculated from (6.1) and listed in table 6.1.

source). The spectral oscillations purely due to the secondary sources are displayed in figure 6.2*c*. It is easily expected that the S2 sub-components ABS-A and TEVS considered above make the strongest phase interaction with each other. According to this the phase relationship between them is predicted to be:

$$\Delta f^*_{\text{ABS-A|TEVS}} = \frac{L_c}{a_\infty}\left(\frac{x_{TE}-\hat{x}_{LE}}{u_\infty} - \frac{x_{TE}-\hat{x}_{LE}}{a_\infty+u_\infty}\right)^{-1}, \tag{6.3}$$

where both ABS-A and TEVS are emitted from TE and therefore the relative acoustic distance is equal. The predicted values of $f^*_{\text{ABS-A|TEVS}}$ are listed in table 6.1 and compared with the actual simulation data in figure 6.6. Again the prediction is correct and accurate, which confirms the additional phase relationship existing between the secondary sources.

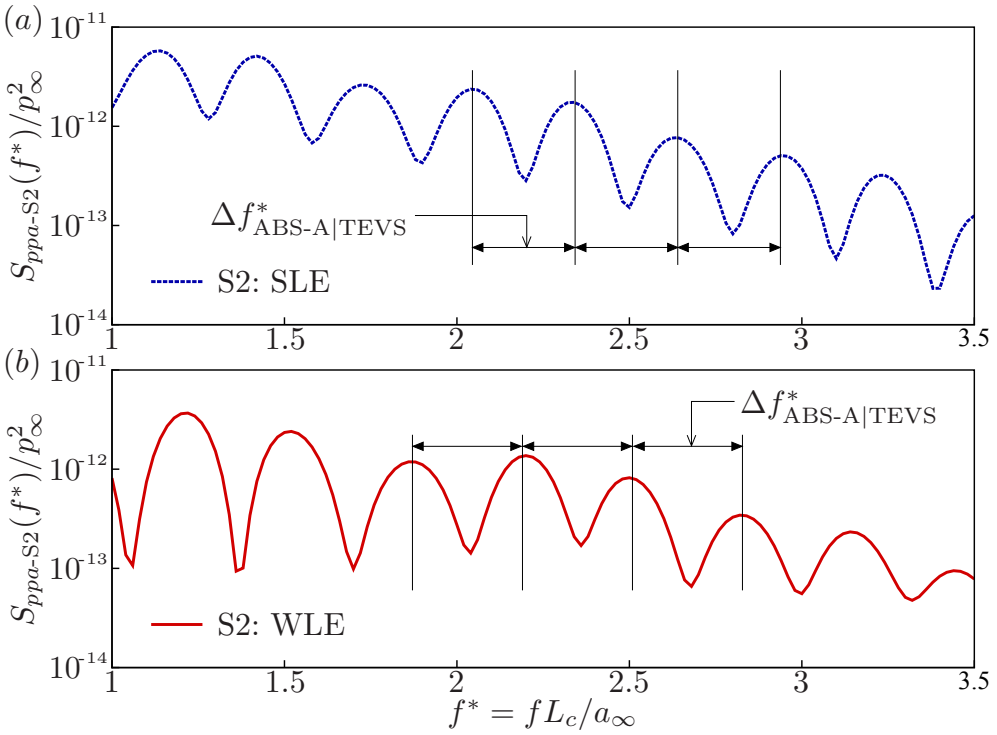

Figure 6.6: Spectral oscillations appeared in the acoustic power spectra from the secondary sources only (figure 6.2*c*) due to the phase relationships between ABS-A and TEVS: the (*a*) SLE and (b) WLE cases. The values of $\Delta f^*_{\text{ABS-A|TEVS}}$ are calculated from (6.3) and listed in table 6.1.

6.3 The effect of secondary sources on acoustic directivity

In this section we further investigate the secondary sources with regard to the directivity of acoustic radiation that changes with the leading-edge geometry. Figure 6.7 shows the acoustic directivity patterns for different noise sources, calculated based on the variance of the acoustic pressure:

$$\langle p_a^2 \rangle = \frac{1}{T} \int_0^T p_a^2(t) \mathrm{d}t, \tag{6.4}$$

which mainly represents the low-frequency contributions. Figure 6.7*a* shows typical dipolar directiviy patterns where the strongest radiation is moderately biased towards the downstream direction for both the SLE and WLE cases. It is apparent that the downstream bias is contributed mainly by LEVS (figure 6.7*b*) and partially by ABS (figure 6.7*d*). TEVS is the weakest of all, except in the upstream direction. It is found that the level of noise reduction (in terms of $OA\Delta SPL$) due to WLE is consistent and omni-directional. However, figure 6.7*c* reveals that there is a contribution towards increasing the noise in all directions made by TEVS, which has been hinted in the previous section but limited in the vertical direction ($\theta = 90°$). The plots shown in figure 6.7 are, however, governed by the low-frequency components as mentioned above, and therefore an additional investigation is required for higher frequencies.

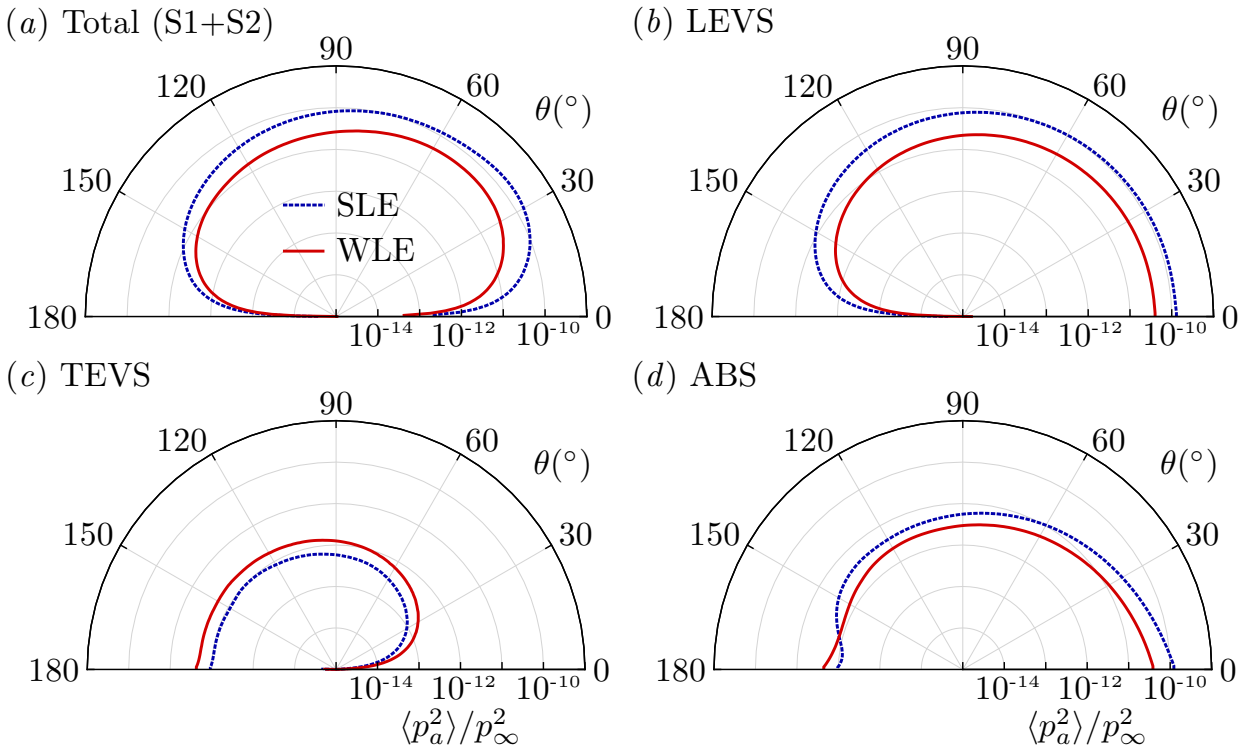

Figure 6.7: Directivity profiles (on a logarithmic scale) of the variance of the acoustic pressure $\langle p_a^2 \rangle / p_\infty^2$ around a circle with a radius of $5L_c$ with its origin at centre of the finite-chord aerofoil (on the centre plane, $z = 0$), obtained from (a) all noise sources combined and, individually from (b) LEVS, (c) TEVS and (d) ABS. Comparisons are made between the SLE and WLE cases. Lower half planes are not repeated due to symmetry.

Figure 6.8 displays a series of acoustic power spectra obtained from each individual noise source at three different observer angles. This figure shows that the directivity trends seen earlier in figure 6.7 are consistent across a wide range of frequencies, not limited to the low frequencies. This is particularly true for TEVS where the same trend holds for all frequencies. However, LEVS and ABS (in the WLE cases) exhibits significant deviations from the consistent trend at various frequencies so that the increase/decrease of noise with the observer angle is not very predictable. On the other hand ABS produces a consistent but reversed trend (to that of the low frequencies) in the high-frequency range (from about $f^* \approx 6$ and 5 for SLE and WLE, respectively) so that the noise (due to ABS) gets louder as the observer angle turns upstream. This was not foreseen in figure 6.7 that was based on $\langle p_a^2 \rangle$, and is likely caused by the ABS-C component.

It is seen in figure 6.8 that ABS (for both SLE and WLE) produces increasingly oscillatory spectra as the observer angle turns upstream. This is due to the phase relationship between ABS-A and ABS-C (see figure 6.2a) that is significant in the upstream direction as the amplitude of ABS-C becomes comparable to that of ABS-A. Based on the same approach used in §6.2 the phase

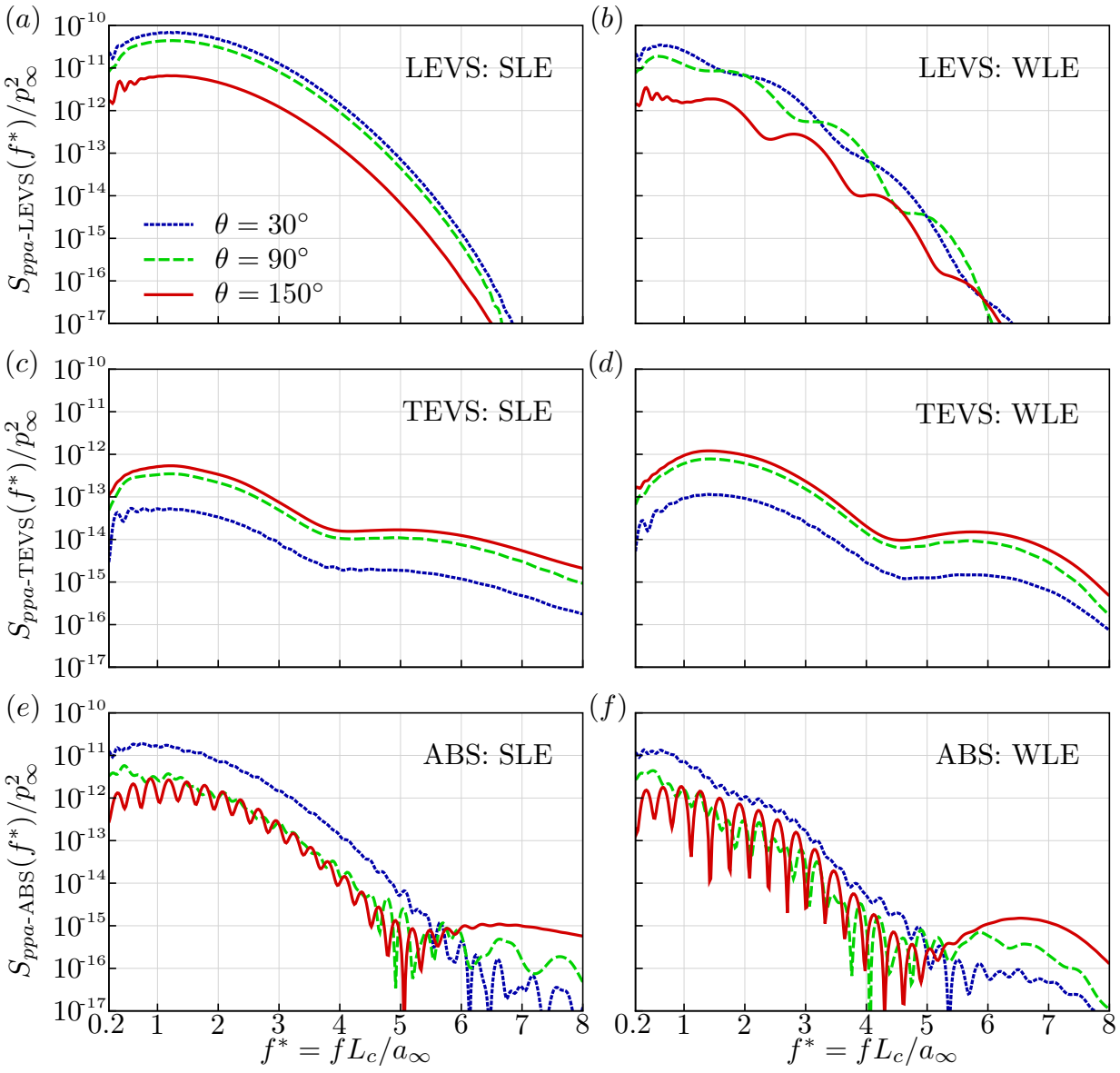

Figure 6.8: Acoustic power spectra obtained from individual noise sources: (*a* & *b*) LEVS, (*c* & *d*) TEVS and (*e* & *f*) ABS, at three different observer locations: $\boldsymbol{x}_o/L_c = (5\cos\theta, 5\sin\theta, 0)$ for $\theta = 30°$, 90° and 150°. The left and right columns are for the SLE and WLE cases, respectively.

relationship between ABS-A and ABS-C is predicted to be

$$\Delta f^*_{\text{ABS-A|ABS-C}} = \frac{L_c}{a_\infty}\left[\frac{x_{TE}-\hat{x}_{LE}}{u_\infty} + \frac{x_{TE}-\hat{x}_{LE}}{a_\infty - u_\infty} + \Delta t_o(\hat{\boldsymbol{x}}_{LE}) - \frac{x_{TE}-\hat{x}_{LE}}{a_\infty + u_\infty} - \Delta t_o(\boldsymbol{x}_{TE})\right]^{-1}. \tag{6.5}$$

The calculated values of $\Delta f^*_{\text{ABS-A|ABS-C}}$ at $\theta = 150°$ are 0.2860 for SLE and 0.3066 for WLE, which match well with those appearing in figure 6.8(*e* & *f*).

Figure 6.9 rearranges figure 6.8 in order to show how the acoustic power spectra of the individual

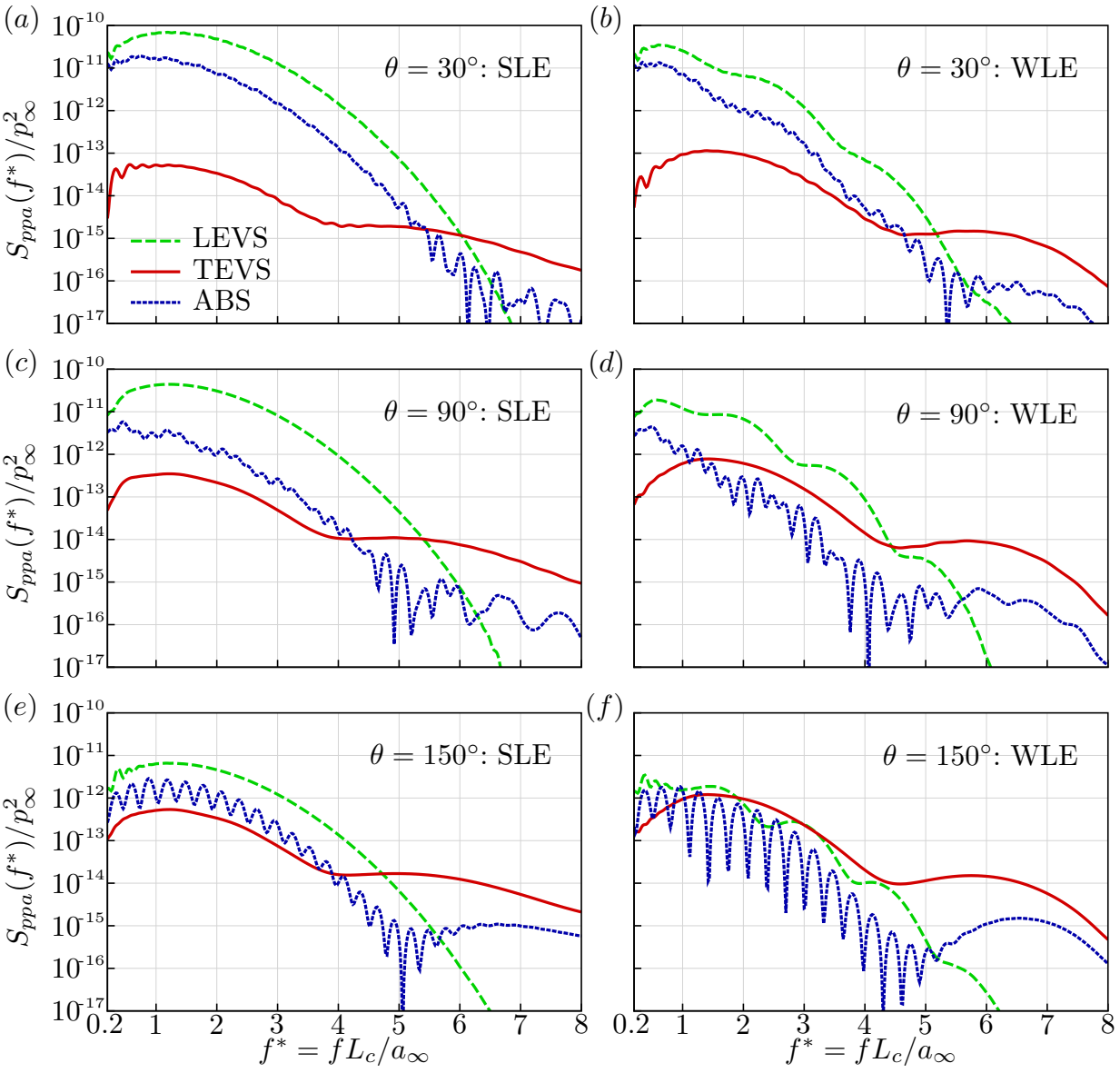

Figure 6.9: Acoustic power spectra obtained at three different observer locations: $\boldsymbol{x}_o/L_c = (5\cos\theta, 5\sin\theta, 0)$ for $(a\ \&\ b)\ \theta = 30°$, $(c\ \&\ d)\ \theta = 90°$ and $(e\ \&\ f)\ \theta = 150°$, from individual noise sources (LEVS, TEVS and ABS). The left and right columns are for the SLE and WLE cases, respectively.

noise sources compare against each other at three different observer angles. One of the main features found is that, with the observer angle turning upstream, the gaps between the spectra significantly decrease at low frequencies but increase at high frequencies. This is due to TEVS strengthens in the upstream directions whereas LEVS and ABS weaken. It is also evident that the dominance of TEVS at high frequencies (as discussed in the previous section) is consistent regardless of the observer angle although the dominance becomes stronger in a wider frequency range in the upstream directions. This tendency is significantly more pronounced in the WLE case so that TEVS is the strongest noise source in the upstream directions at almost all frequencies (except very low frequencies) even exceeding the primary source (LEVS). These unique findings

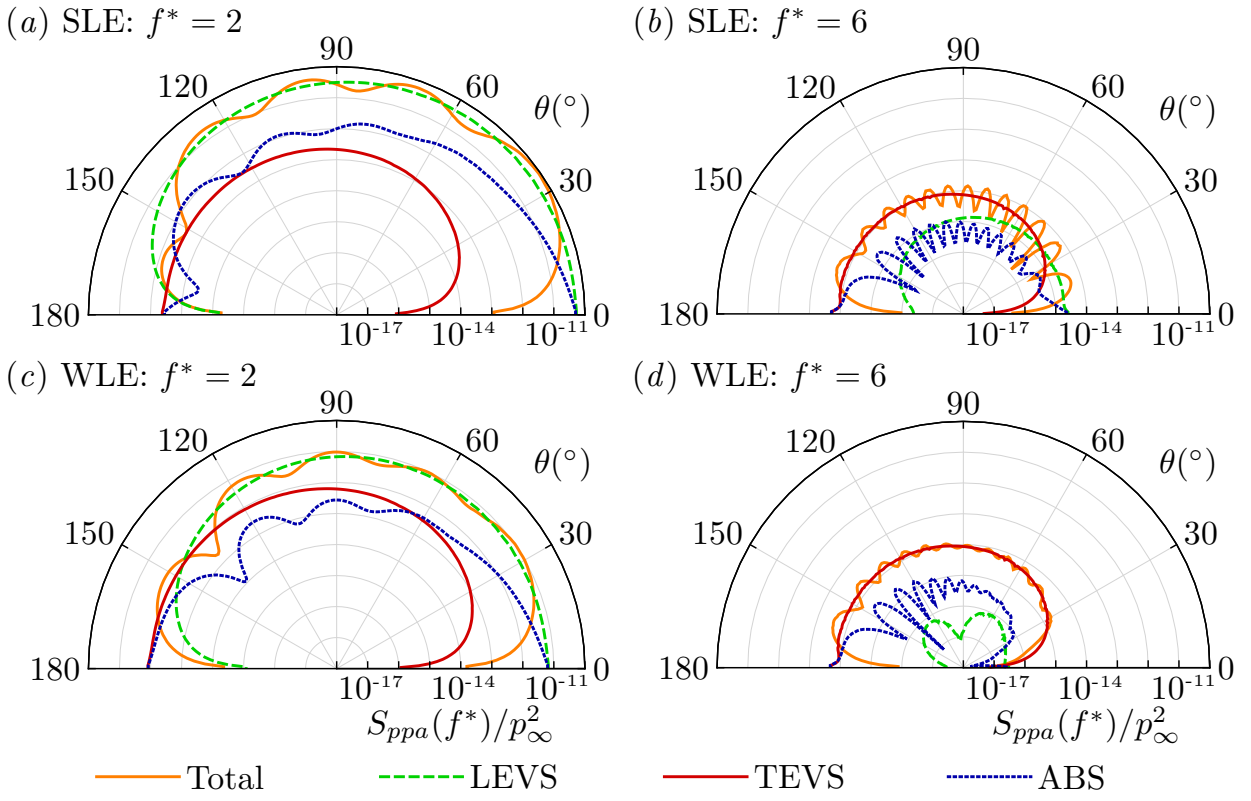

Figure 6.10: Directivity profiles (on a logarithmic scale) of $S_{ppa}(f^*)/p_\infty^2$ at two different frequencies: (a & c) $f^* = 2$ and (b & d) $f^* = 6$, around a circle with a radius of $5L_c$ with its origin at centre of the finite-chord aerofoil (on the centre plane, $z = 0$), obtained from each individual noise source. The top and bottom rows are for the SLE and WLE cases, respectively. Lower half planes are not repeated due to symmetry.

are also confirmed by viewing the directivity patterns of $S_{ppa}(f^*)/p_\infty^2$ for two different (low and high) frequencies shown in figure 6.10.

Based on the result shown in figure 6.10 the directivity profiles of the noise reduction made by WLE (ΔSPL defined in §2.1.8) at the two different frequencies ($f^* = 2$ and 6) are plotted in figure 6.11. The figure shows that the overall ΔSPL (S1+S2) changes tremendously with the observer angle and the frequency by up to multiple tens of decibels. There is a sudden loss of noise reduction (or even noise increase) in the upstream direction at $f^* = 2$ and an unexpected large gain of noise reduction in the downstream direction at $f^* = 6$. These rather surprising events involved with the secondary sources have not been addressed or encountered in the earlier studies based on either semi-infinite-chord aerofoils (Kim *et al.*, 2016; Turner & Kim, 2017*b*) or limited observer angles $50^\circ \leq \theta \leq 130^\circ$ (Chaitanya *et al.*, 2017; Narayanan *et al.*, 2015).

There are additional findings from the directivity plots. First of all, as discussed in the previous section the dominating noise source at $f^* = 2$ is LEVS in most directions and it is TEVS at $f^* = 6$ (figure 6.10), and therefore they determine the main level of overall ΔSPL (S1+S2) at those frequencies (figure 6.11), except the sudden loss/gain in the far upstream/downstream directions mentioned above. The sudden loss/gain in overall ΔSPL (S1+S2) around $150^\circ < \theta \leq 180^\circ$ at

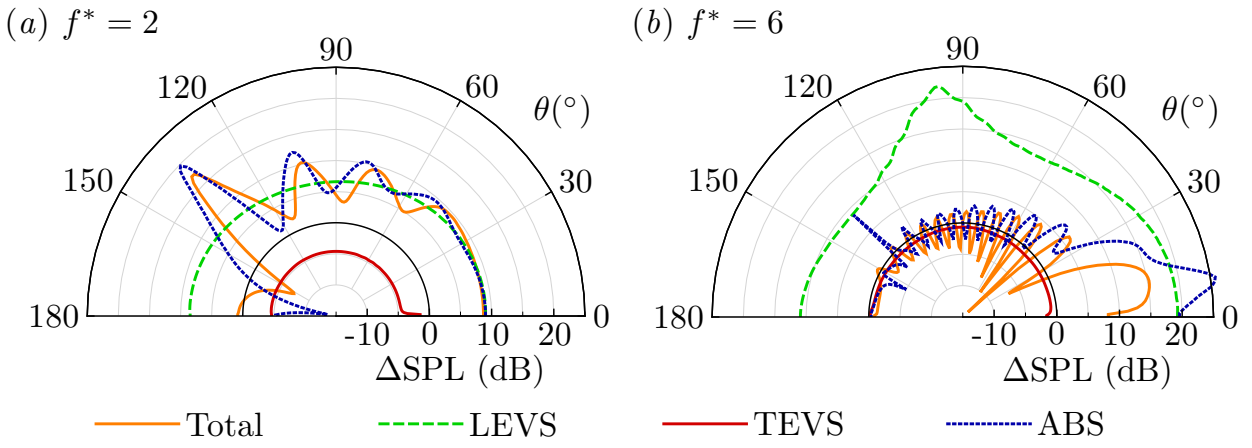

Figure 6.11: Directivity profiles (on a decibel scale) of the noise reduction made by WLE compared to SLE, i.e. ΔSPL defined by (2.61), at two different frequencies: (a) $f^* = 2$ and (b) $f^* = 6$, based on the result shown in figure 6.10. The inner semicircle area outlined indicates noise increase (negative ΔSPL).

$f^* = 2$ and $0^\circ \leq \theta < 30^\circ$ at $f^* = 6$ are mainly due to the fact that there is a changeover of the dominating source within the narrow angles in either of the SLE and WLE cases (or both) shown in figure 6.10. The oscillatory lobes in the directivity plots are a consequence of the phase interactions between different sources discussed in the previous section. Secondly it is noticeable in figure 6.11 that the ΔSPL profiles of ABS show a very good similarity to those of all the sources combined (S1+S2). This is explained by recalling that ABS is the acoustic backscattering of the all other sources combined (LEVS and TEVS), which means that its amplitude depends mainly on the dominating one and its behaviour changes when there is a changeover between them. Therefore the relative change (ΔSPL) in ABS between SLE and WLE is reasonably similar to that from all the sources combined (S1+S2).

6.4 Undulated trailing edge

In this section additional tests are conducted in order to quantify the extent of additional noise reductions which may be available by adopting an undulated trailing edge. The investigated geometries include WLE with wavy trailing edge (WTE) of equal amplitude and phase, π out-of-phase WLE and WTE, and finally SLE with WTE. The resulting acoustic spectra, and noise reduction spectra are contrasted alongside the SLE baseline and WLE-STE case in figures 6.12(a) and (b) respectively.

Over low–medium frequencies undulation of the TE has little impact on the noise level, although it is successful in reducing the degree of spectral oscillations caused by phase interaction between primary and secondary effects. Conversely at high frequency ($fL_c/a_\infty \gtrsim 5.5$) the noise associated with the TEVS scattering is dramatically reduced. Both these effects are more clear from figure 6.13(a)-(d), which show the TEVS and ABS isolated spectra and individual noise reduction spectra respectively.

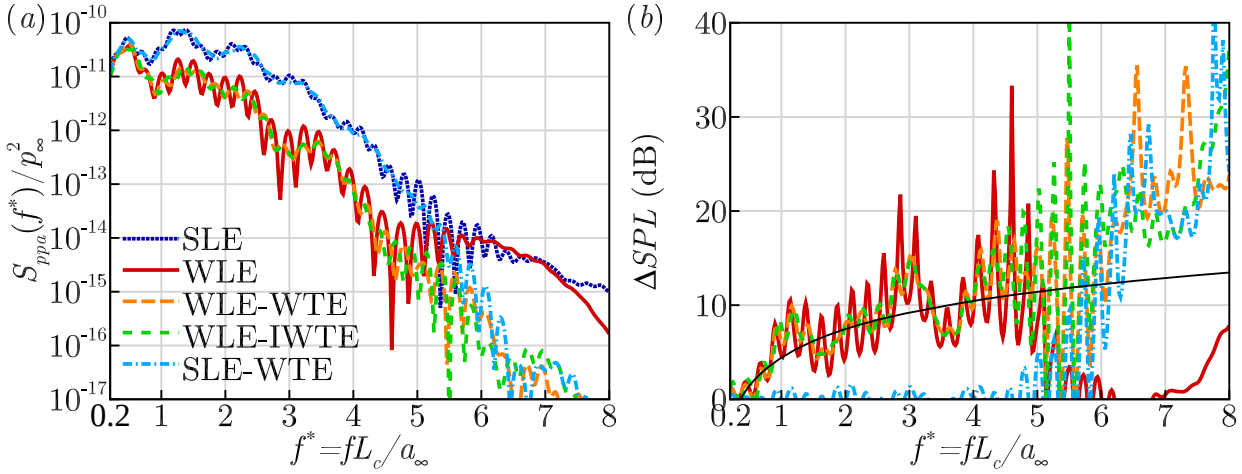

Figure 6.12: (a) Power spectral density of the far field fluctuating pressure ($S_{ppa}(f^*)/p_\infty^2$) obtained by SLE baseline, WLE, WLE+WTE, WLE+IWTE (Inverted WTE) and SLE+WTE cases. The amplitude and wavelength for both LE and TE serrations is $h_{LE}/L_c = 1/15$ and $\lambda/L_c = 2/15$. (b) Noise reduction spectra obtained for each case.

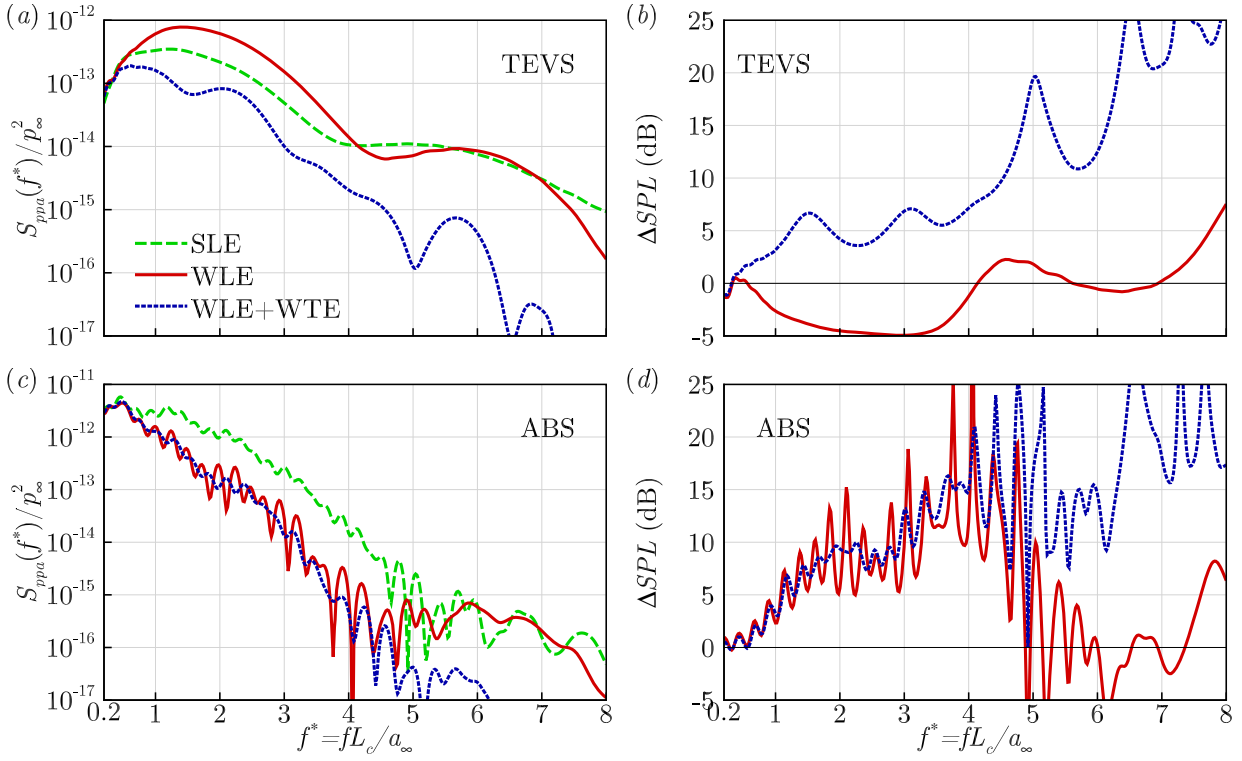

Figure 6.13: (a & c) Acoustic power spectra for S2-TEVS and S2-ABS for SLE, WLE and WLE+WTE cases. (b & d) Secondary source noise reduction spectra obtained by WLE and WLE+WTE cases for TEVS (b) and ABS (d) respectively.

Also plot in figure 6.12(b) is the empirical linear noise reduction relation identified by Chaitanya *et al.* (2017). As mentioned earlier, the simulation noise reduction vs frequency data follows this trend relatively well until high frequency where secondary convective effects become dominant. After significant removal of the TEVS source (through WTE) it may be expected that the noise reduction levels would return to the linear trend, however this is actually exceeded by a significant proportion. The cause of this is currently unknown and may be a worthwhile focus of further investigation.

It is also interesting to note that there is no real preference between the WLE-WTE and WLE-IWTE geometries. A simple explanation for this observation is found in figure 6.14. It shows iso-surfaces of Q-criterion coloured by spanwise vorticity ($\omega_z L_c/a_\infty$) during the LE interaction (a), and when the vortex is close to the TE (b). Equivalent streamwise vorticity plots ($\omega_x L_c/a_\infty$) are also shown in figure 6.14(c) and (d). The vortex disturbance, lacking any streamwise vorticity component, is clearly shown separate from the induced secondary structures. We known from Howe's theory (Howe, 1998) that the scattered sound at the TE is related to the Lamb vector $\boldsymbol{\omega} \times \boldsymbol{u}$, which will be dominated by the $U_\infty \omega_z$ term. Since the spanwise vorticity is approximately constant in span, there are only small differences between the two WTE cases.

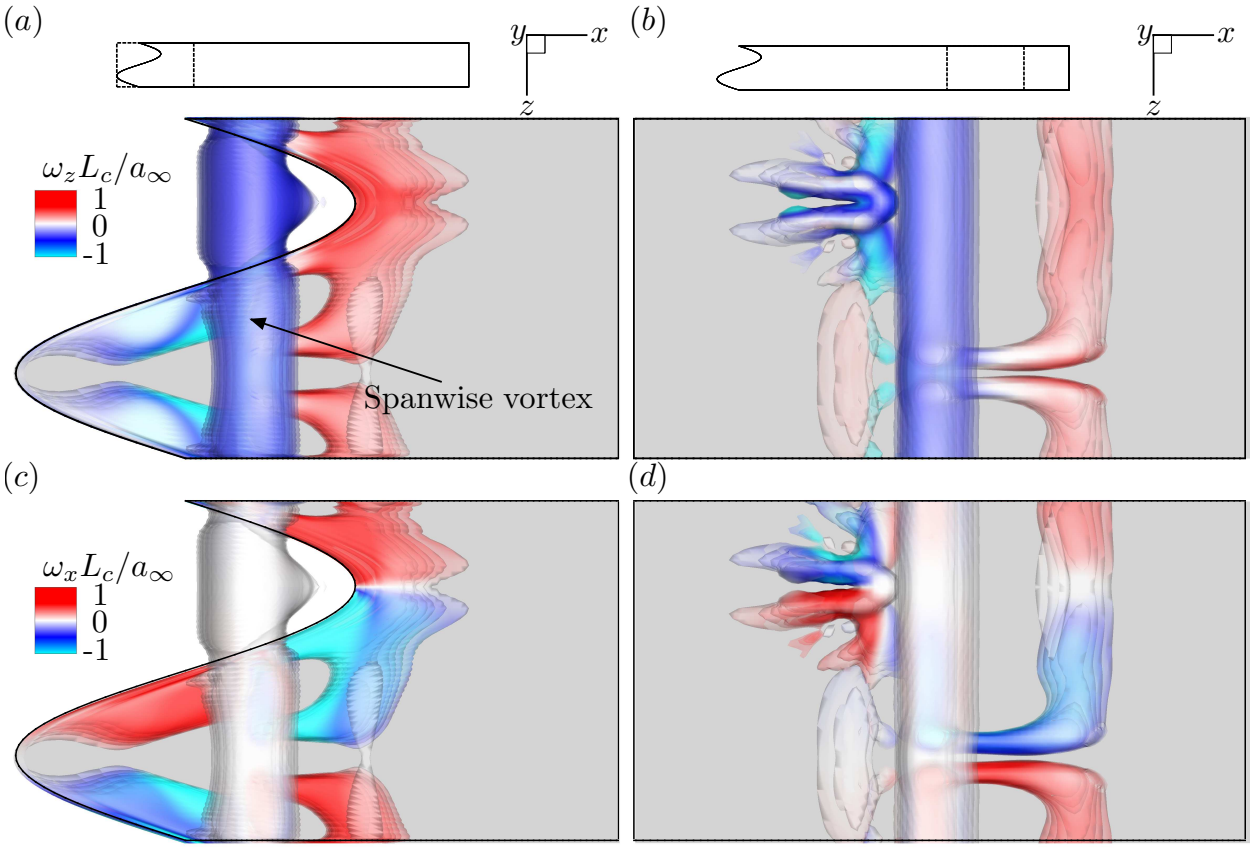

Figure 6.14: Iso-surfaces of Q-criterion ($||\Omega_{ij} L_c/a_\infty||^2 - ||S_{ij} L_c/a_\infty||^2$ where Ω_{ij} and S_{ij} are the vorticity and rate-of-strain tensors, respectively) coloured by spanwise vorticity ($\omega_z L_c/a_\infty$) obtained during interaction of the prescribed vortex and the LE ($t^* = 2.2$) (a), and after the now bisected vortex has travelled further downstream ($t^* = 5.2$) (b). (c) & (d) Equivalent plots recoloured by streamwise vorticity ($\omega_x L_c/a_\infty$).

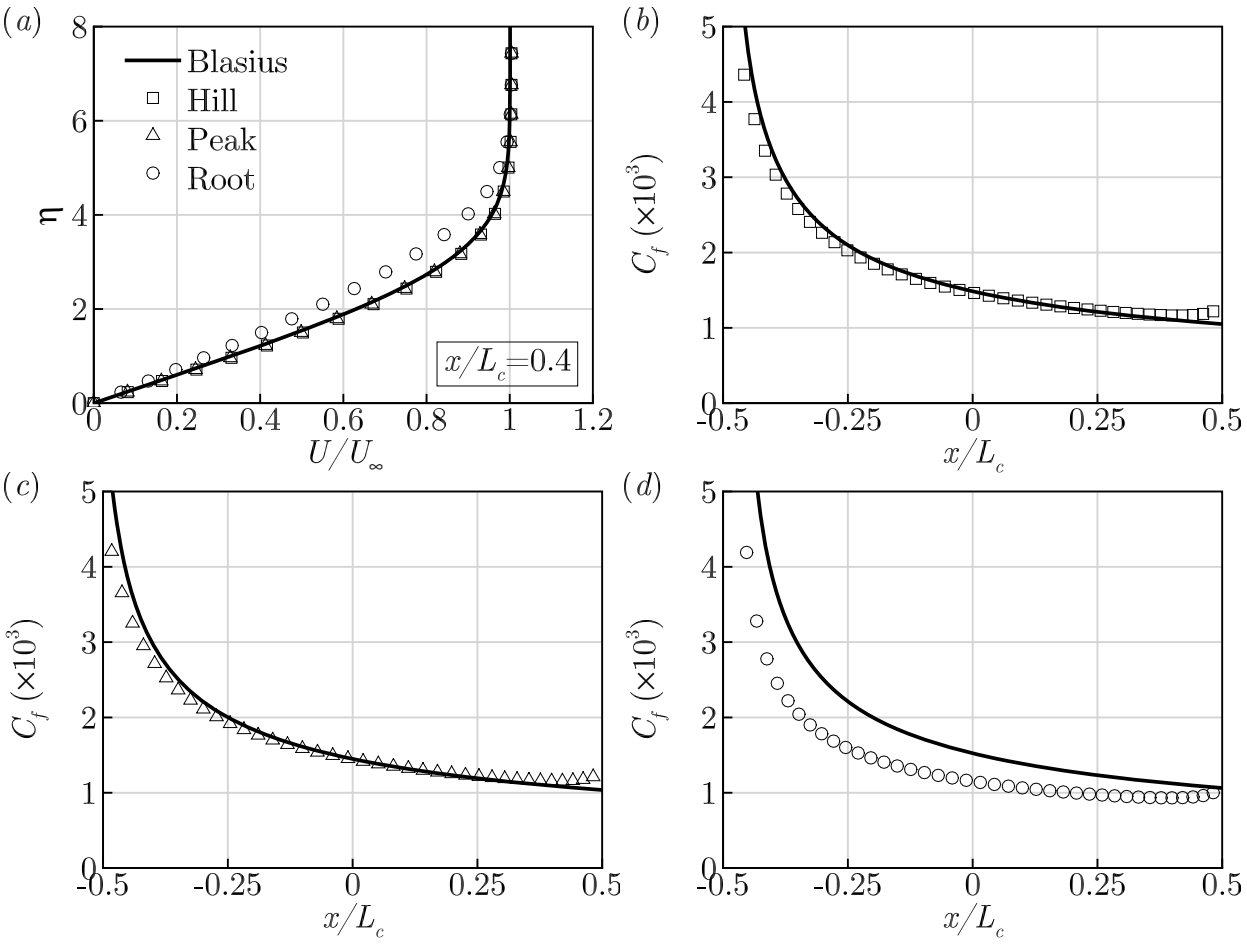

Figure 6.15: Boundary layer profiles obtained for WLE geometry at Reynolds numbers $Re_\infty = 4.0 \times 10^5$: (a) streamwise velocity profile for $x/L_c = 0.4$; (b) skin friction coefficient $C_f = 2\tau_w/(\rho U_\infty^2)$ at WLE hill; (c); WLE peak and (d) WLE root.

6.5 WLEs with a laminar boundary layer profile

In this section the discussions are expanded to include viscous effects in the form of a laminar boundary layer. The same Reynolds number ($Re_\infty = 4.0 \times 10^5$) and grid settings are used as in §5.5 for the 3D SLE case. A relatively small amplitude is selected for the WLE ($h_{LE}/L_c = 1/40$) with one wavelength captured in the spanwise domain ($\lambda_{LE} = L_z = 0.05L_c$). This ensures the LE aspect ratio is not too large ($AR = 1$), which could considerably increase computational cost due to highly skewed cells near the LE.

Firstly the boundary layer profiles developed by the WLE geometry are shown in figure 6.16. The boundary layer is approximately laminar over most of the span, following the Blasius solution. The exception is near the WLE root where the boundary layer profile is more typical of an adverse pressure gradient. This may be caused by a low pressure which is observed in the current simulations at the root, causing the pressure to increase in the streamwise direction.

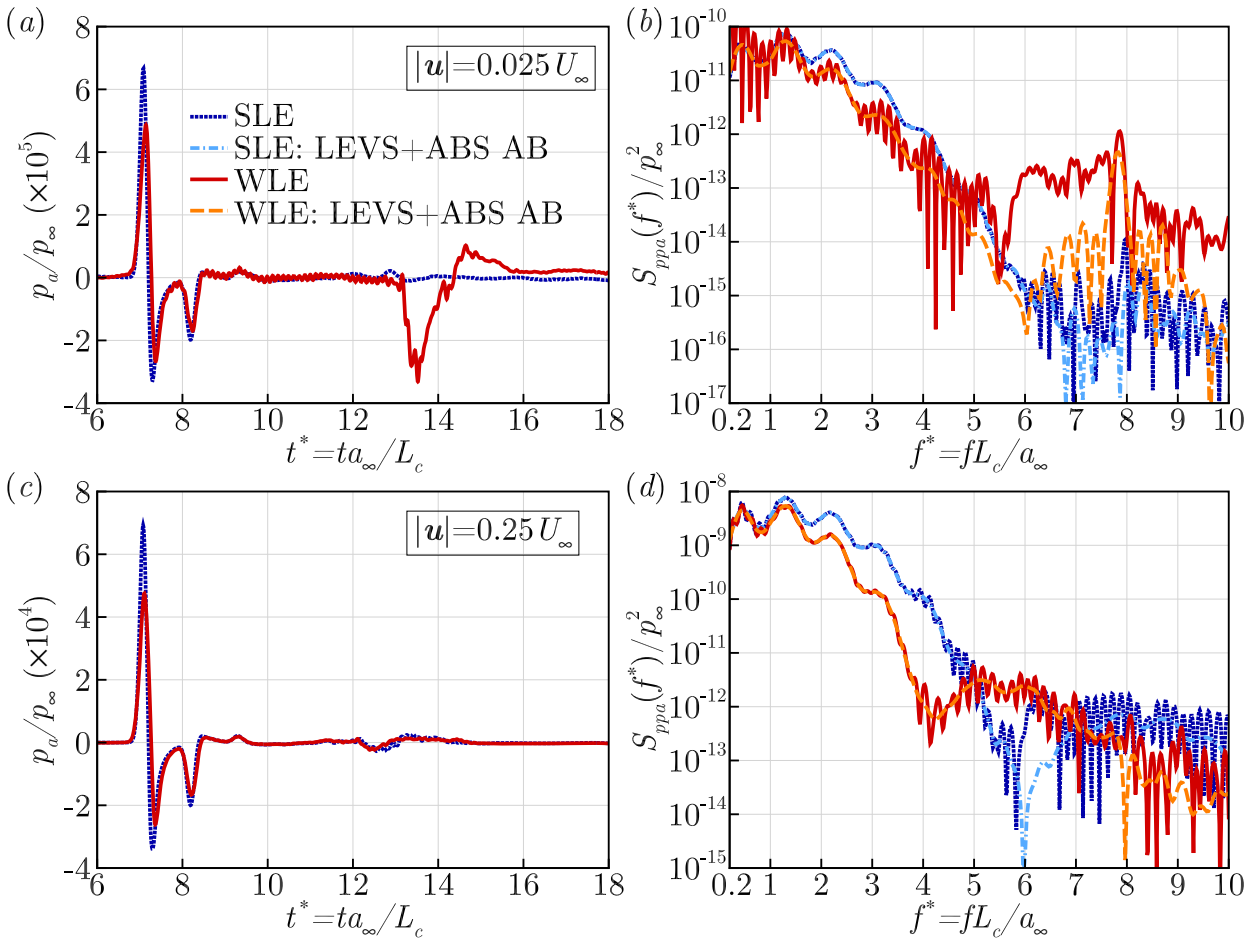

Figure 6.16: Acoustic pressure data obtained for SLE and WLE geometries from the current 3D viscous ($Re_\infty = 4.0 \times 10^5$) simulations based on the linear 2.5% and non-linear 25% strength vortex interactions: (a & c) time signals of $p_a(\boldsymbol{x}_o, t)/p_\infty$ for weak and strong interactions respectively; (b & d) the corresponding power spectra.

The acoustic pressure data for both weak ($|\boldsymbol{u}| = 0.025U_\infty$) and strong ($|\boldsymbol{u}| = 0.25U_\infty$) vortex cases are presented and compared to the SLE case in figure 6.16. The strong vortex interaction (figure 6.16 (c & d) is mostly as expected. In this case both SLE and WLE geometries produce 3D structures and obtain a comparable high frequency noise level. Much more surprising is the weak vortex pressure signal (figure 6.16 (a)) which shows the WLE produces an enormous TEVS wave comparable in magnitude to it's LEVS component. Consequently the spectral oscillations in the WLE PSD are significantly increased even at low frequencies as there are now two competing low frequency events. Additionally there is a significant increase in noise for $fL_c/a_\infty > 5.5$. In order to explain this unusual result the flow is examined in more detail. Figure 6.17 shows iso-surfaces of spanwise vorticity alongside the contours of acoustic pressure obtained in the xy-plane at two instants of time, $ta_\infty/L_c = 8.33$ and 10.0.

As it turns out the secondary vorticity breaks down into 3D tertiary structures on the lower side of the WLE in a similar manner to the strong vortex case (§5.5). However, unlike the strong vortex case which transitions almost immediately, the breakdown does not occur until the vortex has past

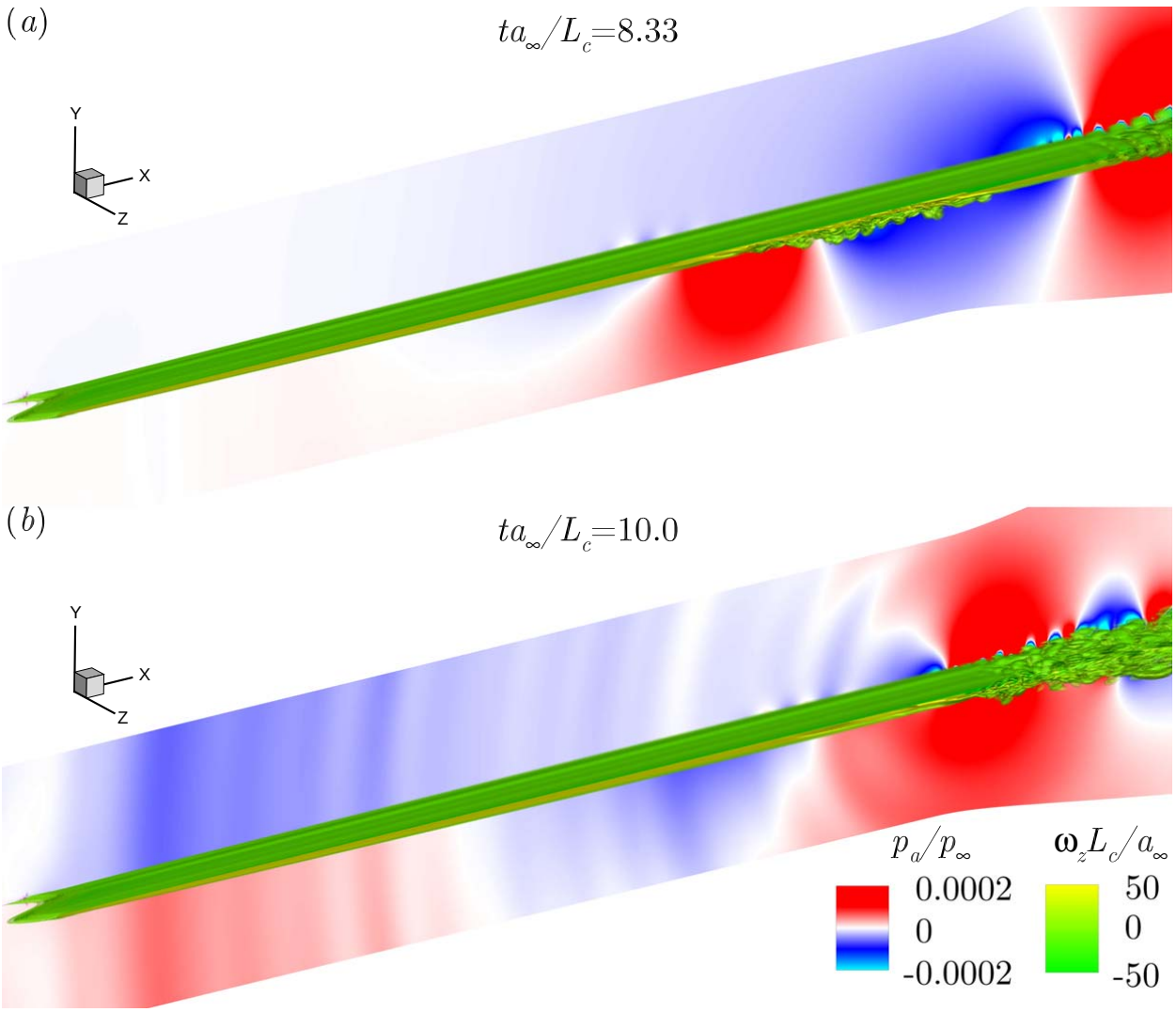

Figure 6.17: Iso-surfaces of spanwise vorticity $\omega_z L_c/a_\infty$ and contours of acoustic pressure p_a/p_∞ obtained during interaction of the weak vortex disturbance and a WLE. (a) Non-dimensional time $ta_\infty/L_c = 8.33$ showing 3D tertiary structures generated on the aerofoil lower side. (b) $ta_\infty/L_c = 10$, when the tertiary structures are scattered by the TE.

the mid-chord. It should be emphasized that the flow remains two-dimensional in the SLE case (when run in 3D), meaning this phenomenon is specific to the WLE. It makes sense that the WLE is more likely to develop three-dimensionality as streamwise vorticity is introduced naturally into the boundary layer by the geometry.

Finally in 6.18 the noise reduction spectra is plot for the two cases and compared to the respective LEVS+ABS result obtained through the same windowing procedure as §5.5. For lower frequencies ($fL_c/a_\infty < 4.5$) the WLE obtains an improved noise reduction during the stronger vortex interaction as well as significantly reduced spectral oscillations. The weak vortex noise reduction on the other hand approximately follows the expected trend line (Chaitanya *et al.*, 2017). The cause of this difference is currently unknown, but likely related to strong non-linearities occurring during the interaction.

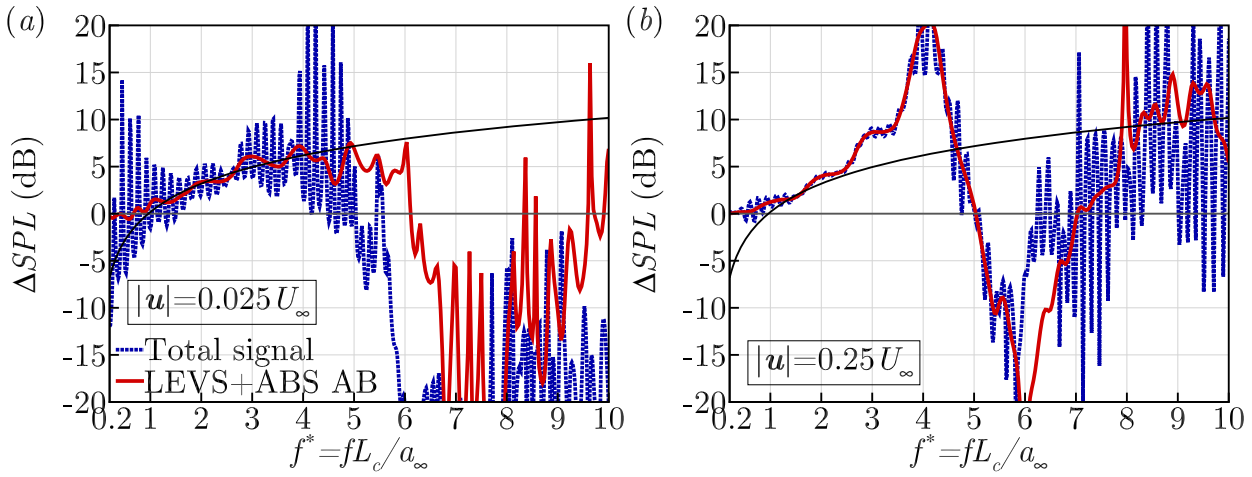

Figure 6.18: Noise reduction spectra obtained by the WLE case at $Re_\infty = 4.0 \times 10^5$ for the total noise and LEVS+ABS AB components. The LEVS+ABS AB contribution is obtained through the windowing procedure described in §5.5. (a) Default weak vortex case; (b) enhanced strength vortex. Also shown is the noise reduction trend of Chaitanya *et al.* (2017) based on $h_{LE}/L_c = 0.025$.

During the weak interaction the TEVS noise begins to dominate for $fL_c/a_\infty > 4$ resulting in a premature loss of noise reduction similar to the inviscid cases. At very high frequency ($fL_c/a_\infty > 6$) the effect is most severe, resulting in excess of 20 dB noise increase relative to SLE. A portion of the high frequency noise increase is actually caused by an increase in LEVS+ABS AB noise. This is likely a consequence of convective disturbance wall pressure fluctuations, as indicated by the source maps in §4). The strong vortex interaction exhibits entirely different behaviour. Although the noise reduction is lost at a similar frequency, it is primarily a consequence of increased WLE LEVS noise. Unlike all other cases presented here the TEVS becomes dominant for the WLE at a higher frequency than the SLE case ($fL_c a_\infty \approx 9$, see figure 6.16(d)). This results in the noise reduction actually improving slightly by including the TEVS contribution where it begins to dominants the SLE solution but not the wavy one (between $6 \leq fL_c/a_\infty \leq 7$). To the author's knowledge there is little work on the interaction of highly non-linear disturbances (such as that presented here) with undulated leading edges. The current results indicate how the known findings are not necessarily translatable to higher strength interactions and therefore represent a opportunity for future research.

6.6 Concluding remarks

Non-linear compressible simulations are conducted in order to investigate the secondary interaction noise effects generated by the impingement of a single spanwise vortex and zero-thickness undulated aerofoils. The secondary effects are categorised as acoustic scattering at the leading and trailing edges, and scattering of the bisected vortex halves at the trailing edge. The secondary effect contributions to the total far field perturbed pressure and PSD are contrasted directly with the primary (vortex-LE scattering). This is achieved by manipulating the time signals of finite chord

(total noise), downstream semi-infinite chord (primary noise), and upstream semi-infinite chord (vortex-trailing edge noise) aerofoil simulations.

The processed numerical results revealed that there were various substantial changes made in the acoustic power spectra and directivity profiles when the secondary sources were present in the solutions compared to the case where only the primary source was considered. The relative impact of the secondary sources was stronger with WLE than SLE since the primary source was reduced due to the presence of WLE. The relative reduction in TEVS due to WLE was insignificant (compared to those of the other sources) at high frequencies, and therefore the reduction of noise (a beneficial effect of WLE) disappeared in the high-frequency range where TEVS dominates. In addition the TEVS event was even strengthened at low frequencies when WLE was used. The combination of this effect and the WLE LEVS reduction means the TEVS dominates almost the entire frequency range at upstream angles.

For both SLE and WLE aerofoils at low frequencies ABS was the more prominent secondary source particularly in the downstream observer directions. ABS was also the main driver to produce oscillatory profiles in the acoustic power spectra due to its phase relationships with the other sources and also between its own sub-components (ABS-A to D). The spectral oscillations were significantly more pronounced at certain frequencies when the two competing sources had equal/similar strength. An interesting observation made was that the noise reduction measured from ABS only and that from all sources combined were fairly similar across all observer directions at a given frequency. This was understood by recalling the fact that ABS is the acoustic backscattering of all sources involved, and therefore it follows the trend of the dominating one that determines the level of noise reduction between the SLE and WLE cases. Phase oscillations initiated by the TEVS compared to the ABS are based on a shorter Δf, and consequently the spectral oscillations are most severe in the range where TEVS is significant (but stills secondary to LEVS). One possible approach to reduce the contribution from the secondary interaction sources is to introduce a undulated trailing edge. This modification successfully damps the ABS phase oscillations, and TEVS high frequency noise. It is also interesting to note that in-phase and out-of-phase WLE and WTEs show little difference in performance.

Additional viscous simulations are also carried out at $Re_\infty = 400,000$ in order to investigate how the WLE TEVS is effected by a laminar boundary layer. Surprisingly the TEVS noise is greatly increased by the WLE geometry as the spanwise waviness triggers breakdown of the secondary vorticity to three-dimensional eddies. Similar behaviour is also exhibited by the SLE for much higher vortex strength (see §5.5). Additionally, viscous simulation are carried out for a higher vortex strength (more similar to that encountered in helicopter rotor noise applications). The noise reduction properties are significantly altered by vortex strength, both in terms of the low frequency noise reduction trend, and dominance range of TEVS. This chapter therefore highlights two potential avenues for future research: The sensitivity of the WLE TEVS to viscosity (particularly concerning the breakdown to 3D flow); and WLE performance for high strength interactions.

The outcomes of the current study deliver a few useful messages to those working on aerofoil-turbulence noise and its reduction by using WLE. First, the results purely relying on the primary source mechanism (LEVS) may result in misleading conclusions for application purposes. The acoustic directivity profiles particularly with respect to the noise reduction may differ by 20dB (or more) in many observer directions even at low frequencies when the secondary sources take part. Secondly, investigating the results only at the vertical direction or within a narrow observer angle (e.g. $50^\circ \leq \theta \leq 130^\circ$ as in the previous experimental work) would be insufficient to complete the knowledge since the secondary sources behave very differently in the upstream ($150^\circ < \theta \leq 180^\circ$) and downstream ($0^\circ \leq \theta < 30^\circ$) directions. Lastly, the loss of noise reduction from the WLE is often attributed to self-noise dominance at high frequencies in experimental work. A fresh investigation into the previous data is required in order to clarify as to how much of the high-frequency spectra was influenced by the self-noise generation in contrast to the dominance of TEVS that is newly identified interaction noise effect (existing for inviscid and viscous flow). One possible approach is to subtract the TE self-noise before calculating the noise reductions as implemented in Roger & Moreau (2016).

This chapter has focused on the most fundamental scenario where the aerofoil is a flat plate. An interesting extension to the current work may be to consider realistic aerofoil geometries, particularly camber and angle of attack, as the asymmetric flow speeds for upper and lower sides may modify the TEVS response.

Chapter 7

Conclusions and Future Work

7.1 Summary of findings

This research presents investigations into the reduction of aerofoil-turbulence interaction (ATI) noise through application of sinusoidal wavy leading edges (WLE). The research methodology consists of high fidelity numerical simulations of the 3D compressible Euler equations based on high order implicit schemes and stretched meshes. It focuses on zero-thickness aerofoils at zero angle of attack undergoing interaction with an upstream vortical disturbances. The prescribed disturbance is a single spanwise vortex, which provides divergence free velocity field. Unlike other single disturbance methods (e.g. harmonic gusts) the approach contains a broadband spectrum of frequencies and is capable of capturing non-linear vortex motions. This approach also has two primary advantages with regards to understanding the mechanisms of ATI noise compared to synthetic turbulence approaches. Firstly, it makes identification of fundamental coherent structures generated during the interaction easier to identify; Secondly, it provides cleaner spectra which helps to reveal underlying noise reduction trends.

The current study includes a comprehensive overview of the existing literature concerning both interaction noise and wavy leading edges (WLE). The WLE geometry is consistently reported as providing significant broadband noise reductions in various scenarios (interactions with HIT, gusts and vortex flows). Studies agree that the main parameter which controls the level of noise reductions is the LE amplitude, followed by flow speed (or Reynolds number), then LE wavelength. Other significant findings in the literature include a linear noise reduction vs. frequency trend, optimum serration wavelength, and the possibility of phase interference and source strength reduction as noise reduction mechanisms.

The papers presented in this thesis provide a comprehensive understanding of the fundamental mechanisms associated with aerofoil-vorticity interaction and WLEs. This includes: in-depth analysis of the acoustic-fluid dynamic interactions occurring at the LE; investigation of proposed noise reduction mechanisms (phase interference and source strength reduction); and identification of secondary interaction noise effects including their significance for WLE noise reduction. A reoccurring

theme of this work is that a restricted view of the problem can result in misleading observations concerning the physics. The results therefore highlight a number of important considerations for future simulation and modelling approaches on the topic. In particular, which mechanisms are crucial in order to properly model the noise reduction associated with WLEs. Moreover, the detailed analysis of the mechanisms should help lead to better designs for noise reduction beyond undulated leading edges. Significant improvements have already been made guided by the earlier source strength findings, particularly the source dominance of the root. This includes slitted-LE and dual-frequency WLEs (Chaitanya *et al.*, 2016; Turner *et al.*, 2016*a*). Additionally, a number of significant discoveries are made concerning the importance of scattering at the TE in inviscid flow, which reveals an area of study neglected by analytical methods. The inviscid TE scattering also raises an important question for experimental approaches concerning its significance relative to self-noise at high frequencies.

The major findings of this work are listed below:

i As LE amplitude is increased the pressure response at the hill is reduced at all frequencies, at the peak it reduces at low frequencies until saturation, and at the root it remains similar to the SLE baseline.

ii Secondary horseshoe vortex structures are responsible for the source dissimilarity between peak and root by modifying the upstream impinging velocity field.

iii The WLE source characteristics are related to the serration aspect ratio.

iv LE amplitude is the main noise reduction parameter as it effects the source characteristics and causes phase-interference to occur at lower frequencies.

v Low frequency source reductions observed at the peak and hill are not observed in the far-field as the source strength over the full aerofoil surface is not significantly reduced.

vi Both source reduction and destructive interference effects become more significant as frequency is increased, although at high frequencies interference is dominant.

vii The source reduction mechanism actually disrupts the interference mechanisms (minimising the interference peaks) due to different source strengths observed between the peak and root.

viii TEVS is demonstrated for inviscid aerofoil-vortex interaction problems, with or without vertical miss distance

ix TEVS is the dominant source of noise at high frequencies (greater than LEVS). Relatively It is more significant for WLEs and for upstream observer angles.

x The dominance of TEVS at high frequency results in the loss of noise reduction from the WLE. This may be remedied by introducing TE undulation.

xi Secondary sources (ABS and TEVS) significantly change the WLE noise reduction directivity.

xii TEVS is also exhibited for viscous flows in the laminar regime. However it is highly dependent on the Reynolds number and vortex strength.

7.2 Future work arising from this study

The work presented in this thesis represents a simplified model of ATI in order to better understand the fundamental physics of the problem. Now that the simplified case is relatively well understood the next step is to increase the complexity of the problem towards more realistic scenarios. This includes introducing realistic geometry including aerofoil thickness, camber and angle of attack. Each of these effects is well understood on its own, but together may introduced interesting interactions between the various parameters. For example, camber will have a significant effect on the TEVS as convective disturbances will travel at different speeds on the upper and lower sides of the aerofoil. In a similar manner, the work presented here considers the source strength and phase-interference effects of a spanwise coherent interaction. It may be interesting to incorporate spanwise incoherence effects by modelling a spherical impinging disturbance. For very small disturbances (where only a small portion of the edge is excited) the phase interference effect is expected to be restricted to higher frequencies (Lyu & Azarpeyvand, 2017). It has also been shown by Chaitanya *et al.* (2017) that spanwise length scale is important for determining an optimal WLE wavelength. Comparatively for the current disturbance (or for $\lambda/\Lambda \leq 1$) larger wavelength is generally better (see §C.2). Another avenue for future research is a parameter study of vortex strength, it is apparent from the later stages of the work that the previous findings for weak disturbance interactions are not transferable to strong interactions.

A number of questions also remain concerning the TEVS. It was revealed how the analytical models of Amiet are capable of replicating the LEVS and ABS spectra produced during AVI, however the TEVS sound is only predictable with ad-hoc knowledge of the surface pressure fluctuations. A more detailed study of the convective disturbances and how they develop in time might be required in order to develop a complete model for AVI. Additionally the effect of Reynolds number on TEVS has been investigated, but only in the laminar regime. This limitation was primarily for practical reasons. Firstly, to avoid contributions from self-noise which may interfere with the TEVS. Secondly, due to the significant computational cost of resolving a turbulent boundary layer. Extending this analysis may lead to interesting conclusions concerning how secondary and tertiary TEVS structures interact with turbulent eddies, perhaps modifying the extent of self-noise or inducing early transition of the boundary layer downstream. Further investigation into the TEVS event in viscous flow for a WLE is also required. It is demonstrated how the WLE may obtain a stronger TEVS response due to breakdown of secondary vortices to tertiary structures. This however has only been shown under one flow condition with one WLE amplitude and wavelength. A sensitivity test for vortex strength, and geometric parameter study may therefore be useful.

Appendix A

Sensitivity test for the measure of interaction obliqueness

The following tables show the estimated angles of the oblique interaction (ϕ) described in §3.3 for various values of the $-v/a_\infty$ contour threshold selected from figure 3.10*c*. The sensitivity test was performed for all three WLE geometries used in §3 (h_{LE}/L_c =1/30, 1/15 and 1/10). The tables show that the choice of the threshold (within the 40% bandwidth tested) makes an insignificant change to the estimated obliqueness angle with a deviation of up to 4.07% at maximum as far as the current test cases are concerned.

Threshold selected	ϕ_1	ϕ_2	$\phi = (\phi_1 + \phi_2)/2$	Relative difference in ϕ
0.00784 (–20%)	30.18°	45.03°	37.61°	–3.39%
0.00882 (–10%)	29.48°	46.34°	37.91°	–2.62%
0.0098 (original)	30.13°	47.72°	38.93°	-
0.01078 (+10%)	34.43°	45.11°	39.77°	+2.16%
0.01176 (+20%)	32.46°	45.01°	38.74°	–0.49%

Table A.1: The estimation of ϕ for various thresholds in the case of $h_{LE}/L_c = 1/30$.

Threshold selected	ϕ_1	ϕ_2	$\phi = (\phi_1 + \phi_2)/2$	Relative difference in ϕ
0.00784 (–20%)	42.85°	61.42°	52.14°	–4.07%
0.00882 (–10%)	44.75°	62.80°	53.78°	–1.05%
0.0098 (original)	45.37°	63.33°	54.35°	-
0.01078 (+10%)	44.34°	61.45°	52.90°	–2.67%
0.01176 (+20%)	43.42°	61.10°	52.26°	–3.85%

Table A.2: The estimation of ϕ for various thresholds in the case of $h_{LE}/L_c = 1/15$.

Threshold selected	ϕ_1	ϕ_2	$\phi = (\phi_1 + \phi_2)/2$	Relative difference in ϕ
0.00784 (–20%)	48.97°	69.55°	59.26°	–1.66%
0.00882 (–10%)	47.97°	69.23°	58.60°	–2.75%
0.0098 (original)	50.76°	69.76°	60.26°	-
0.01078 (+10%)	51.08°	67.97°	59.53°	–1.21%
0.01176 (+20%)	51.00°	67.45°	59.23°	–1.71%

Table A.3: The estimation of ϕ for various thresholds in the case of $h_{LE}/L_c = 1/10$.

Appendix B

Discussion of vortex models

This section of the appendix includes additional discussion of the vortex models utilised in §3 and §4, including comparison to classical models in literature. The most idealised model for a vortex is an irrotational potential vortex:

$$v_\theta(r) = \frac{\Gamma}{2\pi r} \tag{B.1}$$

where v_θ is the tangential velocity, Γ is the circulation, and r is the radial distance from the vortex axis. Clearly (B.1) is not practical for the purpose of simulations due to the singularity occurring at $r = 0$. In real viscous flows a vortex is split into two regions, a core region where the induced velocity is zero at the centre and increases with r, and an outer region where the induced velocity decays with r. A simplest model which accounts for a vortex core is the Rankine vortex. This model assumes solid body rotation of a finite core of radius R surrounded by the potential flow solution.

$$v_\theta = \begin{cases} \frac{\Gamma r}{2\pi R^2} & \text{for} \quad r \leq R \\ \frac{\Gamma}{2\pi r} & \text{for} \quad r > R \end{cases} \tag{B.2}$$

Although this model solves the issue of the singularity at $r = 0$ a discontinuity exists in the vorticity at $r = R$. In reality, this discontinuity will be smoothed by viscous effects. A simple model which accounts for this effect is the Kaufmann (Scully) vortex:

$$v_\theta = \frac{\Gamma r}{2\pi(R^2 + r^2)} \tag{B.3}$$

Figure B.1 compares the velocity profiles produced by (B.1)-(B.3) with the two vortex models implemented in the current simulations ((3.2) and (4.1)). Unlike the above classical models which decay linearly in the outer region, the vortex models implemented in this thesis decay exponentially. They are therefore referred to as r^4 (§3) and r^2 (§4) models, which corresponds to their respective exponential decay rates. The parameters used for the classical models are $R = 0.0225Lc$ and $\Gamma = -0.012\pi R$, additionally the value for σ for the r^4 vortex is changed to 560 for better comparison of the velocity profile. The r^4 vortex velocity profile has a stationary point (zero vorticity) at the

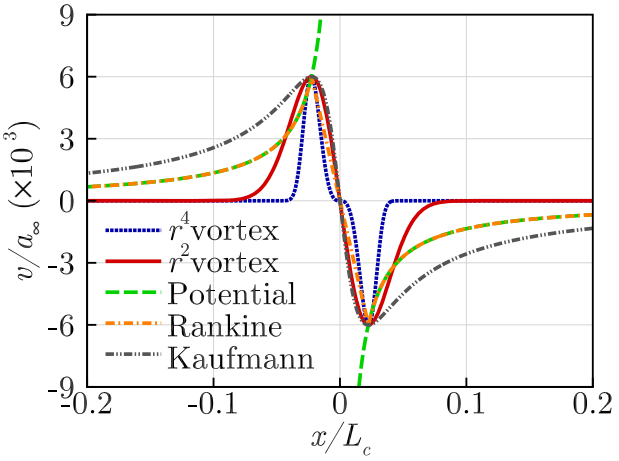

Figure B.1: Comparison of the vertical velocity profiles obtained by the vortex models utilised in the current with classical models from literature.

centre which differs from the classical models. Comparatively the r^2 vortex produces a very similar velocity profile to the Kaufmann model.

The main reason for choosing the current vortex profiles over the classical models is that they produce a more compact velocity disturbance. This allows the vortex to be initialised closer to the aerofoil LE which significantly reduces the run time of the simulation. Additionally there is a less strict requirement on the grid resolution far upstream in order to capture the impinging vortex, which significantly reduces the computational cost. The diameter of the vortex (determined where $v = 0.01v_{max}$)) is $4.5L_c$ for the Rankine and Kaufmann profiles, compared to $0.16L_c$ for the r^2 profile.

Figure B.2 shows the PSD of vertical velocity produced by the two vortex models considered in the current work. Both linear and logarithmic scales are shown in figure B.2(a) and (b) respectively. The r^4 vortex profile produces a multi-modal Gaussian distribution, while the r^2 vortex produces a positively skewed normal distribution. The lobes shown for the r^4 vortex in figure B.2(b) are a result of phase interference between the upwash and downwash strokes, occurring at frequencies $f^* = n/(2\Delta t^*)$, where $\Delta t^* = 1.182$. The frequency bandwidth of the vortex can be easily controlled by changing the vortex diameter (through the parameter σ). This is clearly shown by figure B.3.

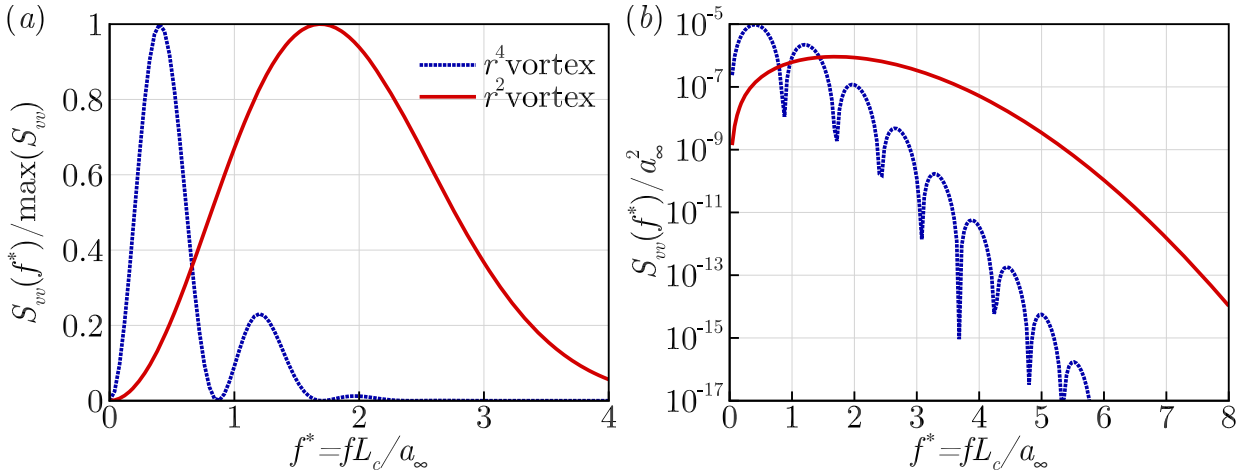

Figure B.2: PSD of vertical velocity fluctuations obtained by the two vortex models utilised in the current study. (*a*) Linear scale; (*a*) Log scale.

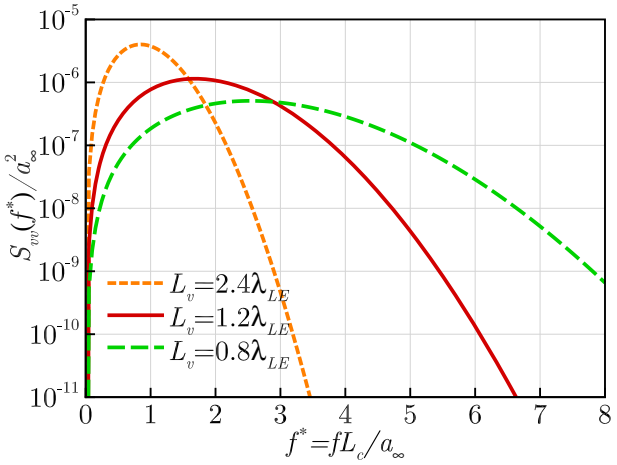

Figure B.3: Effect of changing the vortex size on the frequency bandwidth of the r^2 vortex model. $L_v = 1.2\lambda_{LE}$ is the default vortex size ($\sigma = 44.25$) used in §5-6.

Appendix C

Additional noise reduction trends

C.1 Sensitivity of results to vortex parameters

In this section the generality of the current findings is investigated with respect to vortex strength, size and shape. The vortex strength parameter was selected for consistency with previous studies. Most notably (Chaitanya *et al.*, 2017; Kim *et al.*, 2016; Narayanan *et al.*, 2015) who all consider problems with mean impinging velocity $v_{max} = 0.025u_\infty$. Additionally the default vortex strength used in this thesis is well within the linear regime, which suggests some generality of the current findings. This is demonstrated in figure C.1, which compares the far-field acoustic pressure data presented for default strength ($\epsilon = 0.0377$ and $v_{max} = 0.025u_\infty$) to a case with half the vortex induced velocity ($\epsilon = 0.01885$ and $v_{max} = 0.0125u_\infty$). The acoustic pressure and spectra are normalised by $\max(p_a^{SLE})$ and $\max(p_a^{SLE})^2$ respectively for easier comparisons between the two results. The time signals and spectra collapse almost perfectly (except for a small difference for the SLE at very high frequency).

It is also important to confirm that neither change in shape nor size significantly alters the noise reduction mechanisms. Figure C.2 shows the noise reduction spectra obtained by the default WLE profile with semi-infinite chord for interaction with the two vortex shape functions. The diameter of the r^4 profile has been reduced here to match the r^2 profile ($L_v/L_c = 0.16$ based on the location the induced velocity drops below 1%). The noise reduction profiles are almost identical until high frequencies ($f^* > 5$) where there is a small magnitude offset (< 2 dB). This may be caused by small differences in the secondary vortex dynamics which make a significant impact on the sources at high frequencies (as shown in §4.5).

The impact of changing the vortex size is shown in figure C.3 which compares the noise reduction obtained for three vortex diameters $L_v = 0.17L_c$ ($\sigma = 44.25$), $L_v = 0.255L_c$ ($\sigma = 29.5$), and $L_v = 0.34L_c$ ($\sigma = 22.125$) with default amplitude and wavelength. In each case the NR follows the same trend until a certain frequency where it quickly drops to zero. The range of frequencies where NR is achieved is an indication of the frequency bandwidth of the vortex, which is reduced

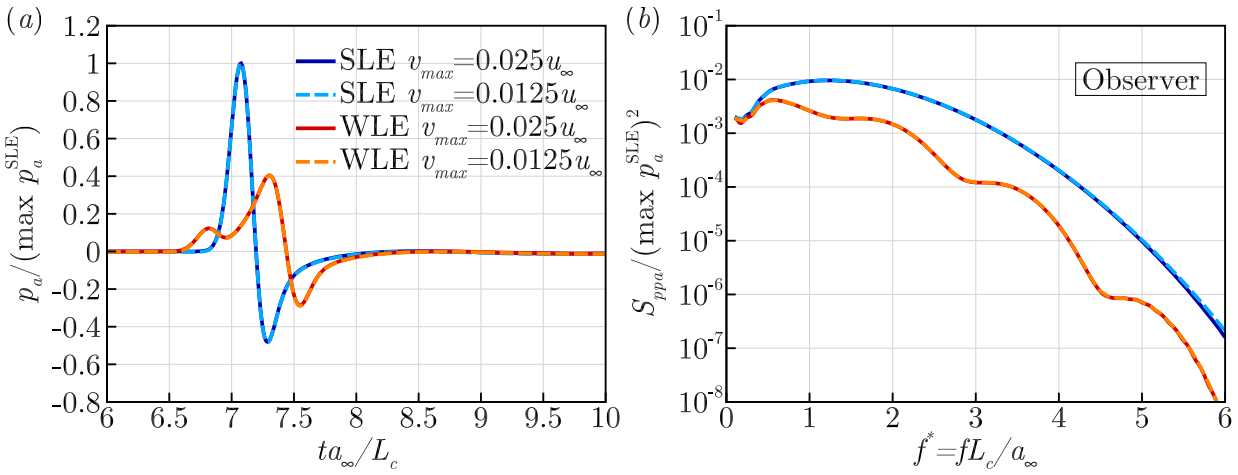

Figure C.1: (a) Time signals of acoustic pressure $p_a(\boldsymbol{x}_o, t)/p_\infty$ obtained at observer location $\boldsymbol{x}_o/L_c = (0, 5, 0)$ for SLE and WLE geometries with two different impinging vortex strengths. (b) The corresponding power spectra of the former. The pressure and spectra are scaled by $\max(p_a^{SLE})$ and $\max(p_a^{SLE})^2$ so that direct comparison can be made.

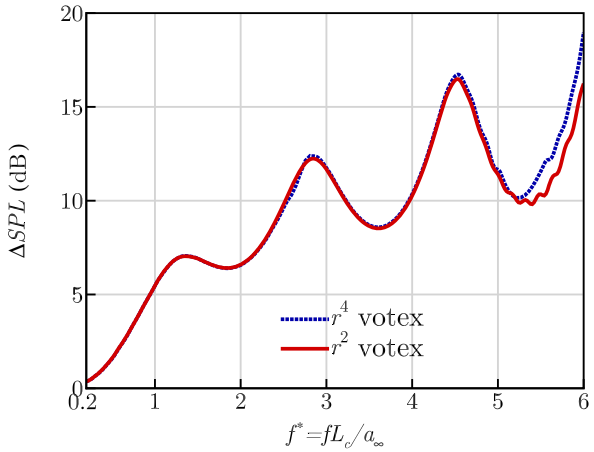

Figure C.2: Comparison of the SIC noise reduction obtained using the two vortex shape functions utilsing the same vortex diameter $L_v|_{1\%} = 0.17L_c$.

as the vortex size is increased. The consistent trends confirms that a single vortex size is sufficient for the current investigations in order to understand the noise reduction mechanisms. A small diameter is desirable as it allows a larger range of frequencies to be evaluated (see figure B.3). The default vortex size is therefore the smallest of the three tested ($L_v = 0.17L_c$). An even smaller vortex could be used in order to analyse even higher frequencies but is avoided as this would incur additional computational cost (finer grid required upstream to resolve the vortex).

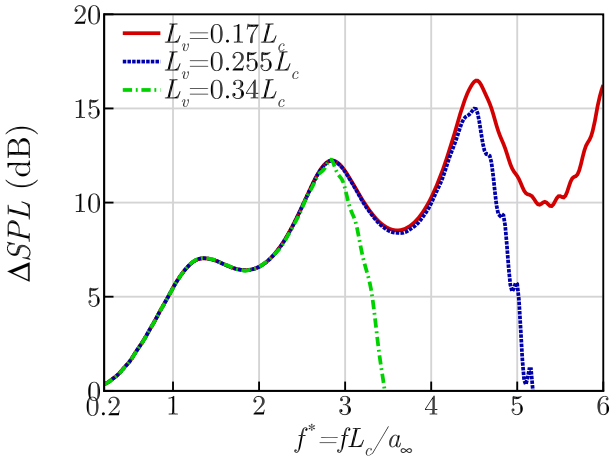

Figure C.3: Effect of changing vortex diameter L_v on the undulated LE noise reduction spectra with WLE amplitude and wavelength fixed at $h_{LE}/L_c = 1/15$ and $\lambda/L_c = 2/15$ respectively.

C.2 Effect of leading edge wavelength for a spanwise infinite disturbance

This section of the appendix considers the impact of LE wavelength λ_{LE} on the far-field noise reduction spectra obtained during interaction with a spanwise infinite disturbance. Figure C.4 revisits the noise reduction predicted by the LE line model introduced in §4. The result is compared to the numerical solution for two WLE profiles, both with default amplitude but with a factor of two difference in wavelength. Overall the larger wavelength case agrees better with the analytical model particularly for the higher frequency noise reduction peak.

As previously discussed (§4) the extent of destructive interference is mainly determined by h_{LE}, with a large h_{LE} allowing noise reductions to occur at a lower frequency. The source strength on the other hand is determined by the LE aspect ratio $AR = 2h_{LE}/\lambda_{LE}$ (§3), with a more consistent spanwise source obtained when aspect ratio is reduced. As wavelength is increased the source characteristics along the LE therefore become more compatible and destructive interference is more severe. In summary, in order to maximise the interference mechanism AR must be minimised and h_{LE} maximised.

It is worth noting here that this result is only general for coherent spanwise interactions ($\lambda/\Lambda \leq 1$). In this case the destructive interference peaks are enhanced as the sources along the LE are always correlated. It has well been documented how the LE wavelength reaches an optimum if the disturbance has a spanwise length scale (Chaitanya *et al.*, 2017, 2015). It is thought that the optimum wavelength will occur when the adjacent roots are excited incoherently, so that they may not constructively interfere.

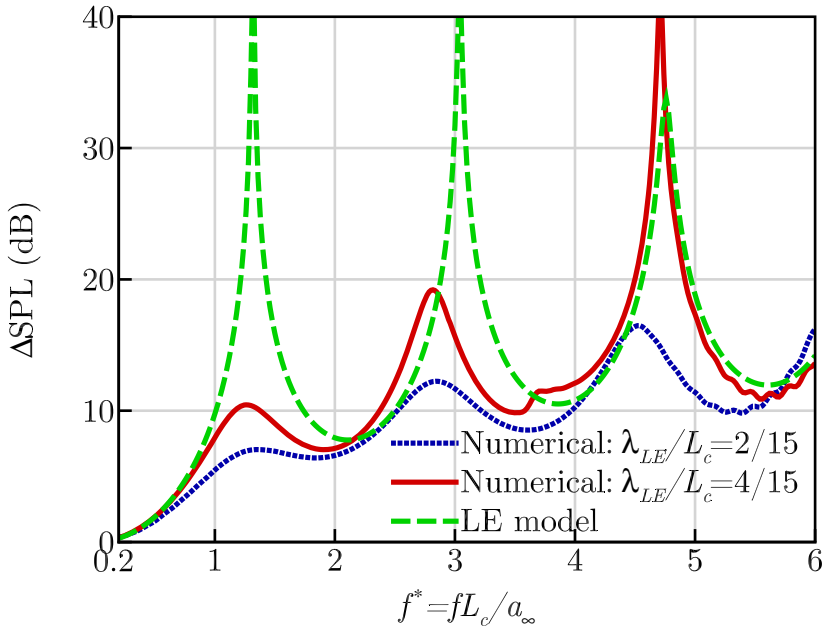

Figure C.4: Comparison of noise reduction spectra obtained by the default WLE ($h_{LE}/L_c = 1/15$ and $\lambda_{LE}/L_c = 2/15$) and one with twice the WLE wavelength compared to the LE line model **B** of §4.4.2.

Appendix D

Additional analysis of WLE TEVS response

D.1 Wall pressure observations

In this section we elaborate on the mechanisms which enable the TEVS to be increased at low frequencies for the WLE, while remaining similar to the SLE at high frequencies. Firstly figure D.1 shows the TEVS time signals and corresponding spectra for observer locations directly downstream of the peak, hill and root locations, in addition to the SLE baseline. It is clear how the peak and hill actually produced an increased low frequency TEVS pressure response relative to the SLE. The root on the other hand exhibits increased magnitude at high frequency and occasionally out-of-phase pressure fluctuations relative to the rest of the edge (as is clear from figure D.1(a). This indicates the similar strength at high frequencies may be related to an interference effect observed between the root (high strength out-of-phase) and rest of the TE (lower strength in-phase). Figure D.2 shows the two-point phase spectrum between the point directly downstream of the peak and other points along the span. The two-point phase spectrum is calculated as follows:

$$\phi_{ppw}(x_1, x_2, f^*) = \mathrm{Im}[\log[S_{ppw}(\boldsymbol{x}_1, \boldsymbol{x}_2, f)]] \tag{D.1}$$

where $S_{ppw}(\boldsymbol{x}_1, \boldsymbol{x}_2, f)$ is the cross power spectral density:

$$S_{ppw}(\boldsymbol{x}_1, \boldsymbol{x}_2, f) = \frac{2}{T}\widehat{\Delta p_w}(\boldsymbol{x}_1, f)\widehat{\Delta p_w}^*(\boldsymbol{x}_2, f) \tag{D.2}$$

It is clear from figure D.2 how the region directly downstream of the root is significantly out of phase for frequencies between $f^* = 4$ and 7, where the TEVS contributions are similar for SLE and WLE. On the other hand at low frequencies the edge is relatively in-phase, the increased wall pressure magnitude directly downstream of the peak and hill will therefore result in TEVS increase at low frequency. Also shown in figure D.3 is a comparison of the ABS and TEVS spectra obtained by two WLE aerofoils of different amplitude ($h_{LE}/L_c = 1/15$ and $h_{LE}/L_c = 1/10$).

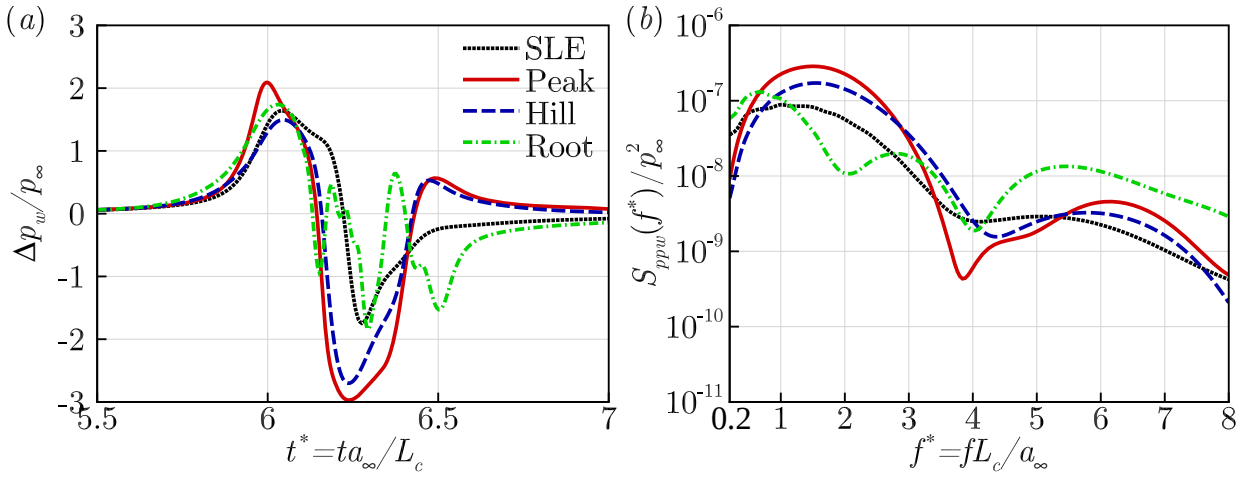

Figure D.1: Comparison of the wall pressure loading fluctuations at the TE due to the TEVS obtained directly downstream of the WLE peak, hill and root compared to the SLE. Signals extracted one grid point upstream of the TE: (a) the time signals of $\Delta p_{\text{w-TEVS}}/p_\infty$ and p_a/p_∞. (b) The corresponding power spectra.

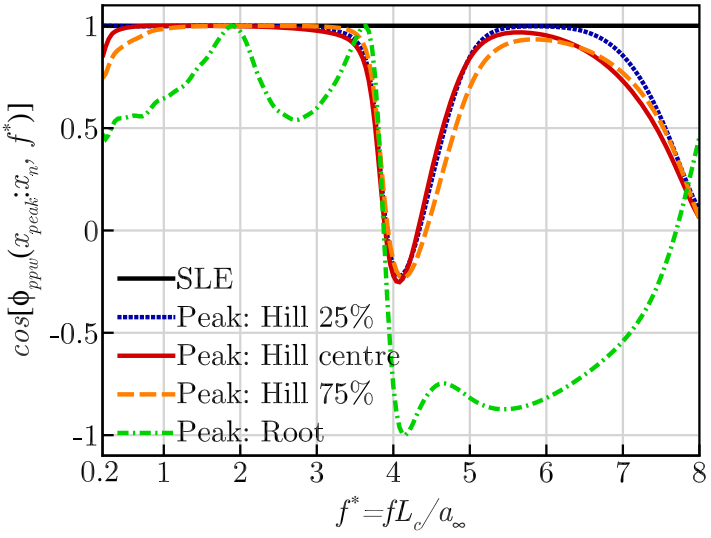

Figure D.2: Cosine of the two-point phase spectra ($\cos[\phi_{ppw}(x_1, x_2, f^*)]$) of wall pressure fluctuations between the TE point directly downstream of the LE peak and four points equally spaced in span. Hill 25% and 75% refer to the mid points of peak–hill, and hill–root respectively.

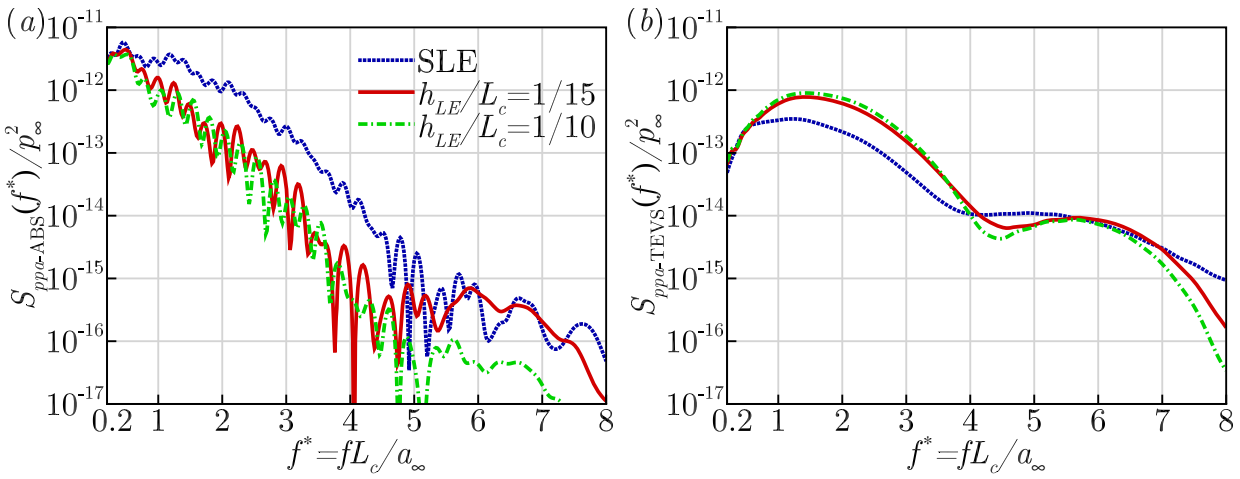

Figure D.3: Acoustic power spectra for ABS (a) and TEVS (b) components of the secondary source obtained with two WLE amplitudes (h_{LE}/L_c = 1/15 and 1/10). The observer location is $\boldsymbol{x}_o/L_c = (0, 5, 0)$.

This demonstrates how the consistent high frequency response of TEVS (and increased WLE low frequency response) is not limited to the single test case in §6.

D.2 Application of Howe's theory

An important part of the future work is to better understand the development of the fluid dynamic structures as they convect over the aerofoil surface and how they relate to the generated TEVS. In order to achieve this outcome it is important to firstly determine which aspects of the flow are related to the generation of sound at the TE. One possible route is to utilise the vortex-sound theory of Howe (1988), which relates the hydrodynamic field to the stagnation enthalpy B in the following manner:

$$B = -\int (\boldsymbol{\omega} \times \boldsymbol{u})(\boldsymbol{y}, \tau) \frac{\partial G}{\partial \boldsymbol{y}}(\boldsymbol{x}, \boldsymbol{y}; t-\tau) \mathrm{d}^3\boldsymbol{y}\mathrm{d}\tau \tag{D.3}$$

Where G is the problem specific Greens function, $\boldsymbol{x}$ represents far-field coordinates, and $\boldsymbol{y}$ source coordinates. It is assumed in the far-field that the acoustic pressure can be approximated by $B = p_a/\rho$ for $M_\infty << 1$. For the TEVS problem we opt for a half-plane Greens function. This is appropriate as the TEVS propagates in an upstream cardioid pattern. From Howe (2014) the compact Green's function is:

$$G(\boldsymbol{x}, \boldsymbol{y}, t-\tau) \approx G_0(\boldsymbol{x}, t-\tau) + G_1(\boldsymbol{x}, \boldsymbol{y}, t-\tau) + \cdots \tag{D.4}$$

G_0 is not a function of $\boldsymbol{y}$ and therefore is neglected ($\partial G_0/\partial \boldsymbol{y} = 0$), yielding:

$$G_1(\boldsymbol{x}, \boldsymbol{y}, t-\tau) \approx \frac{\psi^*(\boldsymbol{x})\psi^*(\boldsymbol{y})}{\pi|\boldsymbol{x}|} \delta\left(t - \tau - \frac{|\boldsymbol{x}|}{c_0}\right), \quad |\boldsymbol{x}| \to \infty \tag{D.5}$$

with

$$\psi^*(\boldsymbol{x}) = \sqrt{r}\sin\left(\frac{\theta}{2}\right) \quad \text{and} \quad \psi^*(\boldsymbol{y}) = \sqrt{r_0}\sin\left(\frac{\theta_0}{2}\right) \tag{D.6}$$

The above equations assumes far-field conditions $|x-y| \to |x|$ and that the distance between the vorticity and the edge is small compared to the acoustic wavelength (compact source approximation). Substituting (D.5) into (D.3) yields:

$$p_a(\boldsymbol{x},t) = -\frac{\rho_0\psi^*(\boldsymbol{x})}{\pi|\boldsymbol{x}|}\int(\boldsymbol{\omega}\times\boldsymbol{u})\left(\boldsymbol{y}, t-\frac{|x|}{c_0}\right)\frac{\partial\psi^*(\boldsymbol{y})}{\partial\boldsymbol{y}}(\boldsymbol{y})\mathrm{d}^3\boldsymbol{y} \tag{D.7}$$

where $\psi^*(\boldsymbol{y}) = \mathrm{Real}(-i\sqrt{y_1+iy_2})$ is the velocity potential around the half plane edge. Considering that $\partial\psi^*(\boldsymbol{y})/\partial y_3 = 0$ and $U_\infty >> |\boldsymbol{u}'|$ it is reasonable to simply (D.7) to the following:

$$p_a(\boldsymbol{x},t) = -\frac{\rho_0\psi^*(\boldsymbol{x})U_\infty}{\pi|\boldsymbol{x}|}\int\omega_z\left(\boldsymbol{y}, t-\frac{|x|}{c_0}\right)\frac{\partial\psi^*(\boldsymbol{y})}{\partial y_2}(\boldsymbol{y})\mathrm{d}^3\boldsymbol{y} \tag{D.8}$$

The above equation demonstrates how spanwise vorticity is directly related to the radiated sound during TEVS. The velocity potential gradient $(\partial\psi^*(\boldsymbol{y})/\partial y_2)$ is zero on the aerofoil surface, maximum at the TE, and decreasing further downstream. This indicates that the sound is generated as the spanwise vorticity is convected past the TE point.

Figure D.4 shows the spanwise vorticity on the aerofoil surface (upper side) for SLE and WLE at $ta_\infty/L_c = 5.5$, shortly before interaction with the TE. Generally the spanwise vorticity agrees well with the wall pressure fluctuation time signals. There is a greater magnitude for the WLE case downstream of the root and peak during the downwash stroke (1st stroke), and for the majority of the span (excluding root) during the upwash stroke. Additionally, there is opposite signed vorticity in span directly downstream of the root during the upwash stroke. According to (D.8) this will reduce the net response at the TE, further confirming an inference mechanism between downstream root and the rest of the TE.

A number of questions still remain concerning the TEVS mechanisms, most notably why the spanwise vorticity decays at a slower rate for the WLE than the SLE. (At the LE a larger magnitude is observed for the SLE, see figure 3.14). Additionally, it is not fully understood why the changed sign spanwise vorticity appears downstream of the root.

D.3 Dynamic mode decomposition

Dynamic mode decomposition (DMD) first utilised by Schmid (2010) may be used to approximate the non-linear dynamics of flow data through eigenvalue decomposition of a linear model (Chen *et al.*, 2012). It is convenient for our purposes as it extracts the frequency information of each dynamic mode through the phase of its eigenvalue. DMD is therefore used in this section to gain some additional insight as to how the spanwise vorticity develops before it is scattered at the TE.

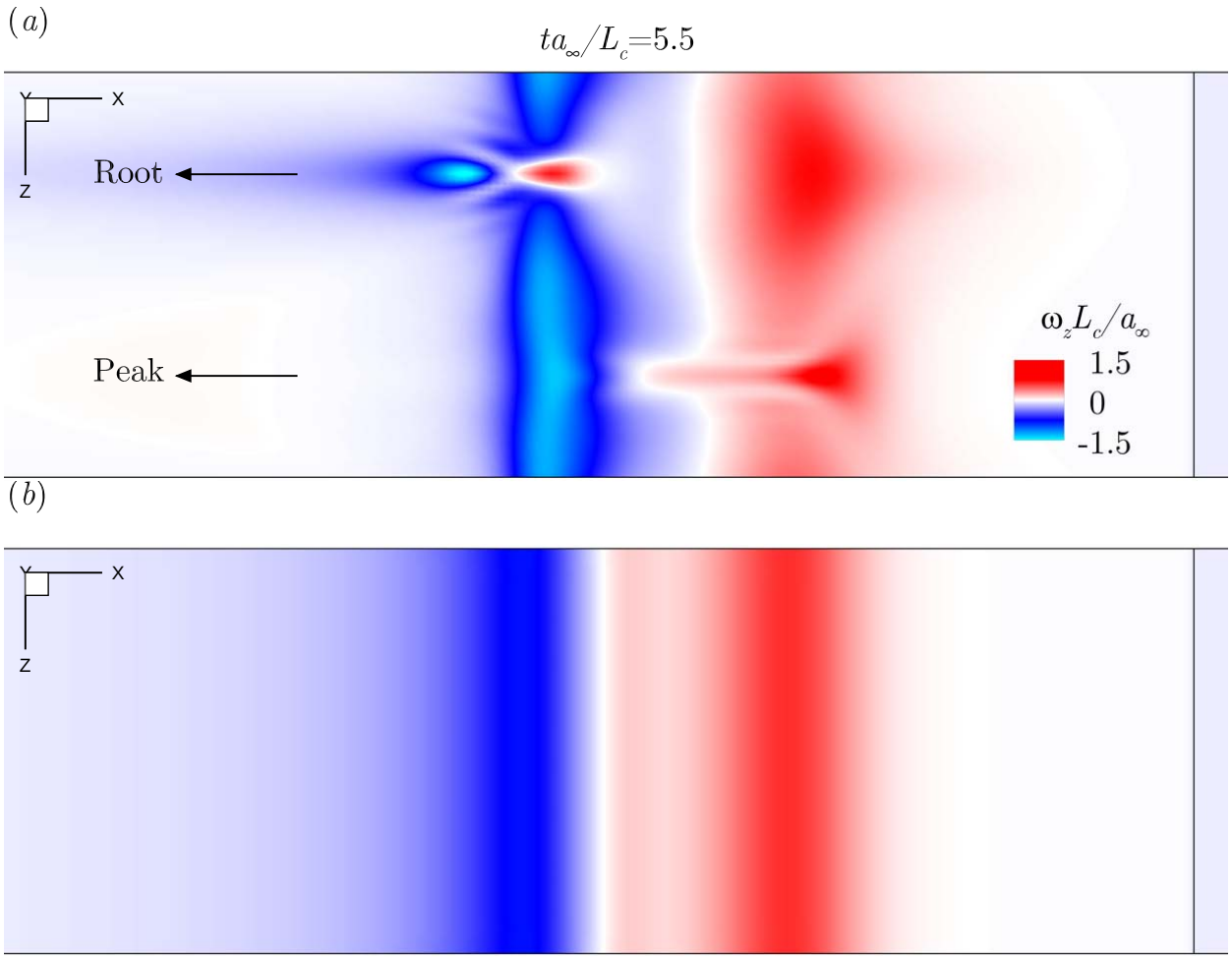

Figure D.4: Contours of spanwise vorticity $\omega_z L_c/a_\infty$ obtained on the aerofoil upper side taken at $ta_\infty/L_c = 5.5$, just before the disturbances are scattered at the TE: (a) WLE; (b) SLE.

In order to perform the DMD algorithm we first require a series of flow field snapshots taken with a constant sampling interval Δt:

$$\mathbf{V}_1^N = \{\mathbf{v}_1, \mathbf{v}_2, \mathbf{v}_3, \cdots, \mathbf{v}_N\} \tag{D.9}$$

where $\mathbf{v}$ represents a flow field variable (ρ, u, v, w, p), and N is the total number of snapshots. It is then assumed that the flow field at subsequent steps may be approximated by a linear mapping $\mathbf{A}$ such that

$$\mathbf{v}_{i+1} = \boldsymbol{A}\mathbf{v}_i \tag{D.10}$$

and consequently:

$$\boldsymbol{V}_1^N = \{\mathbf{v}_1, \boldsymbol{A}\mathbf{v}_1, \boldsymbol{A}^2\mathbf{v}_1, \cdots, \boldsymbol{A}^{N-1}\mathbf{v}_1\} \tag{D.11}$$

it then follows that:

$$\boldsymbol{A}\boldsymbol{V}_1^{N-1} = \boldsymbol{V}_2^N \tag{D.12}$$

(a)

(b)

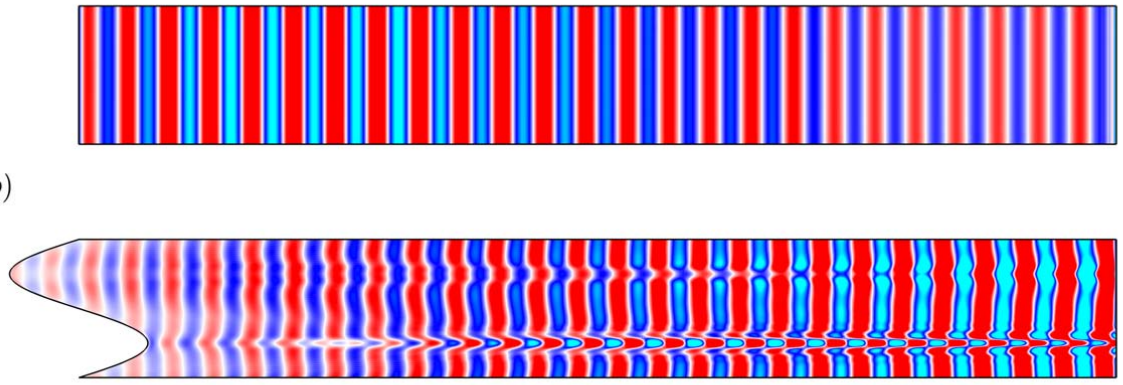

Figure D.5: Dynamic mode for $f^* = 6$ obtained at $y = 0^+$ for SLE (a) and WLE (b) cases

The aim of DMD is to estimate the dynamic behaviour of the process A acting on the snapshot sequence. We may also represent the final snapshot of the sequence $\mathbf{v}_N$ as a linear combination of all the previous:

$$\mathbf{v}_N = a_1\mathbf{v}_1 + a_2\mathbf{v}_2 + \cdots + a_{N-1}\mathbf{v}_{N-1} + \mathbf{r} \tag{D.13}$$

where $\mathbf{r}$ is a residual term due to our discrete approximation of the process. It is then possible to show that:

$$\boldsymbol{V}_2^N = \boldsymbol{V}_1^{N-1}\boldsymbol{S} + \mathbf{r}\mathbf{e}_{N-1}^T \tag{D.14}$$

where $\mathbf{e}_{N-1}$ is the $N-1$th unit vector and

$$\boldsymbol{S} = \begin{pmatrix} 0 & & & a_1 \\ 1 & 0 & & a_2 \\ & \ddots & \ddots & \vdots \\ & & 1 & 0 \; a_{N-2} \\ & & & 1 \; a_{N-1} \end{pmatrix}$$

Equating (D.12) and (D.14) reveals that the eigenvalues of $\boldsymbol{A}$ and $\boldsymbol{S}$ approximate one another. The dynamic mode may then be obtained through calculation of the eigenvalues and vectors of $\boldsymbol{S}$. It was noted by Schmid (2010) that it is preferable to firstly include a prepossessing step to avoid an ill conditioned matrix. This involves a singular value decomposition ($\boldsymbol{V}_1^{N-1} = \boldsymbol{U}\boldsymbol{\Sigma}\boldsymbol{W}^T$). Substitution into (D.12) and (D.14) then yields

$$\boldsymbol{U}^H\boldsymbol{A}\boldsymbol{U} = \boldsymbol{U}^H\boldsymbol{V}_2^N\boldsymbol{W}\boldsymbol{\Sigma}^{-1} \equiv \widetilde{\boldsymbol{S}} \tag{D.15}$$

Finally the DMD modes are extracted from the eigenvectors ($\mathbf{y_i}$) of $\widetilde{\boldsymbol{S}}$ as:

$$\Phi_i = \boldsymbol{U}\mathbf{y_i} \tag{D.16}$$

with frequency and growth rate of each mode are determined by $f_i = atan(\lambda_i))/(2\pi\Delta t)$ and $\sigma_i = \ln(|\lambda_i)|)/(\Delta t)$ respectively.

Figure D.5 shows the dynamic mode obtained for $f^* = 6$ based on spanwise vorticity plot on the aerofoil upper side for SLE (a) and WLE (b) cases. A total of 800 images were used for the DMD analysis during the period $1.5 \leq t^* \leq 7.3$. The figure shows how the high frequency mode develops as the vortex (and secondary structures) convect over the aerofoil surface towards the TE. Generally for the WLE aerofoil the mode grows in the streamwise direction, while for the SLE it initially grows then decays as it approaches the TE. It is clear from figure D.5(b) how initially the spanwise vorticity downstream of the root is in phase with the rest of the span, but gradually drifts as the disturbances convect downstream. This explains the out-of-phase shift observed in figure D.2 at this frequency.

Appendix E

Dual-wavelength wavy leading edges

This section of the appendix covers some of the results presented in Turner *et al.* (2016*a*) concerning dual-wavelength wavy leading edges (DWLE). The aim of introducing an additional LE wavelength is to entice destructive interference, and therefore additional noise reductions, between the two LE root regions. The root has been shown in §3 to be the most prominent noise source for a WLE, remaining comparable to the straight leading edge (SLE) baseline across the majority of the frequency range. The performance benefit obtained by DWLEs was first observed experimentally by Chaitanya *et al.* (2016). The results presented here provide confirmation of the DWLE performance for a different disturbance type. Additionally insight is also provided concerning the root-root interference mechanism.

The DWLE profile is constructed by combining two sinusoidal components of equal amplitude but different wavelength. This results in a LE profile with an additional "peak" (local maximum point) and "root" (local minimum point) per wavelength. Here we keep the amplitude of the two sine components constant while the wavelength is varied by a factor of two. This results in the following equation for the DWLE profile:

$$x_{LE}(z) = \alpha h \left[\sin\left(\frac{2\pi z}{\lambda}\right) + \sin\left(\frac{2\pi z}{\lambda/2} + \phi\right) \right] - \frac{L_c}{2} \tag{E.1}$$

where α is a weighting factor used to scale the DWLE peak-root amplitude ($2h_{LE}$) such that it remains consistent with the single-frequency cases:

$$\alpha = \frac{\max(x_{LE}^{WLE}) - \min(x_{LE}^{WLE})}{\max(x_{LE}^{DWLE}) - \min(x_{LE}^{DWLE})}, \tag{E.2}$$

and ϕ is a phase shift between the two sinusoidal functions. The simulations are conducted with the same vortex profile as in §3. Figure E.1 compares the noise reduction spectra obtained by four DWLE geometries with different amplitudes and phase shifts. This confirms how the DWLE aerofoils offer substantial noise reductions improvements relative to the equivalent WLE cases in small frequency bands. As the amplitude increases the noise reduction peaks shift to a lower

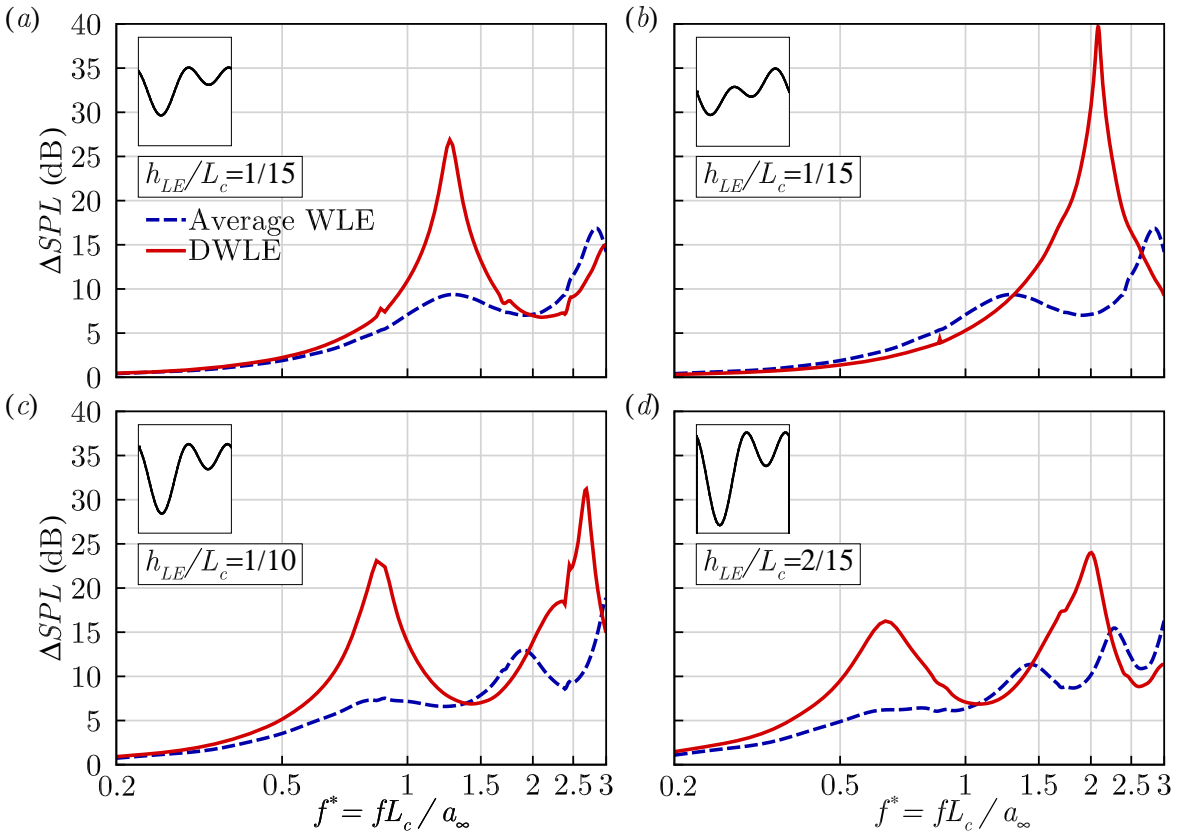

Figure E.1: Comparison of the noise reduction spectra obtained by four DWLE geometries compared to the corresponding averaged WLE components of the same amplitude. (a) $h_{LE}/L_c = 1/15$ and $\phi = 3\pi/2$; (b) $h_{LE}/L_c = 1/15$ and $\phi = 0$; (c) $h_{LE}/L_c = 1/10$ and $\phi = 3\pi/2$; and (d) $h_{LE}/L_c = 2/15$ and $\phi = 3\pi/2$;

frequency which is due to a larger difference in retarded time between the two roots. Another interesting observation is that the case with $\Phi = 0$ significantly out performs the equivalent $\Phi = 3\pi/2$ case. This is likely due to the fact that the same streamwise offset is obtained between adjacent roots, peaks, and surrounding hill regions, meaning a greater portion of the LE interferes destructively at the maximum noise reduction frequency.

A simple approximation for the maximum noise reduction frequencies is obtained by considering when the two roots will be $m\pi$ out of phase:

$$\frac{2\pi f d}{U_\infty} = m\pi \tag{E.3}$$

$$\rightarrow f = \frac{mU_\infty}{2d} \tag{E.4}$$

where d is the streamwise distance between the two roots. Application of the above equation results in the predictions presented in table E.1. This simple and quick prediction obtains reasonable accuracy and is therefore useful for selection of a DWLE targeting a specific frequency band. The error is simple to explain in the context of this thesis. Firstly there is a difference in the sweep angle in the vicinity of the two roots. As pointed out in §3 this will result in different

streamwise vortex production and therefore different surface pressure magnitudes. Consequently more significant phase interference may be obtained between other points with a more comparable source strengths. In addition, it was revealed in §4 that the source cannot be considered restricted to the LE line. In order to get an accurate prediction of the phase interference peaks the distributed source must be taken into account over a significant portion of the surface.

h_{LE}	Φ	Actual	Predicted
1/15	$3\pi/2$	$1.26m$	$1.41m$
1/15	0	$2.08m$	$2.28m$
1/10	$3\pi/2$	$0.84m$	$0.936m$
2/15	$3\pi/2$	$0.64m$	$0.70m$

Table E.1: Predicted maximum noise reduction frequencies obtained via. E.3 for the DWLE geometries presented in figure E.1.

Appendix F

Signal processing code

```
function [Spp,freq] = spectra(t,pa,pb,padfactor)
%Function for calculating PSD/CPSD from AVI time signal
%pa=/=pb returns CPSD
%pa==pb returns PSD (equivalent to matlab pwelch function)
%padfactor specifies the extent of zero-padding, padfactor=1 for no padding
lmt=length(t);
period=t(end)-t(1);
tpop=2*pi/period;
ra0=tpop;
ra1=ra0+lmt*tpop;
fctr=(ra1-ra0)/lmt;
 for j=1:(padfactor*lmt)/2+1
    freq(j)=(j-1)*fctr/padfactor;
 end
 freq=freq*0.5/pi;

nfft=length(t)*padfactor;
fs=lmt/period;

win=tukeywin(lmt,0.2)';
[Spp]=cpsd(pa,pb,win,0,nfft,fs);
end
```

References

Adamczyk, J. J. 1974 The passage of an infinite swept airfoil through an oblique gust. NASA/CR-2395 .

Agrawal, B. R. & Sharma, A. 2016 Numerical analysis of aerodynamic noise mitigation via leading edge serrations for a rod-airfoil configuration. *Int. J. Aeroacoust.* **25** (8), 734–756.

Amiet, R. K. 1974 Compressibility effects in unsteady thin-airfoil theory. *AIAA J.* **12** (2), 252–255.

Amiet, R. K. 1975 Acoustic radiation from an airfoil in a turbulent stream. *J. Sound Vib.* **41**, 407–420.

Amiet, R. K. 1976 Noise due to turbulent flow past a trailing edge. *J. Sound Vib.* **47**, 387–393.

Astley, R., Agarwal, A., Holland, K. R., Joseph, P. F., Self, R. H., Smith, M. G., Sugimoto, R. & Tester, B. J. 2007 Predicting and reducing aircraft noise.

Atassi, H. M. 1984 The Sears problem for a lifting airfoil revisited-new results. *J. Fluid Mech.* **141**, 109–122.

Atassi, H. M., Subramaniam, S. & Scott, J. R. 1990 Acoustic radiation from lifting airfoils in compressible subsonic flow. *AIAA Paper* 90-3911 .

Ayton, L. J. 2016 An analytic solution for gust-aerofoil interaction noise including effects of geometry. *IMA J. Appl. Math.* **00**, 1–25.

Ayton, L. J. 2017 An analytical solution for gust-aerofoil interaction noise for plates with leading-edge serrations. In *23rd AIAA/CEAS Aeroacoustics Conference. AIAA Paper* 2017-3492.

Ayton, L. J. & Paruchuri, C. 2016 Analytical and experimental investigation into the effects of leading-edge radius on gust-aerofoil interaction noise. *J. Sound Vib.* **378**, 28–37.

Ayton, L. J. & Peake, N. 2013 On high-frequency noise scattering by aerofoils in flow. *J. Fluid Mech.* **734**, 144–182.

Biedermann, T. M., Chong, T. P., Kameier, F. & Paschereit, C. O. 2017 Statistical-empirical modeling of airfoil noise subjected to leading-edge serrations. *AIAA J.* **55** (9), 3128–3142.

Blandeau, V. P., Joseph, P.F., Jenkins, G. & Powles, C. J. 2011 Comparison of sound power radiation from isolated airfoils and cascades in turbulent flow. *J. Acoust. Soc. Am.* **129** (6), 3521–3530.

Bolzon, M. D., Kelso, R. M. & Arjomandi, M. 2016 Tubercles and their applications. *J. Aerospace Eng.* **29** (1), 1–10.

Chaitanya, P., Joseph, P., Narayanan, S., Vanderwel, C., Turner, J., Kim, J. W. & Ganapathisubramani, B. 2017 Performance and mechanism of sinusoidal leading edge serrations for the reduction of turbulence-aerofoil interaction noise. *J. Fluid Mech.* **818**, 435–464.

Chaitanya, P., Narayanan, S., Joseph, P. & Kim, J. W. 2016 Leading edge serration geometries for significantly enhanced leading edge noise reductions. In *22nd AIAA/CEAS Aeroacoustics Conference. AIAA Paper* 2016-2736.

Chaitanya, P., Narayanan, S., Joseph, P., Vanderwel, C., Turner, J., Kim, J. W. & Gantapathisubramani, B. 2015 Broadband noise reductions through leading edge serrations on realistic aerofoils. In *21st AIAA/CEAS Aeroacoustics Conference. AIAA Paper* 2015-2202.

Chen, K. K., Tu, J. H. & Rowley, C. W. 2012 Variants of dynamic mode decomposition: boundary conditions, Koopman, and Fourier analyses. *J. Nonlinear Sci.* **22**, 887–915.

Chong, T. P, Vathylakis, A., McEwen, A., Kemsley, F., Muhammad, C. & Siddiqi, S. 2015 Aeroacoustic and aerodynamic performances of an aerofoil subjected to sinusoidal leading edges. In *21st AIAA/CEAS Aeroacoustics Conference. AIAA Paper* 2015-2200.

Christophe, J., Anthoine, J. & Moreau, S. 2009 Amiet's theory in spanwise-varying flow conditions. *AIAA J.* **47** (3), 788–790.

Christophe, J., Anthoine, J., Rambaud, P. & Moreau, S. 2008 Numerical issues in the application of an amiet model for spanwise-varying incoming turbulence. In *14th AIAA/CEAS Aeroacoustics Conference. AIAA Paper* 2008-2865.

Christophe, J., Anthoine, J., Rambaud, P., Schram, C., Mathey, F. & Moreau, S. 2007 Prediction of incoming turbulent noise using a combined numerical/semi-empirical method and experimental validation. In *13th AIAA/CEAS Aeroacoustics Conference. AIAA Paper* 2007-3468.

Clair, V., Polacsek, C., Le Garrec, T., Reboul, G., Gruber, M. & Joseph, P. 2013 Experimental and numerical investigation of turbulence-airfoil noise reduction using wavy edges. *AIAA J.* **51** (11), 2695–2713.

Curle, N. 1955 The influence of solid boundaries upon aerodynamics sound. *Proc. R. Soc. Lond. A* **231**, 505–514.

Department of Transport 2013 UK aviation forecasts. *Tech. Rep.*.

Devenport, W. J., Staubs, J. K. & Glegg, S. A. L. 2010 Sound radiation from real airfoils in turbulence. *J. Sound Vib.* **329**, 3470–3483.

Dieste, M. & Gabard, G. 2012 Random particle methods applied to broadband fan interaction noise. *J. Comput. Phys.* **231**, 369–387.

Evers, I. & Peake, N. 2000 Noise generation by high-frequency gusts interacting with an airfoil in transonic flow. *J. Fluid Mech.* **411**, 91–130.

Ewert, R. 2008 Broadband slat noise prediction based on CAA and stochastic sound sources from a fast random particle-mesh (RPM) method. *J. Comput. Phys.* **37** (4), 369–387.

Farassat, F. 2007 Derivations of formulations 1 and 1a of farassat. NASA/TM-2007-214853 .

Ffowcs Williams, J. E. & Hall, L.H. 1970 Aerodynamic sound generation by turbulent flow in the vicinity of a scattering half plane. *J. Fluid Mech.* **40**, 657–670.

Ffowcs Williams, J. E. & Hawkings, D.L. 1969 Sound generation by turbulence and surface in arbitrary motion. *Philos. Trans. R. Soc. Lond. A* **264**, 321–342.

Fish, F. E., Howle, L. E. & Murray, M. M. 2008 Hydrodynamic flow control in marine mammals. *Integr. Comp. Biol.* **48**, 788–800.

Garrick, I. E. & Watkins, C. E. 1953 A theoretical study of the effect of forward speed on the free-space sound-pressure field around propellers. NACA TN-3018 .

Gea-Aguilera, F. 2017 Aerodynamic and aeroacoustic modelling of engine fan broadband noise. *PhD Thesis* .

Gershfeld, J. 2004 Leading edge noise from thick foils in turbulent flow. *J. Acoust. Soc. Am.* **116**, 1416–1426.

Gill, J., Zhang, X. & Joseph, P. 2013 Symmetric airfoil geometry effects on leading edge noise. *J. Acoust. Soc. Am.* **134** (4), 2669–2680.

Gill, J., Zhang, X. & Joseph, P. 2015 Single velocity-component modeling of leading edge turbulence interaction noise. *J. Acoust. Soc. Am.* **137** (6), 3209–3220.

Glegg, S. A. L. & Devenport, W. 2009 Unsteady loading on an airfoil of arbitrary thickness. *J. Sound Vib.* **319**, 1252–1270.

Glegg, S. A. L. & Devenport, W. 2010 Panel methods for airfoils in turbulent flow. *J. Sound Vib.* **329**, 3709–3720.

Goldstein, M. E. 1978 Unsteady vortical and entropic distortions of potential flows around arbitary obstacles. *J. Fluid Mech.* **89**, 433–468.

Grace, S. 2001 Unsteady blade response: The BVI model vs. the gust model. In *7th AIAA/CEAS Aeroacoustics Conference. AIAA Paper* 2002-2209.

Graham, J. M. R. 1970 Similarity rules for thin aerofoils in non-stationary subsonic flows. *J. Fluid Mech.* **43**, 753–766.

Graham, R. R. 1934 The silent flight of owls. *Aeronaut. J.* **38**, 837–843.

Hansen, K. L., Kelso, R. M. & Dally, B. B 2011 Performance variations of leading-edge tubercles for distinct airfoil profiles. *AIAA J.* **49** (1), 185–194.

Hansen, K. L., Kelso, R. M. & Doolan, C. J. 2010 Reduction of flow induced tonal noise through leading edge tubercle modifications. In *16th AIAA/CEAS Aeroacoustics Conference. AIAA Paper* 2010-3700.

Hansen, K. L., Rostamzadeh, N., Kelso, R. M. & Dally, B. B. 2016 Evolution of the streamwise vortices generated between leading edge tubercles. *J. Fluid Mech.* **788**, 730–766.

Horner, M. B., Saliveros, E. & Galbraith, R. A. McD. 1992 An examination of vortex convection effects during blade-vortex interaction. *Aeronaut. J.* **96**, 373–379.

Howe, M. S. 1976 The influence of vortex shedding on the generation of sound by convected turbulence. *J. Fluid Mech.* **76**, 711–740.

Howe, M. S. 1988 Contributions to the theory of sound production by vortex-airfoil interaction, with application to vortices with finite axial velocity defect. *Proc. R. Soc. Lond. A* **420**, 157–182.

Howe, M. S. 1991 Aerodynamic noise of a serrate trailing edge. *J. Fluid Struct.* **5** (1), 33–45.

Howe, M. S. 1997 Sound generated by fluid-structure interactions. *Comput. Struct.* **65** (3), 433–446.

Howe, M. S. 1998 *Acoustics of fluid-structure interactions*. Cambridge University Press.

Howe, M. S. 2001 Unsteady lift and sound produced by an airfoil in a turbulent boundary layer. *J. Fluids and Struct.* **15**, 207–225.

Howe, M. S. 2002 *Theory of vortex sound*. Cambridge University Press.

Howe, M. S. 2014 *Acoustics and aerodynamic sound*. Cambridge University Press.

Ito, S. 2009 Aerodynamic influence of leading-edge serrations on an airfoil in a low reynolds number-a study of an owl wing with leading edge serrations. *J. Biomech. Sci. Eng.* **4** (1), 117–123.

Jarrin, N., Benhamadouche, S., Laurence, D. & Prosser, R. 2006 A synthetic-eddy method for generating inflow conditions for large-eddy simulations. *Int. J. Heat Fluid Flow* **27** (4), 585–593.

Johari, H., Henoch, C. W., Custodio, D. & Levshin, A. 2007 Effects of leading-edge protuberances on airfoil performance. *AIAA J.* **45** (11), 2634–2642.

Juknevicius, A., Chong, T. P. & Woodhead, P. 2017 Leading edge noise reduction of thin aerofoil by the straight and curved serrations of the add-on type. In *23rd AIAA/CEAS Aeroacoustics Conference. AIAA Paper* 2017-3491.

Karve, R., Gill, J., Gea-Aguilera, F., Angland, D. & Nodé-Langlois, T. 2017 Including wall effects in analytical leading edge noise prediction. In *23rd AIAA/CEAS Aeroacoustics Conference. AIAA Paper* 2017-3198.

Kim, J. W. 2007 Optimised boundary compact finite difference schemes for computational aeroacoustics. *J. Comput. Phys.* **225**, 995–1019.

Kim, J. W. 2010 High-order compact filters with variable cut-off wavenumber and stable boundary treatment. *Comput. Fluids* **39**, 1168–1182.

Kim, J. W. 2013 Quasi-disjoint pentadiagonal matrix systems for the parallelization of compact finite-difference schemes and filters. *J. Comput. Phys.* **241**, 168–194.

Kim, J. W. & Haeri, S. 2015 An advanced synthetic eddy method for the computation of aerofoil-turbulence interaction noise. *J. Comput. Phys.* **287**, 1–17.

Kim, J. W., Haeri, S. & Joseph, P. 2016 On the reduction of aerofoil-turbulence interaction noise associated with wavy leading edges. *J. Fluid Mech.* **792**, 526–552.

Kim, J. W., Lau, A. S. H. & Sandham, N. D. 2010*a* CAA boundary conditions for airfoil noise due to high-frequency gusts. *Proc. Eng.* **6**, 244–253.

Kim, J. W., Lau, A. S. H. & Sandham, N. D. 2010*b* Proposed boundary conditions for gust-airfoil interaction noise. *AIAA J.* **48** (11), 2705–2709.

Kim, J. W. & Lee, D. J. 2000 Generalized characteristic boundary conditions for computational aeroacoustics. *AIAA J.* **38** (11), 2040–2049.

Kim, J. W. & Lee, D. J. 2003 Characteristic interface conditions for multiblock high-order computation on singular structured grid. *AIAA J.* **41** (12), 2341–2348.

Kim, J. W. & Lee, D. J. 2004 Generalized characteristic boundary conditions for computational aeroacoustics, part 2. *AIAA J.* **42** (1), 47–55.

Kim, J. W. & Morris, P. J. 2002 Computation of subsonic inviscid flow past a cone using high-order schemes. *AIAA J.* **40** (10), 1961–1968.

Kitaplioglu, C., Caradonna, C. & Burley, C. L. 1997 Parallel blade-vortex interactions: an experimental study and comparison with computations .

Kraichnan, R. H. 1970 Diffusion by a random velocity field. *Phys. Fluids* **13**, 119101.

Kucukcoskun, K., Christophe, J., Schram, C. & Tournour, M. 2013 Broadband scattering of the turbulence-interaction noise of a stationary airfoil: experimental validation of a semi-analytical model. *Int. J. Aeroacoust.* **12** (1+2), 83–102.

Lau, A. S. H., Haeri, S. & Kim, J. W. 2013 The effect of wavy leading edges on aerofoil-gust interaction noise. *J. Sound Vib.* **332**, 6234–6253.

Lighthill, M. J. 1952 On sound generated aerodynamically I. General theory. *Proc. R. Soc. Lond. A* **211**, 564–587.

Lighthill, M. J. 1956 Drift. *J. Fluid Mech.* **1**, 31–53.

Lockard, D. P. & Morris, P. J. 1998 Radiated noise from airfoils in realistic mean flows. *AIAA J.* **36** (6), 907–914.

Lysak, P. D., Capone, D. E. & Jonson, M. L. 2013 Prediction of high frequency gust response with airfoil thickness effect. *J. Fluids and Struct.* **39**, 258–274.

Lyu, B. & Azarpeyvand, M. 2017 On the noise prediction for serrated leading edges. *J. Fluid Mech.* **826**, 205–234.

Lyu, B., Azarpeyvand, M. & Sinayoko, S. 2016 Prediction of noise from serrated trailing-edges. *J. Fluid Mech.* **793**, 556–588.

Mathews, J. & Peake, N. 2015 Noise generation by turbulence interacting with an aerofoil with a serrated leading edge. In *21st AIAA/CEAS Aeroacoustics Conference. AIAA Paper* 2015-2204.

Mathews, J. & Peake, N. 2018 An analytically-based method for predicting the noise generated by the interaction between turbulence and a serrated leading edge. *J. Sound Vib.* **422**, 506–525.

Migliore, P. & Oerlemans, S. 2004 Wind tunnel aerodynamic tests of six airfoils for use on small wind turbines. *J. Sol. Energy Eng.* **126** (4), 974–985.

Miklosovic, D. S., Murray, M. M., Howle, L. E. & Fish, F. E. 2004 Leading-edge tubercles delay stall on humpback whale (megaptera novaeangliae) flippers. *Phys. Fluids* **16** (5), L39.

Moriarty, P. J., Guidati, G. & Migliore, P. 2005 Prediction of turbulent inflow and trailing-edge noise for wind turbines. In *11th AIAA/CEAS Aeroacoustics Conference. AIAA Paper* 2005-2881.

Myers, M. R. & Kerschen, E. J. 1995 Influence of incidence angle on sound generation by airfoils interacting with high-frequency gusts. *J. Fluid Mech.* **292**, 271–304.

Myers, M. R. & Kerschen, E. J. 1997 Influence of camber on sound generation by airfoils interacting with high-frequency gusts. *J. Fluid Mech.* **353**, 221–259.

Narayanan, S., Chaitanya, P., Haeri, S., Joseph, P., Kim, J. W. & Polacsek, C. 2015 Airfoil noise reductions through leading edge serrations. *Phys. Fluids* **27**, 025109.

Paterson, R. W. & Amiet, R. K. 1976 Acoustic radiation and surface pressure characteristics of an airfoil due to incident turbulence. NASA CR-2733 .

Pérez-Torró, R. & Kim, J. W. 2017 A large-eddy simulation on a deep-stalled aerofoil with a wavy leading edge. *J. Fluid Mech.* **813**, 23–52.

Poinsot, T. J. & Lele, S. K. 1992 Boundary conditions for direct simulations of compressible viscous flows. *J. Comput. Phys.* **101** (1), 104–129.

Pulliam, T. H. & Zingg, D. W. 2014 *Fundamental algorithms in computational fluid dynamics*. Springer.

Reboul, G., Cader, A., Polacsek, C. & Le Garrec, T. 2017 CAA prediction of rotor-stator interaction using synthetic turbulence: application to a low-noise serrated ogv. In *23rd AIAA/CEAS Aeroacoustics Conference. AIAA Paper* 2017-3714.

Rienstra, S. W. 1981 Sound diffraction at a trailing edge. *J. Fluid Mech.* **108**, 443–460.

Rockwell, D. 1998 Vortex-body interactions. *Annu. Rev. Fluid Mech.* **30**, 199–229.

Roger, M. & Carao, A. 2010 Blade-geometry considerations in analytical gust-airfoil interaction noise models. In *16th AIAA/CEAS Aeroacoustics Conference. AIAA Paper* 2010-3799.

Roger, M., Christophe, S. & De Santana, L. 2013 Reduction of airfoil turbulence-impingement noise by means of leading-edge serrations and/or porous materials. In *19th AIAA/CEAS Aeroacoustics Conference. AIAA Paper* 2013-2108.

Roger, M. & Moreau, S. 2010 Extensions and limitations of analytical airfoil broadband noise models. *Intl. J. Aeroacoust.* **9**, 273–305.

Roger, M. & Moreau, S. 2016 Airofil turbulence-impingement noise reduction by porosity or wavy leading-edge cut: experimental investigations. In *Internoise 2016*.

Roger, M., Moreau, S. & Guédel, A. 2006 Vortex-shedding noise and potential-interaction noise modeling by a reversed sears' problem .

Roger, M., Moreau, S. & Kucukcoskun, K. 2016 On sound scattering by rigid edges and wedges in a flow, with applications to high-lift device aeroacoustics. *J. Sound Vib.* **362**, 252–275.

Rostamzadeh, N., Hansen, K. L., Kelso, R. M. & Dally, B. 2014 The formation mechanism and impact of streamwise vortices on naca 0021 airfoil's performance with undulated leading edge modification. *Phys. Fluids* **26**, 107101.

Rozenberg, Y., Roger, M., Guédel, A. & Moreau, S. 2007 Rotating blade self noise: experimental validation of analytical models. In *13th AIAA/CEAS Aeroacoustics Conference. AIAA Paper* 2007-3709.

Sandberg, R. D. & Sandham, N. D. 2006 Noise due to unsteady flow past trailing edges. In *European conference on computational fluid dynamics ECCOMAS CFD*.

Sandberg, R. D. & Sandham, N. D. 2007 A modification of amiet's classical trailing edge noise theory for strictly two dimensional flows. *University of Southampton: Report No.* AFM-07/04 .

Santana, L., Schram, C. & Desmet, W. 2012 Panel method for turbulence-airfoil interaction noise prediction. In *18th AIAA/CEAS Aeroacoustics Conference. AIAA Paper* 2012-2073.

Santana, L., Schram, C. & Desmet, W. 2016 Low-frequency extension of amiet's theory for compact noise predictions. *J. Sound Vib.* **372**, 342–356.

Schmid, P. 2010 Dynamic mode decomposition of numerical and experimental data. *J. Fluid Mech.* **656**, 5–28.

Sears, W. R. 1941 Some aspects of non-stationary airfoil theory and its practical application. *J. Aeronaut. Sci.* **8** (3), 104–108.

Sescu, A. & Hixon, R. 2013 Towards low-noise synthetic turbulent inflow conditions for aeroacoustic calculations. *Intl. J. Numer. Methods Fluids* **73** (12), 1001–1010.

Skillen, A., Revell, A., Pinelli, A., Piomelli, U. & Favier, J. 2015 Flow over a wing with leading-edge undulations. *AIAA J.* **53** (2), 464–472.

Soderman, P. 1973 Leading-edge serrations which reduce the noise of low-speed rotors. NASA/TN-D-7371 .

Straus, J., Renzoni, P. & Mayle, R. E. 1990 Airfoil pressure measurements during a blade vortex interaction and a comparison with theory. *AIAA J.* **28** (2), 222–228.

Thom, A. & Duraisamy, K. 2010 High-resolution simulations of parallel blade-vortex interactions. *AIAA J.* **48** (10), 2313–2324.

Tong, F., Qiao, W., Chen, W., Cheng, H., Wei, R. & Wang, X. 2018*a* Numerical analysis of broadband noise reductions with wavy leading edges. *Chin. J. Aeronaut.* .

Tong, F., Qiao, W., Xu, K., Wang, L., Chen, W. & Wang, X. 2018*b* On the study of wavy leading-edge vanes to achieve low fan interaction noise. *J. Sound Vib.* **419**, 200–226.

Tsuji, Y., Fransson, J. H. M., Alfredsson, P. H. & Johansson, A. V. 2007 Pressure statistics and their scaling in high-Reynolds-number turbulent boundary layers. *J. Fluid Mech.* **585**, 1–40.

Turner, J., Kim, J. W., Chaitanya, P. & Joseph, P. 2016*a* Towards understanding aerofoils with dual-frequency wavy leading edges interacting with vortical disturbances. In *22nd AIAA/CEAS Aeroacoustics Conference. AIAA Paper* 2016-2951.

Turner, J. M., Haeri, S. & Kim, J. W. 2016*b* Improving the boundary efficiency of a compact finite difference scheme through optimising its composite template. *Comput. Fluids* **138**, 9–25.

Turner, J. M. & Kim, J. W. 2017*a* Aeroacoustic effects of the trailing edge of an undulated aerofoil subjected to impinging disturbances. In *23rd AIAA/CEAS Aeroacoustics Conference. AIAA Paper* 2017-3494.

Turner, J. M. & Kim, J. W. 2017*b* Aeroacoustic source mechanisms of a wavy leading edge undergoing vortical disturbances. *J. Fluid Mech.* **811**, 582–611.

World Health Organization 2011 Burden of disease from environmental noise. *Tech. Rep.*.

Yee, H. C., Sandham, N. D. & Djomehri, M. J. 1999 Low-dissipative high-order shock-capturing methods using characteristic-based filters. *J. Comput. Phys.* **150**, 199–238.

Yoon, H. S., Hung, P. A. & Kim, M. C. 2011 Effect of the wavy leading edge on hydrodynamic characteristics for flow around low aspect ratio wing. *Comput. Fluids* **149**, 276–289.